

SYNTHESIS AND CHARACTERIZATION OF BLOCK COPOLYMER-MEDIATED GOLD NANOPARTICLES

By

DEBES RAY

Enrolment No. PHYS01200704032

Bhabha Atomic Research Centre, Mumbai, India

A thesis submitted to the

Board of Studies in Physical Sciences

In partial fulfillment of requirements

For the Degree of

DOCTOR OF PHILOSOPHY

of

HOMI BHABHA NATIONAL INSTITUTE



May, 2012

Homi Bhabha National Institute

Recommendations of the Viva Voce Board

As members of the Viva Voce Board, we certify that we have read the dissertation prepared by Debes Ray entitled “Synthesis and Characterization of Block Copolymer-Mediated Gold Nanoparticles” and recommend that it may be accepted as fulfilling the dissertation requirement for the Degree of Doctor of Philosophy.

_____ **Date:**
Chairman- Dr. S.L. Chaplot

_____ **Date:**
Guide/Convener- Dr. V.K. Aswal

_____ **Date:**
External Examiner (Prof. H.B. Bohidar)

_____ **Date:**
Member 1- Dr. A.G. Wagh

_____ **Date:**
Member 2- Dr. S. Basu

_____ **Date:**
Member 3- Prof. M. Senthil Kumar

_____ **Date:**
Member 4- Dr. P.A. Hassan

Final approval and acceptance of this dissertation is contingent upon the candidate's submission of the final copies of the dissertation to HBNI.

I hereby certify that I have read this dissertation prepared under my direction and recommend that it may be accepted as fulfilling the dissertation requirement.

Date:

Place:

(Guide)

STATEMENT BY AUTHOR

This dissertation has been submitted in partial fulfillment of requirements for an advanced degree at Homi Bhabha National Institute (HBNI) and is deposited in the Library to be made available to borrowers under rules of the HBNI.

Brief quotations from this dissertation are allowable without special permission, provided that accurate acknowledgement of source is made. Requests for permission for extended quotation from or reproduction of this manuscript in whole or in part may be granted by the Competent Authority of HBNI when in his or her judgment the proposed use of the material is in the interests of scholarship. In all other instances, however, permission must be obtained from the author.

Debes Ray

DECLARATION

I, hereby declare that the investigation presented in the thesis has been carried out by me. The work is original and has not been submitted earlier as a whole or in part for a degree / diploma at this or any other Institution / University.

Debes Ray

DECLARATION

I, hereby declare that the queries raised by the examiners of the thesis have been incorporated as suggested.

Dr. V.K. Aswal

(Guide)

Dedicated

To

My Parents and Brother

Acknowledgements

I would like to express my deep sense of gratitude to my thesis supervisor Dr. V.K. Aswal, Solid State Physics Division, Bhabha Atomic Research Centre, for his guidance, continuous support and encouragement throughout the period of my work. It is also my great pleasure to thank Dr. S.L. Chaplot, Head, Solid State Physics Division and Dr. A.G. Wagh, Former Head, Optics and Small Angle Scattering Section, Solid State Physics Division, for their support and encouragement. I am also thankful to all the members of my doctoral committee for their guidance and support.

I would like to thank Dr. P.A. Hassan, Chemistry Division, Bhabha Atomic Research Centre, for many fruitful discussions and help during dynamic light scattering measurements. My thanks are also attributable to Dr. J. Kohlbrecher, for his help in small-angle neutron scattering experiments at the SINQ, Paul Scherer Institute, Switzerland, and Dr. G. Kumaraswamy and Mr. E. Venugopal, in carrying out small-angle X-ray scattering experiments at the National Chemical Laboratory, Pune. I am grateful to Dr. D. Srivastava and Mr. A.P. Srivastava, Materials Science Division, Bhabha Atomic Research Centre, for their support and help during transmission electron microscopy experiments.

I am also thankful to Dr. P.U.M. Sastry, Mr. A.K. Patra, Dr. D. Sen, Dr. S. Abbas and Mr. J. Bahadur, for their constructive support during the period of my thesis work.

I have benefitted immensely from the many fruitful discussions with colleagues Dr. Shirish Chodankar, Mr. Akshay J. Chinchalikar and Mr. Sugam Kumar. Also my special thanks to friends Nazir, Arvind, Sandip, Sourav, Madhumita, Tista, Ripandeep, Neetika, Anuvab, Pankaj, Rohit, Naveen, Sunil, Siba, Lokesh, Sanat, Rajib, Siddharth, Preyoshi, Indu, Anup, Palash and others who directly or indirectly have helped me in achieving my goals.

I take this opportunity especially to thank my parents, brother and all the family members for being supportive in my endeavour and extending encouragement in spite of remaining aloof from my responsibilities towards them. Without their patience and constant encouragement this would not have been easy.

CONTENTS

	Page No.
SYNOPSIS	xiii
LIST OF FIGURES	xxiii
LIST OF TABLES	xxx
1. SYNTHESIS, CHARACTERIZATION AND APPLICATIONS OF GOLD NANOPARTICLES	1-34
1.1. Introduction	1
1.2. Characteristics of Gold Nanoparticles	5
1.3. Synthesis of Gold Nanoparticles	10
1.3.1. Top-Down Approach	11
1.3.2. Bottom-Up Approach	12
1.4. Characterization Techniques	14
1.4.1. Spectroscopic Techniques	14
1.4.2. Microscopic Techniques	17
1.4.3. Scattering Techniques	20
1.5. Applications of Gold Nanoparticles	24
1.5.1. Biology	24
1.5.2. Nanoelectronics	28
1.5.3. Catalysis	30
1.6. Objective of the Thesis	31
1.7. Summary	33

2. BLOCK COPOLYMER-MEDIATED SYNTHESIS OF GOLD NANOPARTICLES	35-55
2.1. Introduction	35
2.2. Block Copolymer	36
2.2.1. Block Copolymer Structure and Classification	37
2.2.2. Amphiphilic Block Copolymers and Self-Assembly	41
2.2.3. Applications of Block Copolymers	46
2.3. Synthesis of Gold Nanoparticles by Block Copolymers	47
2.3.1. Synthesis Method	48
2.3.2. Role of Block Copolymer	50
2.3.3. Mechanism and Tuning of the Synthesis	52
2.4. Layout of the Thesis	54
2.5. Summary	55
3. MULTI-TECHNIQUE APPROACH FOR CHARACTERIZATION OF GOLD NANOPARTICLES	56-82
3.1. Introduction	56
3.2. UV-Visible Spectroscopy	57
3.2.1. Surface Plasmon Resonance	57
3.2.2. Experimental Details	59
3.2.3. Characterization of Gold Nanoparticles by UV-Visible spectroscopy	61
3.3. Transmission Electron Microscopy	63
3.3.1. Experimental Details	63
3.3.2. Gold Nanoparticles as Characterized by Transmission electron Microscopy	65

3.4. Dynamic Light Scattering	67
3.4.1. Theory of Dynamic Light Scattering	67
3.4.2. Experimental Details	68
3.4.3. Characterization of Gold Nanoparticles by Dynamic Light Scattering	70
3.5. Small-Angle Scattering	70
3.5.1. Theory of Small-Angle Scattering	71
3.5.2. Small-Angle X-Ray vs. Neutron Scattering	75
3.5.3. Experimental Details	78
3.5.3.1. Small-Angle X-Ray Scattering	78
3.5.3.2. Small-Angle Neutron Scattering	78
3.5.4. Gold Nanoparticles as Characterized by Small-Angle Scattering	80
3.6. Summary	82

4. OPTIMIZATION OF THE BLOCK COPOLYMER-MEDIATED

SYNTHESIS OF GOLD NANOPARTICLES	83-105
4.1. Introduction	83
4.2. Experimental Procedure	85
4.2.1. Materials	85
4.2.2. Synthesis of Gold Nanoparticles	85
4.2.3. Characterization of Gold Nanoparticles	85
4.3. Results and Discussion	87
4.3.1. Role of Gold Salt Concentration	87
4.3.2. Dependence on Block Copolymer Concentration	96
4.4. Conclusions	104

5. CORRELATING BLOCK COPOLYMER SELF-ASSEMBLY TO THE GOLD NANOPARTICLE SYNTHESIS	106-127
5.1. Introduction	106
5.2. Experimental Procedure	107
5.2.1. Materials	107
5.2.2. Synthesis of Gold Nanoparticles	108
5.2.3. Characterization of Gold Nanoparticles	108
5.3. Results and Discussion	109
5.3.1. Tuning of Block Copolymer Self-Assembly	109
5.3.2. Gold Nanoparticle Synthesis with Different Block Copolymers	116
5.3.3. Temperature-Induced Synthesis	121
5.4. Conclusions	126
6. HIGH-YIELD SYNTHESIS OF GOLD NANOPARTICLES	128-152
6.1. Introduction	128
6.2. Experimental Procedure	129
6.2.1. Materials	129
6.2.2. Synthesis of Gold Nanoparticles	130
6.2.3. Characterization of Gold Nanoparticles	130
6.3. Results and Discussion	131
6.3.1. Step-Addition Method	132
6.3.2. Additional Reductant Method	136
6.4. Conclusions	152

7. INTERACTION OF GOLD NANOPARTICLE WITH PROTEINS	153-169
7.1. Introduction	153
7.2. Experimental Procedure	155
7.2.1. Materials	155
7.2.2. Synthesis of Gold Nanoparticles and their Interaction with Proteins	155
7.2.3. Characterization of Gold Nanoparticles and Nanoparticle-Protein Conjugates	155
7.3. Results and Discussion	156
7.3.1. Optimization of Synthesis	157
7.3.2. Gold Nanoparticle Interaction with Lysozyme and BSA Proteins	161
7.3.3. Structure of Gold Nanoparticle-Protein Conjugates	164
7.4. Conclusions	169
8. SUMMARY	170-175
REFERENCES	176-185
LIST OF PUBLICATIONS	186

**SYNOPSIS OF THE THESIS TO BE SUBMITTED TO
HOMI BHABHA NATIONAL INSTITUTE FOR THE DEGREE OF
DOCTOR OF PHILOSOPHY IN PHYSICAL SCIENCES**



Name of the Candidate : Debes Ray

Name of the Guide : Dr. V. K. Aswal
Solid State Physics Division
Bhabha Atomic Research Centre
Trombay, Mumbai 400 085

Registration Number : PHYS01200704032

Date of Registration : 17th October 2008

Title of the Thesis : Synthesis and Characterization of Block
Copolymer-mediated Gold Nanoparticles

Place of Research Work : Solid State Physics Division
Bhabha Atomic Research Centre
Trombay, Mumbai 400 085

Signature of the Candidate :

Signature of the Guide :

SYNOPSIS

SYNTHESIS AND CHARACTERIZATION OF BLOCK COPOLYMER-MEDIATED GOLD NANOPARTICLES

The field of nanoscience and nanotechnology deals with development and understanding of materials having at least one of its dimensions in nanoscale (1–100 nm). These nanomaterials display properties significantly different from those of compositional atoms and molecules as well as corresponding bulk materials [1]. For example, they dissolve in different ways, take on different magnetic properties, react differently to chemicals or reflect light differently from the way they would at their bulk. The unique properties of nanomaterials primarily originate from their small dimensions (enabling high speed and high functional density), very large surface area (providing high sensitivity and catalytic effects), quantum effects (highly efficient fluorescent quantum dots, superparamagnetism in magnetic materials) and new molecular structures (high strength nanotubes, graphene, nano fibers and nano composites). These features have been widely exploited for various multidisciplinary applications in sensing, photonics, catalysis, biomedical and electronics using different kinds of nanostructures. Nanoparticles, with all the three dimensions in nanoscale, represent the most widespread current form of nanomaterials [2]. A huge variety of different types of particles are already available, ranging from simple ultraviolet absorbers used in sunscreens to highly sophisticated and polyfunctional particles used to control drug delivery and from their use in single electron devices to the absorption, conversion and storage of solar energy. These advances have been made possible with the development of controlled synthesis methodologies and advanced characterization techniques. This thesis provides insight into the synthesis and characterization of one of novel ways of forming gold nanoparticles.

The thesis consists of eight chapters. The different aspects of gold nanoparticles covering synthesis, their characterization and various applications are discussed in Chapter 1. This chapter also describes the objective of the thesis to look into the details of a novel method of synthesizing gold nanoparticles. Chapter 2 provides background of block copolymer-mediated synthesis of gold nanoparticles used in the present thesis. The layout of thesis is also given in Chapter 2. The multi-technique approach has been applied to characterize the gold nanoparticles under study. These different techniques are described in Chapter 3. This thesis aims to understand the role of different components in tuning different parameters (formation rate, yield, stability, shape and size of nanoparticles) of block copolymer-mediated synthesis of gold nanoparticles. Chapter 4 deals with optimization of the

synthesis for its dependence on gold salt and block copolymer concentrations to improve the yield. The correlation of self-assembly of block copolymers by varying chemical composition and temperature to synthesizing gold nanoparticles is studied in Chapter 5. Two methods (step-addition method and additional reductant method) of high-yield synthesis of gold nanoparticles have been developed and are discussed in Chapter 6. The interaction of high-yield gold nanoparticles has been examined with two model proteins (Lysozyme and BSA) and results are presented in Chapter 7. Chapter 8 provides the summary of the thesis.

Gold nanoparticles have been of recent great interest in the context of its diverse applications due to their unique optical, electronic, catalytic and chemical properties [3]. The unusual optical properties of this noble metal, their size-dependent electrochemistry and high chemical stability have made them the model system of choice for exploring a wide range of phenomena including self-assembly, bio-labeling, catalysis etc. They can be synthesized by different ways depending on their applications [4]. **Chapter 1** gives an introduction to different methods to synthesize gold nanoparticles, their characterization and various applications. All the methods of synthesis of gold nanoparticles are broadly classified in two categories as top-down and bottom-up methods. The top-down approach is a subtractive process starting from bulk materials to make nanomaterials while bottom-up is a controlled additive process that deals with the assembly of precursor atoms or molecules to make nanomaterials. In general, top-down approaches are easier to use and less expensive but have less control over the size distribution and also could be destructive. On the other hand, bottom-up methods are chemically controllable and non-destructive. Among all bottom-up methods, the chemical reduction of the metal salt in an aqueous, an organic phase, or two phases, is one of the most popular routes as nanoparticles of a wide range of sizes and shapes can be prepared by controlling the reaction conditions. There is variety of techniques for the characterization of nanoparticles. Spectroscopic techniques (e.g. UV-visible, Raman, IR and NMR) are employed for the confirmation of the presence of molecular species and electronic transitions, monitoring phase transitions and band gap calculations, studying luminescence, fluorescence and chemical species etc. Microscopic techniques (e.g. TEM, SEM, STM and AFM) give the direct visualization of the morphology, particle size, phases, defects etc. Scattering techniques (e.g. XRD, SAXS, SANS and DLS) are extremely reliable for finding the particle size, shape, number density, interactions and crystal structure. Gold nanoparticles are extensively used in the fields of biology, catalysis, electronics, sensing etc. In biology and medicine, gold nanoparticles are used for drug delivery, labeling, sensing and heating. Gold is very popular for being chemically inert and one of the most stable metals, thus resistant to

oxidation. Catalysis with gold nanoparticles, in particular the very active oxide-supported ones, is now an expanding area, and a large number of new catalytic systems for various reactions are now being explored. Further, electronic conduction correlated with single-electron tunnelling involving gold nanoparticles are being studied as basis for future nanoelectronics. Excellent sensory and environmental devices are becoming available for various applications by tuning the spectroscopy, fluorescence, luminescence, and electrochemical characteristics of gold nanoparticles with different substrates including DNA, sugars and other biological molecules. For all these applications, synthesis and characterization of gold nanoparticle play an important role for achieving the better results [5].

This thesis deals with synthesis and characterization of block copolymer-mediated gold nanoparticles. Use of block copolymers for the synthesis of gold nanoparticles has many advantages e.g. block copolymer not only plays the dual role of reductant and stabilizer but also provide an economical and environmentally benign way for the synthesis of gold nanoparticles [6]. **Chapter 2** provides background of block copolymer-mediated synthesis of gold nanoparticles. Copolymers are special type of polymers which have two or more different monomer units linked by covalent bond. PEO-PPO-PEO triblock copolymers are well-known non-ionic surfactants (with commercial name of Pluronics) with two dissimilar moieties, hydrophilic PEO block and hydrophobic PPO block, within the same molecule [7]. These amphiphilic triblock copolymers possess symmetrical structure $(EO)_x(PO)_y(EO)_x$ where x and y denote the number of ethylene oxide and propylene oxide monomers per block, respectively and are available in a range of x and y values in the form of pastes, flakes and liquids. In aqueous solution, the molecules self-assemble to form micelles of various forms and sizes, depending on thermodynamic parameters (entropy or enthalpy driven) [8]. The hydrophobic blocks of the block copolymers (PPO) form the core of these micellar aggregates whereas the hydrophilic ones (PEO) with the surrounding water molecules form the corona. The block copolymers can be used to produce metal nanoparticles because of their ability to reduce metal ions. On mixing the aqueous solution of metal (e.g. gold) salt and block copolymers, these polymeric nanostructured matrixes engulf the ionic metal precursors, which after subsequent reduction form nanoparticles [9]. Self-assembly of block copolymer in this method is utilized to control the synthesis of gold nanoparticles. The reduction of bound gold ions proceeds via oxidation of the oxyethylene and oxypropylene segments by the metal center. PEO is known to form a conformation similar to pseudo-crown ether structure that is able to bind with metal ions. The induced cyclization is caused by ion-dipole

interactions between the templating ion and the electron lone pairs of the ethylene oxide linkages. PPO facilitates growth of gold clusters to nanoparticles by block copolymer adsorption on gold clusters and reduction of gold ions on the surface of these clusters. The formation of gold nanoparticles from gold salt comprises three main steps: (i) reduction of gold ions by the block copolymers in the solution and formation of gold clusters, (ii) adsorption of block copolymers on gold clusters and reduction of gold ions on the surfaces of these gold clusters and (iii) growth of gold particles in steps and finally its stabilization by block copolymers. This thesis aims to look into the improvement of the overall synthesis process by tuning these steps of the reaction mechanism in different ways [10-20].

A multi-technique approach combining spectroscopy, microscopy and scattering techniques has been used in this thesis for the characterization of gold nanoparticles [10, 11]. The use of different techniques is required for obtaining complementary results for understanding and tuning of the synthesis. The different techniques used are UV-visible spectroscopy, small-angle neutron scattering (SANS), small-angle x-ray scattering (SAXS), dynamic light scattering (DLS) and transmission electron microscopy (TEM). The details of these techniques are described in **Chapter 3**. The technique of UV-visible spectroscopy measures the absorbance or transmittance of the sample solution to characterize nanoparticles through the characteristic SPR peak. This peak arises due to the resonance between the incident radiation and collective oscillation of conducting electrons of nanoparticles. The gold nanoparticles show SPR peak at ~ 530 nm. The broadening of peak relates the shape and size of the nanoparticles. The absorbance is proportional to the number density and hence can be used to measure the formation rate and the stability of gold nanoparticle during the synthesis. The high contrast of gold nanoparticles for electrons enables TEM to determine directly the shape and size of gold nanoparticles. However, this technique is statistically less accurate (probes small sample volumes) as well as insensitive to low-Z elements such as block copolymers. The different scattering techniques (SAXS, SANS, DLS) probe systems under native conditions and over large sample volumes. In all these scattering techniques the radiation (X-ray, neutron or light) is scattered by the sample and the resulting scattering pattern is analyzed to provide information about the structure (shape and size), interaction and the order of the components of the samples. X-rays are scattered by the electron density fluctuation, which is proportional to the atomic number and enables SAXS to determine the size distribution of the nanoparticles. The fact that scattering is very different for neutrons from hydrogen and deuterium (isotope effect), contrast variation SANS by mixing hydrogenous and deuterated constituents can be used to study different components (gold

nanoparticle and block copolymer) in these systems. In DLS, time-dependent fluctuations in the intensity of the scattered light are measured. Analysis of intensity fluctuations enables the determination of diffusion coefficients associated with different structures in the system.

The synthesis of gold nanoparticles involves mixing of aqueous solutions of block copolymer and gold salt at room temperature. **Chapter 4** gives the results of the optimization of synthesis of gold nanoparticles for its dependence on block copolymer and gold salt concentration to improve the yield [12-14]. It has been observed that the yield of gold nanoparticles simply does not increase with the increase in block copolymer or gold salt concentration. The yield of gold nanoparticles at a given block copolymer concentration shows a maximum at fixed gold salt concentration [e.g. 0.008 wt% for 1 wt% P85 (EO₂₆PO₃₉EO₂₆)], below and above which the yield decreases. The occurrence of maximum is decided by the minimum molar ratio of block copolymer-to-gold salt (r_{min}) required for block copolymer to reduce the gold ions and hence synthesis. At low concentrations of gold salt corresponds to higher molar ratio of block copolymer to gold salt (r) than r_{min} , the reduction is maintained and therefore the yield increases with the gold salt concentration up to the value of r_{min} . At higher gold salt concentrations with fixed amount of block copolymer, the decrease in their molar ratio suppresses the reduction and hence the decrease in the resultant yields. The similar trend of role of gold salt concentration is observed when the block copolymer concentration is varied. In this case as expected, the value of r_{min} decides the amount of gold salt concentration at which the yield is maximum increases linearly with the block copolymer concentration. However, the yield is not found to be proportional to the gold salt concentration and decreases from linearity with the increase in the block copolymer concentration. SANS data suggests that the most of the block copolymers form their own micelles and only a very small fraction of block copolymers utilized for the stabilization of the nanoparticles. These results have also been confirmed by the DLS. The scattering from gold nanoparticles as compared to that from block copolymer micelles is negligibly small to see gold nanoparticles by SANS or DLS. The size distribution of gold nanoparticles has been determined by TEM and the average size in these systems is found to be in the range 10–20 nm. The stability of gold nanoparticles has been examined by time-dependent UV-visible spectroscopy measurements. All these data show three distinct regions as (i) Formation region, (ii) Saturation region and (iii) Stability region. In the formation region, the yield of nanoparticles increases linearly with time. Higher the values of block copolymer concentration and gold salt concentration, higher will be its tendency to nucleate and grow the nanoparticles. The saturation region is obtained when most of gold ions have been

utilized in the formation of nanoparticles. The substantial decrease in the stability for higher block copolymer concentration arises because of large size of the nanoparticles formed in these systems.

Self-assembly is a characteristic structural phenomenon of amphiphilic block copolymers and its role in the synthesis of gold nanoparticles has been examined in **Chapter 5** [15]. The self-assembly has been tuned by varying the chemical structure of the block copolymer and solution temperature. The synthesis is carried out using three different block copolymers P85, F88 (EO₁₀₃PO₃₉EO₁₀₃) and P105 (EO₃₇PO₅₆EO₃₇), which not only have varying molecular weight but also differ in hydrophobicity to hydrophilicity ratio. It has been found that the yield of gold nanoparticles increases in the order F88 < P85 < P105. The fact that P105 has higher tendency to self-assemble, it results in higher yield as compared to P85 and F88. The formation rate is also found faster for the system having higher yield. The P105 block copolymer, having the highest tendency of self-assembly, forms the nanoparticles with largest sizes whereas the size of the nanoparticles decreases for P85 and F88 and are mostly consists of block copolymer cross-linked small gold nanoparticles. Block copolymers self-assembly leads to a sphere-to-rod micellar shape transition at higher temperatures (e.g. 75 °C for 1 wt% P85) and its effect on the gold nanoparticle synthesis has been studied. Our results show that irrespective of shape of block copolymer micelles the synthesis carried out at different temperature gives rise to the synthesis of similar spherical nanoparticles. This is believed to be because of the differences in the driving force of block copolymer to self-assemble to micelles and in synthesizing nanoparticles. However, it has been found that increasing temperature increases the reaction kinetics drastically, resulting in much faster synthesis of nanoparticles (within few minutes).

All the synthesis carried out so far show relatively low yield in block copolymer-mediated synthesis of gold nanoparticles and is understood to be limited by the capability of the reduction of gold ions by block copolymers. **Chapter 6** discusses the development of two methods of high-yield synthesis of gold nanoparticles, where the yield can be enhanced by manyfold [16-18]. The first method based on step addition, the gold salt is added in small steps to maintain the continuous formation of nanoparticles. The fact that there exists a minimum ratio of block copolymer-to-gold salt (r_{min}) for the reduction to take place and most of the block copolymers remain free from the gold nanoparticles, the step size is decided by the gold salt concentration little less than that of the r_{min} . The time between two steps is decided by the time required to complete the synthesis in each step (about 2–3 hrs). In this method thus the yield can be increased by number of steps used. However, the application of

this method is limited by the longer synthesis time which increases as the number of steps increased to increase the yield. In the second method (additional reductant method), the presence of additional reductant (e.g. trisodium citrate) is utilized to enhance the reduction and hence yield. The nanoparticle yield has been found to increase drastically with gold salt concentration in presence of additional reductant and has been synthesized up to two order higher gold salt concentrations than earlier works. This method can be viewed as the additive effect of the enhanced reduction by trisodium citrate with control and stabilization by the block copolymers. The size of the nanoparticles also increases with the nanoparticle concentration. The time-dependent decrease in the concentration of nanoparticles observed at higher gold salt concentrations is related to the increased surface coating of gold nanoparticles.

Chapter 7 presents optimization of high yield synthesis of gold nanoparticle for probing their interaction with proteins [19, 20]. The stable and high-yield gold nanoparticles have been synthesized at very low block copolymer concentration (decrease of 3 orders) to minimize any direct interaction of proteins with the block copolymer. The faster formation rate of gold nanoparticles is found with higher value of block copolymer concentration in these systems. The stability and yield of nanoparticle remain same irrespective of the large decrease in block copolymer concentration. The nanoparticle structure is also found identical irrespective of block copolymer concentration. The interaction of these gold nanoparticles with two model proteins, lysozyme and bovine serum albumin (BSA) has been examined. It has been found that gold nanoparticles form stable solutions over a wide concentration range of BSA whereas phase separate even with small amount of lysozyme protein at physiological conditions. These results can be explained on the basis of that citrate ions are adsorbed on the gold nanoparticles make it negative, as a result their complex with positively charged lysozyme phase separates whereas it remains stable with similarly charged BSA. The complexes of gold nanoparticles with BSA have been studied using UV-visible spectroscopy, zeta potential and SANS. The presence of BSA shows a red shift in the SPR peak and is believed to be due to the changes in the dielectric nature surrounding the nanoparticles without and with protein conjugation. Further the conjugation of BSA with gold nanoparticles is supported by the zeta potential measurements of nanoparticles in presence of varying protein concentration. SANS data of nanoparticle-protein conjugates have been found to be significantly different than that of addition of individual contributions from gold nanoparticles and BSA. The build-up of scattering intensity in the low-Q region for the

nanoparticle-protein conjugate confirms the adsorption of protein on nanoparticles. The changes in the scattering data arise due to the formation of core-shell structure of adsorbed protein on gold nanoparticles.

Finally the last **8th Chapter** gives the summary of the thesis. This thesis reports the results on synthesis and characterization of block-copolymer mediated gold nanoparticles for understanding the role of different components in tuning the various synthesis parameters (formation rate, yield, stability, shape and size of nanoparticles). A multi-technique approach (combination of UV-visible spectroscopy, TEM, SAXS, SANS and DLS) has been used for the detailed characterization of gold nanoparticles. The main results are:

- i. The optimization of synthesis has been carried out by varying gold salt and block copolymer concentrations. A minimum ratio of block copolymer-to-gold salt is required for maintaining the synthesis. The maximum yield by varying the gold salt or block copolymer concentration is limited by the aggregation of large sized nanoparticles formed at high block copolymer concentrations.
- ii. The role of self-assembly of block copolymer on the synthesis of gold nanoparticles has been investigated. The higher propensity of block copolymer to self-assemble enhances the formation of gold nanoparticles. For block copolymer to self-assemble or mediate in nanoparticle synthesis is driven by different forces.
- iii. Two novel methods (step addition method and additional reductant method) for stable high-yield synthesis of gold nanoparticles have been developed. These methods can enhance nanoparticle yield by manifold than those earlier synthesis methods.
- iv. The gold nanoparticles have been used to examine their interaction with two model proteins lysozyme and BSA. The strong interaction between lysozyme with nanoparticle leads to phase separation whereas BSA adsorption on nanoparticle form a stable complex under physiological conditions.

To conclude, this thesis presents an extensive study of block copolymer-mediated synthesis of gold nanoparticles and their characterization by a combination of spectroscopy, microscopy and scattering techniques. The synthesis has advantages that it is fast, easy to tune and environmentally benign. The role of various components (gold salt, block copolymer and additional reductant) and solution conditions (concentration and temperature) on the optimization various parameters of synthesis such as formation rate, yield, stability, structure of gold nanoparticles has been established. Two novel methods (step addition method and additional reductant method) to achieve stable high yield of gold nanoparticles

have been developed. The interaction of these gold nanoparticles with two model proteins (Lysozyme and BSA) has been studied. The future interest in this work involves utilization of these gold nanoparticles for applications such as in drug delivery and bio-sensing.

REFERENCES

1. G. Cao and Y. Wang, *Nanostructures and Nanomaterials: Synthesis, Properties and Applications*; World Scientific: Singapore (2011).
2. G. Schmid, *Nanoparticles: From Theory to Application*; Wiley-VCH: Weinheim (2010).
3. P.E. Chow, *Gold Nanoparticles: Properties, Characterization and Fabrication*; Nova Science Publishers Inc.: New York (2010).
4. M.C. Daniel and D. Astruc, *Chem. Rev.* **104**, 293 (2004).
5. R. Sardar, A.M. Funston, P. Mulvaney, R.W. Murray, *Langmuir* **25**, 13840 (2009).
6. T. Sakai and P. Alexandridis, *Nanotechnology* **16**, S344 (2005).
7. I.W. Hamley, *Block Copolymers in Solution: Fundamentals and Applications*; Wiley: New York (2005).
8. V.K. Aswal and J. Kohlbrecher, *Chem. Phys. Lett.* **425**, 118 (2006).
9. T. Sakai and P. Alexandridis, *J. Phys. Chem. B* **109**, 7766 (2005).
10. D. Ray and V.K. Aswal, *Nanosci. Nanotechnol. Lett.* **3**, 603 (2011).
11. D. Ray and V.K. Aswal, *AIP Conf. Proc.* **1349**, 405 (2011).
12. D. Ray and V.K. Aswal, *AIP Conf. Proc.* **1202**, 219 (2009).
13. D. Ray, V.K. Aswal and D. Srivastava, *J. Nanosci. Nanotechnol.* **10**, 6356 (2010).
14. D. Ray, V.K. Aswal and D. Srivastava, *Int. J. Nanosci.* **10**, 1035 (2011).
15. D. Ray, V.K. Aswal and D. Srivastava, *J. Nanosci. Nanotechnol.* **11**, 1905 (2011).
16. D. Ray and V.K. Aswal, *J. Macromol. Sci. Part B: Phys.* **49**, 810 (2010).
17. D. Ray, V.K. Aswal and J. Kohlbrecher, *AIP Conf. Proc.* **1313**, 192 (2010).
18. D. Ray, V.K. Aswal and J. Kohlbrecher, *Langmuir* **27**, 4048 (2011).
19. D. Ray and V.K. Aswal, *J. Nanopart. Res.* **14**, 778 (2012).
20. D. Ray, V.K. Aswal and J. Kohlbrecher (Under preparation).

LIST OF FIGURES

Figure 1.1. The length scale of interest in nanoscience (1–100 nm) and its comparison with smaller (atomic) and larger (macroscopic) structures.

Figure 1.2. (a) Gold nanoparticles change colours depending on the particle size (blue to red colour is obtained with decreasing nanoparticle size). (b) Gold nanoparticles absorption for various sizes and shapes.

Figure 1.3. Schematic of a ligand-conjugated gold nanoparticle. The gold core (yellow) is surrounded by stabilizer molecules (red) which provide colloidal stability. Ligands (blue) can be either linked to the shell of stabilizer molecules (as shown here) or directly attached to the gold surface by replacing part of the stabilizer molecules.

Figure 1.4. Schematic representation of the building up of nanoparticles.

Figure 2.1. Schematic of (a) polymer as synthesized through the polymerization of monomer units and (b) different copolymer structures.

Figure 2.2. Schematic of different block copolymer architectures.

Figure 2.3. Structure of Pluronic block copolymer comprising two hydrophilic PEO blocks sandwiched between a hydrophobic PPO block.

Figure 2.4. Schematic of self-assembled amphiphilic block copolymers into supramolecular nanostructure (micelle) in solution.

Figure 2.5. Different structures of self-assembly of block copolymers: (a) spherical micelle, (b) rod-like micelle, (c) vesicle and (d) lamellar.

Figure 2.6. The phase diagram of P85 in D₂O.

Figure 2.7. Schematic of a stimuli-sensitive micellization process.

Figure 2.8. Schematic of synthesis of gold nanoparticles from a mixture of gold salt and block copolymer solutions.

Figure 2.9. The evolution of formation of gold nanoparticles in block copolymer-mediated synthesis.

Figure 2.10. Schematic of a block copolymer-stabilized gold nanoparticle.

Figure 2.11. Scheme of the mechanism of PEO-PPO-PEO block copolymer-mediated formation of gold nanoparticles.

Figure 3.1. Schematic diagram for a UV-visible spectrophotometer.

Figure 3.2. UV-visible spectrum of gold nanoparticles for different sizes ($c > b > a$).

Figure 3.3. UV-visible absorption spectra of different gold nanostructures, e.g. nanoparticles/spheres, decahedra and nanorods.

Figure 3.4. The change in UV-visible spectra of gold nanoparticles on their conjugation with ligand.

Figure 3.5. Schematic of a transmission electron microscope.

Figure 3.6. Carbon film coated copper grid as put on the specimen holder in TEM measurements.

Figure 3.7. (a) TEM micrograph of gold nanoparticles and (b) calculated nanoparticle size distribution.

Figure 3.8. Intensity fluctuations at the detector due the Brownian motion in the sample volume.

Figure 3.9. Schematic of a dynamic light scattering set up.

Figure 3.10. The variation of intensity correlation functions with nanoparticle size. The decay of the function slows down for larger sized particles.

Figure 3.11. Typical curves for (a) $P(Q)$, (b) $S(Q)$ and (c) $d\Sigma/d\Omega(Q)$.

Figure 3.12. Scattering length variation for X-rays and neutrons.

Figure 3.13. Various possible contrast variations in SANS experiment.

Figure 3.14. The schematic of a SAXS instrument.

Figure 3.15. Schematic of SANS facility at BARC.

Figure 3.16. Schematic of the SANS-I facility at PSI, Switzerland.

Figure 3.17. $P(Q)$ -dependence for different shapes of the particles.

Figure 3.18. SAS data from a charged nanoparticle system in presence of varying ionic strength. The increase in the value of cross-section in low- Q region corresponds to the increasing ionic strength.

Figure 4.1. Photograph of gold nanoparticles in aqueous solutions of 1 wt% P85 with varying $\text{HAuCl}_4 \cdot 3\text{H}_2\text{O}$ concentration. The labels show the concentration of gold salt in wt%.

Figure 4.2. UV-visible absorption spectra of the samples of 1 wt% P85 with varying concentration of $\text{HAuCl}_4 \cdot 3\text{H}_2\text{O}$ in aqueous solution.

Figure 4.3. (a) The gold salt concentration normalized SPR peak in UV-visible absorption spectra of 1 wt% P85 with varying concentration of $\text{HAuCl}_4 \cdot 3\text{H}_2\text{O}$ in aqueous solution. (b) Variation of SPR peak absorbance in UV-visible absorption spectra.

Figure 4.4. (a) TEM image of gold nanoparticles in 1 wt% P85 + 0.008 wt% $\text{HAuCl}_4 \cdot 3\text{H}_2\text{O}$. Inset shows the calculated nanoparticle size distribution. (b) TEM image of gold nanoparticles in 1 wt% P85 + 0.016 wt% $\text{HAuCl}_4 \cdot 3\text{H}_2\text{O}$.

Figure 4.5. Time-dependent UV-visible absorption spectra of 1 wt% P85 with 0.008 wt% $\text{HAuCl}_4 \cdot 3\text{H}_2\text{O}$. The different data sets from bottom to top correspond to increase in the absorbance with time. Inset: The variation of the integrated absorbance of SPR peak as a function of time.

Figure 4.6. SANS data of 1 wt% P85 with varying concentration of $\text{HAuCl}_4 \cdot 3\text{H}_2\text{O}$ in aqueous solution. The solid curve is a theoretical fit to the experimental data.

Figure 4.7. Plots of the intensity autocorrelation functions in DLS data of 1 wt% P85 with varying concentration of $\text{HAuCl}_4 \cdot 3\text{H}_2\text{O}$ in aqueous solution. The solid curve is a theoretical fit to the experimental data.

Figure 4.8. UV-visible spectra of (a) 0.5 wt% and (b) 2 wt% P85 with varying $\text{HAuCl}_4 \cdot 3\text{H}_2\text{O}$ concentration.

Figure 4.9. UV-visible spectra of gold nanoparticles corresponding to the maximum yield for block copolymer concentrations of 0.5, 1 and 2 wt%.

Figure 4.10. (a) The variation of $\text{HAuCl}_4 \cdot 3\text{H}_2\text{O}$ concentration required for the maximum yield with block copolymer concentration. (b) The variation of SPR peak absorbance with the increase in the block copolymer concentration.

Figure 4.11. Comparison of integrated intensity of SPR peaks as a function of time for 0.5, 1 and 2 wt% P85 at their corresponding gold salt concentrations of maximum yield. All these data show three different regions (i) Formation, (ii) Saturation and (iii) Stability. Inset: Enlarged view of the formation region of the gold nanoparticles.

Figure 4.12. SANS data with varying block copolymer concentration. The solid curves are the theoretical fits to the experimental data.

Figure 4.13. DLS data with varying block copolymer concentration. The solid curve is a theoretical fit to the experimental data. Inset: The variation of integrated scattering intensity from the sample as a function of block copolymer concentration.

Figure 4.14. SANS data of 0.5, 1 and 2 wt% P85 without and with the addition of gold salt concentrations of the corresponding maximum yield of nanoparticles. The hollow and filled symbols represent data of P85 without and with gold salt, respectively.

Figure 4.15. (a) TEM image of gold nanoparticles in 2 wt% P85 + 0.016 wt% $\text{HAuCl}_4 \cdot 3\text{H}_2\text{O}$ and (b) calculated nanoparticle size distribution.

Figure 5.1. SANS data of pure 1 wt% block copolymer solutions. The solid lines are the theoretical fits to the experimental data.

Figure 5.2. SANS data of 1 wt% block copolymer systems with varying temperature for (a) F88, (b) P85 and (c) P105. The solid curves are theoretical fits to the experimental data.

Figure 5.3. The gold salt concentration normalized SPR peaks of (a) 1 wt% F88 and (b) 1 wt% P105 with varying $\text{HAuCl}_4 \cdot 3\text{H}_2\text{O}$ concentration.

Figure 5.4. Comparison of SPR peaks for 1 wt% block copolymers (F88, P85 and P105) with gold salt concentration corresponding to their maximum yields.

Figure 5.5. Time-dependent variation of yield of gold nanoparticles for 1 wt% block copolymers (F88, P85 and P105) at their corresponding gold salt concentrations of maximum yields.

Figure 5.6. SANS data of 1 wt% block copolymer solutions without and with the gold salt corresponding to their maximum yields.

Figure 5.7. TEM images of gold nanoparticles synthesized using 1 wt% block copolymers (a) P105, (b) P85 and (c) F88 with gold salt in samples corresponding to their maximum yields.

Figure 5.8. UV-visible absorption spectra of 1 wt% block copolymers with $\text{HAuCl}_4 \cdot 3\text{H}_2\text{O}$ corresponding to their maximum yields with varying temperature.

Figure 5.9. (a) Absorbance (Abs_{max}), (b) maximum wavelength (λ_{max}) and (c) full width at half-maximum ($FWHM$) of SPR peak of gold nanoparticles containing 1 wt% block copolymers as a function of temperature.

Figure 5.10. SANS data of 1 wt% P85 with 0.2 wt% $\text{HAuCl}_4 \cdot 3\text{H}_2\text{O}$ in presence of 0.2 wt% Na_3Ct at different temperatures. The solid curves are theoretical fits to the experimental data. The data of 50 and 75 °C are shifted vertically for clarity.

Figure 5.11. TEM images of gold nanoparticles in 1 wt% P85 with 0.2 wt% $\text{HAuCl}_4 \cdot 3\text{H}_2\text{O}$ in presence of 0.2 wt% Na_3Ct at different temperatures.

Figure 6.1. UV-Visible spectra of 1 wt% P85 with varying $\text{HAuCl}_4 \cdot 3\text{H}_2\text{O}$ concentration. The gold salt concentration is added in step of 0.004 wt%. Inset shows the yield-dependence on gold salt concentration.

Figure 6.2. UV-Visible spectra of 1 wt% P85 with 0.02 wt% $\text{HAuCl}_4 \cdot 3\text{H}_2\text{O}$ compared with and without step-addition.

Figure 6.3. SANS data of 1 wt% P85 with 0.02 wt% $\text{HAuCl}_4 \cdot 3\text{H}_2\text{O}$ as obtained with and without step-addition.

Figure 6.4. Photograph of gold nanoparticles in aqueous solutions of 1 wt% P85 + 0.02 wt% $\text{HAuCl}_4 \cdot 3\text{H}_2\text{O}$ with varying trisodium citrate (Na_3Ct) concentration. The labels show the concentration of Na_3Ct in wt%.

Figure 6.5. The variation of SPR peak absorbance in UV-visible absorption spectra of the gold nanoparticles for 1 wt% P85 with 0.01 wt% $\text{HAuCl}_4 \cdot 3\text{H}_2\text{O}$ and varying Na_3Ct concentration.

Figure 6.6. Photograph of gold nanoparticles in aqueous solutions of 1 wt% P85 with varying ($\text{HAuCl}_4 \cdot 3\text{H}_2\text{O}$ + Na_3Ct) concentration. The labels show the concentration in wt%.

Figure 6.7. UV-visible absorption spectra of 1 wt% P85 with varying ($\text{HAuCl}_4 \cdot 3\text{H}_2\text{O}$ + Na_3Ct) concentration.

Figure 6.8. The calculated yield of gold nanoparticles in 1 wt% P85 with varying ($\text{HAuCl}_4 \cdot 3\text{H}_2\text{O}$ + Na_3Ct) concentration. The comparison of nanoparticle concentration without the use of block copolymer is also shown.

Figure 6.9. SANS data of 1 wt% P85 with varying ($\text{HAuCl}_4 \cdot 3\text{H}_2\text{O}$ + Na_3Ct) concentration in D_2O at 30 °C.

Figure 6.10. Schematic of structure of block copolymer-stabilized gold nanoparticles. The samples in cells show that the concentration of gold nanoparticles in presence of additional reductant can be enhanced.

Figure 6.11. SANS data of 1 wt% P85 with varying ($\text{HAuCl}_4 \cdot 3\text{H}_2\text{O} + \text{Na}_3\text{Ct}$) concentration in D_2O at 15 °C.

Figure 6.12. SANS data of 1 wt% P85 with varying ($\text{HAuCl}_4 \cdot 3\text{H}_2\text{O} + \text{Na}_3\text{Ct}$) concentration at 15 °C. The block copolymers are contrast-matched to the solvent (15% D_2O). The solid curves are theoretical fits to the experimental data.

Figure 6.13. The calculated size distributions of gold nanoparticles in 1wt% P85 at varying gold nanoparticle concentration.

Figure 6.14. SAXS data of 1 wt% P85 with varying ($\text{HAuCl}_4 \cdot 3\text{H}_2\text{O} + \text{Na}_3\text{Ct}$) concentration. The solid curves are theoretical fits to the experimental data.

Figure 6.15. TEM micrographs and the calculated size distribution histograms of gold nanoparticles in 1 wt% P85 with varying ($\text{HAuCl}_4 \cdot 3\text{H}_2\text{O} + \text{Na}_3\text{Ct}$) concentration.

Figure 6.16. DLS data of 1 wt% P85 with varying ($\text{HAuCl}_4 \cdot 3\text{H}_2\text{O} + \text{Na}_3\text{Ct}$) concentration. The solid curves are the theoretical fits to the experimental data.

Figure 6.17. Time-dependent UV-visible absorption spectra of 1 wt% P85 with 0.05 wt% $\text{HAuCl}_4 \cdot 3\text{H}_2\text{O} + 0.05$ wt% Na_3Ct . The different data sets from bottom to top correspond to increase in absorbance with time. Inset gives the variation of the integrated absorbance of SPR peak as a function of time.

Figure 6.18. The time-dependent variation of the integrated absorbance (400–800 nm) of SPR peak in 1wt% P85 at different nanoparticle concentrations.

Figure 7.1. Photograph of stable gold nanoparticles at different P85 concentration for 0.2 wt% gold salt and in presence of 0.2 wt% Na_3Ct .

Figure 7.2. SPR peak in UV-visible absorption spectra of varying P85 concentration for 0.2 wt% $\text{HAuCl}_4 \cdot 3\text{H}_2\text{O}$ with 0.2 wt% Na_3Ct .

Figure 7.3. SANS data of varying P85 concentration for 0.2 wt% $\text{HAuCl}_4 \cdot 3\text{H}_2\text{O}$ with 0.2 wt% Na_3Ct in D_2O at 15 °C. The solid curves are the theoretical fits to the experimental data.

Figure 7.4. TEM micrographs of gold nanoparticles for 0.2 wt% $\text{HAuCl}_4 \cdot 3\text{H}_2\text{O}$ with 0.2 wt% Na_3Ct as prepared with varying P85 concentration (a) 0.001, (b) 0.01, (c) 0.1 and (d) 1 wt%.

Figure 7.5. Integrated absorbance of SPR peaks as a function of time for varying P85 concentration with 0.01 wt% $\text{HAuCl}_4 \cdot 3\text{H}_2\text{O}$ and 0.01 wt% Na_3Ct .

Figure 7.6. Photograph of solutions of lysozyme protein with gold nanoparticles. The gold nanoparticles are prepared from 0.01 wt% P85 for 0.2 wt% $\text{HAuCl}_4 \cdot 3\text{H}_2\text{O}$ with 0.2 wt% Na_3Ct whereas lysozyme concentration is varied. The labels show the lysozyme concentrations in wt%.

Figure 7.7. Photograph of solutions of BSA protein with gold nanoparticles. The gold nanoparticles are prepared from 0.01 wt% P85 for 0.2 wt% $\text{HAuCl}_4 \cdot 3\text{H}_2\text{O}$ with 0.2 wt% Na_3Ct whereas BSA concentration is varied. The labels show the BSA concentrations in wt%.

Figure 7.8. Zeta potential of gold nanoparticle-protein conjugates with varying BSA concentration.

Figure 7.9. UV-Visible spectra of gold nanoparticles without and with BSA.

Figure 7.10. SANS data of gold nanoparticles, BSA and their conjugates. The gold nanoparticles in these studies are prepared using 0.01 wt% P85 + 0.2 wt% $\text{HAuCl}_4 \cdot 3\text{H}_2\text{O}$ + 0.2 wt% Na_3Ct system. The pH for BSA is kept at 7.

Figure 7.11. SANS data of gold nanoparticles, BSA and their conjugates in the gold nanoparticle contrast-matched solvent. The gold nanoparticles in these studies are prepared using 0.01 wt% P85 + 0.2 wt% $\text{HAuCl}_4 \cdot 3\text{H}_2\text{O}$ + 0.2 wt% Na_3Ct system. The pH for BSA is kept at 7.

Figure 7.12. SANS data of BSA-gold nanoparticle conjugates of gold nanoparticles (0.01 wt% P85 + 0.2 wt% $\text{HAuCl}_4 \cdot 3\text{H}_2\text{O}$ + 0.2 wt% Na_3Ct) with 1 wt% BSA for two different pH values.

Figure 7.13. SANS data of gold nanoparticles (0.01 wt% P85 + 0.2 wt% $\text{HAuCl}_4 \cdot 3\text{H}_2\text{O}$ + 0.2 wt% Na_3Ct) with varying concentration of BSA. Inset shows the SANS data of corresponding pure BSA system. The pH in all the samples was 7.

LIST OF TABLES

Table 1.1. Some of the widely used gold nanoparticle synthesis methods.

Table 2.1. Chemical structure of various PEO-PPO-PEO block copolymers.

Table 3.1. The complementary observed colours of nanoparticles to that absorbed in SPR.

Table 4.1. Fitted parameters of the micelle structure at different P85 concentrations.

Table 5.1. Details of chemical structure of the PEO-PPO-PEO block copolymers used.

Table 5.2. Fitted structural parameters of self-assembled micellar structures of block copolymers.

Table 5.3. Hydrodynamic size of self-assembly of block copolymers as obtained by DLS.

Table 5.4. Fitted structural parameters of self-assembled micellar structures of block copolymers F88, P85 and P105 with varying temperature. The dimension of spherical micelles is represented by radius (R), ellipsoidal micelles by semi-major axis (a) and semi-minor axis ($b = c$), and rod-like micelles by radius (R) and length (L). The fitted values of radii of gyration of unimers for F88, P85 and P105 are 3.5, 2.4 and 2.8 nm, respectively.

Table 5.5. Fitted structural parameters of gold nanoparticles as obtained by SANS in 1 wt% P85 with 0.2 wt% $\text{HAuCl}_4 \cdot 3\text{H}_2\text{O}$ in presence of 0.2 wt% Na_3Ct at different temperatures.

Table 6.1. The neutrons and X-rays scattering length densities (ρ) of different components in block copolymer-mediated gold nanoparticle system.

Table 6.2. Fitted micellar structure of 1 wt% P85 with varying gold salt and Na_3Ct concentration obtained from SANS data at 30 °C.

Table 6.3. Size parameters of gold nanoparticles as obtained by SAXS in 1 wt% P85 with varying ($\text{HAuCl}_4 \cdot 3\text{H}_2\text{O} + \text{Na}_3\text{Ct}$) concentration.

Table 6.4. Fitted parameters for the system of block copolymer P85 with varying gold salt and Na_3Ct concentration obtained from DLS data at 30 °C. The diffusion coefficient of micelles ($32.4 \times 10^{-6} \text{ cm}^2/\text{sec}$) is kept constant that obtained for the pure block copolymer solution.

Chapter 1

Synthesis, Characterization and Applications of Gold Nanoparticles

1.1. Introduction

The field of nanoscience and nanotechnology deals with development and understanding of materials with at least one of its dimensions in nanoscale in the range 1–100 nm (**Figure 1.1**). Properties of these nanomaterials have been found to be significantly different from that of the compositional atoms as well as corresponding bulk materials [1,2]. Most importantly, properties of materials change as their size approaches the nanoscale and the percentage of atoms at the surface of a material becomes more significant. Nanostructures, whether synthetic or natural, exhibit fascinating properties e.g. quantum confinement in semiconductor particles, surface plasmon resonance in noble metal particles, superparamagnetism in magnetic materials, metallic or semiconducting properties of single wall carbon nanotubes depending upon their diameter, extremely high electron mobility of graphene, significant decrease in electrical resistance in presence of a magnetic field for giant magnetoresistance etc [3-5]. Nanoparticles, with all the three dimensions in nanoscale, represent the most widespread current form of nanomaterials and their striking features have been widely exploited for various multidisciplinary applications in sensing, photonics, catalysis, biomedical, electronics etc [6-9]. These advances have been made possible with the development of controlled synthesis methodologies and advanced characterization techniques.

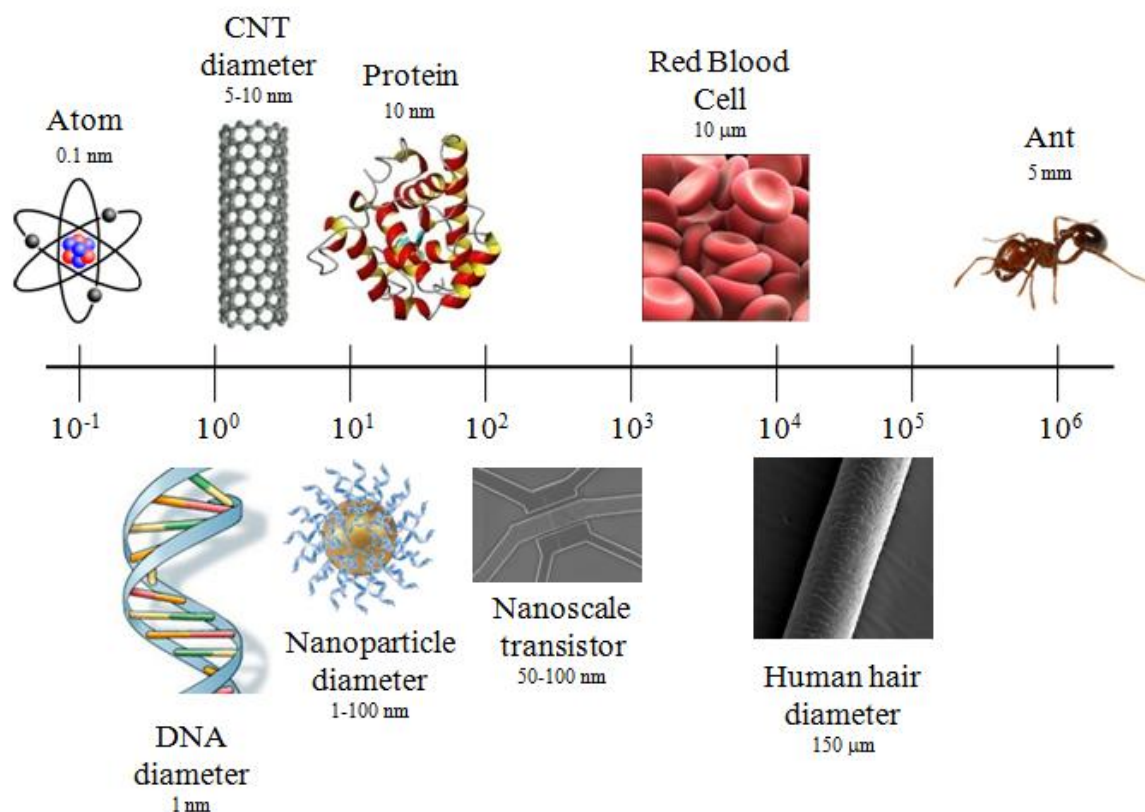


Figure 1.1. The length scale of interest in nanoscience (1–100 nm) and its comparison with smaller (atomic) and larger (macroscopic) structures.

Many nano forms of matter exist around us and their historical milestones spans over centuries. One of the earliest nano-sized objects known to us was made of gold. Faraday prepared colloidal gold in 1856 and called the particles he made the ‘divided state of gold’ which can be suspended in water [10]. In 1890, the German bacteriologist Robert Koch found that compounds made with gold inhibited the growth of bacteria and for this he was awarded Nobel Prize for medicine in 1905. The use of gold in medicinal preparations is not new. In the Indian medical system called Ayurveda, gold is used in several preparations. One popular preparation is called ‘Saraswatharishtam’, prescribed for memory enhancement. All these preparations use finely ground gold. The metal was also used for medical purposes in ancient Egypt where the Egyptians used gold in dentistry [11]. Colloidal gold had been incorporated in glasses and vases to give them colour [12]. The oldest of these is the 4th Century AD

Lycurgus cup made by the Romans. The cup appears red in transmitted light (if a light source is kept within the cup) and appears green in reflected light (if the light source is outside). Modern chemical analysis showed that the glass is not much different from that used today but contains very small amounts of gold (about 40 parts per million) and silver (about 300 parts per million) in the form of nanoparticles to give the cup a dichroic property [13,14].

The science of nanometer scale objects however was not discussed until much later. The Nobel Prize winning physicist, Richard P. Feynman in 1959 gave a talk at the annual meeting of the American Physical Society entitled “There’s plenty of room at the bottom’, stating “The principles of physics, as far as I can see, do not speak against the possibility of maneuvering things atom by atom” [15,16]. He, in a way, suggested the bottom-up approach, “... it is interesting that it would be, in principle, possible (I think) for a physicist to synthesize any chemical substance that the chemist writes down. Give the orders and the physicist synthesizes it. How? Put the atoms down where the chemist says, and so you make the substance. The problems of chemistry and biology can be greatly helped if our ability to see what we are doing, and to do things on an atomic level, is ultimately developed—a development which I think cannot be avoided” [15,16]. However, the world had to wait a long time to put down atoms at the required place. Many would credit this talk as the genesis of the modern field of nanotechnology, the science of manipulating molecular- and atomic-level structures to engineer microscopic devices. Gold nanoparticles have recently become a fundamental building block in nanotechnology due to their unique optical, electronic, catalytic and chemical properties. The high surface-to-volume ratio, size and shape dependent optical features, their size-dependent electrochemistry, high chemical stability and facile surface chemistry have made them the model system of choice for exploring a wide range of phenomena including self-assembly, bio-labeling, catalysis etc. Additional functionality can

be imparted to these particles when they are modified with ligands such as small molecules, polymers or biomolecules [6].

One attractive feature of gold nanoparticles is that their surfaces can be derivatized with thiols, phosphines, alkynes and amines in both aqueous and organic solvents, allowing a range of chemistry to be utilized in particle modification [17]. Gold nanoparticles are often modified by soaking the colloid in a solution of the ligand of interest, making modification straightforward. Another advantage is that gold nanoparticle size can be easily modified to suit the needs of the experiment. For example, larger gold nanoparticles (> 80 nm) scatter light very effectively, making them useful labels in optical microscopy. In contrast, smaller nanoparticles (~ 5 nm) can be used as a size-control template for biomimetic high density lipoprotein structures. A fascinating and useful trait of gold nanoparticles is that their electronic interactions cause a distance dependent color change. This effect is observed in solutions when the particles come within less than one particle diameter of each other. Importantly, almost any surface modification that can be made to the gold nanoparticle that can cause particle cross linking in the presence of a specific analyte, in principle, can result in a colorimetric sensor. Again, the facile and flexible surface chemistry of gold nanoparticles allows for a very wide range of creative surface modifications to achieve this effect. The gold nanoparticle surface enables one to create tailorable, multivalent interfaces, directing the particle to interact with its environment in a highly programmable manner in three dimensions [18]. Gold nanoparticles, thus unmodified or modified, have been of great recent interest in the context of its diverse applications due to their unique properties. They can be synthesized by different ways depending on their application requirements. This thesis provides insight into the synthesis and characterization of gold nanoparticles for a recently developed novel method using block copolymers.

1.2. Characteristics of Gold Nanoparticles

Gold nanoparticles are one of the most commonly used nanoparticles for various applications because of their unique optical, electronic, surface and thermal properties [19].

(i) Optical Properties

Noble metals including gold nanoparticles exhibit different colours depending on the particle size due to surface plasmon resonance (SPR) which is both metal and size dependent. SPR excitation is based on the interaction with the electromagnetic field of the incoming light resulting in a collective oscillation of the electrons on the nanoparticle surface [20,21]. The SPR for gold nanoparticles occur throughout the visible and near-infrared region of the electromagnetic spectrum depending on the size of the nanoparticles (**Figure 1.2**). Besides size, the peak position is influenced by the nanostructure shape and the surrounding media, including the nature of the ligand shell and the interparticle distances in dispersions [22]. In the case when anisotropy is added to the nanoparticle, such as growth of nanorods, the optical properties of the nanoparticles change dramatically.

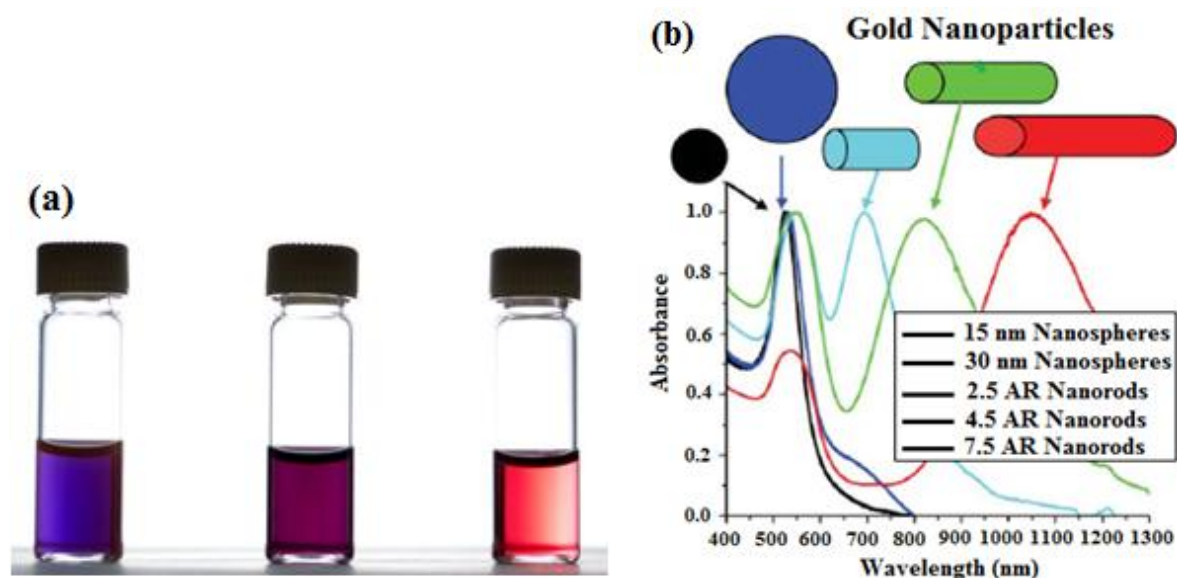


Figure 1.2. (a) Gold nanoparticles change colours depending on the particle size (blue to red colour is obtained with decreasing nanoparticle size). (b) Gold nanoparticles absorption for various sizes and shapes.

Many applications became possible due to the large enhancement of the surface electric field on the gold nanoparticles surface. The plasmon resonance absorption has an absorption coefficient orders of magnitude larger than strongly absorbing dyes. Anisotropic shapes have plasmon resonance absorptions that are even stronger, leading to increased detection sensitivity. Gold nanoparticles generate enhanced electromagnetic fields that affect the local environment. The field is determined by the geometry of the nanoparticle and can enhance fluorescence of the metal itself, the Raman signal of a molecule on the surface, and the scattering of light. The optical properties of noble gold nanoparticles lead to many uses as sensing and imaging techniques. The use of DNA has been pioneered in assembling and studying their interaction and their application in colorimetric detection of biological targets based on the binding events of target DNA [23,24]. Also the use of gold nanoparticles in the field of photonics is immense.

(ii) Electronic Properties

Gold nanoparticles, in particular, exhibit good chemical stability. In principle, they can be surface functionalized with almost every type of electron-donating molecule including biomolecules. Beyond that, in the meantime, several protocols have been developed that allow their assembly into one, two and three dimensions. Altogether, these facts triggered the development of concepts for the design of novel materials with very specific properties based on the unique size-dependent properties of single nanoparticles and their collective properties in assemblies, owing to dipolar, magnetic or electronic coupling. Single nanoparticles with sizes in the range of a few nanometers exhibit an electronic structure that corresponds to an intermediate electronic structure between the band structure of the bulk metal and the discrete energy levels of molecules with a characteristic highest occupied molecular orbital (HOMO)–lowest unoccupied molecular orbital (LUMO) gap [25].

In the size range of approximately 2 nm and below, single particles can be considered as quantum dots. With modern microelectronics, transistors and other microelectronic devices get smaller and smaller. Along with miniaturization, distances between transistors and related switching elements on a chip get shorter and quantum effects become relevant. Today's nanolithographic fabrication techniques allow scaling down to 50nm or below. This has already made a great impact on the performance of traditional semiconductor circuits, and it opens up new opportunities utilizing quantum effects. Following the utilization of charging effects, the so-called Coulomb effects, in metallic circuits comprising tunnel junctions with submicron sizes, allow us to handle individual charge carriers. This field has been named single electronics (SE). It relies on the discreteness of the electric charge, and the tunneling of electrons [single electron tunneling (SET)] in a system of such junctions can be affected by Coulomb interaction of electrons, which can be varied by an externally applied voltage or by injected charges [8,26]. As the continuous miniaturization in microelectronics reaches its physical limits, new concepts are used to achieve component sizes of tens of nanometers or less, or, ideally, the molecular level. Thus, the idea of utilizing the principle of SE for the development of logic and memory cells, which in principle could lead to the construction of a computer working on single electrons, realizing a 'single-electron logic', has triggered intense research activities related to SET phenomena.

(iii) Surface Properties

The surface properties of nanoparticles including surface reactivity are distinctly different from larger particles and have an effect on surface composition, termination, charge and functionalization for nanoparticles [27,28]. Gold nanoparticles are surrounded by a shell of stabilizing molecules. With one of their ends these molecules are either adsorbed or chemically linked to the gold surface, while the other end points towards the solution and

provides colloidal stability. After synthesis of the particles the stabilizer molecules can be replaced by other stabilizer molecules in a ligand exchange reaction. As thiol moieties bind with high affinity to gold surfaces, most frequently thiol-modified ligands are used which bind to the surface of the gold nanoparticles by formation of Au–sulfur bonds. Ligand exchange is motivated by several aspects [29]. Ligand exchange allows, for example, the transfer of gold particles from an aqueous to an organic phase (and vice versa) by exchanging hydrophilic surfactants with hydrophobic surfactants (and vice versa). In this way, by choosing the surfactant molecules, it is possible to adjust the surface properties of the particles.

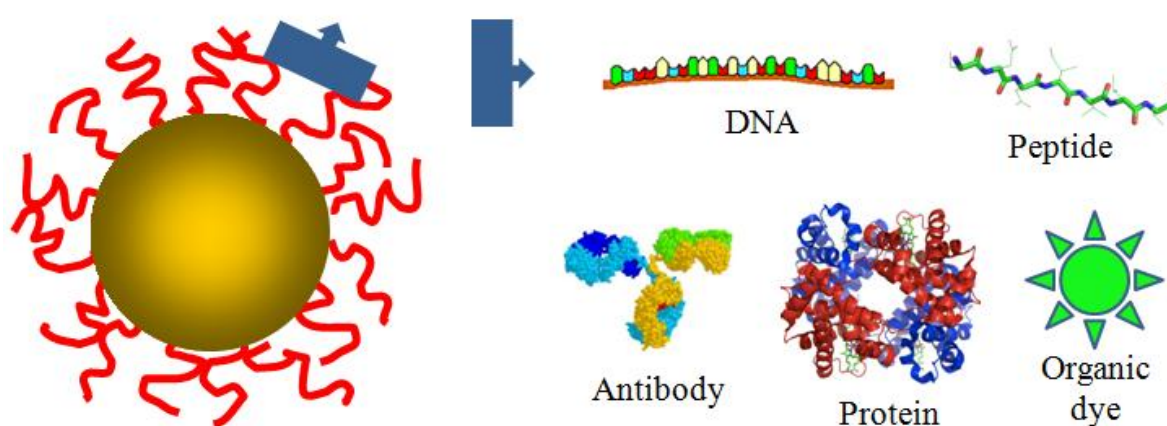


Figure 1.3. Schematic of a ligand-conjugated gold nanoparticle. The gold core (yellow) is surrounded by stabilizer molecules (red) which provide colloidal stability. Ligands (blue) can be either linked to the shell of stabilizer molecules (as shown here) or directly attached to the gold surface by replacing part of the stabilizer molecules.

Biological molecules can be attached to the particles in several ways. If the biological molecules have a functional group which can bind to the gold surface (like thiols or specific peptide sequences), the biological molecules can replace some of the original stabilizer molecules when they are added directly to the particle solution [7]. **Figure 1.3** shows the schematic of ligand-conjugated gold nanoparticle. In this way, molecules like

oligonucleotides, peptides or PEG can be readily linked to gold nanoparticles and subsequent sorting techniques even allow particles with an exactly defined number of attached molecules per particle to be obtained. Alternatively, biological molecules can also be attached to the shell of stabilizer molecules around the gold nanoparticles by bioconjugate chemistry. The most common protocol is the linkage of amino-groups on the biological molecules with carboxy groups at the free ends of stabilizer molecules by using EDC (1-ethyl-3-(3-dimethylaminopropyl)-carbodiimide-HCl). With related strategies almost all kinds of biological molecules can be attached to the particle surface. Though such protocols are relatively well established, bioconjugation of gold nanoparticles still is not trivial and characterization of synthesized conjugates is necessary, in particular to rule out aggregation effects or unspecific binding during the conjugation reaction.

(iv) Thermal Properties

The remarkable optical properties of gold nanoparticles associated with the surface plasmon resonance phenomenon have usually been thought mostly responsible for its applications such as in the nano-photonics. However, one cannot but notice that the main recent breakthroughs have rather been achieved in the domain of thermal applications of these optical properties. Indeed, as optical and thermal responses are in fact closely bound, gold nanoparticles can be considered together as nanometric heat sources and probes for local temperature variations via their optical behaviour. The energetic conversion realized by gold nanoparticles which are able to transform at the nanoscale an electromagnetic radiation into heat emitted toward their environment may be relevant in numerous fields. For example, in plasmonic devices local heating may alter the guiding of the electromagnetic wave by gold nanostructures and therefore requires to be well controlled. Gold nanoparticles are also expected to be used in microscopy for labelling biologic cells: nanoparticle heating by light

absorption enables to modify the optical response of their local environment [9]. In the medical area, photo-thermal cancer therapy based on gold nanoparticles is a very promising technique, where gold nanoparticles absorb light energy transmitted through biologic tissues and transform it into heat which diffuses toward local environment. By using an appropriate targeting method for carrying particles close to affected cells, the latter will be destroyed by overheating. One may also take advantage of this local heating around particles for inducing local phase or morphology transformation in the surrounding medium. On the one hand, this can enable the measurement of nanoscale heat transfer through the investigation of such phase transformations. On the other hand, this could be used to modify the global medium optical properties. This effect has been supposed to be at the origin of the optical limitation phenomenon in colloidal solutions (induced light scattering by formation of gas bubbles around gold colloids) [30]. Metal nanoparticles are also considered as model defects for studying the damage of optical devices induced by powerful lasers. The dynamics of the light-heat conversion in a gold nanoparticle and of the thermal release toward its environment appears then to be a relevant issue in all these domains.

1.3. Synthesis of Gold Nanoparticles

Methods to synthesize gold nanoparticles have been known for centuries, but only in the last half century have reliable methods been developed to synthesize them in high yield and in a variety of sizes and shapes [31-35]. Since most of the applications, particularly biological, are dependent on size and shape of gold nanoparticles, therefore use of appropriate method for their controlled synthesis is one the important issues of consideration. Gold nanoparticles can be synthesized in organic or aqueous media. There are two approaches for synthesis of nanomaterials, top-down and bottom-up, as shown in **Figure 1.4**. Both approaches play very important role in modern industry involving nanotechnology [36].

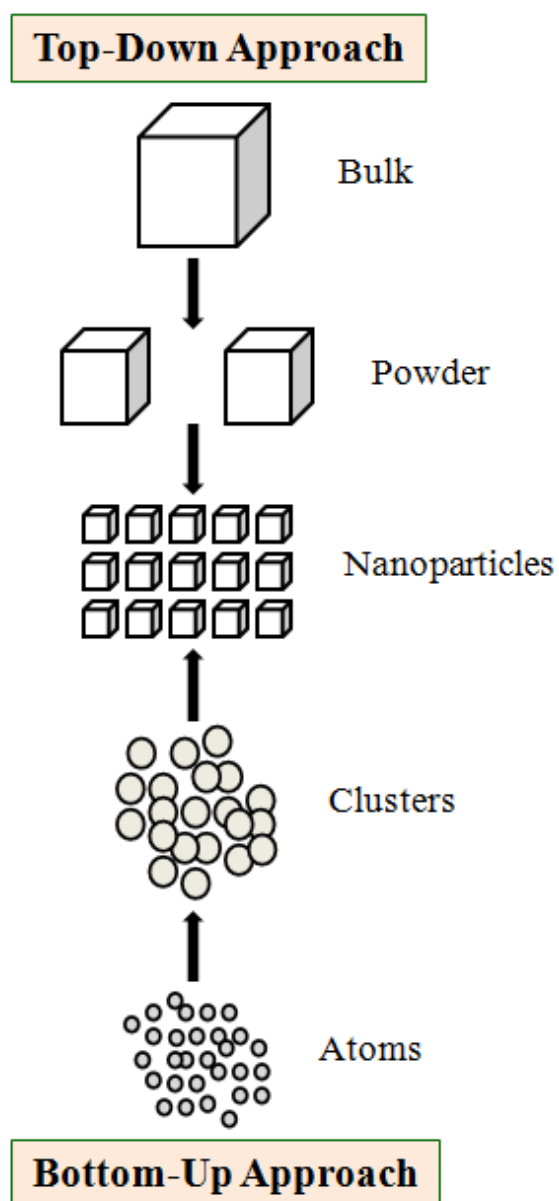


Figure 1.4. Schematic representation of the building up of nanoparticles.

1.3.1. Top-Down Approach

The top-down approach is a subtractive process starting from bulk materials to make nanomaterials. This approach involves division of bulk material or miniaturization of bulk fabrication process to produce the desired structure with the appropriate properties. This includes some of the following commonly used methods:

- (i) Attrition or Ball milling

- (ii) Photolithography
- (iii) Electron beam lithography
- (iv) Machining.

In general, top-down approaches are easier to use and less expensive but have less control over the size distribution and also could be destructive. Among others, the biggest problem with top-down approach is the imperfection of the surface structure. It is well known that the conventional top-down techniques such as lithography can cause significant crystallographic damage to the processed patterns and additional defects may be introduced even during the etching steps. For example, nanowires made by lithography are not smooth and may contain a lot of impurities and structural defects on surface. Such imperfections would have a significant impact on physical properties and surface chemistry of nanostructures and nanomaterials, since the surface-to-volume ratio in nanostructures and nanomaterials is very large. The surface imperfection would result in a reduced conductivity due to inelastic surface scattering, which in turn would lead to the generation of excessive heat and thus impose extra challenges to the device design and fabrication. Regardless of the surface imperfections and other defects that top-down approaches may introduce, this is the method of choice when highly complex structures are made. This is the case in the integrated circuit industry, where nanosized structures are cut in plain silica wafers using laser techniques.

1.3.2. Bottom-Up Approach

Bottom-up approach is a controlled additive process that deals with the assembly of precursor atoms or molecules to make nanomaterials. In this approach, atoms, molecules or clusters are used as the building blocks for the creation of complex nanostructures. Though the bottom-up approach mostly used in nanotechnology, it is not a newer concept. All the living beings in

nature observe growth by this approach only. Bottom-up methods are chemically controllable and non-destructive. The synthesis of nanoparticles from molecular solutions is a good example of a bottom-up approach. The size of the nanostructures, which can be obtained with a bottom-up approach, spans the full nano scale. An advantage of the bottom-up approach is the better possibilities to obtain nanostructures with less defects and more homogeneous chemical compositions. This is due the mechanisms utilized in the synthesis of nanostructures reducing the Gibbs free energy, so that the produced nanostructures are in a state closer to a thermodynamic equilibrium [1]. Some of the important methods involved are:

- (i) Sol-gel method
- (ii) Vapour phase deposition method
- (iii) Chemical reduction method.

The bottom-up approach usually employs solution-phase colloid chemistry for the synthesis. In a typical colloidal synthesis, atoms of the desired component are produced in the solution at very high supersaturation to induce the assimilation of these atoms into particles to reduce the system Gibbs free energy. Due to the flexibility in selecting different reducing agents, particle capping agents, solvent systems as well as synthesis conditions, colloidal synthesis offers a great variety of options for composition, shape, size and surface chemistry control. The bottom-up approach is also suitable for controlling monodispersity of the nanoparticles. With all these advantages, the bottom-up approach has become the main route to nanomaterial production.

Among all bottom-up methods, the chemical reduction of the metal salt in an aqueous, an organic phase or two phases, is one of the most popular routes as nanoparticles of a wide range of sizes and shapes can be prepared by controlling the reaction conditions. The reduction of gold salts in existing of a stabilizing agent is a facile and easy technique to produce desired sizes of nanoparticles [37]. A stabilizing agent, also called as capping

material, prevents aggregation and precipitation of metal nanoparticles as well as plays a role in determining size and shape of gold nanoparticles. **Table 1.1** summarizes some of the popular and widely used synthesizing methods for various size gold nanoparticles.

Table 1.1. Some of the widely used gold nanoparticle synthesis methods.

Nanoparticle Size	Methods	Capping Agents
1 – 2 nm	AuCl(PPh ₃) reduction by diborane or sodium borohydride [38]	Phosphine
2 – 5 nm	Biphasic reduction of HAuCl ₄ by sodium borohydride with thiol as a capping agent [39,40]	Alkanethiol
10 – 100 nm	HAuCl ₄ reduction with sodium citrate in water [31,32,41]	Citrate

1.4. Characterization Techniques

Several techniques are available under the broad umbrella of characterization of materials, which may be used to study nanoparticles in one way or the other. The resulting information can be processed to yield images or spectra which reveal the topographic, geometric, structural, chemical or physical details of the nanomaterials. Different techniques based on the use of photon (light and X-ray), electron and neutron probes, which are complementary with respect to their sensitivity on different length scales, have been used. These techniques can be broadly classified into three categories: (i) spectroscopic, (ii) microscopic and (iii) scattering techniques.

1.4.1. Spectroscopic Techniques

Optical spectroscopic techniques are widely used in the study of optical properties of different materials including nanoparticles. The different techniques are usually based on

measuring absorption, scattering or emission of light that contains information about properties of the materials. Commonly used techniques include UV-visible electronic absorption spectroscopy, photoluminescence, infrared absorption and Raman scattering. These different techniques can provide different information about the nanoparticle properties of interest [42].

(i) UV-Visible Spectroscopy

The basic operating principle of electronic absorption spectroscopy is based on the measurement of light absorption due to electronic transitions in a sample. Since the wavelength of light required for electronic transitions is typically in the UV and visible region of the electromagnetic radiation spectrum, electronic absorption spectroscopy is usually called UV-visible or UV-vis spectroscopy [43]. It is named electronic absorption spectroscopy because the absorption in the UV-visible regions involves mostly electronic transitions. The spectrum is characteristic of a given sample and reflects the fundamental electronic properties of the sample. For nanoparticles, UV-visible spectroscopy provides vital information of nanoparticles through surface plasmon resonance (SPR) studies. This absorption strongly depends on the particle size, dielectric medium and chemical surroundings [44].

(ii) Photoluminescence Spectroscopy

At the fundamental level, the principle underlying photoluminescence (PL) spectroscopy is very similar to that of electronic absorption spectroscopy. They both involve electronic transition of initial and final states coupled by the electrical dipole operator. The main difference is that the transition involved in PL is from a higher energy level or state to a lower energy level [45]. There is also an important practical difference between the two techniques

in that PL is a zero background experiment, i.e. no signal detected when there is no PL, which is in contrast to absorption spectroscopy that is a non-zero background experiment.

A typical PL spectrum is just a plot of the PL intensity as a function of wavelength for a fixed excitation wavelength. A photoluminescence excitation spectrum, however, is a measure of PL at a fixed emission wavelength as a function of excitation wavelength. Gold nanoparticles show PL, which has been correlated with their well-defined plasmon resonances [46]. It is found that there is strong relationship between PL and surface plasmon peak. For example, PL is very intense if SPR is broad and PL intensity is reduced when the plasmon absorption sharpens.

(iii) Infrared Spectroscopy

The mechanical molecular and crystal vibrations are at very high frequencies ranging from 10^{12} to 10^{14} Hz (3–300 μm wavelength), which falls in the infrared (IR) region of the electromagnetic spectrum. In infrared Spectroscopy, the oscillations induced by certain vibrational frequencies provide a means for matter to couple with an impinging beam of infrared electromagnetic radiation and to exchange energy with it when the frequencies are in resonance [47]. These absorption frequencies represent excitations of vibrations of the chemical bonds and thus, are specific to the type of bond and the group of atoms involved in the vibration. In Fourier transform infrared spectroscopy, the intensity-time output of the interferometer is subjected to a Fourier transform to convert it to the familiar infrared spectrum (intensity-frequency) and atomic arrangement, surrounding environments and concentrations of the chemical bonds that are present in the sample can be determined. The studies relating the quantification of the coverage and binding strength of ligands, surfactants etc. on the gold nanoparticle surface are usually investigated using FTIR spectroscopy [48].

(iv) Raman Scattering

Raman scattering is another vibrational technique and differs from the infrared spectroscopy by an indirect coupling of high-frequency radiation with vibrations of chemical bonds. When the incident photon interacts with the chemical bond, the chemical bond is excited to a higher energy state. The scattering process is inelastic and thus the scattered light can have a lower (Stokes, by depositing energy into the molecule) or higher energy (anti-Stokes, by gaining energy from the molecule) than the incident light (Rayleigh scattering). The energy shift is characteristic for the chemical structure where the scattering occurred and complex molecules have therefore a characteristic Raman spectrum that allows for detection and identification. A Raman spectrum serves as a “molecular fingerprint” of a sample, yielding information on molecular bonds, conformations, and intermolecular interactions. In spite of its advantages, its practical uses have been significantly limited because the Raman scattering signal is intrinsically weaker than most other fluorescence signals. Methods of enhancement have been developed to extend the detection limit. Among various methods, enhancement with noble metal nanostructures, a technique termed surface-enhanced Raman scattering (SERS), has been found to enhance the efficiency dramatically [49,50]. Using this method, it is possible to probe single molecules adsorbed onto a single gold nanoparticle [51].

1.4.2. Microscopic Techniques

Microscopic techniques for the characterization of nanoparticles involve interaction of electron beams with the specimen, and the subsequent collection of transmitted or scattered electrons in order to create an image. This process may be carried out by scanning of a fine beam over the sample (e.g. scanning electron microscopy) or by wide-field irradiation of the sample (e.g. transmission electron microscopy). Scanning probe microscopy involves the interaction of a scanning probe with the surface of the object of interest. The

advantage of microscopic techniques is that it allows the direct visualization of the nanoparticles [1,42].

(i) Scanning Electron Microscopy

Scanning electron microscopy (SEM) is a powerful and popular technique for imaging the surfaces of almost any material with a resolution down to about 1 nm. The image resolution offered by SEM depends not only on the property of the electron probe, but also on the interaction of the electron probe with the specimen. The interaction of an incident electron beam with the specimen produces secondary electrons, the emission efficiency of which sensitively depends on surface geometry, surface chemical characteristics and bulk chemical composition. SEM can thus provide information about the surface topology, morphology and chemical composition [52]. The high resolution capability afforded by SEM makes it convenient for probing nanoparticles of which the structural features on the nanoscale are critical to their properties and functionalities.

Interaction between the electron beam and the sample generates back scattered electrons (BSE), X-ray, secondary electrons (SE) and Auger electrons in a thick or bulk sample. These various electrons are detected in SEM and the signal detected contains information about the specimen under investigation. BSE is more sensitive to heavier elements than SE. The X-ray radiation can be detected in a technique called energy dispersive X-ray (EDX) spectroscopy that can be used to identify specific elements [53].

(ii) Transmission Electron Microscopy

Transmission electron microscopy (TEM) is a high spatial resolution structural and chemical characterization tool. A modern TEM has the capability to directly image atoms in crystalline specimens at resolutions close to 0.1 nm, smaller than interatomic distance. An electron beam can also be focused allowing quantitative chemical analysis from a single nanoparticle. This

type of analysis is extremely important for characterizing materials at a length scale from atoms to hundreds of nanometers. TEM can be used to characterize nanomaterials to gain information about particle size, shape, crystallinity, and interparticle interaction [42,54].

One major difference between SEM and TEM is that TEM detects transmitted electrons whereas SEM detects backscattered and/or secondary electrons. While both techniques can provide topological, morphological and compositional information about the sample, TEM can provide crystallographic information as well. In addition, TEM allows for diffraction patterns to be detected that also contain useful crystallographic information about the sample [42].

(iii) Scanning Probe Microscopy

Scanning probe microscopy (SPM) represents a group of techniques, including scanning tunneling microscopy (STM) and atomic force microscopy (AFM), that have been extensively applied to characterize nanostructures with atomic or subatomic spatial resolution. A common characteristic of these techniques is that an atom sharp tip scans across the specimen surface and images are formed by either measuring the current flowing through the tip or the force acting on the tip. SPM can be operated in a number of environmental conditions, in a variety of different liquids or gases, allowing direct imaging of nanoparticle surfaces. It allows viewing and manipulation of objects on the nanoscale and its invention is a major milestone in nanotechnology [55].

The STM is based on the concept of quantum tunneling. When a conducting tip is brought very near to the surface to be examined, a bias (voltage difference) applied between the two can allow electrons to tunnel through the vacuum between them. The resulting tunneling current is a function of tip position, applied voltage and the local density of states of the sample. Information is acquired by monitoring the current as the tip's position

scans across the surface, and is displayed in image form. STM is applicable mainly for conductive samples [1,55].

For nonconductive nanomaterials, AFM is a better choice. AFM is based on measuring the force between the tip and the solid surface. The interaction between two atoms is repulsive at short-range and attractive at long-range. The force acting on the tip reflects the distance from the tip atom(s) to the surface atom, thus images can be formed by detecting the force while the tip is scanned across the specimen [1,55].

1.4.3. Scattering Techniques

Scattering techniques constitute powerful probes for characterizing nanoparticles. Different techniques based on different radiations (light, X-ray and neutron) have been extensively used. The important techniques used are X-ray diffraction, light scattering (static light scattering and dynamic light scattering) and small-angle scattering (small-angle X-ray scattering and small-angle neutron scattering). In each of these techniques the radiation (light, X-ray or neutron) is scattered by a sample and the resulting scattering pattern is analyzed to provide information about the structure (shape and size), interaction, ordering in the sample. These techniques can be utilized over a wide range of length scales 1 to 1000 nm [56]. Since most of the measurements are performed in solution, these techniques provide unique structural information under different conditions. Moreover, it is also possible to investigate structural evolutions. These techniques are often used as a complementary tool with each other, providing detailed information about the system.

(i) X-Ray Diffraction

X-ray diffraction (XRD) is an important experimental technique that has long been used to address the issues related to the crystal structure of solids, including lattice constants and geometry, identification of unknown materials, orientation of single crystals, preferred

orientation of polycrystals, defects, stresses, etc. In XRD, a collimated beam of X-rays, with a wavelength typically ranging from 0.7 to 2 Å, is incident on a specimen and is diffracted by the crystalline phases in the specimen according to Bragg's law: $2d \sin\theta = n\lambda$, where d is the spacing between atomic planes in the crystalline phase and λ is the X-ray wavelength. The intensity of the diffracted X-rays is measured as a function of the diffraction angle 2θ and the specimen's orientation. This diffraction pattern is used to identify the specimen's crystalline phases and measure its structural properties. XRD is non-destructive and does not require elaborate sample preparation, which explains the wide usage of XRD method in materials characterization. One of the disadvantages of XRD is the low intensity of diffracted X-rays, particularly for low-Z materials. XRD is more sensitive to high-Z materials and for low-Z materials, neutron diffraction is more suitable [57].

The XRD from the powder nanoparticles is also used for determining the size of the particle (D) using the Scherrer equation as [58]

$$D = \frac{K\lambda}{B \cos \theta_B} \quad (1.1)$$

where λ is the X-ray wavelength, B is the full width of height maximum (FWHM) of a diffraction peak, θ_B is the diffraction angle and K is the shape factor. The dimensionless shape factor has a typical value of about 0.9, but varies with the actual shape of the crystallite. The Scherrer equation is limited to nanoscale particles and not applicable to sizes larger than about 0.1 μm . It is important to realize that the Scherrer formula provides a lower bound on the particle size. The reason for this is that a variety of factors can contribute to the width of a diffraction peak besides crystallite size, the most important of these are usually inhomogeneous strain and instrumental effects. If all of these other contributions to the peak width were zero, then the peak width would be determined solely by the crystallite size and the Scherrer formula would apply. If the other contributions to the width are non-zero, then

the crystallite size can be larger than that predicted by the Scherrer formula, with the additional peak width coming from the other factors [59].

(ii) Light Scattering

Light scattering experiments can be performed as a function of two variables: the scattering angle (θ) and the observation time (t). There are two classes of light scattering techniques: (1) the static (elastic) light scattering (SLS) and (2) the dynamic (quasielastic) light scattering (DLS). In SLS one measure the time averaged scattered intensity as a function of the scattering angle. The scattered intensity bears information on the static properties of the scattering medium such as size and shape of the scatterers. SLS is sensitive to the length scales that are of the order of wavelength of light (~ 100 nm). It cannot therefore measure the nanoparticles as such but is useful to see the aggregation of nanoparticles [60].

DLS is based on the scattering of light by diffusing particles and can measure length scale in the range 1 to 1000 nm. At any instant the suspended particles will have a particular set of positions within the scattering volume. The particles scatter the light to the detector, but the relative phase of scattered wavelets differs, due to differing incident phases which they experienced and due to different particle-detector distances. The intensity at the detector is the superposition of all the scattered wavelets and will have a value $I(t)$ at time t . At the time $(t + \tau)$, which is very small time later than t , the diffusing particles will have new positions and the intensity at the detector will have a value $I(t + \tau)$. As time progress, the intensity at the detector will fluctuate as the Brownian processes in the sample volume continue [61]. Small rapidly diffusing particles will yield fast fluctuations, whereas larger particles and aggregates generate relatively slow fluctuations [62]. The rate of fluctuations can be determined through the technique of autocorrelation analysis and the particle hydrodynamic radius R_H is calculated by the Stokes-Einstein relation. If the system is monodisperse, there should only be one population, whereas a polydisperse system would show multiple particle populations.

Stability studies can be done conveniently using DLS. Periodical DLS measurements of a sample can show whether the particles aggregate over time by seeing whether the hydrodynamic radius of the particle increases. If particles aggregate, there will be a larger population of particles with a larger radius [60,63].

(iii) Small-angle Scattering

Small-angle scattering (SAS) is a technique to study the materials at nanoscale. It is a diffraction experiment, covering a small wave vector transfer Q , typically in the range of 10^{-3} to 1 \AA^{-1} . Since the smallest Q values occur at small scattering angles ($\sim 1^\circ$), the technique is called as small-angle neutron scattering. In SAS experiment one measures the scattered intensity as given by $I(Q) \sim (\rho_p - \rho_m)^2 P(Q) S(Q)$, where $P(Q)$ is the intra-particle structure factor and $S(Q)$ is the inter-particle structure factor. $P(Q)$ is the square of the particle form factor and is decided by the shape and size of the particle. $S(Q)$ depends on the spatial arrangement of particles and is thereby sensitive to inter-particle interactions. SAS thus gives the information about the structure (shape and size) and the interactions of the particles dispersed in a medium [64].

The term $(\rho_p - \rho_s)^2$ is referred as a contrast factor. The scattering expressions are same for both the SAXS and the SANS experiments. The contrast factor, however, depends on the radiation used. The values of ρ_p and ρ_s depend on the chemical composition of the particle and the solvent and are different for neutrons and X-rays. The differences in ρ values for neutrons and X-rays arise from the fact that while neutrons are scattered by the nucleus of an atom, the X-rays are scattered by the electron clouds around the nucleus. It is seen that as one goes across the periodic table, the neutron scattering lengths vary in a random way and the X-ray scattering lengths increase with the atomic number of the atom [60,65]. For example, unlike X-rays where $\rho_s(\text{H}_2\text{O}) = \rho_s(\text{D}_2\text{O})$, the values of ρ_s changes significantly for neutrons when solvent is changed from H_2O to D_2O . X-rays are scattered more strongly from heavy

elements as compared to light elements such as C, H etc. This means whereas SAXS will be mostly sensitive to the scattering from gold nanoparticles, SANS can be used to measure both the gold nanoparticles and the functional group attached to it [65,66].

1.5. Applications of Gold Nanoparticles

Nanoparticles are at the forefront of the nanotechnology wave. The ability to fabricate and control the structure of nanoparticles allows influencing the resulting properties and ultimately to design materials to get desired properties. The current and potential applications for nanoparticles are growing and cover an extremely broad range of markets industries including biomedical and cancer treatment, renewable energy, environmental protection, pharmaceuticals, electronics, personal care, surface coatings, plastics, textiles, food, building materials, automobiles etc [1,19]. Some of these applications are discussed below.

1.5.1. Biology

Gold nanoparticles have led to new and exciting developments with enormous potential in biology. The uses of gold nanoparticles are classified into four concepts of applications as labeling, delivering, heating and sensing [9].

(i) Gold Nanoparticles for Labeling

Traditionally, gold nanoparticles have been primarily used for labeling applications. In this regard, the particles are directed and enriched at the region of interest and they provide contrast for the observation and visualization of this region. Gold nanoparticles are a very attractive contrast agent as they can be visualized with a large variety of different techniques. The most prominent detection techniques are based on the interaction between gold nanoparticles and light. Gold particles strongly absorb and scatter visible light. In particular, close to the surface plasmon resonance frequency the absorption cross-section is very high.

Absorbed light ultimately leads to heating of the particles and upon heat transport subsequently to heating of the particle environment [67]. This can be observed in two ways. Photothermal imaging records density fluctuations (i.e. local variations of the refractive index) of the liquid environment around the particles by differential interference contrast microscopy. Photoacoustic imaging, on the other hand, makes use of the fact that the liquids expand due to heat. A local heat-pulse due to light absorption leads to expansion of the liquid surrounding the gold particles and thus to the creation of a sound wave which can be detected by a microphone. Both photothermal and photoacoustic imaging make use of the large light absorption cross-section of gold nanoparticles. Small gold particles have recently also been reported to emit fluorescence upon photo-excitation and thus can be visualized with fluorescence microscopy. All of the above mentioned methods involving photoexcitation (phase contrast/interference contrast microscopy, dark field microscopy, photothermal imaging, photoacoustic imaging and fluorescence microscopy) provide sufficient sensitivity to allow for detection at the single particle level [68].

Besides the interaction with visible light, the interaction with both electron waves and X-rays can also be used for visualization of gold nanoparticles. Due to their high atomic weight gold nanoparticles provide high contrast in transmission electron microscopy. Gold particles also scatter X-rays efficiently and thus provide contrast in X-ray imaging [69]. Gold nanoparticles can also be radioactively labeled by neutron activation and can be detected in this way by gamma radiation.

(ii) Gold Nanoparticles as a Vehicle for Delivery

Gold nanoparticles have been used for a long time for delivery of molecules into cells. For such delivery applications gold nanoparticles is exploited as they are small, optically active, colloidally stable, inert and relatively easy to conjugate with ligands [70]. For this purpose the molecules are adsorbed on the surface of the nanoparticles and the whole conjugate is

introduced into the cells. Introduction into cells can either be forced as in the case of gene guns or achieved naturally by particle ingestion. Inside cells the molecules will eventually detach themselves from the gold nanoparticles. In gene guns, the nanoparticles are shot as a ballistic projectile into the cells. The ballistic acceleration of the drug-loaded micro- or nanoparticles is realized by different means like macroscopic bullets, gas pressure or electric discharges and some types of guns are commercially available [71].

Cells naturally ingest colloidal nanoparticles whereby particle incorporation can be specific (via receptor–ligand interaction) or nonspecific. The goal is again to transfer molecules which are adsorbed on the surface of the gold nanoparticles into the cells. For specific uptake ligands specific to receptors on the cell membrane, such as transferrin which binds to membrane-bound transferrin receptors, are conjugated to the surface of the gold particles. As specific uptake is more effective than nonspecific uptake, in this way ligand-modified nanoparticles are predominantly incorporated by cells which possess receptors for these ligands, but not by other cells. In this way, it is for example possible to direct particles specifically to cancer cells by conjugating them with ligands specific to receptors which are over expressed on the surface of cancer cells but that are less present on healthy cells [72]. After incorporation nanoparticles are stored in endosomal/lysosomal vesicular structures inside cells. In order to release the particles from the vesicular structures to the cytosol their surface can be coated with membrane-disruptive peptides or the particles can be modified with peptides which allow for direct transfer across the cell membrane [73]. In this way it is possible to deliver molecules which are adsorbed on the surface of the gold nanoparticles upon particle incorporation inside the cells.

(iii) Gold Nanoparticles as a Heat Source

When gold particles absorb light the free electrons in the gold particles are excited. Excitation at the plasmon resonance frequency causes a collective oscillation of the free electrons. Upon

interaction between the electrons and the crystal lattice of the gold particles, the electrons relax and the thermal energy is transferred to the lattice. Subsequently the heat from the gold particles is dissipated into the surrounding environment [74]. Besides its combination with imaging techniques (see above in section 3), controlled heating of gold particles can be used in several ways for manipulating the surrounding tissues [75,76].

Cells are very sensitive to small increases in temperature. Even temperature rises of a few degrees can lead to cell death. For human beings temperatures above 37 °C lead to fever and temperatures above 42 °C are lethal. This fact can be harnessed for anti-cancer therapy in a concept called hyperthermia. The idea is to direct colloidal nanoparticles to the cancerous tissue. This can be done by conjugating the particle surface with ligands that are specific to receptors over expressed on cancer cells. The particles are then locally enriched in the cancerous tissue (either adherent to the cell membranes or inside the cells after internalization). If the particles can be heated by external stimuli then the temperature of cells close to the particles is raised and in this way cells in the vicinity of the particles can be selectively killed [77]. As mentioned above, Au particles can be heated by absorption of light, whereby the absorbed light energy is converted into thermal energy. Thus the idea is to enrich cancerous tissues with gold nanoparticles and to illuminate the tissue. Due to the heat mediated by the gold particles to the surrounding tissue, cancerous tissues can be destroyed locally without exposing the entire organism to elevated temperatures.

(iv) Gold Nanoparticles as Sensors

Besides using gold nanoparticles as (passive) labels they can also be used for (active) sensor applications. Their aim in a sensor is to specifically register the presence of analyte molecules and provide a read-out that indicates the concentration of the analyte. When an optical read-out is used, the presence of analyte can, for example, be indicated by changes in the optical

properties of gold nanoparticles. Due to their small size, gold particle-based sensors could have an important impact in diagnostics [78].

The plasmon resonance frequency is a very reliable intrinsic feature present in gold nanoparticles (with wavelengths around 510–530 nm for Au nanoparticles of around 4–40 nm diameter) that can be used for sensing [79]. The binding of molecules to the particle surface can change the Plasmon resonance frequency directly, which will lead to a change in the color of the solution. Besides the detection of analytes, such colour changes can also be used to measure lengths. The concept of such ‘rulers on the nanometer scale’ is again based on colour changes of gold particles if the gold particles are in close proximity. Different sites of a macromolecule can be linked to gold particles. By observing the colour of the gold particles the distance between these sites can be measured and in this way for example conformation changes in molecules can be observed [80,81].

1.5.2. Nanoelectronics

According to the present paradigm of electronic information storage and exchange, continuous miniaturization of microelectronic devices turns out to be the only evident concept for improving the performance of integrated circuits. One of the most promising concepts is the development of single-electron (SE) devices which retain their scalability down to the molecular level [8,82]. At present, due to exploitation of charging effects or so-called Coulomb effects in metallic single-electron devices comprising tunnel junctions with sub-micrometer size, individual charge carriers can be handled. The discreteness of the electric charge becomes essential and the tunneling of electrons in a system (SET) of such junctions can be affected by the Coulomb interaction of electrons which can be varied by an externally applied voltage or by injected charges. The simplest arrangement for a two-terminal device is a metal island between two metallic electrodes separated from each other

by a dielectric environment. By transferring a single electron from the electrodes to the island by applying a certain voltage, the island is charged negatively and the electrodes keep the positive image charge, whereas the overall charge is kept to zero. In this situation, the electrostatic energy, i.e. the single electron charging energy $E_c = e^2/2C$ where e is the elementary charge and C is the self-capacitance of the metallic island, is stored in the arrangement. If $E_c \gg k_B T$, thermal fluctuation of the charge is suppressed and the threshold voltage has to overcome the Coulomb blockade to add an electron via the source electrode or to let it leave via the drain electrode. If, for instance, the diameter of the metal island is about micron size, E_c exceeds $k_B T$ only for very low temperature around 10 K. Consequently, by decreasing the island size down to nanoscale (1–2 nm), single electron movements can be controlled even in the range of room temperature [8].

Gold nanoparticles have been synthesized with diameters as small as 2 nm. However, integrating individual nanoparticle into devices and gating them effectively can be extremely challenging. This is due to the challenges in (i) fabricating nanometer-spaced electrodes and (ii) precise placement of the nanoparticles between the electrodes. Several techniques have been developed to realize the fabrication of metallic SETs using gold nanoparticles [83,84]. In some cases, individual SETs have been fabricated by creating sub-10 nm electrodes via electromigration of ultra-thin gold nanowires defined by high resolution electron beam lithography and then depositing gold nanoparticles via physical vapor deposition of gold or via self-assembly from solution. In other case, lithographically defined electrodes have been used of a gap size larger than 50 nm to assemble gold nanoparticles [85,86]. However, because of the larger gap size multiple particles were assembled, leading to multiple SETs connected in series.

1.5.3. Catalysis

Catalysis drives many reactions, with the ability to lower the activation energy of the reaction, and thus increases the rate of reaction and the yield of the desired products. The use of nanoparticles as catalysts has increased exponentially as nanoparticle properties and reactions are better understood. The possibility of using less material and having different properties for different shapes of nanoparticles is very attractive. Nanoparticle catalysis has been investigated for both homogeneous (catalyst and reactants are both in solution) and heterogeneous (catalyst supported on a substrate) systems. In homogeneous catalysis, it has been that shapes with more corners and edge atoms have a higher reactivity than similar nanoparticles with fewer corner and edge atoms. Thus shape and crystal structure difference can lead to different catalytic rates. There are a lot of studies being carried out to observe the connection between structure and function for nanoscale catalysts [87].

Although gold nanoparticles have been used for many different purposes, their catalytic properties were for decades considered to be weak or absent [87]. It was an exciting discovery when Haruta and Hutchings simultaneously and independently showed that gold could be very active, in particular, for the heterogeneous low-temperature oxidation of CO [88,89]. It was found that bare gold nanoparticles were not active but when on a metal oxide support, such as Co_3O_4 , Fe_2O_3 or TiO_2 , became excellent catalysts for the oxidation of CO. It was first considered that the high activity resulted from a new type of composite oxide catalyst, but after a detailed electron microscopy study, it was found that the most active catalysts were small gold nanoparticles approximately 2–5 nm in diameter. The catalytically active nanoparticles form a reconstructed structure with the substrate and CO adsorption would proceed on the adjacent metal oxide. The reaction is thought to involve carbonate-like intermediates decomposing to CO_2 upon desorption from the surface. This catalytic discovery has spurred a substantial body of other studies on heterogeneous gold catalysis, including the

hydrogenation of alkenes or alkynes, hydrosilylation, oxidation of alcohols and photocatalysis [90].

Many possible explanations have been proposed for the difference in reactivity between nanoparticles and bulk gold. They include the electronic and chemical properties of nanoparticles or the shape, size and oxidation state of the nanoparticles. The surface support is also suggested to be responsible for the catalytic activity. The crystal structure of gold has also been proposed to be important in the catalytic properties. This demonstrates new properties for nanoparticles, which are unexpected based on bulk behavior since bulk gold has no catalytic activity and nano particles are efficient catalysts, generating further interest in nanomaterials as new functionality is present on the nanoscale [90,91].

1.6. Objective of the Thesis

This thesis aims to look into the synthesis and characterization of one of the novel ways of forming gold nanoparticles. The development of simple and versatile methods for the preparation of nanoparticles in a size- or shape-selected and controlled manner has been a challenging. The nanoparticle morphology often emerges as a result of a competitive growth of different crystallographic surfaces. This is typically achieved by altering the relative growth rates of different facets by the selective localization of surface-modifying or capping agents, but also by the modulation of nucleation and reaction parameters such as time, temperature, reagent concentration and pH. The preparation of metal nanoparticles in solution is most commonly based on the chemical reduction of metal ions and invariably involves organic solvents and ligands [92,93]. The gold nanoparticles thus synthesized are covered with strongly bound ligands that render them difficult to disperse in water and may hinder further surface modification and functionalization of particles for particular applications.

A methodology based on the use of water as the solvent would provide an environmentally benign route to the production of gold nanoparticles and result in a product that can be easily integrated in applications involving aqueous media. In aqueous solutions, gold nanoparticles have been typically produced from the chemical reduction of AuCl_4^- ions by reducing agents such as citric acid and ascorbic acid. Such reduction takes place in the presence of one or more water-soluble polymers, surfactants or capping agents, and with the aid of externally supplied energy such as photo-irradiation, ultrasound irradiation or heating [31,32,38,39]. These methods allow for adequate control of the size and concentration of the dispersed particles. Moreover, the surface-modifying or capping agents confer colloidal stabilization and prevent nanoparticle aggregation. While the most common strategy to achieve colloidal stability proceeds via the chemical binding of ligands at the surface of the nanoparticles, a covalent linkage between the ligand and the nanoparticle may alter the properties of the nanoparticles through a modification of their electronic density and the dielectric constant of the surrounding medium. A strategy based on the physical adsorption of ligands on the surface of the nanoparticles may be preferable, in order to maintain the intended properties of the nanomaterial. Despite the progress achieved, concerns and problems with the preparation of metal nanoparticles remain, such as the byproducts from the reducing agent, the multiple steps often required, and the high concentration of protective agents [94].

The utilization of nontoxic chemicals, environmentally benign solvents, and renewable materials are emerging issues that merit important consideration in the development of synthetic strategies. Recently, it has been discovered that poly(ethylene oxide)-poly(propylene oxide)-poly(ethylene oxide) (PEO-PPO-PEO) block copolymers can act as a reductant and stabilizer in the single-step synthesis and stabilization of gold

nanoparticles from hydrogen tetrachloroaurate(III) hydrate ($\text{HAuCl}_4 \cdot 3\text{H}_2\text{O}$) in aqueous solutions, at ambient temperature, in the absence of any additional reductants or energy input [95]. This synthesis proceeds quite fast and is environmentally benign and economical since it involves only water and nontoxic polymers. The gold nanoparticle dispersions formed are highly stable [96-98]. The thesis provide insight into the role of various components and solution conditions used in this novel block copolymer-mediated synthesis of gold nanoparticles on the optimization of various parameters of synthesis such as formation rate, yield, stability and structure of nanoparticles.

1.7. Summary

Gold nanoparticles have been of recent great interest in the context of its diverse applications due to their unique optical, electronic, catalytic and chemical properties. The unusual optical properties of this noble metal, their size-dependent electrochemistry and high chemical stability have made them the model system of choice for exploring a wide range of phenomena including self-assembly, bio-labeling, catalysis etc. They can be synthesized by different ways depending on their applications. All the methods of synthesis of gold nanoparticles are broadly classified in two categories as top-down and bottom-up methods. The top-down approach is a subtractive process starting from bulk materials to make nanomaterials while bottom-up is a controlled additive process that deals with the assembly of precursor atoms or molecules to make nanomaterials. On the other hand, bottom-up methods are chemically controllable and non-destructive. Among all bottom-up methods, the chemical reduction of the metal salt in an aqueous, an organic phase, or two phases, is one of the most popular routes as nanoparticles of a wide range of sizes and shapes can be prepared by controlling the reaction conditions. There is variety of techniques for the characterization of nanoparticles. Spectroscopic techniques (e.g. UV-visible, photoluminescence, IR and

Raman scattering) are employed for the confirmation of the presence of molecular species and electronic transitions, monitoring phase transitions and band gap calculations, studying luminescence, fluorescence and chemical species etc. Microscopic techniques (e.g. SEM, TEM, STM and AFM) give the direct visualization of the morphology, particle size, phases, defects etc. Scattering techniques (e.g. XRD, DLS, SAXS and SANS) are extremely reliable for finding the particle size, shape, number density, interactions and crystal structure. Gold nanoparticles are extensively used in the fields of biology, catalysis, electronics, sensing etc. In biology and medicine, gold nanoparticles are used for drug delivery, labeling, sensing and heating. Gold is very popular for being chemically inert and one of the most stable metals, thus resistant to oxidation. Catalysis with gold nanoparticles, in particular the very active oxide-supported ones, is now an expanding area, and a large number of new catalytic systems for various reactions are now being explored. Further, electronic conduction correlated with single-electron tunnelling involving gold nanoparticles are being studied as basis for future nanoelectronics. Excellent sensory and environmental devices are becoming available for various applications by tuning the spectroscopy, fluorescence, luminescence, and electrochemical characteristics of gold nanoparticles with different substrates including DNA, sugars and other biological molecules. For all these applications, synthesis and characterization of gold nanoparticle play an important role for achieving the better results. A novel method of gold nanoparticles synthesis using block copolymers has been investigated in this thesis.

Chapter 2

Block Copolymer-mediated Synthesis of Gold Nanoparticles

2.1. Introduction

Self-assembly of either molecular or non-molecular components by non-covalent interactions is an enormously powerful tool in modern material science, which enables the formation of structures often not accessible by any other fabrication process [99-101]. This concept was initially associated with the use of synthetic strategies for the preparation of nanostructures about two decades earlier [102-104] and since then the interest in developing bottom-up approaches with the aim of offering an alternative to traditional top-down fabrications has grown dramatically. It is thus reasonable to assume that self-assembled materials in general, and those with a length scale smaller than the actual limits of conventional manufacturing in particular, are going to occupy a privileged position for a long time. In this context, polymers are likely to play a key role, not just for the same reasons that have made them successful materials so far, i.e. ease of synthesis and processing, low cost, variability of chemical functionality and physical properties, but also because of their intrinsic dimensions (typically tens of nanometers) and, even more important, the peculiar mesophase segregation in the case of block copolymers [105].

Block copolymers are a particular class of polymers that belong to a wider family known as soft materials that, independent of the procedure of synthesis, can simply be considered as being formed by two or more chemically homogeneous polymer fragments (blocks) joined together by covalent bonds [106]. In the simplest case of two distinct monomers, conventionally termed A and B, linear diblock (A-B), triblock (A-B-A), multi-

block or star block copolymers can be prepared. The phase behaviour of such block copolymers has been the subject of numerous theoretical and experimental studies and is now well understood [107-110].

In recent times, among various techniques for synthesizing gold nanoparticles the use of block copolymers has found several advantages. This chapter provides the background of block copolymer-mediated synthesis of gold nanoparticles through the introduction of block copolymer and its role in the synthesis mechanism. Poly(ethylene oxide)-poly(propylene oxide)-poly(ethylene oxide) PEO-PPO-PEO triblock copolymers are one of the most commonly used amphiphilic block copolymers comprising two dissimilar moieties, hydrophilic PEO block and hydrophobic PPO block, within the same molecule [111-115]. In aqueous solution, the molecules self-assemble to form micelles of various forms and sizes, where the hydrophobic PPO blocks form the core of these micellar aggregates and the hydrophilic PEOs with the surrounding water molecules form the corona. The block copolymers can be used to produce metal nanoparticles because of their ability to reduce metal ions, enhance nucleation and growth of nanoparticles as well as stabilize them. Self-assembly of block copolymer in this method is utilized to control the synthesis of gold nanoparticles [116]. This thesis aims to look into the improvement of the overall synthesis process by tuning the different steps of the reaction mechanism in different ways.

2.2. Block Copolymers

Environmentally-sensitive bio-inspired block copolymers represent a new class of functional materials with tremendous applications in nanotechnology, biomedical and electronics. By integrating environmentally-sensitive homopolymers into amphiphilic block copolymers, self-assembled supramolecular structures that exhibit stimuli or environmentally responsive

properties can be obtained [112,114-116]. Hence, the interest in these families of novel block copolymers has increased enormously in the recent years [115].

Block copolymers are defined as large blocks that are made up of chemically distinct monomers that are covalently linked together. The interactions amongst the building blocks (hydrophobic, electrostatic etc.) are what drive these block copolymers to self-assemble into different structures in solution. In block copolymers, one can manipulate self-assembly by changing the chemical moiety of the monomers, the length of the blocks, the chain architecture such as linear or star block copolymers and solution environments. Adjusting these parameters results in unique chemical and physical properties for self-assembly that makes block copolymers promising materials for a variety of applications [112,114-116].

2.2.1. Block Copolymer Structure and Classification

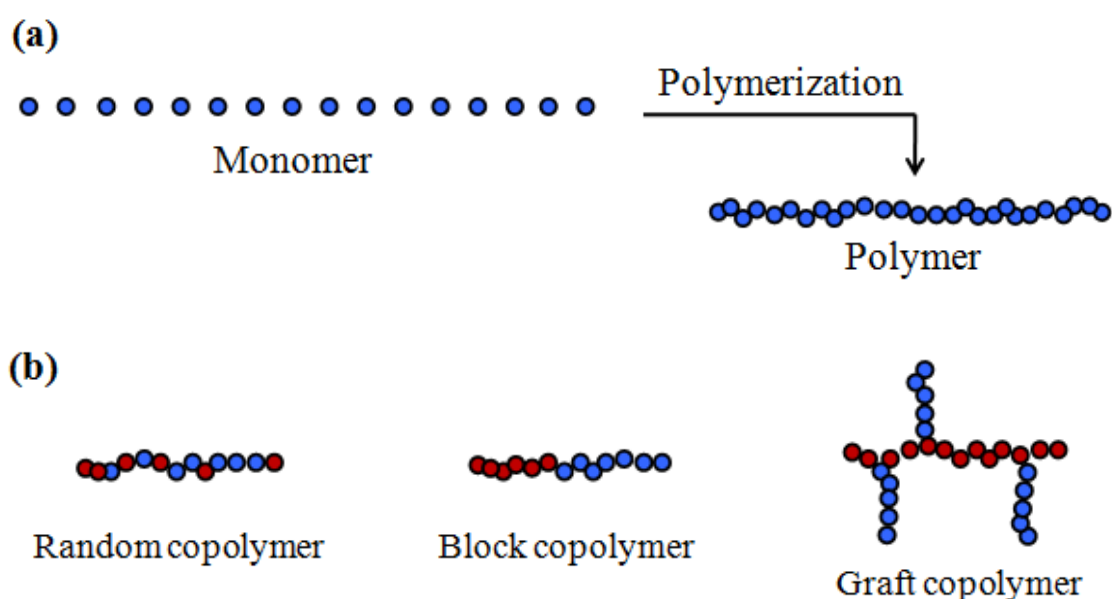


Figure 2.1. Schematic of (a) polymer as synthesized through the polymerization of monomer units and (b) different copolymer structures.

Polymers are long chain molecules with high molecular weight and made of small repetitive units, named monomer. Most polymers are organic and formed from hydrocarbon molecules,

which can have single, double or triple carbon bonds. Structure of polymer as synthesized through the polymerization of monomer units is shown in **Figure 2.1**. Depending on the monomer types, polymers can be classified as homopolymer and copolymers. When all the monomers are same, the molecule is called a ‘homopolymer’ while there is more than one type of monomer are present, the molecule is called a ‘copolymer’. In copolymer, the possible arrangements are random copolymer, alternating copolymer, block copolymer and graft copolymer. These different copolymers are classified based on how the different monomers are arranged along the chain [106,112,114-117].

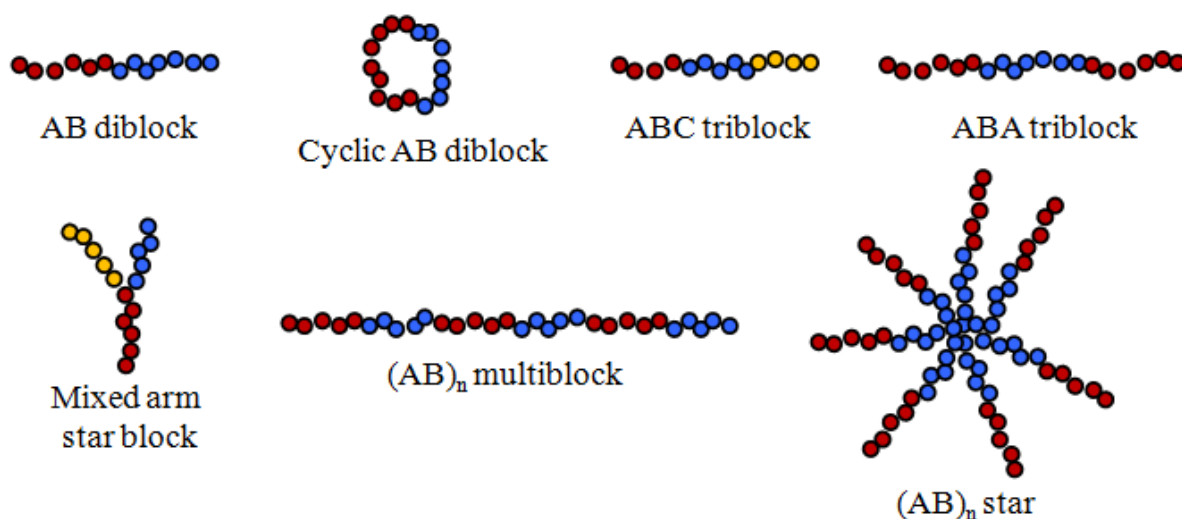


Figure 2.2. Schematic of different block copolymer architectures.

A block copolymer molecule contains two or more polymer segments (blocks) joined in some arrangement. Block copolymers are further classified by the number of blocks each molecule contains and how they are arranged. Linear block copolymers comprise two or more polymer chains in sequence, whereas a star-block copolymer comprises more than two linear block copolymers attached at a common branch point. The standard notation for block copolymers is accepted whereby *A-b-B* denotes a diblock copolymer of polymer blocks A and B. However, sometimes the *b* is replaced by the full term block (*A-block-B*) or alternatively is omitted (*A-B*). Block copolymers with two, three and more blocks are called

diblock copolymer (A-B), triblock copolymer (A-B-A/A-B-C) and star-block copolymer (multi-block) [112,114-117]. Thus, an A-B-C linear triblock consists of three monomer types, whereas an ABA linear triblock consists of two monomer types. In linear arrangement the blocks are connected end-to-end and in star all the blocks are connected via one of their ends at a single junction. Different block copolymer architectures are shown in **Figure 2.2**.

As one becomes familiar with the literature on different block copolymers, it is clear that most of these have been used are from BASF Corporation with the Pluronic[®] and Tetronic[®] trademarks for products initiated with propylene glycol by their Pluronic designation and that with ethylenediamine by the Tetronic designation, rather than by their chemical names. For the Pluronic tradename, coding of these copolymers starts with a letter to define its physical form at room temperature (L = liquid, P = paste, F = flake) followed by two or three digits. The first digit (two digits in a three-digit number) in the numerical designation, multiplied by 300, indicates the approximate molecular weight of the hydrophobic part. The last digit multiplied by 10 gives the percentage of hydrophilic content. For example, pluronic P85 stands for in paste form with a PPO molecular weight of 2400 and a 50% PEO content [116-117].

Pluronic PEO-PPO-PEO block copolymers are synthesized by sequential addition of PO and EO monomers in the presence of an alkaline catalyst, such as sodium or potassium hydroxide [118]. The reaction is initiated by polymerization of the PO block followed by the growth of EO chains at both ends of the PO block. Anionic polymerization usually produces polymers with a relatively low polydispersity index (M_n/M_w). Further chromatographic fractionation is employed in procedures for the manufacture of highly purified block copolymers. This reduces the presence of admixtures, particularly, of the PO homopolymer and block copolymers with lower content of EO than expected. This arrangement results in an amphiphilic copolymer, in which the number of hydrophilic EO (x) and hydrophobic PO

(y) units can be altered. The structure formula of Pluronic block copolymers is shown in **Figure 2.3**. A list of selected Pluronic copolymers having different number of units of EO and PO in the copolymers is given in **Table 2.1** [111].

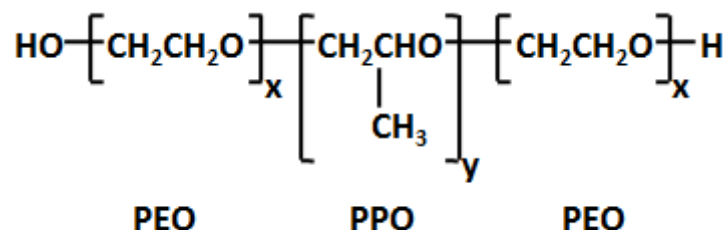


Figure 2.3. Structure of Pluronic block copolymer comprising two hydrophilic PEO blocks sandwiched between a hydrophobic PPO block.

Table 2.1. Chemical structure of various PEO-PPO-PEO block copolymers.

Pluronic	Molecular Formula	Average Molecular Weight	PEO [wt%]	PPO Block Molecular Weight
L35	EO ₁₁ PO ₁₆ EO ₁₁	1900	50	950
L42	EO ₄ PO ₂₂ EO ₄	1630	20	1300
L62	EO ₆ PO ₃₄ EO ₆	2500	20	2000
L64	EO ₁₃ PO ₃₀ EO ₁₃	2900	40	1740
P65	EO ₁₉ PO ₂₉ EO ₁₉	3400	50	1700
P85	EO ₂₆ PO ₄₀ EO ₂₆	4600	50	2300
P105	EO ₃₇ PO ₅₆ EO ₃₇	6500	50	3250
P123	EO ₁₉ PO ₆₉ EO ₁₉	5750	30	4025
F68	EO ₇₆ PO ₂₉ EO ₇₆	8400	80	1680
F88	EO ₁₀₄ PO ₃₉ EO ₁₀₄	11400	80	2280
F108	EO ₁₃₂ PO ₅₀ EO ₁₃₂	14600	80	2920
F127	EO ₁₀₀ PO ₆₅ EO ₁₀₀	12600	70	3780

2.2.2. Amphiphilic Block Copolymers and Self-Assembly

Amphiphiles are molecules which have an affinity for two different types of environments. This dual affiliation is built into the molecules by the covalent joining of blocks of different chemical character and solution properties. Given the opportunity, the two (or more) different blocks strive to minimize their contact, and can thus coerce the amphiphilic molecules to attain a preferential orientation. As a result, amphiphilic molecules self-organize at interfaces and in solution and, in doing so, modify the interfacial properties to a great extent. Amphiphilic block copolymers self-assemble both in solution and in bulk and are capable of generating a variety of micro domain morphologies due to the covalently bonded blocks with different physical and chemical properties [117]. The two blocks are incompatible and interact differently with their environment due to the chemical nature and also behave distinctively in solution which results in micro phase separation not only in aqueous media but also in organic solvents. This self-assembly process is driven by an unfavourable mixing enthalpy and a small mixing entropy, while the covalent bond connecting the blocks prevents macroscopic phase separation.

Block copolymers are known to self-assemble in block selective solvents, which solubilize one but not the other block, forming micelles of various shapes [119,120]. In a solvent, block copolymer phase behaviour is controlled by the interaction between the segments of the polymers and the solvent molecules as well as the interaction between the segments of the two blocks. A defining property of amphiphilic block copolymers is the ability of individual block copolymer molecules (unimers) to self-assemble into micelles in dilute solutions. The unimers form molecular solutions in water at block copolymer concentrations below that of the critical micelle concentration (CMC). At concentrations of the block copolymer above the CMC, unimer molecules aggregate and form micelles, a process called ‘micellization’ as depicted in **Figure 2.4**. The hydrophobic blocks of

amphiphilic copolymers self-associate in aqueous solutions to form supramolecular aggregates consisting of hydrophobic domains surrounded by swollen hydrophilic blocks. Hydrophobic interactions are a fundamental driving force in the assembly of amphiphilic systems which helps in the macromolecular self-association and the formation of nanoscale ordered structures through hydrophobic attraction [121]. The number of block copolymer molecules forming one micelle is called the ‘aggregation number’. The hydrophobic core can serve as a ‘pool’ for the incorporation of various hydrophobic compounds into the micelles. As a result of the incorporation into the core water-insoluble compounds are transferred into the micellar solution, a process called ‘solubilization’. Depending on the length of the hydrophilic and hydrophobic blocks as well as solution environments, the morphology of the micelles can be spherical, cylindrical or lamellar [122]. **Figure 2.5** illustrates different self-assembled micellar structures formed by amphiphilic block copolymers with morphologies like spherical, rod-like, vesicular and lamellar.

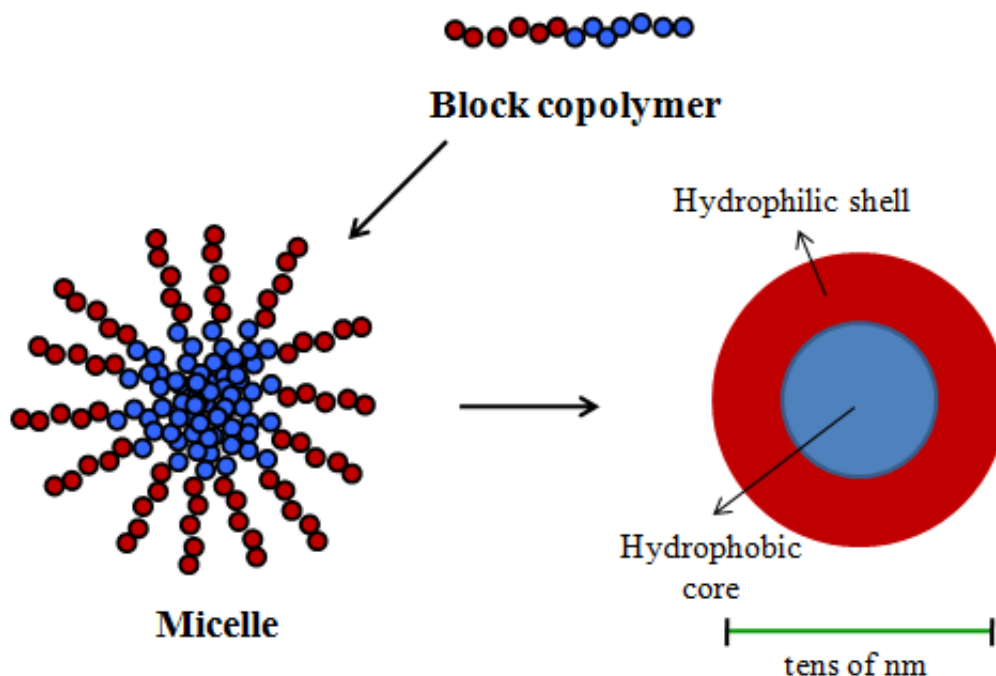


Figure 2.4. Schematic of self-assembled amphiphilic block copolymers into supramolecular nanostructure (micelle) in solution.

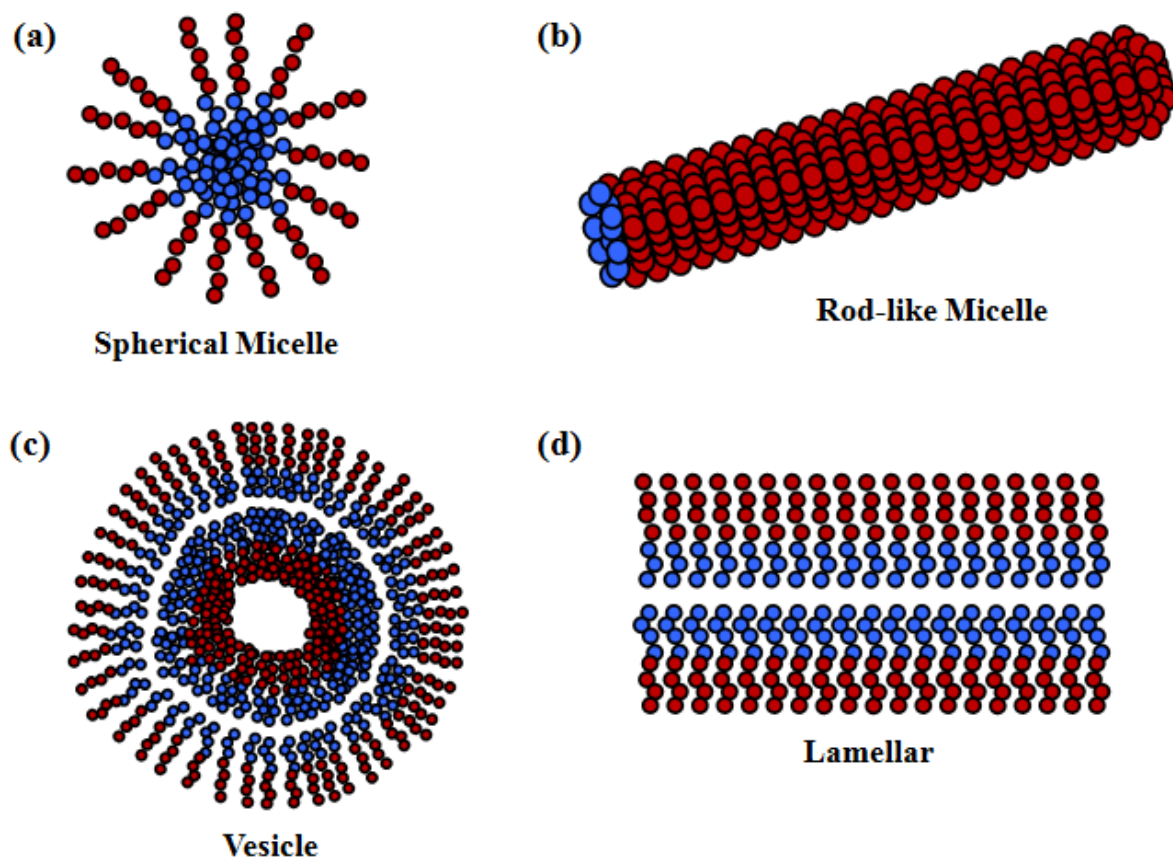


Figure 2.5. Different structures of self-assembly of block copolymers: (a) spherical micelle, (b) rod-like micelle, (c) vesicle and (d) lamellar.

Like surfactants, the micellization process for block copolymers is mainly governed by two parameters, critical micellization temperature (CMT) and critical micellization concentration (CMC). Self assembly will not occur if either of these is not reached and the block copolymer will remain as unimers in the solution [123]. The CMC can be located by a variety of techniques. The most commonly used being surface tensiometry where the CMC is located as the point at which the surface tension becomes essentially independent of concentration. On the other hand, if micelle formation is triggered, a thermodynamic equilibrium will be reached between micelles and unimers. Several parameters have to be considered to characterize a micellar system, such as the equilibrium constant, the quality of the solvent, CMT, CMC, the overall mass molecular weight of the micelle, aggregation number and morphology. These variables affect the hydrodynamic radius R_H , the radius of

gyration R_g , the core radius R_c and the thickness t of the corona. The simplest approach to observe morphology changes in block copolymer micelles consists in changing one variable of the phase diagram of such a system. **Figure 2.6** shows a phase diagram (temperature vs. concentration) of P85 in aqueous solution, where different micellar structure and liquid-crystalline phases can be observed by varying the concentration and temperature [124].

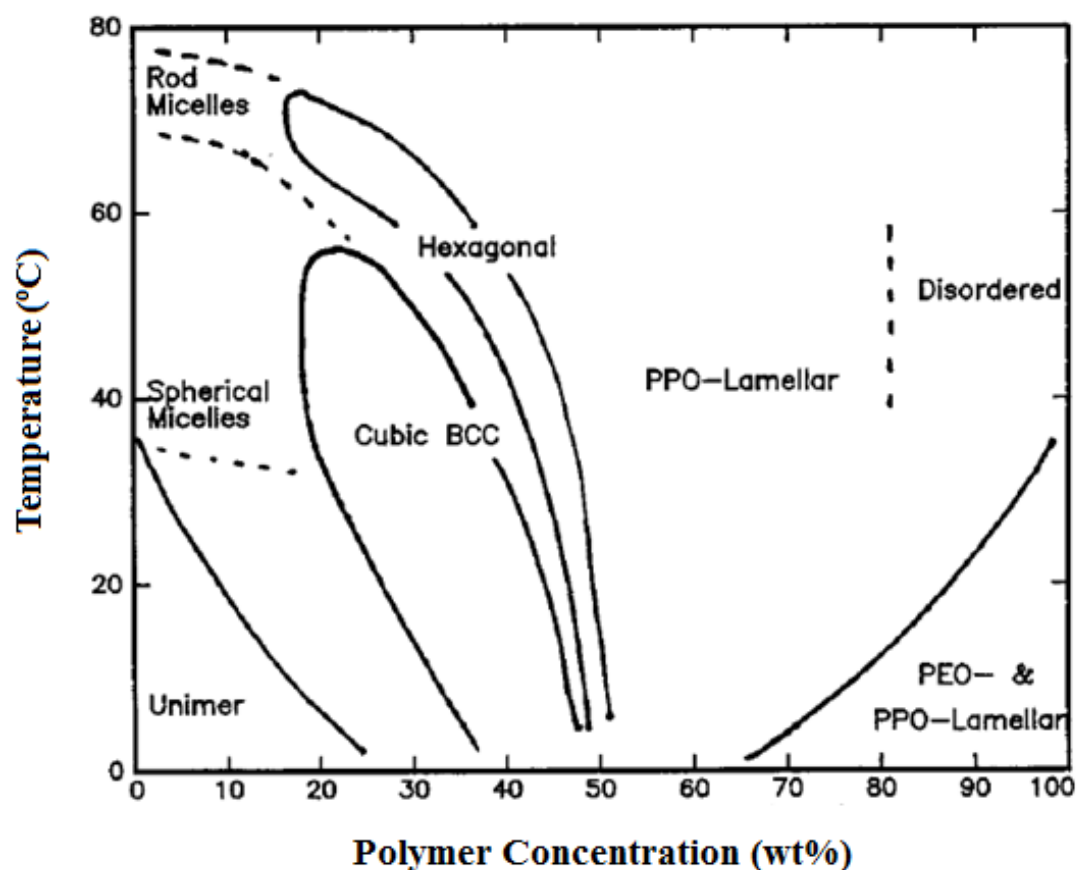


Figure 2.6. The phase diagram of P85 in D_2O .

In some cases, micellization is stimuli-responsive, e.g. double-hydrophilic AB block copolymers containing two water-soluble blocks. Under normal conditions, double hydrophilic block copolymer chains have no tendency to aggregate in aqueous media and are thus observed as unimers. However, once an adequate stimulant is applied, one of the hydrophilic blocks becomes hydrophobic. The initial double hydrophilic copolymer is then transformed into an amphiphilic copolymer and micelle formation is observed as shown in

Figure 2.7. This transition is generally observed to be reversible and results in a sharp modification of the macroscopic characteristic features of the aqueous medium. For example, one can expect a sharp modification to the viscosity of the solution once the system is shifted from unimers to micelles. This stimulant can be temperature, pH, ionic strength etc [125,126]. For example, in PEO-PPO block copolymers micellization is driven by an increase in temperature [127]. This arises from the fact that dehydration of the PPO block takes place with increasing temperature and the initial double hydrophilic copolymer then transformed into an amphiphilic one above the CMT. At further higher temperatures, dehydration of the PEO blocks results in a completely hydrophobic system, which precipitates out from the solution (cloud point). A typical example of pH-responsive micellization has been observed for P2VP-PEO copolymers that exist as unimers at $\text{pH} < 5$ and form micelles at higher pH values [127,128]. This behaviour is directly linked to the deprotonation of the P2VP blocks with increase in pH as P2VP blocks are protonated and positively charged at low pH and thus water soluble. Deprotonation results in hydrophobic P2VP blocks, which then aggregate into micellar cores. The hydrophobization of the P2VP blocks results in micelles rather than in precipitated particles because the P2VP blocks are linked to water-soluble PEO segments. Although the deprotonation process is continuous, it is more significant around the pK_a of the P2VP blocks, which explains why micellization is observed around $\text{pH} = 5$ [128].

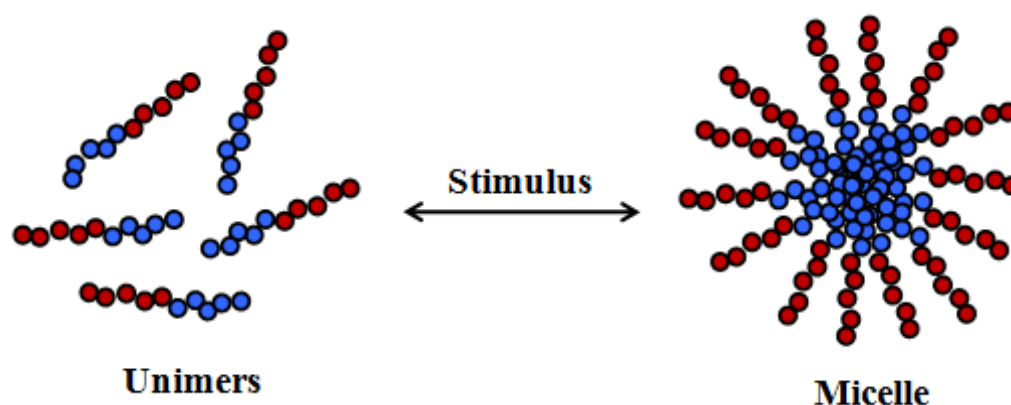


Figure 2.7. Schematic of a stimuli-sensitive micellization process.

2.2.3. Applications of Block Copolymers

The potential applications of amphiphilic block copolymers include solubilization, stabilization, drug delivery, nanostructure synthesis, growth template for mesoporous inorganic materials etc [111,113,115,129]. Some of these applications are summarized below:

(i) Solubilization: There have been numerous studies on the use of amphiphilic block copolymers to solubilize molecules, in particular the use of water soluble block copolymers to solubilize organic compounds (oils) which are immiscible in water. In fact, industrial applications of block copolymers, such as agrochemical dispersions or pharmaceutical formulations, rely on this solubilization capacity [129].

(ii) Emulsification and Stabilization: Amphiphilic block copolymers are widely used to stabilize emulsions and microemulsions. Due to their interfacial activity, they segregate to the oil-water interface, reducing the interfacial tension to facilitate mixing. The interfacial tension is reduced dramatically upon addition of the block copolymer and the microemulsion can swell to a greater extent [130].

(iii) Drug delivery: Mainly PEO-based block copolymers have been used for targeted delivery. They are utilized for improved drug delivery in efficient patient-acceptable formulations, for coatings to reduce protein adhesion or clotting and for structural gels and wound coverings etc [131]. Applications of block copolymer gelation in the development of thermally controlled delivery systems for slow drug release (e.g. biodegradable hydrogels or thermo-responsive block copolymers) have also been explored in a great extent [132].

(iv) Templating: Block copolymers have been extensively used to template the formation of mesoporous materials [133]. Compared with the conventional non-ionic surfactants, amphiphilic block copolymers offer the advantage of having larger pore sizes. Since the pore size and wall thickness can be varied according to the processing conditions, copolymers act as structure directing agents [133,134]. For example, production of mesoporous silica in thin

films using block copolymers has been achieved via selective solvent evaporation, which leads to cooperative self-assembly of the block copolymer and silicate to produce mesoporous silica with hexagonally arranged pores, vesicular structures or rods [135,136].

(v) Nanoreactors: Block copolymer domains can be used as nanoreactors for the synthesis of inorganic nanoparticles [133,137]. Two basic approaches have been developed. The first one involves the binding of inorganic species to the monomer prior to polymerization or to one of the blocks of a copolymer prior to micellization (which may be induced by the ion binding). The most important approach, however, involves the loading in the preformed micelles, whether in solution or in bulk [138].

2.3. Synthesis of Gold Nanoparticles by Block Copolymers

The preparation of metal nanoparticles in solution is most commonly based on the chemical reduction of metal ions and invariably involves organic solvents and ligands [137,139-144].

The utilization of nontoxic chemicals, environmentally benign solvents and renewable materials are emerging issues that merit important consideration in the development of synthetic strategies. A methodology based on the use of water as the solvent provides an environmentally benign route to the production of gold nanoparticles and result in a product that can be easily integrated in applications involving aqueous media [139-144]. It has been recently shown that gold nanoparticles can be synthesized from $\text{HAuCl}_4 \cdot 3\text{H}_2\text{O}$ using Pluronic block copolymers, without additional reducing agents and external energy. Block copolymers not only act as a reducing agent but also enhance the nucleation and growth of nanoparticles as well as provide stability to the nanoparticles [94-98,145].

2.3.1. Synthesis Method

In block copolymer-mediated synthesis method, gold nanoparticles are prepared by simply mixing an aqueous solution of gold salt [e.g. hydrogen tetrachloroaurate(III) hydrate ($\text{HAuCl}_4 \cdot 3\text{H}_2\text{O}$)] with an aqueous solution of amphiphilic block copolymer (e.g. PEO-PPO-PEO). The synthesis is carried out at ambient temperature and without any additional reductant or energy input. This reaction can take place under both ambient light and dark conditions. This synthesis proceeds fast to completion within few hours. The synthesis is environmentally benign and economical since it involves only water and nontoxic block copolymers. The gold nanoparticle dispersions remain highly stable for several weeks. Compared to other methods for gold nanoparticle synthesis, besides the advantages of ambient conditions, fast completion and economical, this methodology offers the use of minimal number of reactants and results in a ready-to-use product [95-98].

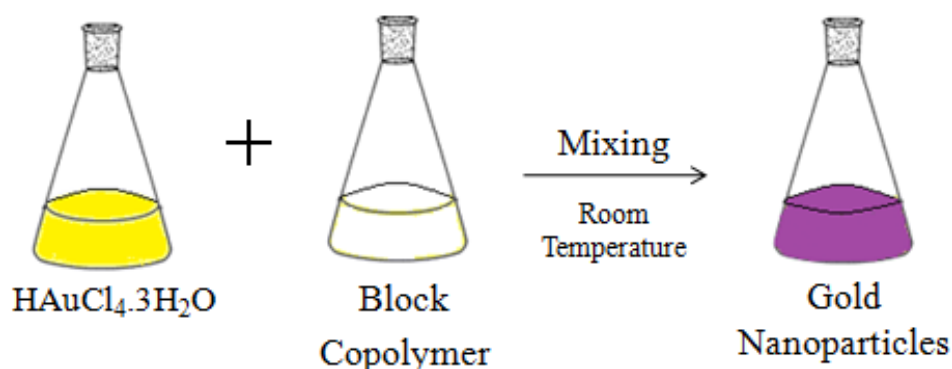


Figure 2.8. Schematic of synthesis of gold nanoparticles from a mixture of gold salt and block copolymer solutions.

Figure 2.8 shows the schematic of mixing of aqueous solution of gold salt and block copolymer. It is seen that both the pure components are clear solutions (gold salt is yellowish at higher concentration) whereas the mixed solution becomes coloured due to the formation of gold nanoparticles. The synthesis of gold nanoparticles has been found to be depending on

the block copolymer and gold salt concentrations, temperature, chemical structure of block copolymer, pH etc [96,98,146]. The molar ratio of block copolymer to gold salt required is quite high, typically of the order of 10 and higher. Most of the syntheses carried out using block copolymers have sizes reported in the range 10 to 50 nm [96,98,146].

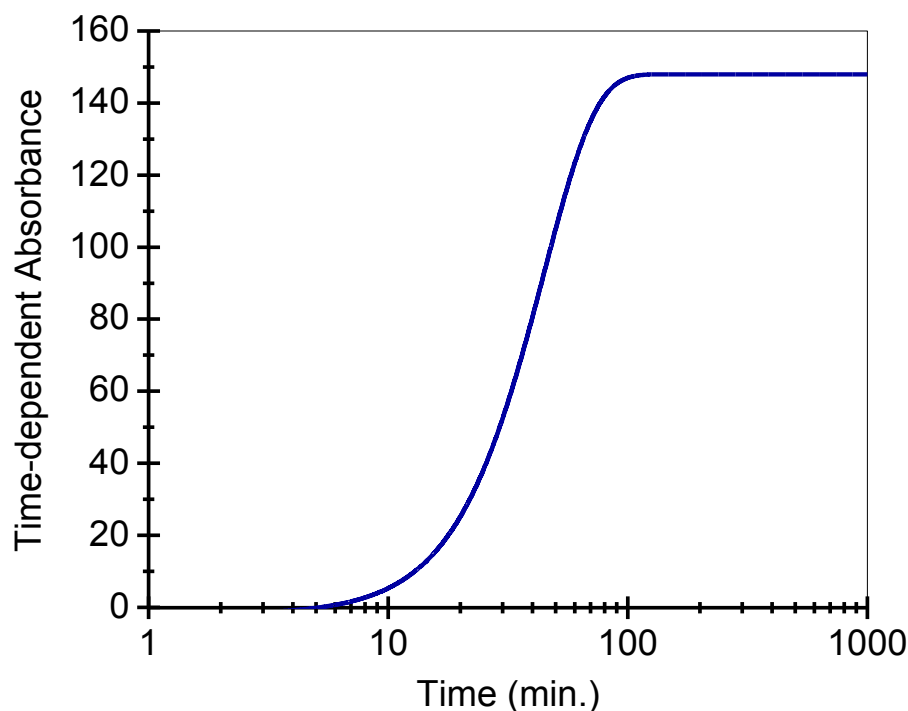


Figure 2.9. The evolution of formation of gold nanoparticles in block copolymer-mediated synthesis.

A typical evolution of formation of gold nanoparticles in block copolymer-mediated synthesis is shown in **Figure 2.9**. The formation of nanoparticle starts after some time (few minutes) on mixing the block and gold salt solutions. The initial region of nanoparticle formation is followed by a linear region where the yield increases almost linearly with time and finally slowing down on approaching the saturation. It has been found that the typical time for the synthesis to complete is in the range of 1–3 hrs for most of the block copolymers. The self-assembly of block copolymers can be utilized in tuning the formation rate as well as the size of the nanoparticles [95-98].

2.3.2. Role of Block Copolymer

The PEO-PPO-PEO block copolymers participate in different roles in the reduction, nucleation and growth, and stabilization in the synthesis of gold nanoparticles from its salts in aqueous solution [94,97,98,146].

(i) Gold Ion Reduction by PEO-PPO-PEO Block Copolymers

The following three possibilities exist by which AuCl_4^- ions can be reduced by the PEO-PPO-PEO block copolymers based on reduction of metal ions reported for the PEO-type surfactant, PEO homopolymer and PEO containing polymers [97,98].

(a) The alcohol (hydroxyl) functionality at the two ends of a PEO-PPO-PEO block copolymer molecule could act as reductant for the metal ions [147,148]. Alcohols are often used as reductants for the synthesis of metal nanoparticles [147,148]. However, alcohols (e.g. methanol, ethanol, 1-propanol, 2-propanol, ethylene glycol and glycerol) at lower concentrations (consistent with the typical PEO-PPO-PEO block copolymer concentration used) do not lead to observable reduction of gold ions.

(b) Hydroperoxides (ROCOOH) that can be formed by polyethers such as PEO-PPO-PEO block copolymers upon reaction with oxygen from the air has both oxidizing and weakly reducing properties [148-151]. In the case even if PEO-PPO-PEO block copolymers form hydroperoxides in air-saturated water, this effect is found significantly small.

(c) The PEO in PEO-PPO-PEO block copolymers forms cavities (pseudo-crown ether structure) that can bind metal ions [152-156] and reduction of bound AuCl_4^- ions can proceed via oxidation of the oxyethylene and oxypropylene segments by the metal center [157]. PEO in aqueous solution is known to form a conformation similar to crown ethers (pseudo-crown ether structure) that is able to bind with metal ions [153,154]. The induced cyclization is caused by ion-dipole interactions between the templating ion and the electron lone pairs of

the ethylene oxide linkages [152,155]. The interaction between metal ions and PEO becomes important for longer PEO chains [152,155]. Several oxygen atoms in the PEO chain interact with one ion and therefore the strength of the attraction depends on the length of the PEO chain [152,155,156]. This method is believed to be primarily responsible for metal ion reduction in PEO-PPO-PEO block copolymer systems.

(ii) Amphiphilicity of PEO-PPO-PEO Block Copolymers for Nucleation and Growth of Gold Nanoparticles

Although the reduction capability of PEO homopolymers is expected to be much more effective than that of the PEO-PPO-PEO block copolymers (the metal ion complexation of PPO is found to be much smaller than PEO), PEO homopolymers have not been found to be effective in the synthesis of gold nanoparticles [94-98]. The differences in synthesis of gold nanoparticles using PEO homopolymer and PEO-PPO-PEO block copolymer suggest that the nucleation and growth of the nanoparticles is enhanced in the case of block copolymer, which is attributed to the amphiphilic character of the block copolymers. The comparison of gold nanoparticle synthesis with various PEO-PPO-PEO block copolymers reveals that the overall block copolymer (i.e. both PEO and PPO blocks) contributes to AuCl_4^- ions reduction and particle formation. PEO is more dominate than PPO in the initial stages of reduction. PPO facilitates block copolymer adsorption on gold clusters and reduction of AuCl_4^- ions on the surface of these gold clusters and/or particles [94-98].

(iii) Stabilization of Gold Nanoparticles by PEO-PPO-PEO Block Copolymers

Block copolymers also provide stability to the gold nanoparticles in solution. It is achieved by the adsorbed layer of block copolymers around the surface of the nanoparticles. The adsorption takes place because of the amphiphilic character of the block copolymers [94-98]. The PPO blocks are expected to be in contact with the nanoparticle surface. On the other

hand, PEO blocks projecting outward in the solution give rise steric stabilization to the nanoparticles. The schematic of a block copolymer-stabilized gold nanoparticle is shown in **Figure 2.10**. The larger the size of the PEO blocks, larger will be its reduction and stabilization capabilities. However, the right balance of PEO to PPO is required for the amphiphilicity of block copolymer for controlling the nucleation and growth of the nanoparticles [94-98].



Figure 2.10. Schematic of a block copolymer-stabilized gold nanoparticle.

2.3.3. Mechanism and Tuning of the Synthesis

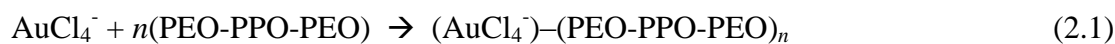
The amphiphilic PEO-PPO-PEO block copolymers can act as efficient reductant as well as stabilizer in a single step synthesis of stable gold nanoparticles from gold salt $\text{HAuCl}_4 \cdot 3\text{H}_2\text{O}$ in aqueous solution. The formation of gold nanoparticle from AuCl_4^- consists of following three steps (**Figure 2.11**) [94-98]:

1. Reduction of gold ions in solution by block copolymers
2. Nucleation and gold cluster formation
3. Growth and stabilization of gold nanoparticles

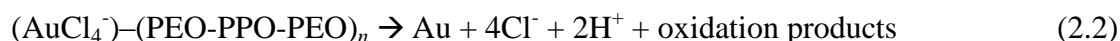
Step 1: Reduction of gold ions in solution by block copolymers

The mechanism of gold ion reduction by the PEO-PPO-PEO block copolymers in aqueous solution is believed to be same as proposed in the case of PEO homopolymer solutions [157].

The polymers form pseudo-crown ether structures (cavities) with AuCl_4^- ions as

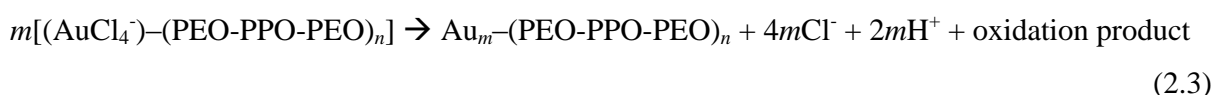


where $(\text{AuCl}_4^-)\text{-(PEO-PPO-PEO)}_n$ represents AuCl_4^- ions bound to cavities that are formed from PEO and PPO blocks [157]. The reduction of bound AuCl_4^- ions proceeds via oxidation of the polymer by metal (gold) center [157] through the reaction



Step 2: Nucleation and gold cluster formation

The amphiphilic character of PEO-PPO-PEO block copolymers [111,113] favours the nucleation of reduced gold atoms and their cluster formation.



where $\text{Au}_m\text{-(PEO-PPO-PEO)}_n$ represents a gold clusters with adsorbed block copolymers.

The adsorbed block copolymer can form pseudo-crown ether structures that bind the AuCl_4^- ions, $\text{Au}_m\text{-(PEO-PPO-PEO)}_n\text{-(AuCl}_4^-)$, and facilitate their further reduction at the surface of the cluster [97].

Step 3: Growth and stabilization of gold nanoparticles

The reduction of AuCl_4^- ions and formation of gold clusters of that of step 2 is repeated on the surface of gold nanoparticles allowing particles to grow. The optimization of solution conditions controls the size of the nanoparticle. The attached block copolymer at the nanoparticle surface makes the nanoparticles sterically stabilized in solution [97].

The gold nanoparticle synthesis using block copolymers can be controlled by tuning any of the above steps. Some of the common important parameters to control different steps of synthesis are chemical structure of block copolymer, concentrations of block copolymer and gold salt, temperature and pH. The reduction step is believed to be quite fast (order of seconds) and therefore formation rate of gold nanoparticles is decided mainly by the nucleation and growth steps of the mechanism [94-98].

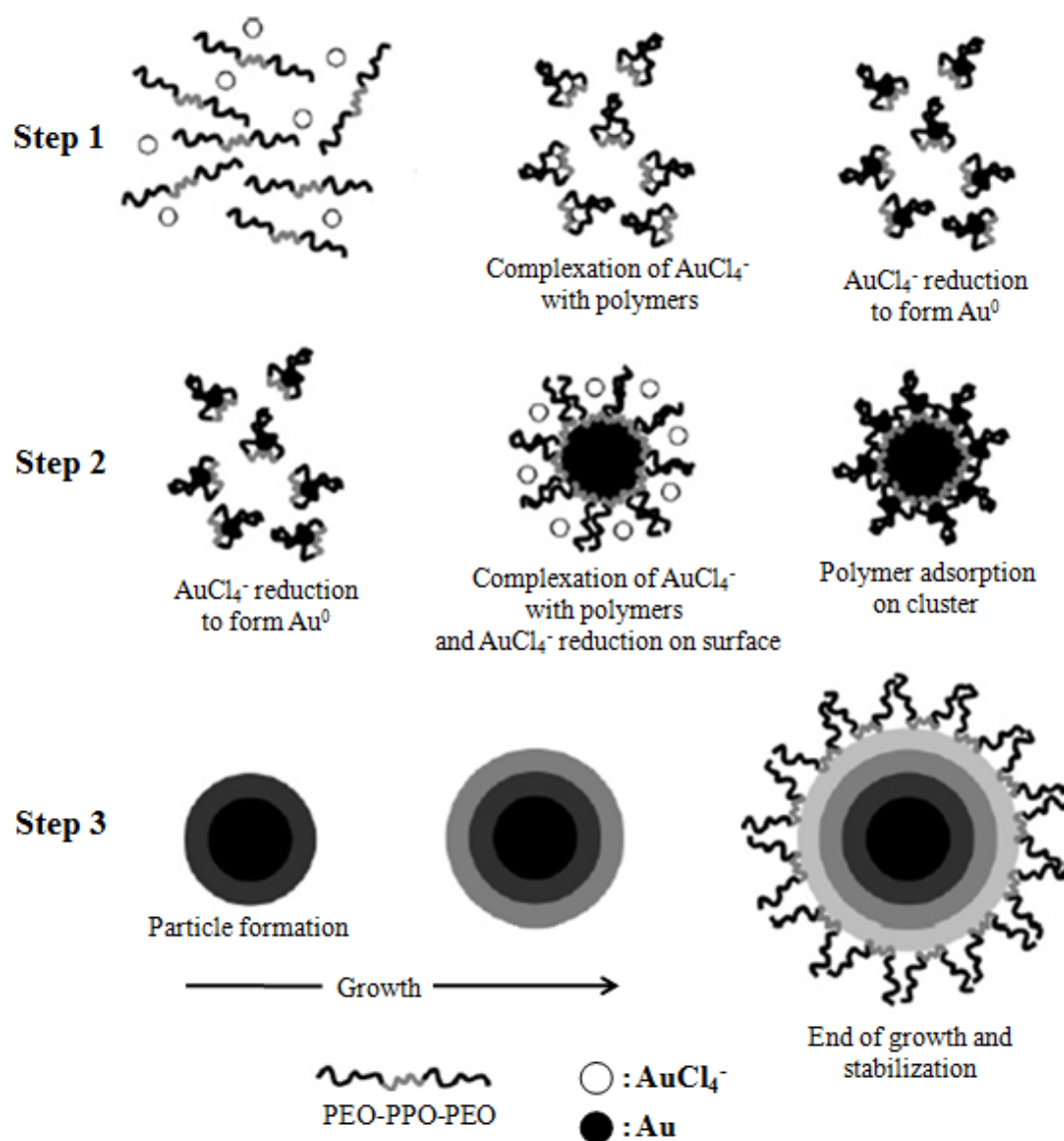


Figure 2.11. Scheme of the mechanism of PEO-PPO-PEO block copolymer-mediated formation of gold nanoparticles.

2.4. Layout of the Thesis

The synthesis of gold nanoparticles using a number of block copolymers in aqueous solution has been reported recently. However, the dependence of synthesis on different parameters is not fully understood as well as the yield achieved so far in this method has been quite low. This thesis deals with the study of synthesis and characterization of block-copolymer mediated gold nanoparticles for understanding the role of different components in tuning the various synthesis parameters (formation rate, yield, stability, shape and size of nanoparticles).

The synthesis has been characterized by a combination of techniques which are discussed in the next chapter (chapter 3). The synthesis of gold nanoparticles involves mixing of aqueous solutions of block copolymer and gold salt at room temperature. The yield of gold nanoparticles simply does not increase with the increase in block copolymer or gold salt concentration in these systems. Chapter 4 provides the study on the optimization of synthesis of gold nanoparticles for its dependence on block copolymer and gold salt to improve the yield. Self-assembly of block copolymer plays an important role in the synthesis of gold nanoparticles. The correlation of self-assembly of block copolymer as varied by different means with formation of gold nanoparticles has been examined in chapter 5. Chapter 6 discusses development of methods of high-yield synthesis of gold nanoparticles, where the yield can be enhanced by manyfold. Chapter 7 presents optimization of high yield synthesis of gold nanoparticle for probing their interaction with proteins. The interaction of these gold nanoparticles with two model proteins (lysozyme and bovine serum albumin) has been studied. The summary of the thesis is given in chapter 8.

2.5. Summary

The background of block copolymer-mediated synthesis of gold nanoparticles has been discussed. The block copolymers can be used to produce metal nanoparticles because of their amphiphilic character and ability to reduce metal ions. On mixing the aqueous solution of metal (e.g. gold) salt and block copolymers, these polymeric nanostructured matrixes engulf the ionic metal precursors, which after subsequent reduction form nanoparticles. It has found several advantages e.g. block copolymer not only plays the dual role of reductant and stabilizer but also provide an economical, fast and environmentally benign way for the synthesis of gold nanoparticles. This thesis aims to look into the improvement of the overall synthesis process by tuning these steps of the reaction mechanism in different ways.

Chapter 3

Multi-Technique Approach for Characterization of Gold Nanoparticles

3.1. Introduction

Nanoparticle characterization is necessary to establish understanding and control of nanoparticle synthesis and applications [1,19,158-160]. The need to fine-tune different nanoparticle properties to make them suitable for specific applications has evolved a large number of worldwide research efforts aimed at their tailoring. However, full use of these structures in these applications requires more detailed information and a feedback of data coming from reliable characterization techniques. In general as discussed in chapter 1, there are number of techniques for the characterization of nanomaterials, for the understanding of their structure, properties and interactions. For example, spectroscopic techniques (e.g. UV-visible, photoluminescence, IR and Raman spectroscopy) are employed for the confirmation of the presence of molecular species and electronic transitions, monitoring phase transitions and band gap calculations, studying luminescence, fluorescence and chemical species etc [1,19,158-160]. Microscopic techniques (e.g. SEM, TEM, STM and AFM) give the direct visualization of the morphology, particle size, phases, defects etc [1,19,158-160]. Scattering techniques (e.g. XRD, DLS, SAXS and SANS) are extremely reliable for finding the particle size, shape, number density, interactions and crystal structure [1,19,158,159]. Each technique has its own advantages and disadvantages to get the required information under the required conditions. Therefore, many times combination of different techniques is used for obtaining complementary results.

A multi-technique approach combining spectroscopy, microscopy and scattering techniques has been used in this thesis for the characterization of gold nanoparticles. The use of different techniques is required for understanding the role of different components and tuning of the synthesis. The different techniques used are UV-visible spectroscopy, TEM, DLS, SAXS and SANS. This chapter gives the details of these techniques and the kind of information that can be obtained from them is discussed.

3.2. UV-Visible Spectroscopy

UV-visible spectroscopy is based on the absorption of photons by the samples to produce electronic transitions from the ground state to an excited state. As a result the absorption spectra are generated reflecting the identity and concentration of molecules in solution [161]. Some of the nanoparticles display UV-visible spectrum because of the existence of the surface plasmon resonance (SPR) that is sensitive to size, shape, concentration, agglomeration state and refractive index near the nanoparticle surface, which makes UV-visible spectroscopy a valuable tool for characterization of nanoparticles [162].

3.2.1. Surface Plasmon Resonance

At the nanometer scale, particles display properties that are not inherent in individual atoms or to those in the bulk macroscopic material [1,19,158-160]. The optical properties of gold nanoparticles depend on their size and shape, interparticle distance, type of attachment (e.g. protein), dielectric constant of the dispersion medium etc [159-162]. In a nanoparticle, many of the atoms are located on the surface due to large surface-to-volume ratio, hence unusual properties are observed which are not present in the bulk or in individual atoms [1,19,158-160]. One of these optical phenomena is surface plasmon resonance. The deep coloured nature from orange through to deep purple, of colloidal gold is a result of the surface

plasmon. At this nanometer scale the 'quantum size effect' becomes significant as the de Broglie wavelength of the valence electrons is in the same size range as the particle itself. The particles are then considered to be zero-dimensional quantum dots or quantum boxes and are subject to quantum mechanical rules. Freely mobile electrons are trapped effectively in quantum boxes and hence exhibit a collective oscillation frequency associated with the plasmon resonance in the presence of light [160-162].

Surface plasmon resonance manifests itself when the electric field of the incoming radiation induces a dipole on the nanoparticle. When a gold nanoparticle, with a diameter of between about 10 and 100 nm, is irradiated by light with a wavelength much greater than the particle diameter, the conduction band free electrons (e^- cloud) are displaced relative to the fixed background of immovable positive ions by the oscillating electric field of the incident light. As a result, a net charge difference appears on the surface at one side of the particle. Its attraction with the lattice ions on the opposite side leads to a restoring force. It tries to compensate for this dipole, so that a unique resonance frequency is formed which matches the electron oscillation frequencies within the particle and this results in an oscillation of the e^- cloud known as a dipole plasmon resonance. This frequency of oscillation is equal to the frequency of resonant light and as the particle is much smaller than the wavelength of incoming light it is homogeneously polarised [160-162]. The plasmon resonance band is observed at approximately 530 nm for gold nanoparticles of diameter 5–20 nm [159]. The resonance frequency is mainly determined by the strength of the restoring force. This force depends on the separation of the surface charges i.e. the particle dimensions and the polarizability of the medium between and around the charges. In other words the frequency, intensity and bandwidth of the SPR absorption and scattering depend on the incident wave, metal composition, nanoparticles size and shape, dielectric properties of surrounding medium/substrate, spaced particles inter-particle interaction and particle-to-particle

interactions [163,164]. These different information thus regarding nanoparticles can be obtained by the UV-visible spectroscopy [159-162].

The nanoparticle systems because of surface plasmon effects can appear different coloured as given in **Table 3.1**. When particles are small (~ 10 nm) they appear red due to the absorption of blue-green light at around 520 nm. If these particles are allowed to coalesce in a controlled fashion by the addition of electrolytes, a colour change is observed. The red goes through violet and blue to green as the nanoparticles grow. This is due to a change in the absorption spectrum upon aggregation, causing the increased absorption of red light.

Table 3.1. The complementary observed colours of nanoparticles to that absorbed in SPR.

Wavelength of the Maximum Absorption (nm)	Colour Absorbed	Colour Observed
380 – 420	Violet	Green-Yellow
420 – 440	Violet-Blue	Yellow
440 – 470	Blue	Orange
470 – 500	Blue-Green	Red
500 – 520	Green	Purple
520 – 550	Green-Yellow	Violet
550 – 580	Yellow	Violet-Blue
580 – 620	Orange	Blue
620 – 680	Red	Blue-Green
680 – 780	Purple	Green

3.2.2. Experimental Details

The schematic diagram for a UV-visible spectrophotometer is shown in **Figure 3.1**. Radiation from the source passes through monochromator which select and transmits the light of

particular wavelength. The transmitted light is splitted into two beams by beam splitter and each splitted beam passes through sample and reference to photo detector. The signals are amplified and spectrum is displayed in a computer. Intensity of light (I_0) at a given wavelength passes through a sample solution that absorbs light in certain wavelength. Intensity of transmitted light (I) from the sample is detected by the detector [160]. The amount of radiation absorbed can be measured either by transmittance or absorbance, where transmittance $T = P / P_0$ and absorbance $A = \log_{10} (P_0/P) = -\log_{10} T$. P_0 and P are the radiant power of the incident and transmitted radiation, respectively. Further, the absorbance (A), concentration of the absorbing species c (in mol/l or M) and path length of the sample cuvette b (in cm) are related through Beer-Lambert law as $A = \epsilon cb$, where ϵ is the molar absorptivity or molar extinction coefficient ($M^{-1}cm^{-1}$) [165,166].

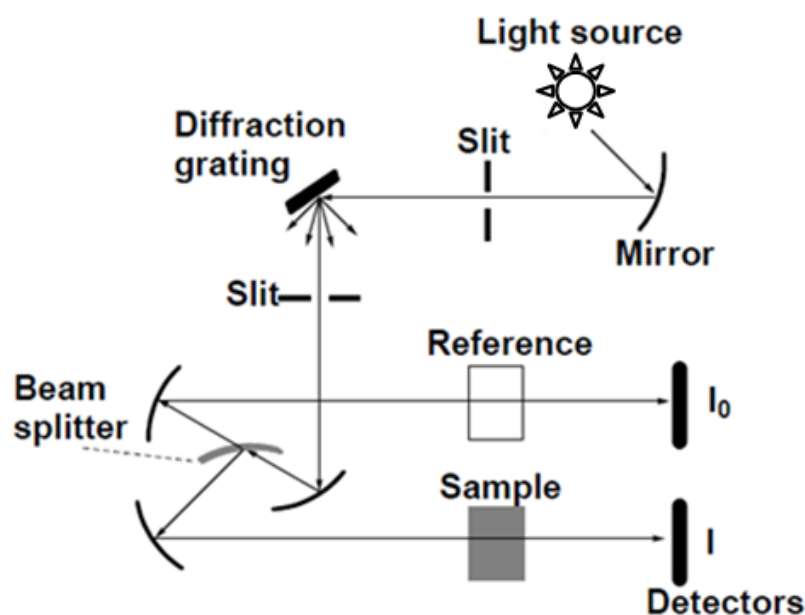


Figure 3.1. Schematic diagram for a UV-visible spectrophotometer.

In this thesis, the measurements were carried out using 6505 Jenway UV-visible spectrophotometer. This instrument is suitable for measurements in the scanning wavelength range between 190 nm and 1100 nm (with an accuracy of ± 1 nm). It makes use of tungsten halogen lamp as a visible light source and deuterium discharge lamp for the UV light source.

The instrument can operate in spectrum mode with a wavelength interval 1 nm and the samples held in quartz cuvettes of path length 10 mm.

3.2.3. Characterization of Gold Nanoparticles by UV-Visible Spectroscopy

Gold nanoparticles show a characteristic SPR peak around 540 nm observed in the UV-visible spectrum as shown in **Figure 3.2**. The SPR profile can be used to obtain information on the nanoparticle composition, its size and shape and dielectric properties of the surrounding medium [163,164]. Figure 3.2 also shows the UV-visible spectra of gold nanoparticles for different sizes of nanoparticles. The SPR peak position shifts to higher wavelength with the increase in the particle size and can be explained by the particle in a box problem in quantum mechanics. The absorption energy of quantum dots (QDs) shifts to higher wavelength [$E_g(R) > E_g$] with increasing radius of QDs (R) with a dependence of $1/R^2$ [167].

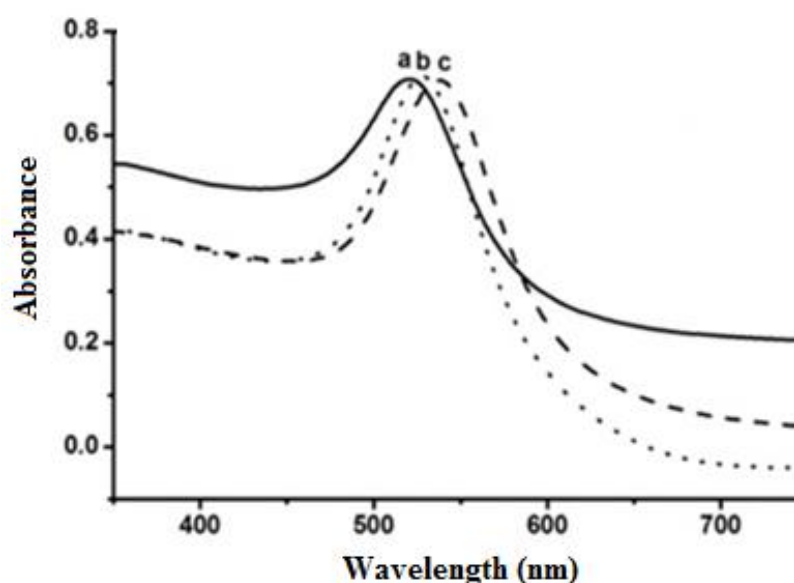


Figure 3.2. UV-visible spectrum of gold nanoparticles for different sizes ($c > b > a$).

UV-visible absorption spectra are known to be strongly depending on the shape of the nanoparticle. In particular, shape anisotropy results in an anisotropic response towards

incoming light, which allows the further modulation of optical effects through alignment [163,164]. **Figure 3.3** shows variation of UV-visible spectra with the change in the particle morphology. One-peak SPR peak for spherical nanoparticles transforms to two-peaks SPR for nanorods which typically display longitudinal and transverse plasmon resonances (electron oscillations along or across their long axis, respectively). Rod length affects longitudinal plasmon wavelength (a strong extinction peak in the upper visible or near-infrared parts of the spectrum). As the aspect ratio increases, the position of the longitudinal plasmon band red-shifts and the transverse plasmon band position stay relatively constant. Thus, the particle shape dictates what wavelengths of light can be absorbed, and elastically scattered; gold nanorods of moderate aspect ratio (2 – 5) display plasmon bands with tunable maxima from ~700 to 900 nm and high-aspect ratio nanorods exhibit a longitudinal plasmon band past 1500 nm [163,164,167].

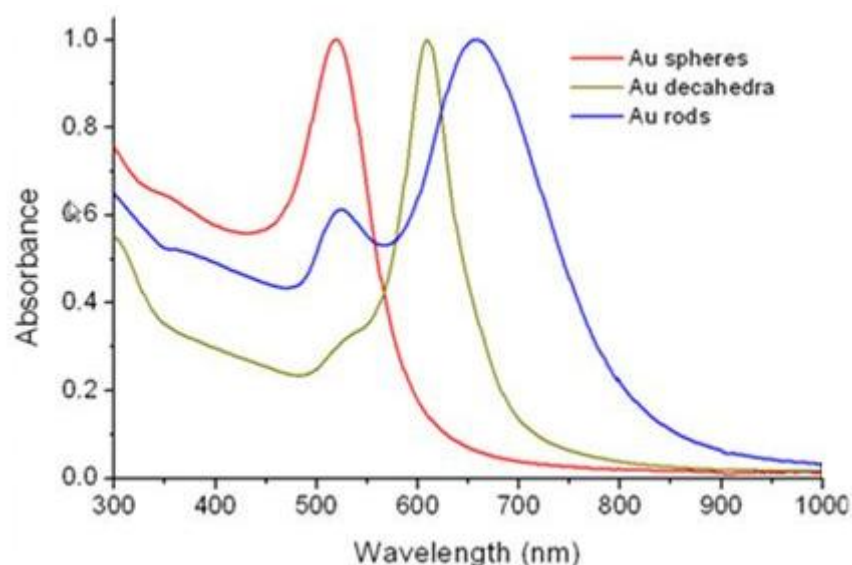


Figure 3.3. UV-visible absorption spectra of different gold nanostructures, e.g. nanoparticles/spheres, decahedra and nanorods.

UV-visible absorbance spectra can also be used to investigate different ligands (proteins, antibodies etc.) on the nanoparticles (**Figure 3.4**). The adsorption of ligand onto gold nanoparticle surface results in red shift in absorbance peak for the nanoparticle. It is

believed to be due to the changes in the dielectric nature (modification of the refractive index) surrounding the nanoparticles after the formation of ligand layer on the surface of the gold nanoparticles [163,164,168].

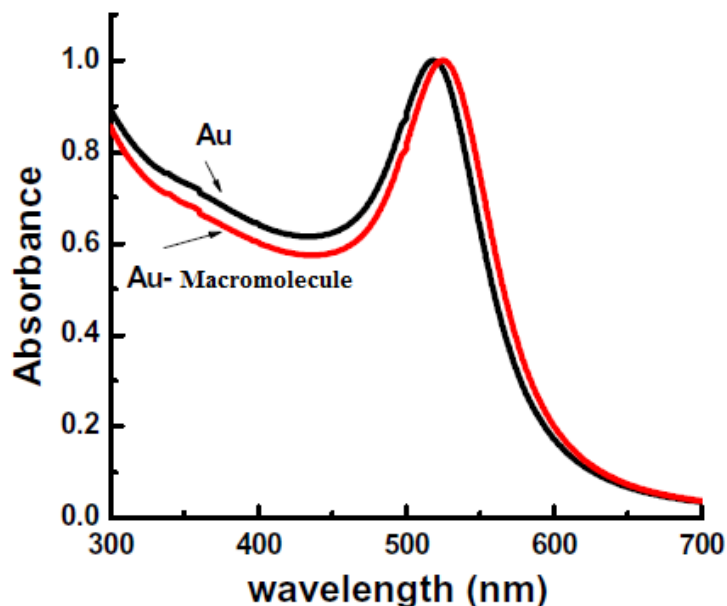


Figure 3.4. The change in UV-visible spectra of gold nanoparticles on their conjugation with ligand.

3.3. Transmission Electron Microscopy

For the study of structure and morphology of nanomaterials with magnifications down to the atomic scale transmission electron microscopy is an important direct method. TEM uses electrons instead of light waves to generate magnified images. It has higher resolution than optical microscopes (due to $\Delta\lambda$) and allows one to visualize objects that are as small as 1 nm, hence atomic resolution is possible. In this way, it bridges the 1 nm - 1 μm gap between X-ray diffraction and optical microscopy [54,160,169,170].

3.3.1. Experimental Details

In transmission electron microscopy, a beam of electrons is passed through the sample with high accelerating voltage. It uses magnetic lenses to deflect the electron beam where the

electrons are transmitted through the sample and detected by a camera before being focused by an objective lens. The resulting pattern of electron reflection and absorption is magnified on a fluorescent screen and an image appears on the screen corresponding to the size and shape of the particles present in the sample [54,160,169].

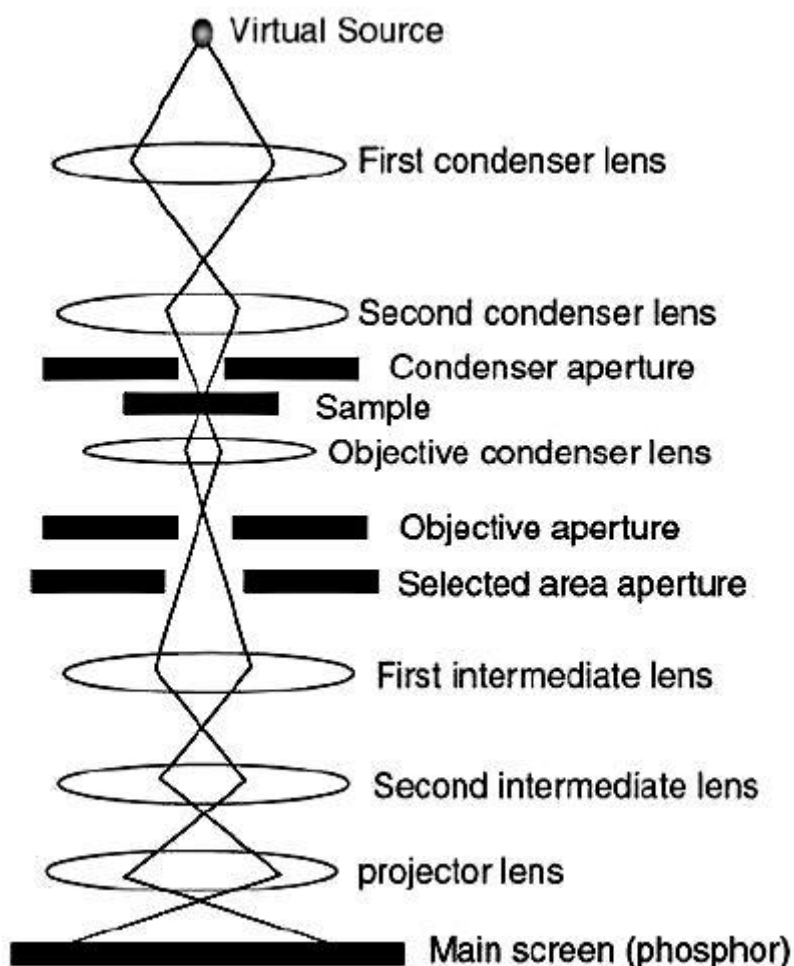


Figure 3.5. Schematic of a transmission electron microscope.

Schematic of a typical transmission electron microscope is shown in **Figure 3.5**. The electron gun, a hairpin-shaped tungsten filament (cathode) is usually used as the source of electrons through thermo-ionic emission. An accelerating voltage (fixed amount of negative high voltage) is applied to the surrounding cathode cap and a small emission current is then applied to the filament to achieve the release of electrons. The anode located below the gun

assembly, is electrically at ground, thus creating a positive attraction for the negatively charged electrons, which overcome the negative repulsion of the cathode cap and accelerate through the small hole in the anode. As glass lenses impede electrons, electromagnetic converging lenses are used to direct and focus the electron beam inside the column. A tightly wound wrapping of copper wire produces the magnetic field that is the essence of the lens. The electron moves through the centre hole in this solenoid. The electrons follow a tight spiral path as they are accelerated through the lenses. The path and trajectory taken by the electrons are influenced by the lens current as they pass through a small opening in the lens. Then there is an opening to insert specimen holder into the high-vacuum chamber for observation. A series of pumps are used to accomplish an adequate vacuum as electrons are easily deflected by hydrocarbons or gas molecules. The final image is viewed by the projection onto a phosphorescent screen which gives off photons when irradiated by the electron beam. A film camera beneath the phosphorescent screen or a CCD camera is used to capture the image. An operation panel for sample alignment, beam focusing and image magnification gives the control over the instrument [54,160,169].

3.3.2. Gold Nanoparticles as Characterized by Transmission Electron Microscopy

The uniformly suspended nanoparticles in the liquid solvent are first obtained by stirring the solution in an ultrasonic stirrer. For the TEM sample preparation, few drops of the sample are put on a carbon amorphous film coated microscopic copper grid. Carbon film coated copper grid and the specimen holder are shown in **Figure 3.6**. Then the sample is dried in air allowing the solvent to evaporate under ambient conditions. Alternatively, a drop of sample solution can be attached on one side of the copper grid, which is then gently placed on filter

paper with the opposite site facing down. We have used JEOL 2000 FX transmission electron microscope for the characterization of gold nanoparticles in this thesis. All the TEM microphotographs were taken at acceleration voltage 160 kV, recorded on a photographic film. A typical TEM micrograph of gold nanoparticles is shown in **Figure 3.7**. A large number of such micrographs are usually taken to determine the size distribution of the nanoparticles [170].

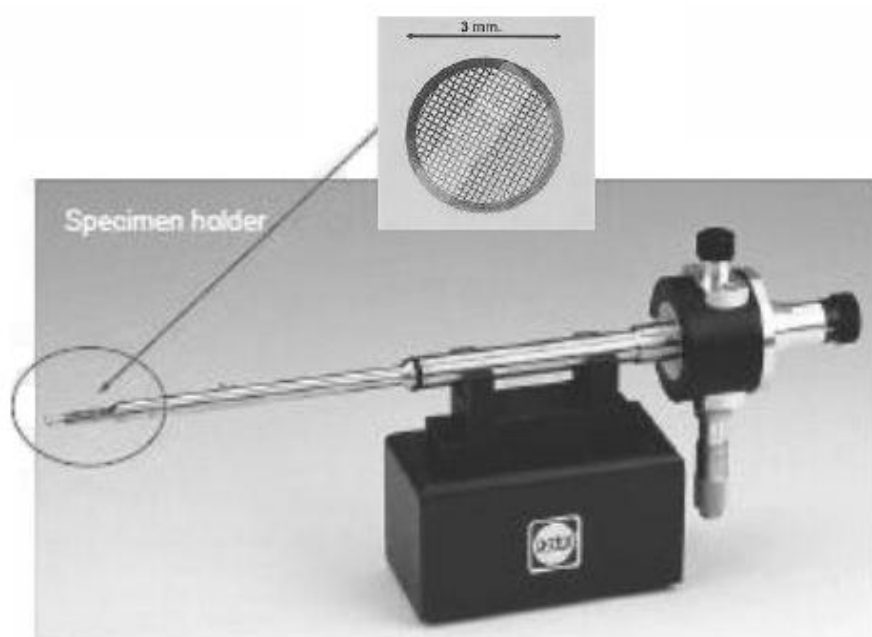


Figure 3.6. Carbon film coated copper grid as put on the specimen holder in TEM measurements.

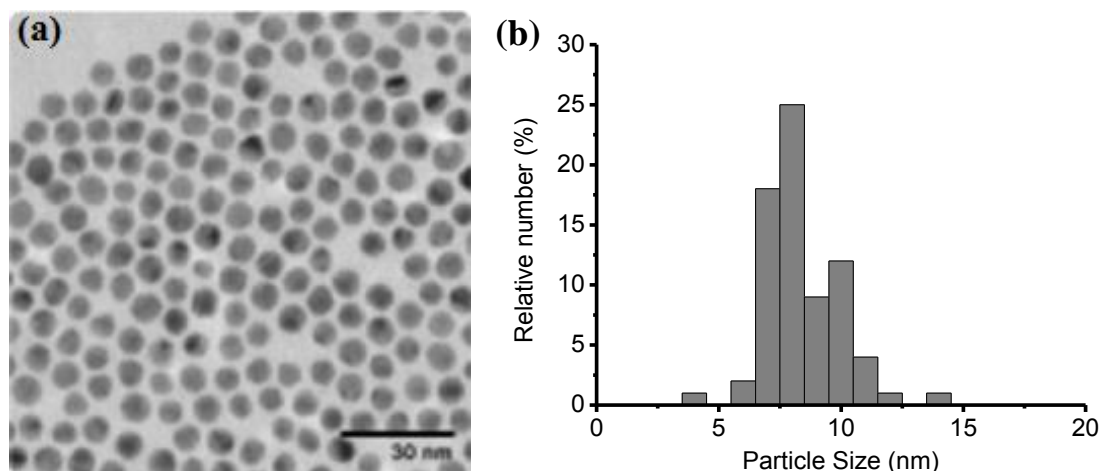


Figure 3.7. (a) TEM micrograph of gold nanoparticles and (b) calculated nanoparticle size distribution.

3.4. Dynamic Light Scattering

Unlike static light scattering (SLS) which is sensitive to the length scale that of order of wavelength of light, dynamic light scattering (DLS) can measure sizes down to 1 nm. SLS measures the time averaged scattered intensity as a function of the scattering angle. On the other hand, DLS gathers information on the Brownian motion in a sample by analyzing the fluctuations of the scattered light intensity. This time dependence of the fluctuations in the net scattered intensity forms the basis of the DLS which yields structural information of the particle by measuring its diffusion coefficient [63,64,171-175].

3.4.1. Theory of Dynamic Light Scattering

The signal generated by the light scattering from diffusing particles can be analyzed by its intensity autocorrelation function $G^I(\tau)$ as given by

$$G^I(\tau) = \langle I(t)I(t + \tau) \rangle \quad (3.1)$$

where $I(t)$ is the scattered light intensity at time t and $I(t + \tau)$ is the scattered light intensity at some later time $(t + \tau)$. **Figure 3.8** shows a typical pattern of intensity fluctuations as a function of time. The normalized intensity autocorrelation function $g^I(\tau)$ is

$$g^I(\tau) = \frac{G^I(\tau)}{\langle I(t) \rangle^2} \quad (3.2)$$

The electric field autocorrelation function $g^E(\tau)$ is related to the normalized intensity autocorrelation function by

$$g^I(\tau) = 1 + B[g^E(\tau)]^2 \quad (3.3)$$

where B is experimental parameter which mainly depends on the detection optics and alignment. It is roughly equal to the inverse of the number of speckle from which light is collected (a speckle pattern is a random intensity pattern produced by the mutual interference

of a set of wave fronts). For a monodisperse system of particles, $g^E(\tau)$ follows a simple exponential decay with decay constant Γ [173],

$$g^E(\tau) = \exp[-\Gamma \tau] \quad (3.4)$$

The apparent diffusion coefficient (D_a) is obtained from relation $\Gamma = D_a Q^2$ ($Q = 4\pi n \sin \theta / \lambda$, where 2θ is the scattering angle, n is refractive index of medium and λ is wavelength of light) and the corresponding effective hydrodynamic radius R_H is given by the Stokes-Einstein relation [173],

$$R_H = \frac{k_B T}{6\pi\eta D_a} \quad (3.5)$$

where k_B is Boltzmann constant, T is the temperature and η is the solvent viscosity.

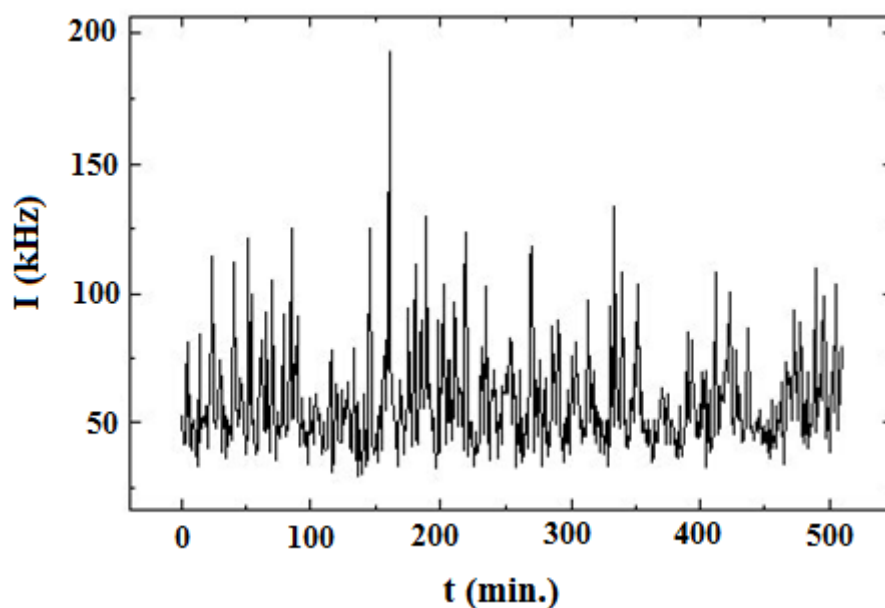


Figure 3.8. Intensity fluctuations at the detector due the Brownian motion in the sample volume.

3.4.2. Experimental Details

DLS experiment involves scattering of a monochromatic beam of light from the sample through an angle 2θ and then recording the scattered photon intensity at small intervals (~ 50

ns) of time. A photon correlator card is used to store these intensities in different channels and to generate the intensity correlation spectrum $g^I(\tau)$ [174]. The schematic of the dynamic light scattering instrument is shown in **Figure 3.9**.

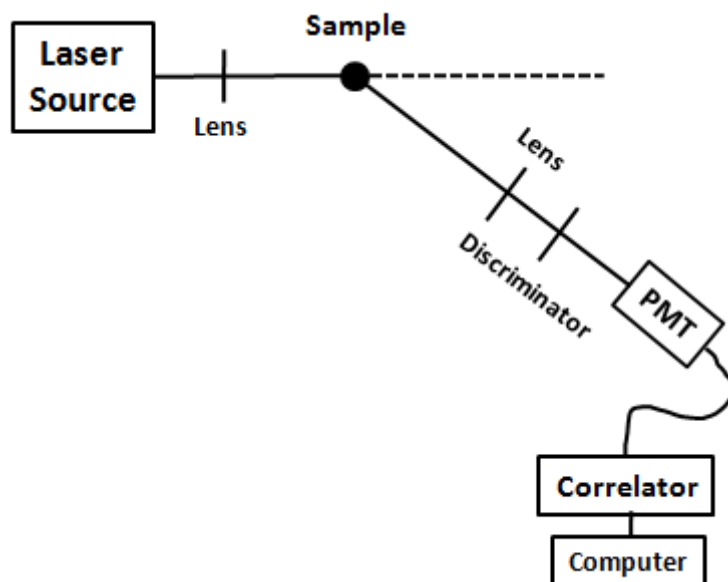


Figure 3.9. Schematic of a dynamic light scattering set up.

A typical DLS setup consists of a laser source such as He-Ne (632.8 nm) or Ar-ion (514.5 nm) is used to obtain a monochromatic beam of light. The beam is further converged by using a lens. Light is scattered by the sample at all angles. However, a DLS instrument uses a single detector and the measurement is usually done at one particular angle. The scattered light is focused on the detector using a lens. The detector comprises a photomultiplier tube (PMT) and a photon counter. PMT is used to amplify the photon signal, whereas photon counter does the actual counting job. The intensity fluctuations of the scattered light are converted into electrical pulses, which are fed into a digital correlator. This generates the autocorrelation function.

We have carried out DLS studies using Autosizer 4800 (Malvern Instruments, UK) equipped with 7132 digital correlator and coherent (Innova 70C) Ar-ion laser source operated at wavelength 514.5 nm with a maximum output power of 2 W.

3.4.3. Characterization of Gold Nanoparticles by Dynamic Light Scattering

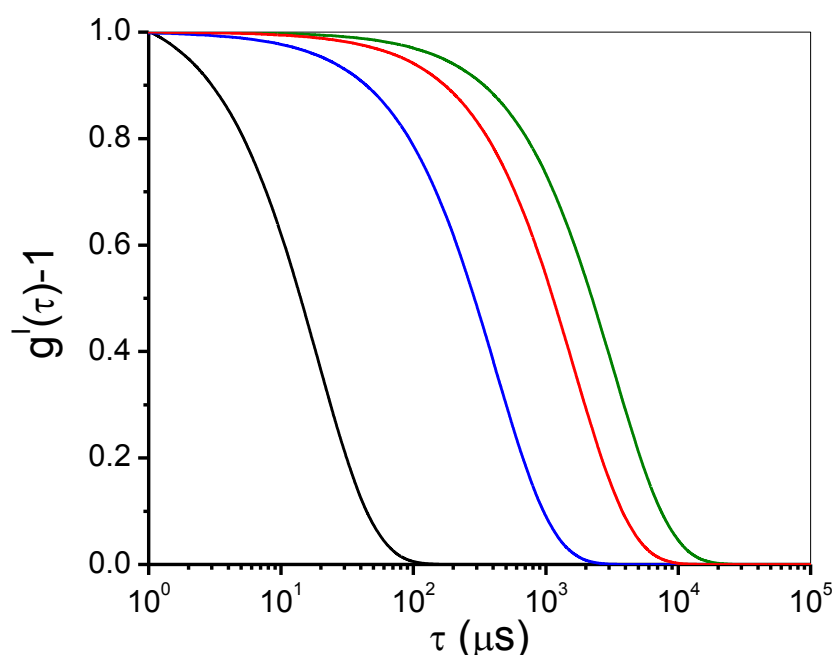


Figure 3.10. The variation of intensity correlation functions with nanoparticle size. The decay of the function slows down for larger sized particles.

Small particles diffuse rapidly and yield fast fluctuations, whereas large particles and aggregates generate relatively slow fluctuations. The rate of the fluctuations is determined through the autocorrelation analysis technique. The calculated autocorrelation function $[g^I(\tau)]$ enables the determination of the diffusion coefficient, which then can be converted to a size using the Stokes-Einstein relationship [63,171-175]. The calculated variation in the intensity autocorrelation function with increasing nanoparticle sizes is shown in **Figure 3.10**. The profile broadens as the size of the particle increases [175].

3.5. Small-Angle Scattering

Small angle X-ray scattering (SAXS) and small-angle neutron scattering (SANS) have been referred to as small-angle scattering. The basics and the data analysis methods used in the two techniques are similar and the only difference is in the radiation used [64]. The contrast factor

for a system could be different because of differences in their interactions with matter and therefore provide complementary information.

3.5.1. Theory of Small-Angle Scattering

The scattering of radiation (X-ray/neutron) by a scatterer is characterized by a single parameter b referred as the scattering length. If the wave vectors of incident and scattered waves are \mathbf{k}_i and \mathbf{k}_f respectively, a wave scattered by a scatterer at a point r in the sample will thus be phase shifted with respect to that scattered at the origin by a phase factor $e^{-i\mathbf{Q}\cdot r}$, where $\mathbf{Q} = \mathbf{k}_f - \mathbf{k}_i$ is the wave vector transferred in the scattering process. The integral scattering cross-section for a nucleus is given by $\sigma = 4\pi b^2$ and it can be looked upon as an effective area presented by the scatterer to the incident radiation. The scattering cross-section describing the flux scattered into the solid angle $d\Omega$ and normalized to the irradiated sample (V_T) volume is called macroscopic differential scattering cross section and is expressed for an assembly of scatterers in a macroscopic sample as [176-179]

$$\frac{d\Sigma}{d\Omega}(\mathbf{Q}) = \frac{1}{V_T} \left\langle \left| \sum_j b_j \exp(-i\mathbf{Q}\cdot \mathbf{r}_j) \right|^2 \right\rangle \quad (3.6)$$

where b_j is the bound scattering length and r_j is the position vector of j^{th} scatterer in a sample, and the bracket represents an average over all possible orientations.

Since SANS deals with the study of large scale heterogeneities rather than locating the individual scattering centers, the summation over b_j can be replaced by a volume integral over scattering length density $\rho(r)$ as defined as

$$\sum_j b_j = \int_{V_T} \rho(\mathbf{r}) d\mathbf{r} \quad (3.7)$$

The summation in the above equation extends over all the nuclei in the volume V_T .

For the two-component system, particles dispersed in a medium having scattering length densities ρ_p and ρ_m , respectively, equation simplified to

$$\frac{d\Sigma}{d\Omega}(Q) = n(\rho_p - \rho_m)^2 V^2 P(Q) S(Q) \quad (3.8)$$

where n is the number density of particles in the sample and V is the volume of the single particle. $P(Q) = \langle |F(Q)|^2 \rangle$ is intra-particle structure factor and $S(Q)$ is the inter-particle structure factor. $F(Q)$ is the form factor associated with the particle and $F(Q)$ is defined as

$$F(Q) = \frac{1}{V} \int_V \exp(-i\mathbf{Q}\cdot\mathbf{r}) d\mathbf{r} \quad (3.9)$$

and is normalized so that $|F(0)|^2 = 1$.

In the case particles are randomly oriented in the sample and the scattering is isotropic, $S(Q)$ is given by

$$S(Q) = 1 + \frac{1}{n} \left\langle \sum_k \sum_{k'} \exp[-i\mathbf{Q}\cdot(\mathbf{R}_k - \mathbf{R}_{k'})] \right\rangle \quad (3.10)$$

where \mathbf{R}_k is the position vector of the k^{th} particle.

The typical functionality of $P(Q)$, $S(Q)$ and $d\Sigma/d\Omega(Q)$ as a function of Q are plotted in **Figure 3.11**.

Determination of Intra-Particle Structure Factor

For some of the regular shapes, having an axis of symmetry, the analytical expressions for $P(Q)$ are available in literature [180,181]. It is assumed that the particles are randomly oriented in the sample so that the theoretical form factors for anisotropic particles have to be averaged over orientation. $P(Q)$ expressions for some standard shapes are given below:

(i) Spherical Particle

For spherical particle of radius R and having uniform scattering length density the form factor is given as [176-181]

$$P(Q) = \left[\frac{3(\sin QR - QR \cos QR)}{(QR)^3} \right]^2 \quad (3.11)$$

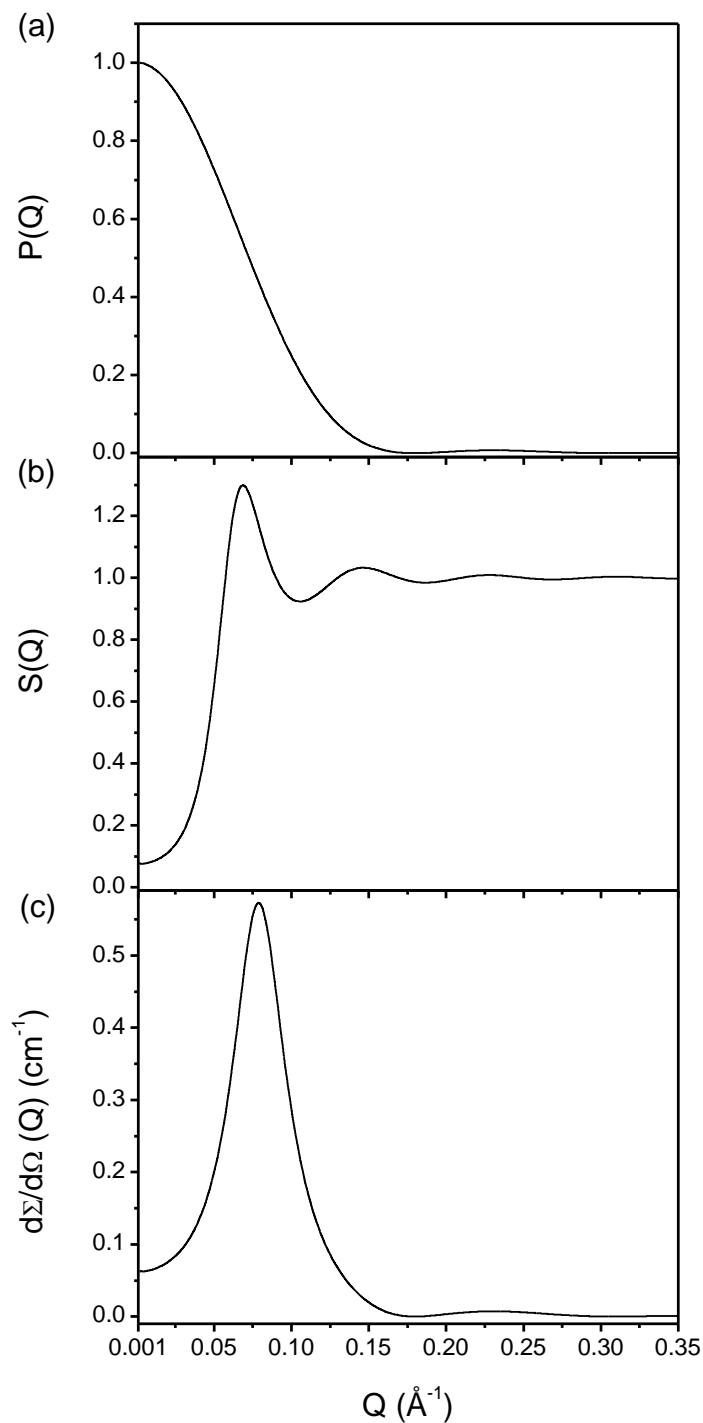


Figure 3.11. Typical curves for (a) $P(Q)$, (b) $S(Q)$ and (c) $d\Sigma/d\Omega(Q)$.

(ii) Spherical Shell (Core-Shell Particle)

The form factor for spherical shell with inner radius R_1 and outer radius $R_2 (= R_1 + t)$, where t is thickness can be obtained by subtracting the empty core of radius R_1 from sphere of radius R_2 with proper weighting by the volumes. $P(Q)$ for spherical shell is written as [180,181]

$$P(Q) = \left[(\rho_c - \rho_{shell})V_1 \frac{3j_1(QR_1)}{QR_1} + (\rho_{shell} - \rho_m)V_2 \frac{3j_1(QR_2)}{QR_2} \right]^2 \quad (3.12)$$

where ρ_c , ρ_{shell} and ρ_m are the scattering length densities of core, shell and solvent, respectively, j_1 is first order Bessel function.

(iii) Prolate Ellipsoidal Particle

The expression for form factor of prolate ellipsoidal particle with semi-major axis a and semi-minor axis $b = c$ is given by [176-181]

$$P(Q) = \int_0^1 F(Q, \mu)^2 d\mu \quad (3.13)$$

where $F(Q, x) = \left[\frac{3(\sin x - x \cos x)}{x^3} \right]^2$, $x = Q [a^2 \mu^2 + b^2(1 - \mu^2)]^{\frac{1}{2}}$ and μ is the cosine of the angle between the direction of major axis and wave vector transfer Q .

(iv) Rod-like/Cylindrical Particle

The form factor of randomly oriented cylindrical particles with the radius R and length $L (= 2l)$ is given by [176-181]

$$P(Q) = \int_0^{\pi/2} \frac{4j_1^2(QR \sin \theta)}{Q^2 R^2 \sin^2 \theta} \frac{\sin^2[(Ql) \cos \theta]}{(Ql)^2 \cos^2 \theta} \sin \theta d\theta \quad (3.14)$$

where $j_1(x)$ is first order Bessel function and θ is the angle subtended by the principal axis of the cylinder with Q .

$P(Q)$ variation on log-log scale shows a linear region in the intermediate Q -range $1/l < Q < 1/R$. The slope of the linear region is -1 . On the other hand, $P(Q)$ for a disc-like particle having radius R and thickness t has a slope of -2 in the intermediate Q -range of $1/R < Q < 1/t$.

(v) Gaussian Coil

The form factor of Gaussian chain coils with the radius of gyration R_g is given by [176-181]

$$P(Q) = \frac{2(e^{-x} + x - 1)}{x^2}, \quad x = Q^2 R_g^2 \quad (3.15)$$

Determination of Inter-Particle Structure Factor

When the concentration of particles is high they start interacting with each other. The nature of $S(Q)$ depends on the structure and the organization of the particles and the type of interactions between the particles. In general, $S(Q)$ shows several maxima and minima of decreasing amplitude. The first peak in $S(Q)$ occurs at $Q_{max} \approx 2\pi/d$, where d is the average distance between the particles.

The expression for $S(Q)$ depends on the relative positions of the particles. For an isotropic system, $S(Q)$ can be written as

$$S(Q) = 1 + 4\pi n \int (g(r) - 1) \frac{\sin Qr}{Qr} r^2 dr \quad (3.16)$$

where $g(r)$ is the radial distribution function. $g(r)$ is the probability of finding another particle at a distance r from a reference particle centered at the origin. The details of $g(r)$ depend on the interaction potential $U(r)$ between the particles [181-185]. Thus, one has to have the knowledge of $U(r)$ for calculating $S(Q)$. This in turn implies that measured $S(Q)$ can be used to obtain information about the interaction potential $U(r)$.

3.5.2. Small-Angle X-Ray vs. Neutron Scattering

The fundamental difference between X-rays and neutrons is the mechanism by which the incident radiation interacts with matter. X-rays are scattered by electrons surrounding atomic nuclei whereas neutrons by the nuclei. It is seen that as one goes across the periodic table, the X-ray scattering lengths increase with the atomic number of the atom, whereas the neutron

scattering lengths vary in a random way (**Figure 3.12**). For neutrons, neighbouring elements as well as isotopes of the same element can have different scattering lengths. For example, the scattering length of hydrogen is negative (-0.3741×10^{-12} cm) and that of deuterium is positive (0.6674×10^{-12} cm) [186]. To complement the SAXS data that has higher sensitivity for the gold nanoparticles, SANS has been used to highlight the structural features of the block copolymer phases in our multi-component colloidal systems.

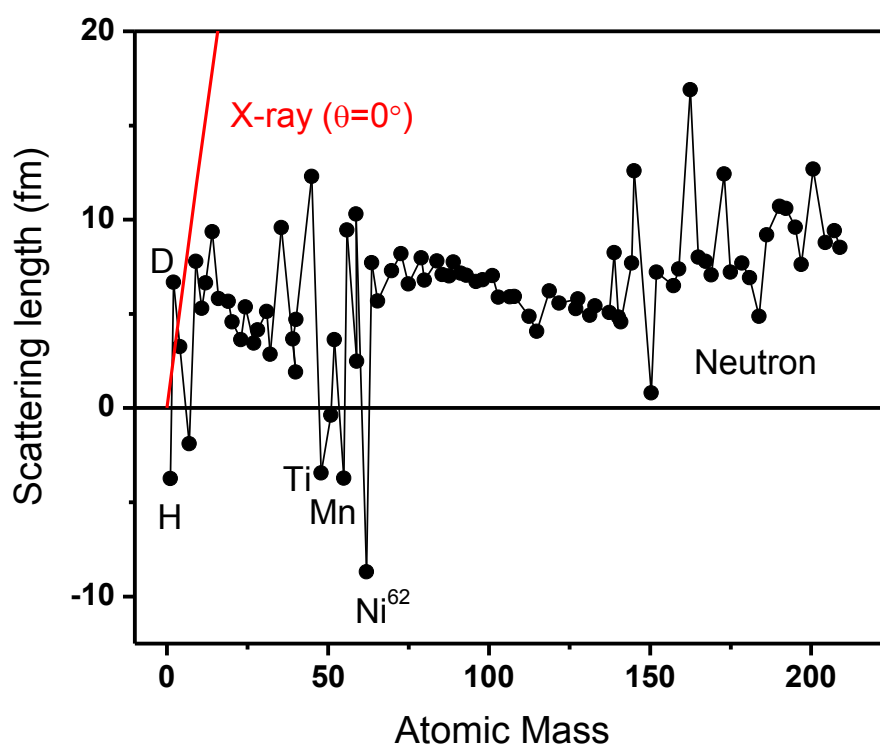


Figure 3.12. Scattering length variation for X-rays and neutrons.

Concept of Contrast in SAS

In SAS, the term $(\rho_p - \rho_s)^2$, the square of the difference of scattering length density of a particular component of the system and solvent is called as contrast factor and decides the visibility of that component in the measurement [186,187]. The values of ρ_p and ρ_s depend on the chemical composition of the particle and the solvent. Scattered intensity in a SAS experiment depends on the contrast factor. This factor, however, depends on the radiation used. Since scattering length is proportional to the atomic number in the case of X-rays, there

is very low contrast for hydrogenous systems such as block copolymer whereas higher Z elements such as gold show a strong contrast. In case of neutrons, due to the difference in the scattering length between H and D, it is possible to have a very good contrast between the hydrogenous particle and the solvent by deuterating either the particle or the solvent. The contrast between the particle and the solvent can be varied continuously by using mixed hydrogenated and deuterated solvents. Various possibilities of contrast variation by using D_2O as solvent are shown in **Figure 3.13**.

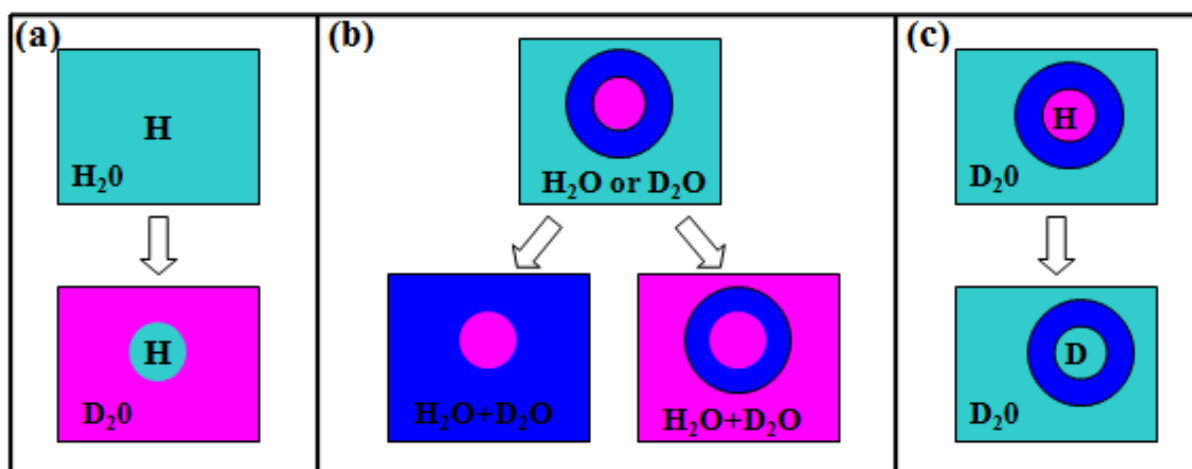


Figure 3.13. Various possible contrast variations in SANS experiment.

Figure 3.13(a) shows a hydrogenous spherical particle suspended in H_2O . Let the scattering length densities be ρ_p of the particle and ρ_H of the solvent. In this case $\rho_p = \rho_H$ and thus the particle is not visible for neutrons. However, the solvent can be replaced with D_2O , so the scattering length density of D_2O is ρ_D which is different from ρ_p and thus the SANS distribution is determined from the particle. Figure 3.13(b) shows a spherical core-shell particle suspended in H_2O . The constituents of the inner core are different from those of the outer shell of the particle. Let ρ_{pc} and ρ_{ps} be the scattering length densities of the core and shell. The solvent has a scattering length density ρ_m , which can be varied by varying the relative amounts of H_2O and D_2O in the solvent. Thus ρ_m can be either matched with ρ_{ps} so that the SANS distribution is determined by the core alone or ρ_m can be matched with ρ_{pc} so

that the SANS distribution is determined by shell alone. Deuterium labeling is another way of contrast matching as shown in Figure 3.13(c) where the same spherical shell particle is now placed in a D₂O solvent, by deuterating the core of the particle, the ρ_{pc} gets equal to ρ_D , thus for neutron only the shell is visible.

3.5.3. Experimental Details

3.5.3.1. Small-Angle X-Ray Scattering

There exist both laboratory instruments based on more conventional sources and synchrotron based instrumentation for SAXS measurements. The schematic of a laboratory-based SAXS instrument is shown in the **Figure 3.14**. In a SAXS experiment, the incident neutron beam is collimated with a pin-hole arrangement. This X-ray beam is scattered by the sample and the angular distribution of scattered radiation is recorded using a 2-D detector [176]. We have carried out SAXS measurements using a Bruker Nanostar instrument equipped with 18 kW rotating anode generator. The X-rays are collimated through a 3 pin-hole system and data can be acquired using a 2-D gas filled detector over a Q -range of 0.01 to 0.2 Å⁻¹.

3.5.3.2. Small-Angle Neutron Scattering

SANS requires a neutron source i.e. a nuclear reactor or an accelerator-based spallation source and therefore the experiments are performed at large scale facilities. The small-angle neutron scattering experiments presented in this thesis have been performed at the SANS diffractometer at the Guide Tube Laboratory, Dhruva Reactor, Bhabha Atomic Research Centre, India [37] and at the SANS-I facility, Swiss Spallation Neutron Source SINQ, Paul Scherrer Institute, Switzerland [38]. **Figure 3.15** shows the schematic of SANS diffractometer installed at the Guide Tube Laboratory, Dhruva Reactor, BARC. It makes use of polycrystalline block of beryllium oxide (BeO) filter as monochromator. The mean

wavelength of the monochromatized beam is 5.2 \AA with a spread of $\Delta\lambda/\lambda \sim 15\%$. The angular distribution of neutrons scattered by the sample is recorded using a 1 m long one-dimensional He^3 position sensitive detector. The instrument covers a Q -range of $0.015 - 0.35 \text{ \AA}^{-1}$ [188].

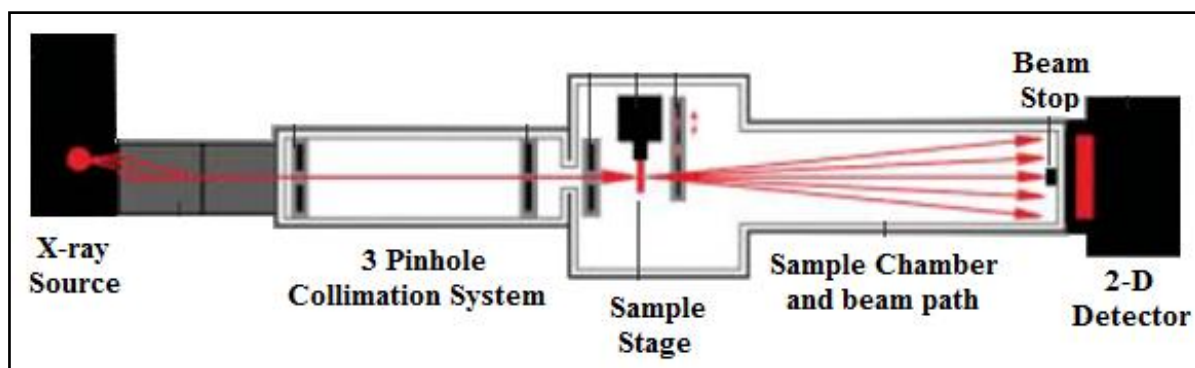


Figure 3.14. The schematic of a SAXS instrument.

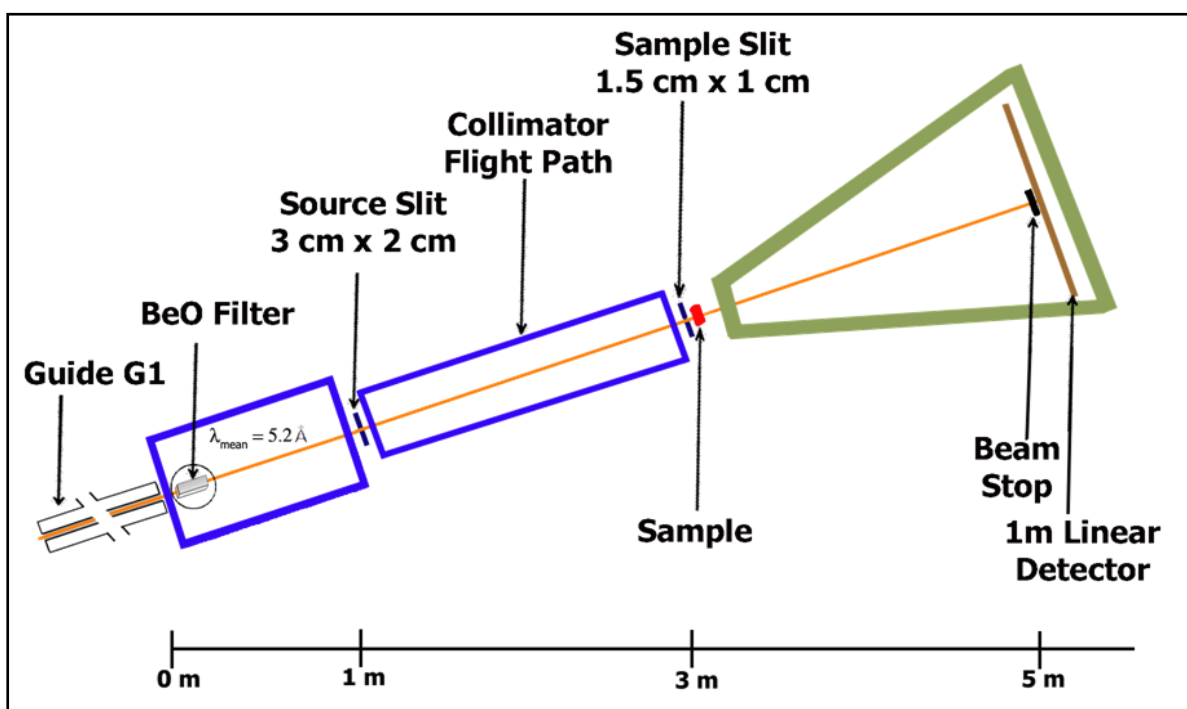


Figure 3.15. Schematic of SANS facility at BARC.

The samples requiring high signal to background and wide Q -range were measured at the SANS-I facility at Swiss Spallation Neutron Source SINQ, Paul Scherrer Institute, Switzerland (**Figure 3.16**). This is a 40 m-long state-of-art instrument. It makes use of

velocity selector and the sample-to-detector distance can be varied from 1 to 20 m. The scattered neutrons are detected using two-dimensional $96 \times 96 \text{ cm}^2$ detector. This instrument can collect the data in the Q -range of 0.001 to 1 \AA^{-1} [189].

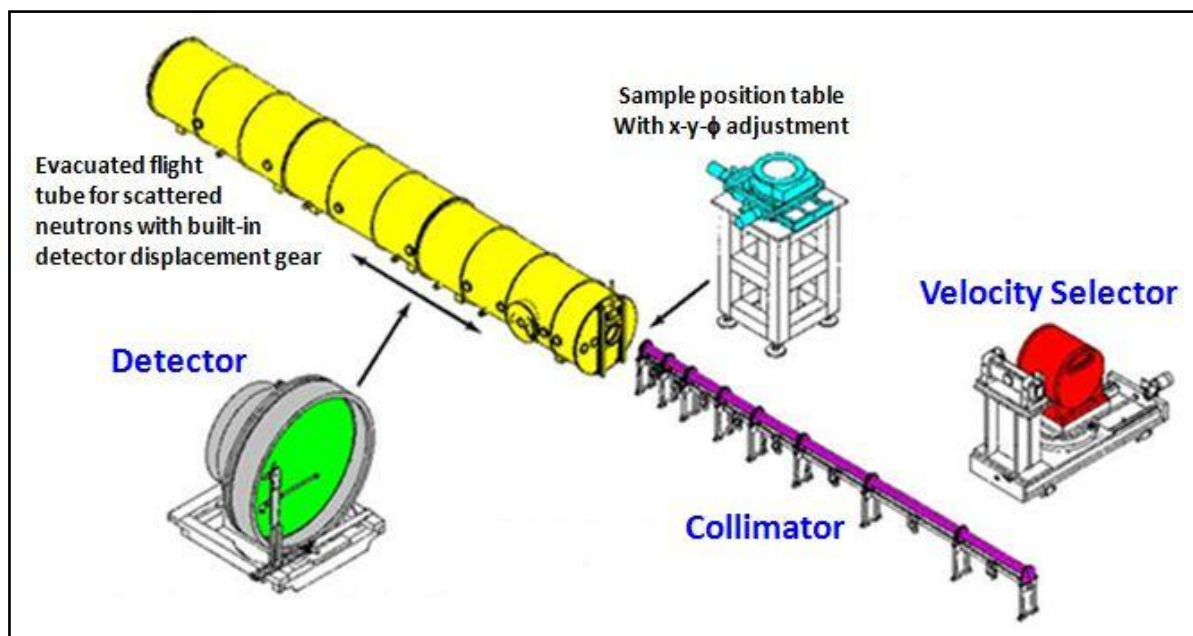


Figure 3.16. Schematic of the SANS-I facility at PSI, Switzerland.

3.5.4. Gold Nanoparticles as Characterized by Small-Angle Scattering

Small-angle scattering has been widely used for the determination of the structure and interaction in variety of nanoparticle systems [64]. The shape information of the particles is obtained from the fact that the Q -dependence of scattering is different for different particles.

Figure 3.17 shows the comparison of scattering for spherical, rod-like and disc-like particles. The rod-like particles show $1/Q$ dependence in the intermediate Q -range whereas $1/Q^2$ dependence is observed for disc-like particles. The cut-offs of these Q -dependent power-law scattering are decided by the dimension of the particles. The interaction of the particles from

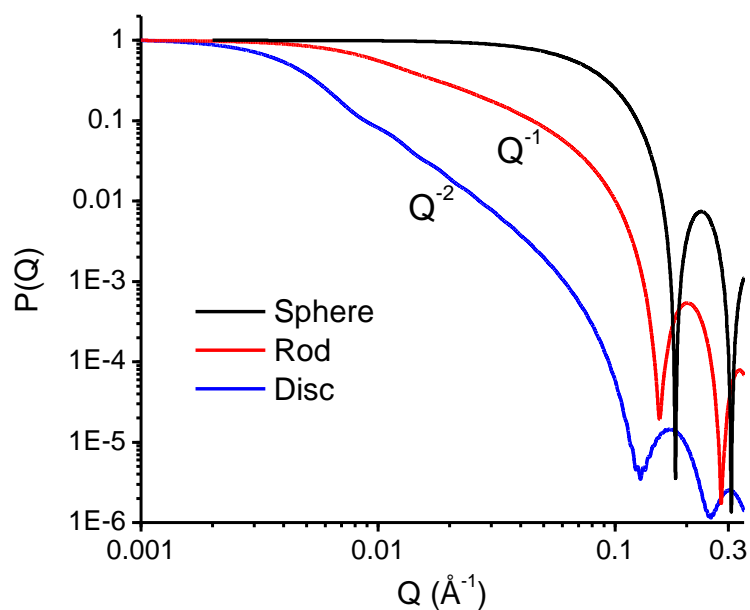


Figure 3.17. $P(Q)$ -dependence for different shapes of the particles.

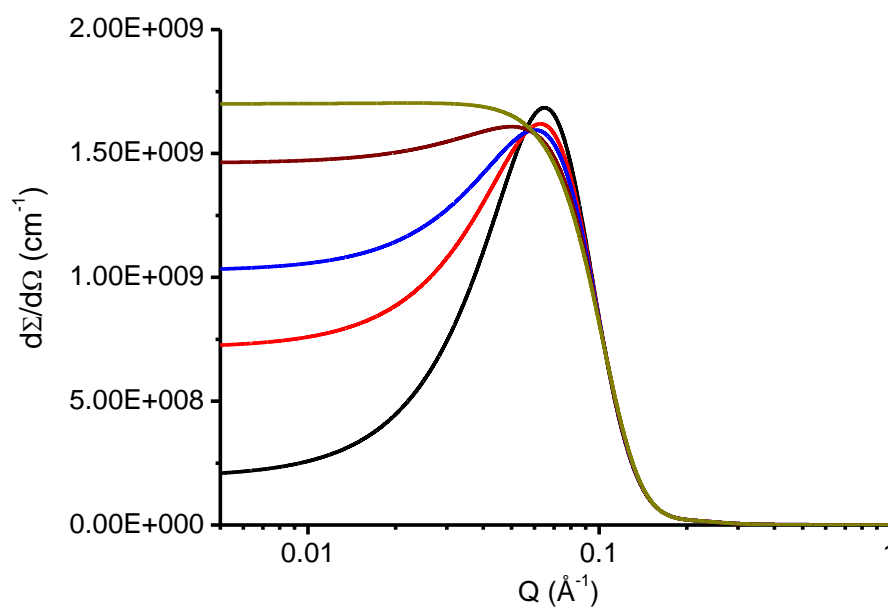


Figure 3.18. SAS data from a charged nanoparticle system in presence of varying ionic strength. The increase in the value of cross-section in low- Q region corresponds to the increasing ionic strength.

SAS data is obtained from the structure factor $S(Q)$. The SAS data usually show a correlation peak for interacting systems, whose position and width is decided by the number density and interaction of the particles, respectively. **Figure 3.18** shows typical SAS data from a charged nanoparticle system in presence of varying salt (e.g. NaCl) concentration. It is seen that the

correlation peak broadens while the peak position remains unchanged. The broadening of peak is as a result of screening of charge between the particles and corresponds to increasing compressibility with increase in salt concentration.

3.6. Summary

This chapter has provided details on a number of techniques involving spectroscopy, microscopy and scattering methods, which can be used for obtaining complementary results for understanding and tuning of the gold nanoparticle synthesis. The different techniques of interest have been discussed are UV-visible spectroscopy, TEM, DLS, SAXS and SANS. UV-visible spectroscopy measures the absorbance of the sample solution to characterize nanoparticles through the characteristic SPR peak whereas the changes in peak height and peak width relates changes in the shape, size and number density of the gold nanoparticles. Time-dependent UV-visible spectra can be used to measure the evolution and the stability of gold nanoparticle during the synthesis. The high contrast of gold nanoparticles for electrons enables TEM to determine directly the shape and size of gold nanoparticles. A range of scattering techniques (DLS, SAXS and SANS) probes the systems under native conditions. In all these scattering techniques the radiation (light, X-ray or neutron) is scattered by the sample and the resulting scattering pattern is analyzed to provide information about the structure (shape and size), interaction and the order of the components of the samples. In DLS, analysis of intensity fluctuations enables the determination of diffusion coefficients associated with different structures in the system through the measurement of time-dependent fluctuations in the intensity of the scattered light. X-rays are scattered by the electron density fluctuation, which is proportional to the atomic number and enables SAXS to determine the size distribution of the nanoparticles. SANS can be used to study the role of different components on the synthesis of gold nanoparticles in these systems by varying the contrast of the individual components using suitable solvents. The results of a multi-technique approach by combining above different methods for the characterization of block copolymer-mediated synthesis of gold nanoparticles in this thesis are reported in Chapters 4–7.

Chapter 4

Optimization of the Block Copolymer-mediated Synthesis of Gold Nanoparticles

4.1. Introduction

The intrigue of nanotechnology comes from the ability to control the material properties by assembling such materials at the nanoscale. For this purpose a variety of synthesis techniques have been developed. The usefulness of a technique is decided by where one can easily control the synthesis output such as nanoparticle size and shape, time of synthesis, yield etc. This requires investigation of dependence of various factors on the synthesis. This includes the role the synthesis constituents and solution conditions such as reaction temperature, pH, ionic strength, reaction time etc [190].

Among the conventional methods of synthesis of gold nanoparticles, the most popular one has been through the citrate reduction of the metal precursors in water [31,32,41]. In a typical synthesis, aqueous trisodium citrate is rapidly added to a vigorously stirring boiling aqueous solution of tetrachloroauric acid ($\text{HAuCl}_4 \cdot 3\text{H}_2\text{O}$). The synthesis in this method is primarily controlled by variations in temperature and the ratio between the reducing/stabilizing agents. Further, this method is often used when a rather loose shell of ligands is required around the gold core in order to prepare a precursor to gold nanoparticle-based materials such as nanorods, nanosheets etc. However, problem with this method is the nanoparticles cannot be synthesized at room temperature and works for low particle yields [31,32,41].

Block copolymer-mediated gold nanoparticles synthesis involves mixing of constituents (triblock copolymer and gold salt) in aqueous solution and at room temperature [94-98,145]. The formation of gold nanoparticles from gold ions can be described comprising three main steps as previously discussed in Chapter 3 [94-98]: (i) reduction of gold ions by the block copolymers in the solution, (ii) formation of gold clusters and adsorption of block copolymers on gold clusters and further reduction of gold ions on the surfaces of these gold clusters and (iii) growth of gold particles in steps and finally its stabilization by block copolymers. In principle, the synthesis can be tuned if we can control any of these three steps. Basically, the propensity of block copolymer to reduce gold ions controls the capability of this synthesis method. This chapter examines the role of varying gold salt and block copolymer concentrations on the optimization of block copolymer-mediated synthesis of gold nanoparticles [191-196]. The different factors that control the synthesis in these systems have been discussed.

The hydrophilic parts of block copolymers are known to form pseudo-crown ether structure that can bind metal ions and reduction of bound gold ions proceeds via oxidation of the monomer segments in block copolymer by the metal center [94-98]. These block copolymers behave as rather a weak reducing agent in a sense that a very high block copolymer-to-gold salt molar ratio may be required for the reduction and hence maintaining the synthesis. Therefore, concentration dependence of both the components (gold salt and block copolymer) becomes very important to decide the overall synthesis of gold nanoparticles in the present method. This has been examined by keeping the concentration of block copolymer fixed with varying the gold salt concentration and repeated for several block copolymer concentrations. The synthesis has been characterized by UV-visible spectroscopy, TEM, SANS and DLS [191-196].

4.2. Experimental Procedure

4.2.1. Materials

Pluronic P85 (EO₂₆PO₃₉EO₂₆, M.W. = 4600) was obtained from BASF Corp., New Jersey. The gold salt of hydrogen tetrachloroaurate(III) hydrate (HAuCl₄.3H₂O) was purchased from Sigma-Aldrich. All the solutions were prepared in millipore H₂O except in the case of neutron scattering experiments. D₂O (99.9 atom %D) was purchased from Sigma. All products were used as received.

4.2.2. Synthesis of Gold Nanoparticles

The gold nanoparticles were synthesized from 1 wt% (2.2 mM) P85 block copolymer solution with varying concentration 0 to 0.02 wt% (0 to 0.508 mM) of HAuCl₄.3H₂O in aqueous solution. All the solutions were kept at room temperature without any disturbances for about 3 hrs for the completion of the synthesis. The transparent solution of P85 in the presence of gold salt (yellow) was observed to become coloured (purple) on the formation of nanoparticles.

To examine the role of block copolymer concentration on the synthesis of the gold nanoparticles, the synthesis was carried out for different P85 concentrations as a function of gold salt concentration. The samples were prepared for different P85 concentrations (0.5, 1 and 2 wt%) with gold salt (HAuCl₄.3H₂O) concentrations varying in the range 0 to 0.02 wt% for each P85 concentration.

4.2.3. Characterization of Gold Nanoparticles

The formation of gold nanoparticles is confirmed using UV-visible spectroscopy [19]. The measurements were carried out using 6505 Jenway UV-visible spectrophotometer. This

instrument is suitable for measurements in the scanning wavelength range between 190 nm and 1100 nm (with an accuracy of ± 1 nm). It makes use of tungsten halogen lamp as a visible light source and deuterium discharge lamp for the UV light. The instrument was operated in spectrum mode with a wavelength interval of 1 nm and the samples were held in quartz cuvettes of path length 10 mm.

SANS is used to examine the role of gold salt as well as block copolymer in optimizing the synthesis of gold nanoparticles [197]. The measurements were performed on the SANS instrument at the Guide Tube Laboratory, Dhruva Reactor, BARC, India [188]. This diffractometer uses a polycrystalline BeO filter as monochromator and the mean wavelength of the incident neutron beam is 5.2 Å with a resolution ($\Delta\lambda/\lambda$) of about 15%. The angular distribution of the scattered neutron was recorded using a linear 1m long He³ position sensitive detector. The data were collected in the accessible Q -range of 0.015 – 0.35 Å⁻¹. The sample solutions were kept in a 0.5 cm thick quartz cell with Teflon stoppers.

DLS experiments were also performed to probe the variation in the nanoparticle systems with varying gold salt concentration and different block copolymer concentrations [63]. Measurements were carried out using Autosizer 4800 (Malvern Instruments, UK) equipped with 7132 digital correlator and coherent (Innova 70C) Ar-ion laser source operated at wavelength 514.5 nm with a maximum output power of 2 W.

After obtaining the suspended particle uniformly in the liquid solvent by stirring in an ultrasonic stirrer, specimens for TEM examination were prepared by putting few drops of the sample on a carbon amorphous film supported by the microscopic copper grid. Then the sample was dried in air for the solvent to evaporate [169]. Conventional transmission electron microscopy was carried out in a JEOL 2000 FX transmission electron microscope. All TEM microphotographs were taken at an acceleration voltage 160 kV, recorded on a photographic film.

4.3. Results and Discussion

The optimization of block copolymer-mediated synthesis of gold nanoparticles for its dependence on gold salt and block copolymer concentrations has been examined in the following sections [191-196].

4.3.1. Role of Gold Salt Concentration

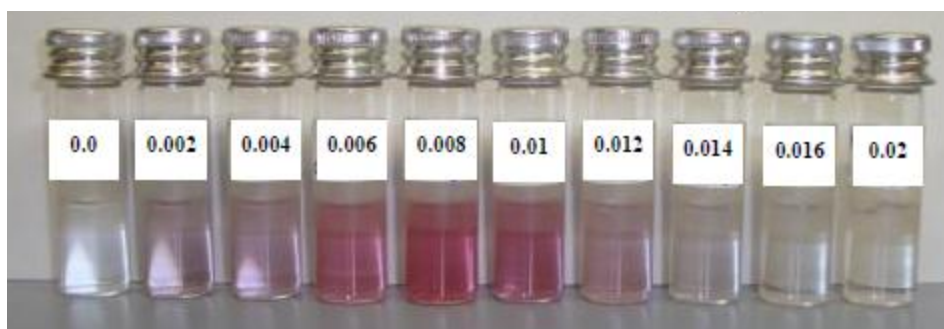


Figure 4.1. Photograph of gold nanoparticles in aqueous solutions of 1 wt% P85 with varying $\text{HAuCl}_4 \cdot 3\text{H}_2\text{O}$ concentration. The labels show the concentration of gold salt in wt%.

Gold nanoparticles have been synthesized from freshly prepared samples of 1 wt% P85 block copolymer with varying $\text{HAuCl}_4 \cdot 3\text{H}_2\text{O}$ concentration in aqueous solution. It is observed that a transparent P85 solution becomes coloured on addition of gold salt. The purple colour seen in these samples is different from that of the pure salt solutions (yellow) and indicates the formation of gold nanoparticles since the surface plasmon resonance (SPR) of gold nanoparticles is known to show such colour [19]. Photograph of gold nanoparticles in aqueous solutions of 1 wt% P85 with varying $\text{HAuCl}_4 \cdot 3\text{H}_2\text{O}$ concentration is shown in **Figure 4.1**. There is an interesting variation in the colour intensity with the increase in the salt concentration. It is observed that the colour intensity simply does not increase with the increase in the gold salt concentration. The maximum in the colour intensity is found at 0.008 wt% $\text{HAuCl}_4 \cdot 3\text{H}_2\text{O}$ for 1 wt% of P85. The colour intensity decreases beyond this maximum and finally the colour of the samples becomes yellow to that of gold salt at higher

concentrations. These results show that the ratio of block copolymer-to-gold salt plays an important role in the formation of gold nanoparticles.

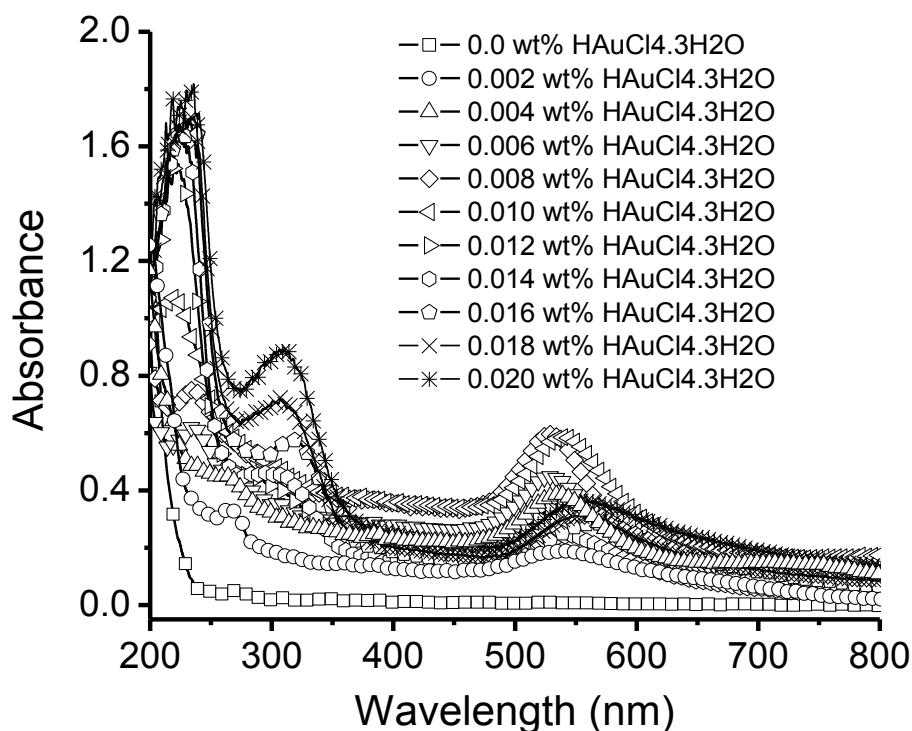


Figure 4.2. UV-visible absorption spectra of the samples of 1 wt% P85 with varying concentration of $\text{HAuCl}_4 \cdot 3\text{H}_2\text{O}$ in aqueous solution.

UV-visible absorption spectra of the samples of 1 wt% P85 with varying $\text{HAuCl}_4 \cdot 3\text{H}_2\text{O}$ concentration are shown in **Figure 4.2**. The spectra have three distinct peaks, first around 230 nm, second at ~ 310 nm and the third at about 530 nm. The peaks centered at ~ 230 nm are due to free gold (III) chloride ions formed in the reduction of the gold salt while the peak at ~ 310 nm corresponds to the presence of some gold clusters composed of few gold atoms, mostly formed in the initial stage of the growth of the nanoparticle [95-97]. The peaks centered at ~ 530 nm originate from the SPR of the gold nanoparticles and the build up of these SPR peaks with increase in the salt concentration confirms the formation of the nanoparticles [19]. The magnitude of this peak depends on the nanoparticle concentration and structure of gold nanoparticles. The variation of SPR peak with gold salt concentrations in

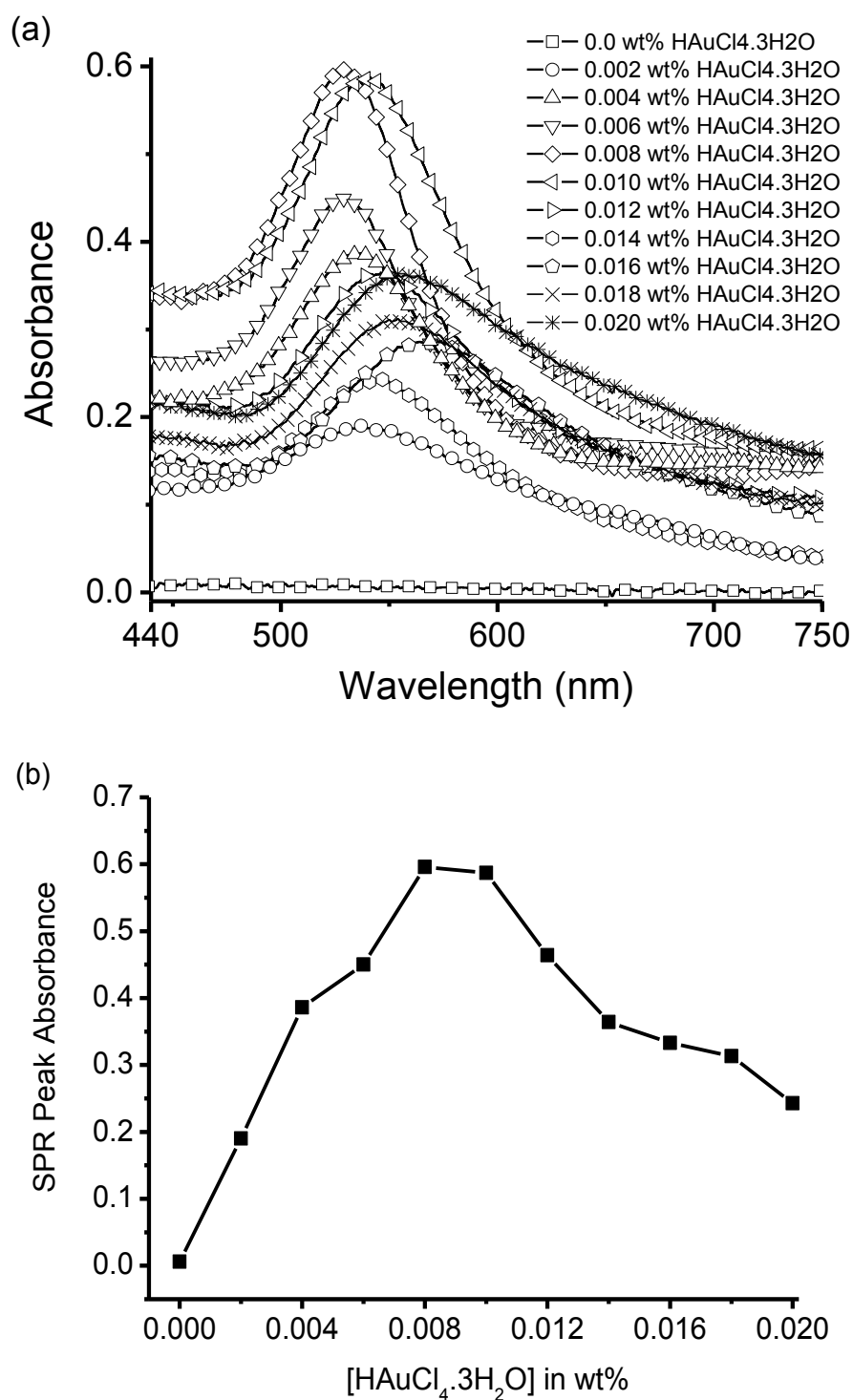


Figure 4.3. (a) The gold salt concentration normalized SPR peak in UV-visible absorption spectra of 1 wt% P85 with varying concentration of $\text{HAuCl}_4 \cdot 3\text{H}_2\text{O}$ in aqueous solution. (b) Variation of SPR peak absorbance in UV-visible absorption spectra.

Figure 4.2 is magnified for clarity in **Figure 4.3(a)**. The SPR peak height increases with salt up to 0.008 wt% concentration in consistent with the colour variation seen in Figure 1. The

peak height decreases along with the peak broadening for gold salt concentrations beyond 0.008 wt%. The variation of SPR peak height (absorbance) with gold salt concentration is shown in **Figure 4.3(b)**. The symmetric SPR peaks observed up to the maximum of Figure 4.3(b) indicate the formation of spherical gold nanoparticles in these systems. The departure from this behaviour with increasing salt concentration suggests the formation of large non-spherical and/or highly polydispersed gold nanoparticles. These results thus clearly show that the ratio of block copolymer-to-gold salt is important in deciding both the formation and structure of the gold nanoparticles.

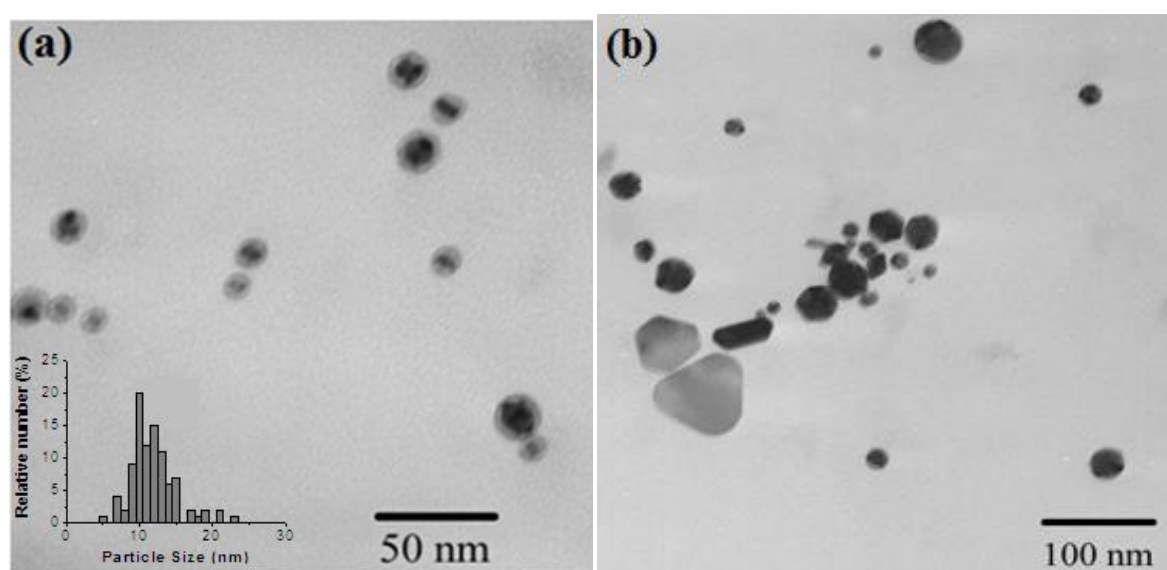


Figure 4.4. (a) TEM image of gold nanoparticles in 1 wt% P85 + 0.008 wt% HAuCl₄.3H₂O. Inset shows the calculated nanoparticle size distribution. (b) TEM image of gold nanoparticles in 1 wt% P85 + 0.016 wt% HAuCl₄.3H₂O.

TEM has been used to provide the direct visualization of the structures of synthesized gold nanoparticles. In this case few drops of the samples were put on the microscopic copper grid and dried in air for solvent to evaporate. **Figure 4.4(a)** shows TEM image of gold nanoparticles as obtained for the system of 1 wt% P85 with 0.008 wt% HAuCl₄.3H₂O. The image shows the core-shell structure with gold nanoparticle as core (darker contrast) and the block copolymer coating as shell (seen in comparatively lighter contrast). The size distribution of the nanoparticles is obtained by considering such large number of micrographs

and is shown in the **inset of Figure 4.4(a)**. The nanoparticles have a mean size of about 12 nm. Further, **Figure 4.4(b)** shows TEM image of gold nanoparticles for the system of 1 wt% P85 at one of the higher gold salt concentrations (0.016 wt% $\text{HAuCl}_4 \cdot 3\text{H}_2\text{O}$) indicating formation of both non-spherical and polydispersed nanoparticles and thus consistent with the SPR data [Figure 4.3(a)] observed for such systems.

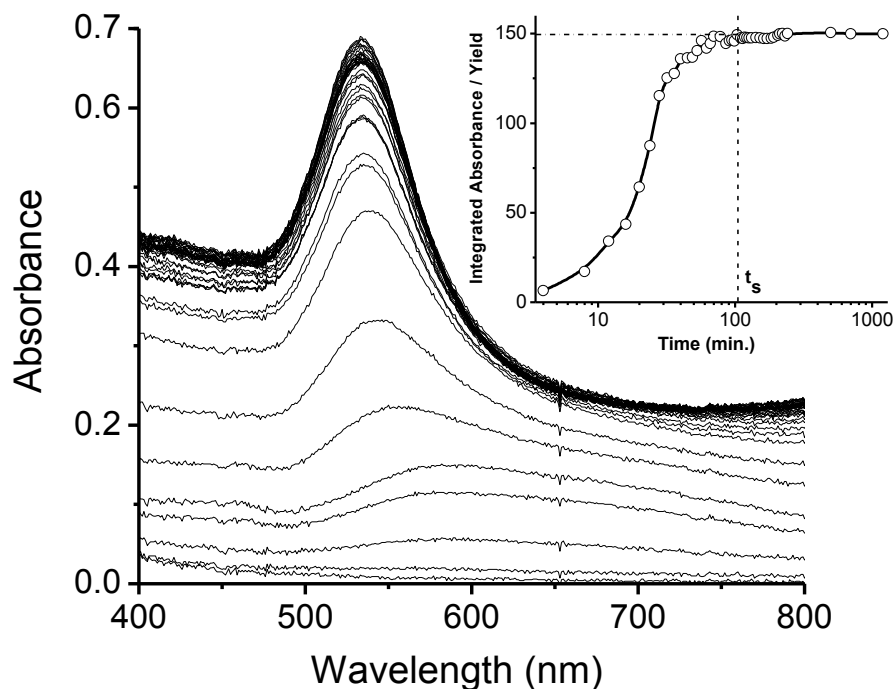


Figure 4.5. Time-dependent UV-visible absorption spectra of 1 wt% P85 with 0.008 wt% $\text{HAuCl}_4 \cdot 3\text{H}_2\text{O}$. The different data sets from bottom to top correspond to increase in the absorbance with time. Inset: The variation of the integrated absorbance of SPR peak as a function of time.

Figure 4.5 shows the time-dependent UV-visible spectra recorded during the synthesis of gold nanoparticles for 1 wt% P85 with 0.008 wt% $\text{HAuCl}_4 \cdot 3\text{H}_2\text{O}$ over a long period of time (up to 16 hrs). After these two components are mixed, the formation was monitored with an initial interval of 5 minutes for about 4 hours and afterwards with a period of 30 minutes. Data show that nanoparticles start forming with the mixing as seen through the building of SPR peak. The peak intensity increases with time and gets saturated at about 60

minutes and remains almost unchanged thereafter. The integrated absorbance or yield (proportional to nanoparticle concentration) of the synthesis has been calculated from the area under the SPR peak in wavelength range 450 to 800 nm. The evolution of formation of gold nanoparticles as a function of time is shown in the **inset of Figure 4.5**. This figure shows two distinct regions of synthesis (i) Formation region and (ii) Saturation region. In the formation region, the yield of nanoparticles increases almost linearly with time while the saturation region is obtained when most of the gold ions have been utilized in the formation of nanoparticles. The constant value in the saturation region suggests the formation of highly stable nanoparticles in these systems.

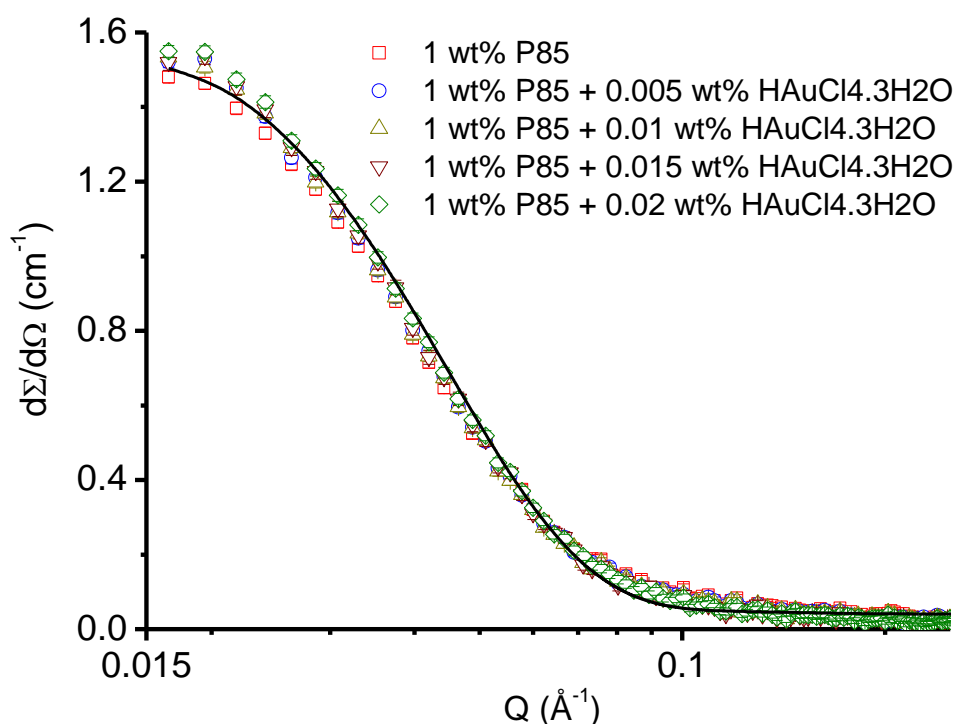


Figure 4.6. SANS data of 1 wt% P85 with varying concentration of $\text{HAuCl}_4 \cdot 3\text{H}_2\text{O}$ in aqueous solution. The solid curve is a theoretical fit to the experimental data.

SANS has been used to examine the role of block copolymer in the formation of gold nanoparticles. **Figure 4.6** shows the SANS data of pure 1 wt% P85 and with the addition of varying $\text{HAuCl}_4 \cdot 3\text{H}_2\text{O}$ concentration. The data without and with the addition of salt have similar features. Block copolymers in salt solutions can either participate in the formation of

gold nanoparticles or form their own micelles. In the case of nanoparticles, block copolymers get coated on the particles, and will have a very different scattering pattern than that for their micelles. Therefore, the scattering from block copolymer-coated gold nanoparticles is expected to be significantly different than that from the micelles. The fact that the scattering curve does not change with varying salt concentration, even when the yield of the nanoparticles is maximum, indicates only a very small fraction of gold nanoparticles has been formed in these systems. In other words, the most of the block copolymers seem not part of the coating on the nanoparticles and form their own micelles, which could be because of very low number density of gold nanoparticles compared to the micelles. It is thus not possible to separate the small scattering contribution of block copolymer coating from that of the micelles.

The scattering for block copolymer micelles are fitted as core-shell particles with different scattering length densities for core and shell. The structure of these micelles is described using a model consisting of non-interacting Gaussian PEO chains attached to the surface of the PPO core. The form factor (intraparticle structure factor) of the micelles comprises four terms: the self-correlation of the core, the self-correlation of the chains, the cross term between core and chains, and the cross term between different chains. It is given by [181]

$$F_m(Q) = N_s^2 b_s^2 F_s(Q) + 2N_s b_c^2 F_c(Q) + 2N_s(2N_s - 1)b_c^2 F_{cc}(Q) + 4N_s^2 b_s b_c F_{sc}(Q)$$

where b_s and b_c are excess scattering length of the core and chain, respectively and N_s is the aggregation number of the micelles. The subscript s (= core) and c (= chain) are used here. They can be calculated as $b_s = V_s(\rho_s - \rho_{solv})$ and $b_c = V_c(\rho_c - \rho_{solv})$, respectively, where V_s and V_c are the total volumes of a block in the core and in the corona. ρ_s and ρ_c are the corresponding scattering length densities and ρ_{solv} is the scattering length density of the surrounding solvent. The structure factor is taken to be unity, as valid in the case of dilute

system. The analysis shows that P85 micelles have a PPO core radius of $R_c = 3.70 \pm 0.05$ nm and radius of gyration of PEO chain as $R_g = 1.2 \pm 0.1$ nm. These micellar parameters of P85 are in good agreement with those reported in the literatures earlier [124,198-201].

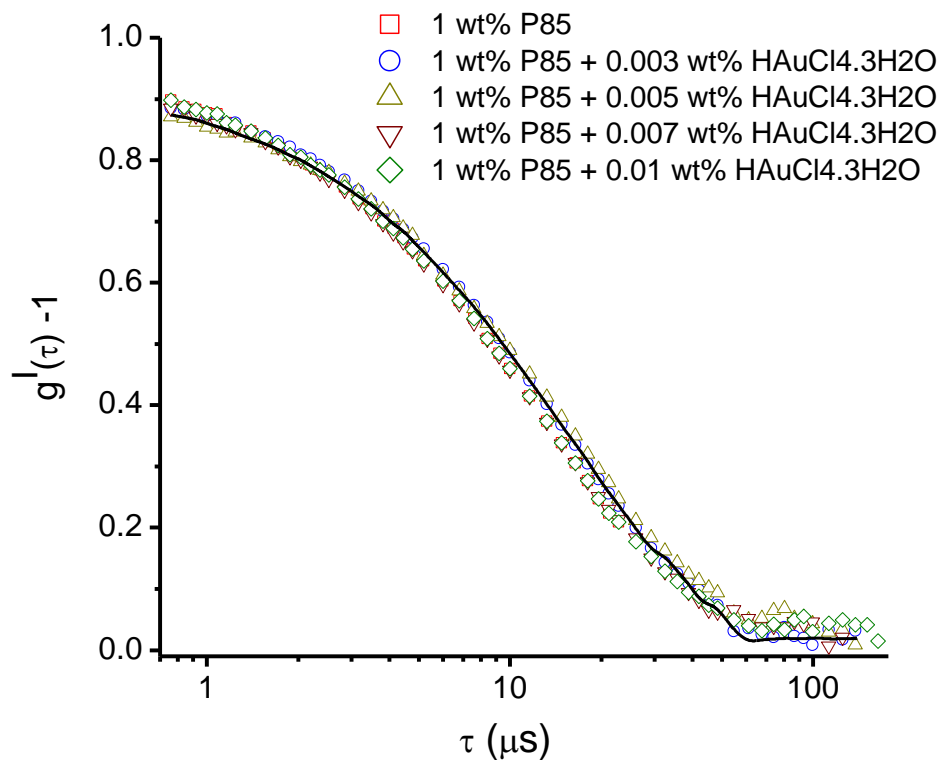


Figure 4.7. Plots of the intensity autocorrelation functions in DLS data of 1 wt% P85 with varying concentration of $\text{HAuCl}_4 \cdot 3\text{H}_2\text{O}$ in aqueous solution. The solid curve is a theoretical fit to the experimental data.

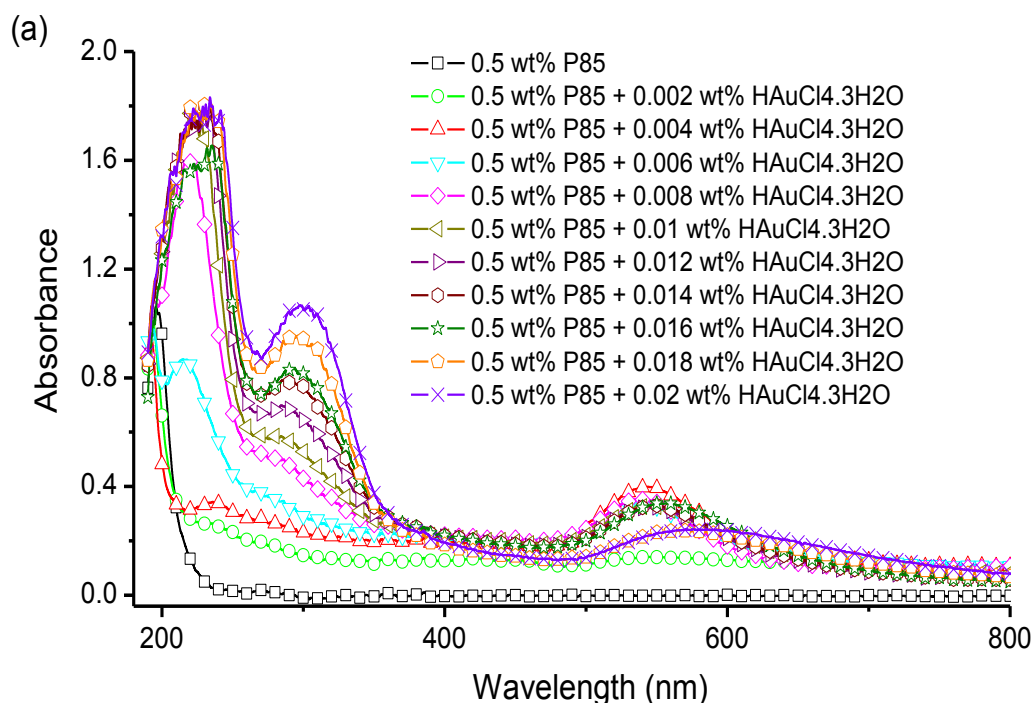
It has been found that a large ratio of block copolymer-to-gold salt concentration is required for the formation of gold nanoparticles whereas only a very small fraction of block copolymers remains part of the gold nanoparticles. These results have been further confirmed by DLS. **Figure 4.7** shows the DLS data of the intensity autocorrelation function $[g^I(\tau)]$ of the nanoparticle systems. The data do not show any significant change with the addition of salt. The functionality of the autocorrelation function depends on the diffusion coefficient of the particles and the data suggest that it is dominated by only one type of the particles (i.e. micelles). The analysis shows that the micelles have a diffusion coefficient of 30×10^{-6} cm^2/sec , which corresponds to the hydrodynamic size of 9 nm. This hydrodynamic size of the

micelles comprises PPO core plus PEO shell along with hydration attached to the shell. Thus both SANS and DLS suggest that most of the block copolymers form their own micelles and only a very small fraction of block copolymers is associated with the coating on the gold nanoparticles.

We have observed that the maximum yield of gold nanoparticles for 1 wt% P85 with varying gold salt occurs at concentration of 0.008 wt%. This concentration corresponds to the block copolymer-to-gold salt molar ratio of 11 and is related to the minimum number of block copolymer molecules (n) required for the reduction of a gold ion to take place. At lower salt concentrations when the molar ratio of block copolymer to salt ions (r) is much larger than $n = 11$, the yield increases with salt concentrations up to 0.008 wt%. Beyond this concentration the ratio r decreases and thus the probability of the reduction reaction in the sample to take place decreases. The distribution of a large number of gold salt ions and block copolymers makes it possible that a significant fraction of ions can still find n number of block copolymers and become reduced even though the average ratio r is less than n . Based on this explanation, the nanoparticle yield is expected to be suppressed with increase in salt concentration, as has been experimentally observed (Figure 4.3). UV-visible spectroscopy suggests the increase in the size of the nanoparticles with the increase in the salt concentration beyond 0.008 wt% could be because of nanoparticle aggregation occurring due to insufficient stabilization by the block copolymers on the surface of the nanoparticles as the block copolymer-to-gold ion ratio decreases with the increase in the gold salt concentration. As a result, we have observed that nanoparticles in these systems phase separate after some time (~ 1 day). At higher salt concentrations ($\gg 0.008$ wt%) the ratio r is too low to provide any significant probability within the system of being able to reduce the gold ions. For these systems, thus UV-visible spectra only show the peak of unreduced gold ions and no SPR peak of gold nanoparticles is seen.

The maximum yield for 1 wt% P85 occurs at 0.008 wt% of gold salt means this system comprises a very low number density of gold nanoparticles compared to that of block copolymers. For the typical size of gold nanoparticles of 10 nm, the fraction of block copolymers ($R_g \sim 1.8$ nm) coated on the particles is calculated to be only about 0.25%. It is therefore clear that only a very small fraction of block copolymers are part of the nanoparticles and most of the block copolymers remain as unimers and/or micelles. This explains why SANS and DLS data do not show any significant change on the formation of the nanoparticles in the present systems (Figures 4.6 and 4.7). The fact that maximum yield for gold nanoparticles is decided by the molar ratio of block copolymer-to-gold salt, therefore the dependence of block copolymer concentration on synthesis of gold nanoparticles has been investigated in the next section.

4.3.2. Dependence on Block Copolymer Concentration



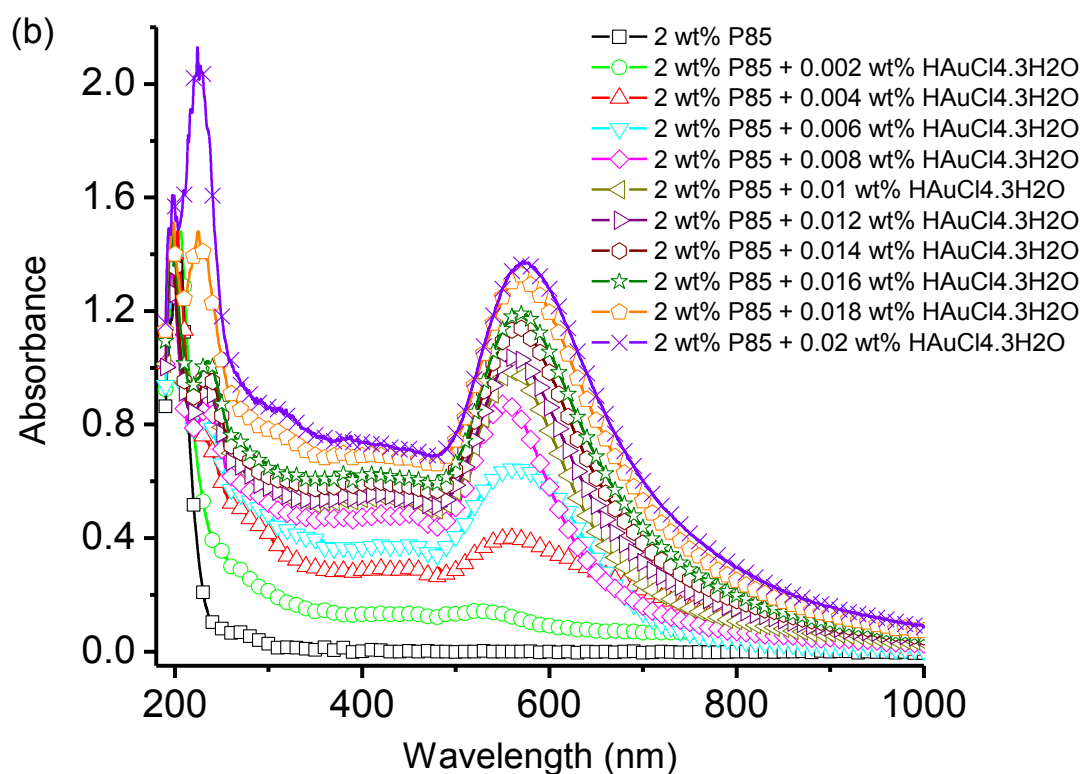


Figure 4.8. UV-visible spectra of (a) 0.5 wt% and (b) 2 wt% P85 with varying $\text{HAuCl}_4 \cdot 3\text{H}_2\text{O}$ concentration.

The dependence of block copolymer concentration on the synthesis of gold nanoparticles has been examined for different block copolymer concentration with varying the gold salt concentration [192-194]. **Figure 4.8** shows the UV-visible absorption spectra for 0.5 wt% and 2 wt% P85 to compare with that of 1 wt% P85 as a function of gold salt concentration. The effect of varying gold salt on the yield of synthesis shows the same trend for all block copolymer concentrations as shown in Figure 4.2. However, the concentration of gold salt at which the yield is the maximum has been found to be increasing with the block copolymer concentration. **Figure 4.9** show the UV-visible spectra with maximum absorbance of 0.5, 1 and 2 wt% P85 as obtained for 0.004, 0.008 and 0.016 wt% $\text{HAuCl}_4 \cdot 3\text{H}_2\text{O}$, respectively. This suggests that block copolymer concentration can be used to enhance the yield.

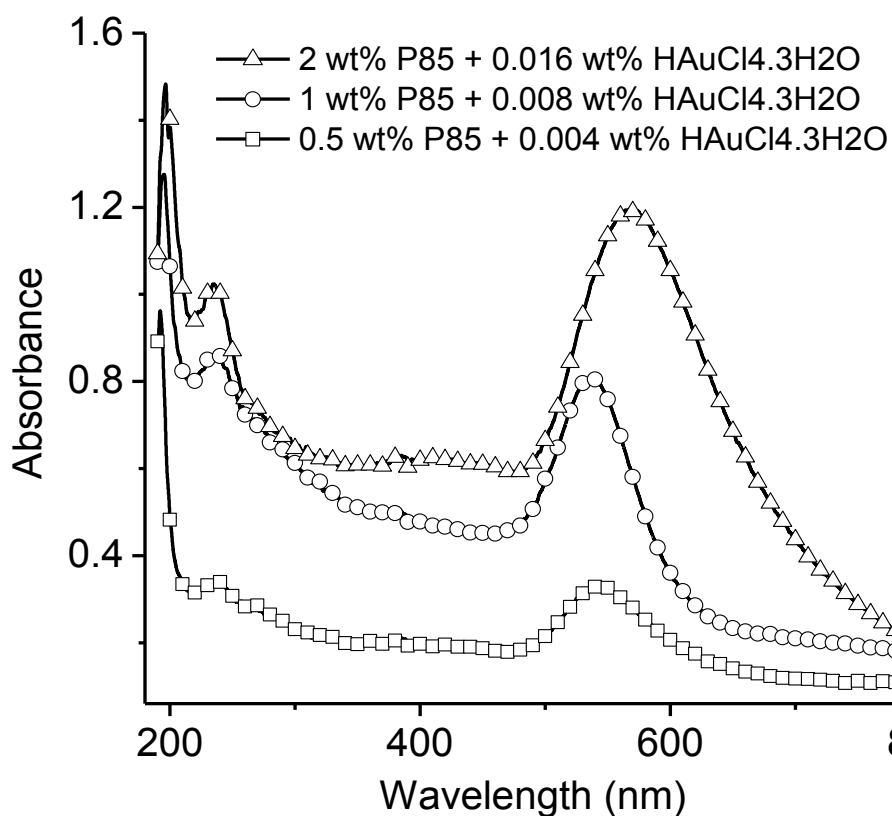
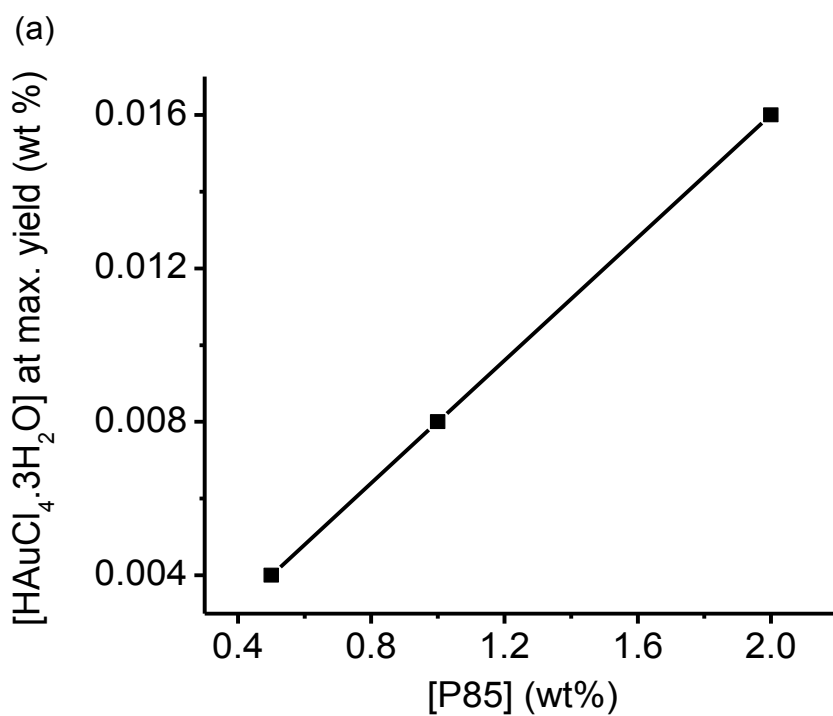


Figure 4.9. UV-visible spectra of gold nanoparticles corresponding to the maximum yield for block copolymer concentrations of 0.5, 1 and 2 wt%.



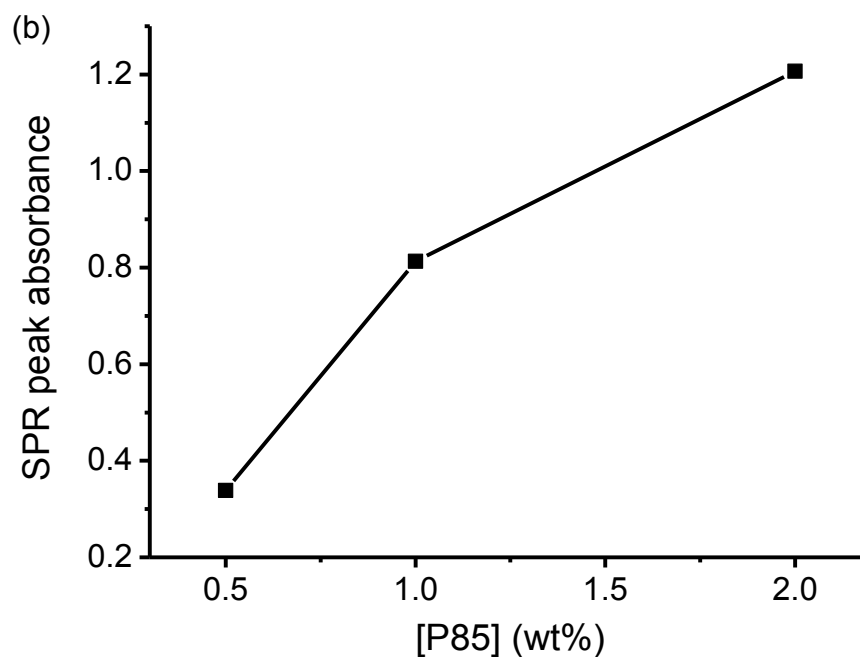


Figure 4.10. (a) The variation of $\text{HAuCl}_4 \cdot 3\text{H}_2\text{O}$ concentration required for the maximum yield with block copolymer concentration. (b) The variation of SPR peak absorbance with the increase in the block copolymer concentration.

The gold salt concentration at which the yield of the nanoparticles is the maximum with increasing block copolymer concentration shows a linear dependence as shown in **Figure 4.10(a)**. This linear dependence arises as a result of the maximum yield decided by the minimum molar ratio of block copolymer-to-gold salt. The overall dependence of yield on block copolymer concentration is shown in **Figure 4.10(b)**. It is clear that the dependence of resultant yield on block copolymer concentration (Figure 4.10(b)) does not follow the same trend to that of occurrence of maximum (Figure 4.10(a)). This could be due to formation of much larger-sized nanoparticles for higher block copolymer concentration consistent with the broader SPR peak at 2 wt% P85 and shift towards higher wavelength as compared to those of 0.5 and 1 wt% P85 concentrations. Thus the concentration-dependent enhancement of yield in this method is limited by the stability of the particles which has been further examined using time-dependent UV-visible spectroscopy.

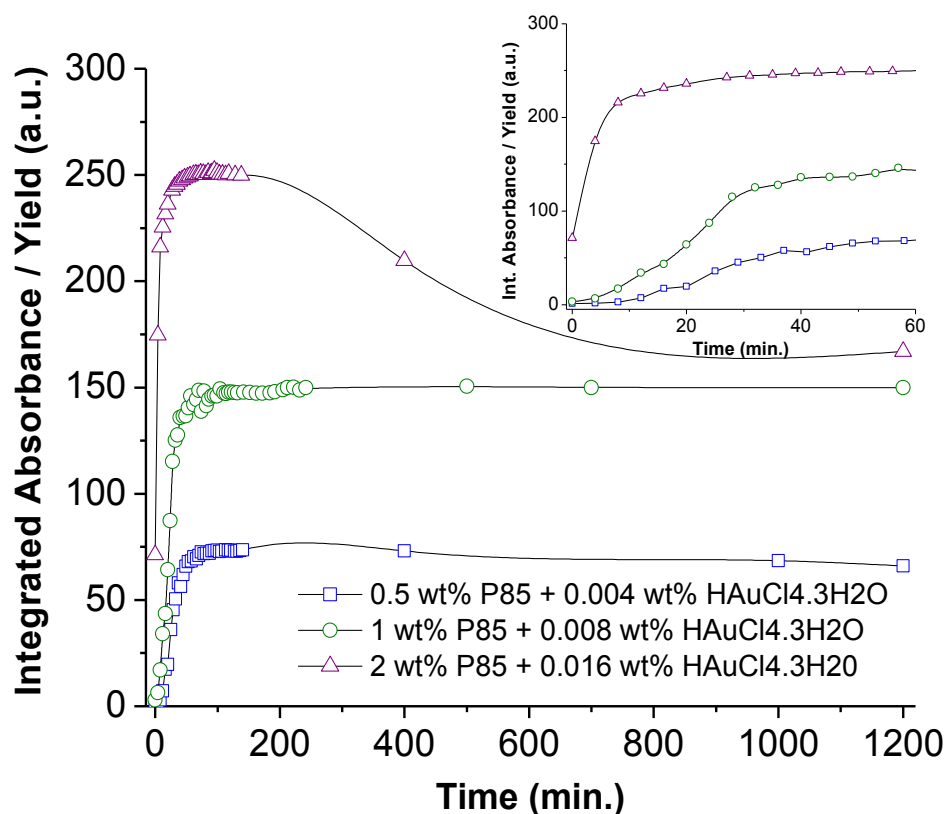


Figure 4.11. Comparison of integrated intensity of SPR peaks as a function of time for 0.5, 1 and 2 wt% P85 at their corresponding gold salt concentrations of maximum yield. All these data show three different regions (i) Formation, (ii) Saturation and (iii) Stability. Inset: Enlarged view of the formation region of the gold nanoparticles.

The evolution of synthesis is examined by time-dependent UV-visible spectroscopy over a wide period of time (up to 20 hrs) similar to as shown in Figure 4.5. The integrated absorbance or yield of the synthesis has been calculated from the area under the SPR peak covering wavelength range 450 to 800 nm. The comparison of the synthesis for three block copolymer concentrations is shown in **Figure 4.11**. The time-dependence of nanoparticles synthesis shows three distinct regions for all the concentrations: (i) Formation region, (ii) Saturation region and (iii) Stability region. In the formation region, the yield of nanoparticles increases linearly with time. Higher the values of block copolymer concentration, higher will be its tendency to nucleate and hence faster formation rate of nanoparticles (**inset of Figure 4.11**). The saturation region is obtained when most of the gold ions have been utilized in the

formation of nanoparticles. The value of saturation represents the maximum yield obtained from that system. The decrease in the integrated absorbance beyond saturation region, if any suggests aggregation of particles in that system. The substantial decrease in the stability for 2 wt% P85 could be because of large size of the nanoparticles formed with increase in this system.

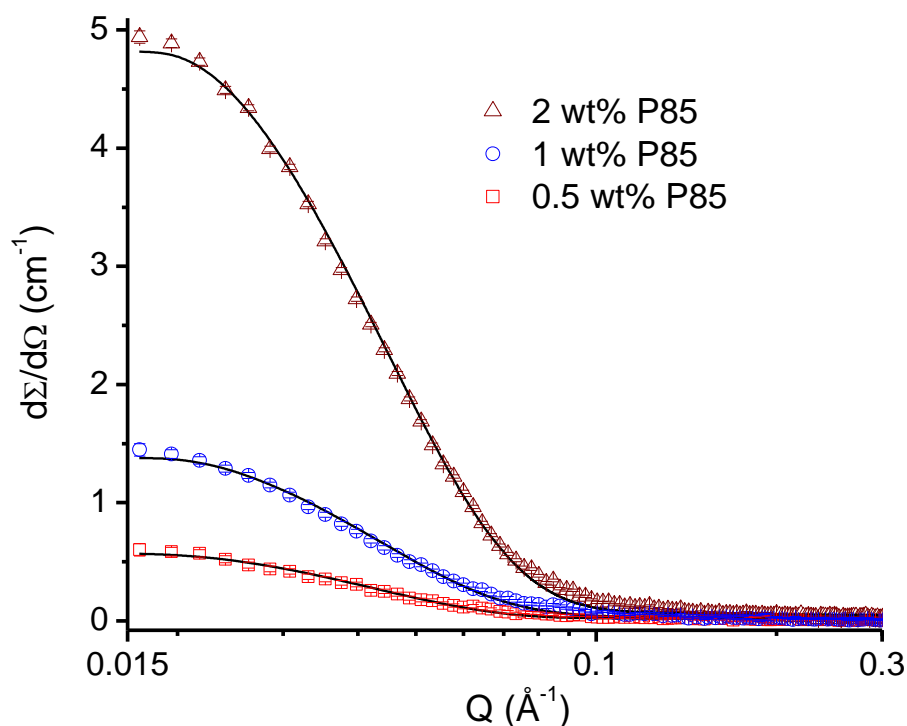


Figure 4.12. SANS data with varying block copolymer concentration. The solid curves are the theoretical fits to the experimental data.

Table 4.1. Fitted parameters of the micelle structure at different P85 concentrations.

[P85] (wt%)	Core Radius R_c (nm)	Radius of Gyration R_g (nm)	Aggregation Number N	Number Density N_d (m^{-3})
0.5	3.63	1.2	53	6.6×10^{23}
1.0	3.63	1.2	53	13.2×10^{23}
2.0	3.62	1.2	53	26.4×10^{23}

SANS studies were performed to understand the mechanism of varying concentration of block copolymer leading to their different behaviour. **Figure 4.12** shows the SANS data of pure 0.5, 1 and 2 wt% P85 block copolymer solutions, where the scattering cross-section increases with the block copolymer concentration. The fitted parameters of the micelles at different concentrations are given in **Table 4.1**. It is found that irrespective of the block copolymer concentration, micelles have the same PPO core radius ($R_c = 3.63$ nm) surrounded by Gaussian PEO chain ($R_g = 1.2$ nm) and aggregation number ($N = 53$). Only the number density of micelles (n) for different systems varies in proportion to the block copolymer concentration. The increase in the number density of the micelles means there will be larger probability to the nucleation of the gold nanoparticles and hence the enhancement in the yield observed at higher block copolymer concentration.

The above SANS results have been further confirmed by the DLS data of the intensity autocorrelation function [$g^I(\tau)$] as shown in **Figure 4.13**. The functionality of the autocorrelation function depends on the diffusion coefficient of the particles and the data obtained suggest that it is dominated by only one type of the particles (i.e. micelles). The analysis shows that irrespective of the block copolymer concentration, micelles have a diffusion coefficient of 30×10^{-6} cm²/sec, which corresponds to the hydrodynamic radius of about 9 nm. This hydrodynamic size of the micelles comprises PPO core plus PEO shell along with hydration attached to the shell. It has also been found out that there is not any significant change in the DLS data of these block copolymer samples with nanoparticles, which is consistent with SANS results of a very small fraction of nanoparticles as compared to that of the free block copolymer micelles. The linear dependence of count rate at the detector with variation in block copolymer concentration suggests increase in the number density of the micelles consistent to that observed by SANS (**inset of Figure 4.13**).

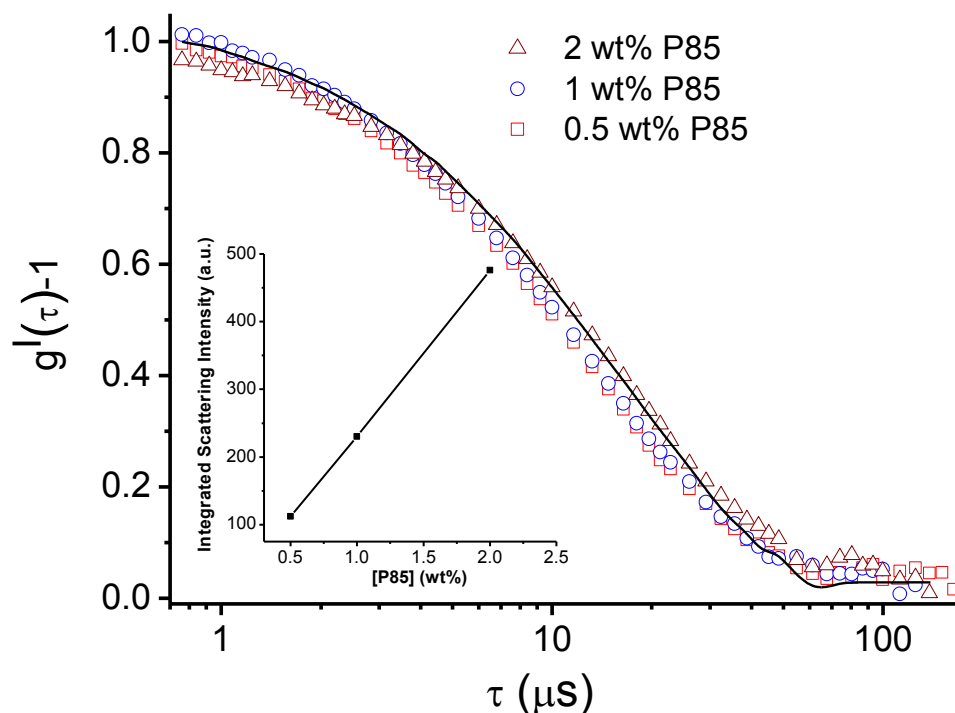


Figure 4.13. DLS data with varying block copolymer concentration. The solid curve is a theoretical fit to the experimental data. Inset: The variation of integrated scattering intensity from the sample as a function of block copolymer concentration.

Figure 4.14 shows the SANS data of P85 with the presence of corresponding $\text{HAuCl}_4 \cdot 3\text{H}_2\text{O}$ concentration of the maximum yield. The data without and with the addition of gold salt do not show any significant differences. Block copolymers in salt solutions can either participate in the formation of gold nanoparticles or form their own micelles. In the case of nanoparticles, they get coated on the particles, and have a very different scattering pattern than that for the micelles. Therefore, the scattering from block copolymer coated gold nanoparticles is expected to be significantly different than from the micelles. The fact that the scattering curve does not change with varying salt concentration, even at the maximum yield of the nanoparticles, suggests only a very small fraction of gold nanoparticles are formed in these systems. In other words, most of the block copolymers remain their own as unimers and/or micelles. It is thus not possible with present SANS experiments to separate the scattering of block copolymer coating from that of the micelles.

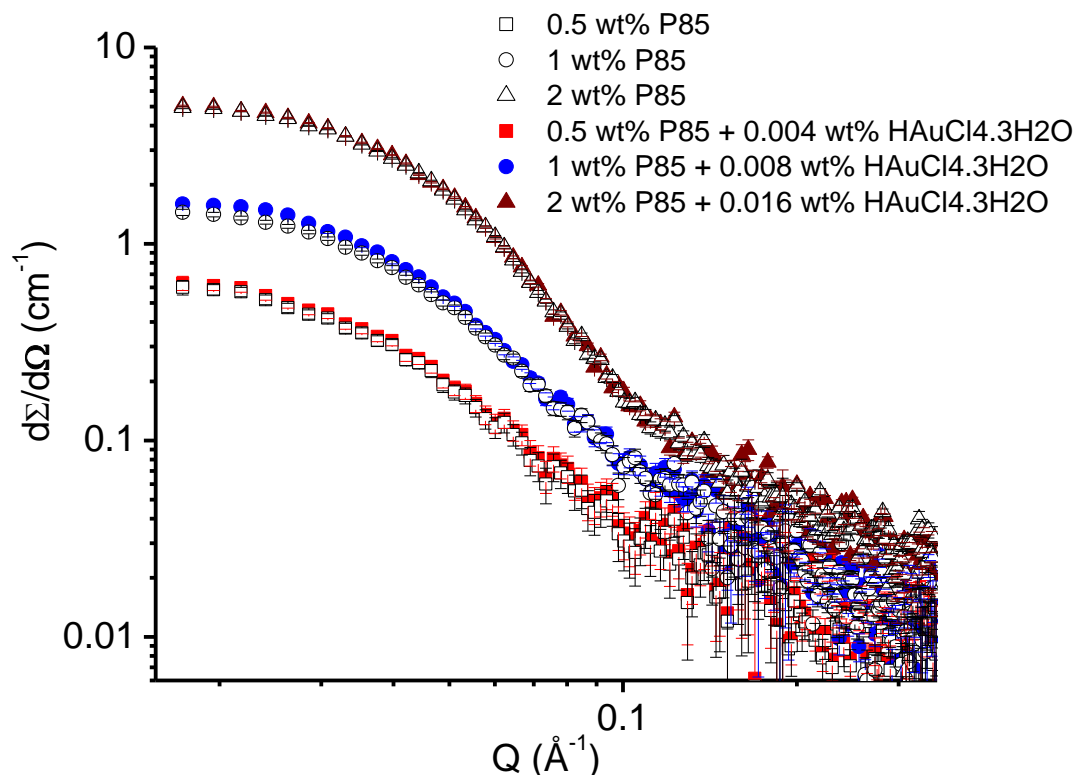


Figure 4.14. SANS data of 0.5, 1 and 2 wt% P85 without and with the addition of gold salt concentrations of the corresponding maximum yield of nanoparticles. The hollow and filled symbols represent data of P85 without and with gold salt, respectively.

Figure 4.15(a) shows TEM images of gold nanoparticles as obtained from 2 wt% P85 + 0.016 wt% $\text{HAuCl}_4 \cdot 3\text{H}_2\text{O}$ systems. The size distribution of the nanoparticles is obtained by considering such large number of images and is shown in **Figure 4.15(b)**. The nanoparticles have a mean size of about 20 nm. The average size of the gold nanoparticles in this system when compared with 1 wt% P85 + 0.008 wt% $\text{HAuCl}_4 \cdot 3\text{H}_2\text{O}$ (Figure 4.4) is found to increase with block copolymer concentration. This increase in size is consistent with the broadening of the UV-visible spectra for gold nanoparticles sample at higher block copolymer concentration (Figure 4.9). It has been observed that increase in the block copolymer concentration increases the yield of gold nanoparticles which is related to availability of more number of micelles to enhance the probability of nucleation and growth of the nanoparticles (Table 4.1). Unfortunately, the increase in concentration also leads to large size of the gold nanoparticles,

which is responsible for the decrease in the stability (Figure 4.11). These results thus suggest that in block copolymer-mediated synthesis of gold nanoparticles, the copolymer concentration is an important parameter to control the size, yield and the stability of nanoparticles.

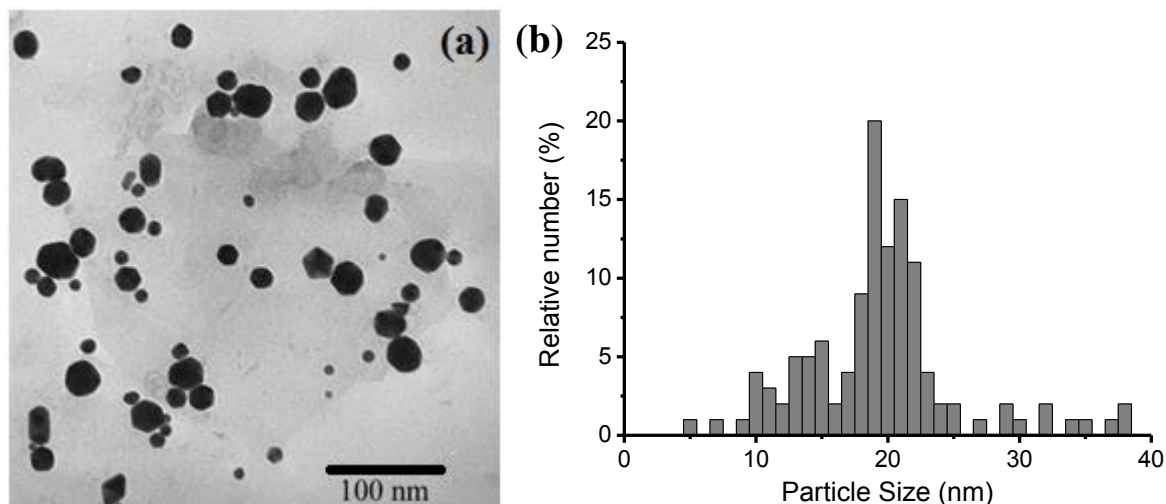


Figure 4.15. (a) TEM image of gold nanoparticles in 2 wt% P85 + 0.016 wt% $\text{HAuCl}_4 \cdot 3\text{H}_2\text{O}$ and (b) calculated nanoparticle size distribution.

4.4. Conclusions

The optimization of synthesis of gold nanoparticles for its dependence on block copolymer and gold salt concentrations to improve the yield has been studied. It has been observed that the yield of gold nanoparticles simply does not increase with the increase in block copolymer or gold salt concentration. The yield of gold nanoparticles at a given block copolymer concentration shows the maximum at a gold salt concentration, below and above which the yield decreases. The occurrence of this maximum is decided by the minimum molar ratio of block copolymer-to-gold salt (r_{min}) required for block copolymer to reduce the gold ions and hence synthesis. At higher gold salt concentrations, the decrease in their molar ratio suppresses the reduction and hence the decrease in the resultant yield. The value of r_{min} for block copolymer P85 and gold salt ($\text{HAuCl}_4 \cdot 3\text{H}_2\text{O}$) is found to be 11. SANS and DLS

suggest that these systems are mostly dominated by the presence of large number of block copolymers as unimers and/or micelles not associated with gold nanoparticles. TEM has been used to obtain the size-distribution of the nanoparticles. The time-dependence UV-visible spectroscopy shows that the nanoparticles can be formed from these systems as early as in few minutes (~ 5 min.) whereas the completion of the synthesis takes about 2 hrs.

The similar trend of role of gold salt concentration has been observed when the block copolymer concentration is varied. Although the gold salt concentration at which the yield of nanoparticles is maximum with increasing block copolymer concentration shows a linear dependence, the overall yield increases but is not found to be proportional to the gold salt concentration and decreases from linearity with the increase in the block copolymer concentration. The yield increases as the nucleation and growth of the gold nanoparticles is enhanced with the increase in the block copolymer concentration while maintaining the copolymer-to-gold salt ion ratio. This mechanism works as there exists a minimum ratio of block copolymer-to-gold salt ion for reduction of gold ions to occurs and hence the formation of nanoparticles. The increase in yield also increases the probability of particle aggregation which decreases their stability. The size of the nanoparticles depends on the block copolymer concentration and has been found to be increasing with the concentration.

Chapter 5

Correlating Block Copolymer Self-Assembly to the Gold Nanoparticle Synthesis

5.1. Introduction

In block copolymer-mediated synthesis of gold nanoparticles, block copolymers assist in reduction of gold salt, nucleation and growth of gold clusters and stabilization of gold nanoparticles [94-98]. The block copolymers required are amphiphilic, comprising two distinct hydrophobic and hydrophilic parts. It may be mentioned that in the case of homopolymer such as PEO the efficiency of formation of gold nanoparticles has been found to be very low [94-98]. While both hydrophilic and hydrophobic blocks in amphiphilic block copolymers contribute to the reduction of gold salt ion through the formation of crown ether-like domain, the contribution of hydrophilic is believed to be more dominant. The amphiphilicity of block copolymer helps in enhancing the nucleation as well growth of nanoparticles. The nucleation is enhanced by self-assembly of amphiphilic block copolymers to form gold clusters. Further, the adsorption of block copolymers on the surface of gold clusters as governed by the hydrophobicity of block copolymer decides the growth and stabilization of nanoparticles. It is therefore clear that amphiphilicity of block copolymer is important and can be varied to control the synthesis of gold nanoparticle [94-98].

The amphiphilic nature or self-assembly of block copolymers can be varied by varying their chemical architect and solution conditions such as temperature, pH, ionic strength etc [96,98,146]. These block copolymers self-assemble to micelle above a critical concentration (CMC) or critical temperature (CMT). There exists a concentration range at a

given constant temperature and similarly a temperature range at a given concentration when block copolymers coexist both as unimers and self-assembled micelles [119,120]. At much higher concentrations/temperatures than CMC/CMT leads to different micellar structures and liquid crystalline phases. The PEO-PPO-PEO block copolymers can be obtained having different block sizes of PPO and PEO to control the self-assembly. The higher the ratio of PPO to PEO enhances the propensity of self-assembly. The increased dehydration with increasing temperature is also known enhance the self-assembly. It is not clear how the synthesis will be influenced by the change of these structures. The correlation of self-assembly with the synthesis of gold nanoparticles has been addressed in the chapter.

The role of block copolymer self-assembly on the synthesis of gold nanoparticles has been studied by varying the block copolymer chemical structures and temperature [202-205]. The synthesis has been carried using three different block copolymers F88 ($\text{EO}_{103}\text{PO}_{39}\text{EO}_{103}$), P85 ($\text{EO}_{26}\text{PO}_{39}\text{EO}_{26}$) and P105 ($\text{EO}_{37}\text{PO}_{56}\text{EO}_{37}$). Block copolymers F88 and P85 have the same hydrophobicity (same molecular weight of PPO block) but differ in their overall molecular weights, whereas P85 and P105 have different molecular weights with same ratio of hydrophilicity to hydrophobicity [94]. The block copolymer F88 forms spherical micelles over a wide temperature range whereas P85 and P105 show sphere-to-rod like micelle transition at higher temperatures. The gold nanoparticles have also been synthesized using F88, P85 and P105 at different temperatures. The synthesis of gold nanoparticles in these systems has been characterized by UV-visible spectroscopy, TEM, SANS and DLS.

5.2. Experimental Procedure

5.2.1. Materials

Pluronic block copolymers F88, P85 and P105 were obtained from BASF Corp., New Jersey. The gold salt of hydrogen tetrachloroaurate(III) hydrate ($\text{HAuCl}_4 \cdot 3\text{H}_2\text{O}$) was

purchased from Sigma-Aldrich. All the solutions were prepared in millipore H₂O other than those used in neutron scattering experiments for which D₂O (99.9 atom %D Sigma Make) was used. All products were used as received.

5.2.2. Synthesis of Gold Nanoparticles

The synthesis of the gold nanoparticles for each block copolymer was carried out by varying the concentration of gold salt at a fixed concentration of block copolymers. The block copolymer concentration used was 1 wt% and the concentration of gold salt varied in the range from 0 to 0.02 wt%. After mixing all the components for synthesis, samples were kept at room temperature without any disturbances for about 3 hours for the completion of the reaction. The transparent solution of block copolymers in the presence of gold salt was observed to become coloured on the formation of nanoparticles. For temperature-induced synthesis, before mixing, all the components were maintained at that particular temperature and kept at that temperature for the time required to reaction to be completed.

5.2.3. Characterization of Gold Nanoparticles

The formation of gold nanoparticles is confirmed using UV-visible spectroscopy [19]. The measurements were carried out using 6505 Jenway UV-visible spectrophotometer. The instrument was operated in spectrum mode with a wavelength interval 1 nm and the samples were held in quartz cuvettes of path length 10 mm.

SANS is used to correlate concentration dependence of self-assembly of block copolymer with the synthesis of gold nanoparticles. The measurements were performed on the SANS instrument at the Guide Tube Laboratory, Dhruva Reactor, BARC, India [188]. The data were recorded in the accessible Q -range of 0.015 – 0.35 Å⁻¹. Some of the measurements requiring higher sample to background and wider Q -range were also carried out at SANS-I facility, Swiss Spallation Neutron Source SINQ, Paul Scherrer Institut,

Switzerland [189]. The wavelength of neutron beam used was 6 Å. The experiments were performed at sample-to-detector distances of 2 and 8 m to cover Q -range of 0.007 to 0.32 Å⁻¹. The scattered neutrons were detected using two-dimensional 96 × 96 cm² detector.

DLS experiments were also performed to probe the variation of the size of the nanostructures in the system with different chemical structure of block copolymers [63]. Measurements were carried out using Autosizer 4800 (Malvern Instruments, UK) equipped with 7132 digital correlator and coherent (Innova 70C) Ar-ion laser source operated at wavelength 514.5 nm with a maximum output power of 2 W.

The direct visualization of nanoparticles has been obtained by TEM [169]. Conventional transmission electron microscopy was carried out using a JEOL 2000 FX transmission electron microscope. All TEM microphotographs were taken at acceleration voltage 160 kV, recorded on a photographic film.

5.3. Results and Discussion

The self-assembly of block copolymers is tuned by varying its chemical structure and solution temperature, whose effect on the synthesis of gold nanoparticle has been examined [202-205].

5.3.1. Tuning of Block Copolymer Self-Assembly

The self-assembly of block copolymer is known to be strongly dependent on the chemical structure of the block copolymer [197]. We have used three different block copolymers F88, P85 and P105 for studying the effect of chemical structures of the block copolymers on the self-assembly [202-204]. The details of the chemical structures of these block copolymers are given in **Table 5.1**. Block copolymer P85 and P105 have different molecular weights with same ratio of hydrophilicity to hydrophobicity. On the other hand, F88 and P85 have the

same hydrophobicity (same molecular weight of PPO block) but differ in their overall molecular weights [94].

Table 5.1. Details of chemical structure of the PEO-PPO-PEO block copolymers used.

Block Copolymer	Formula	Mol. Wt.	Hydrophilicity (PEO wt%)	PPO Block Mol. Wt.	PEO Block Mol. Wt.	CMT for 1 wt% (°C)
F88	EO ₁₀₃ PO ₃₉ EO ₁₀₃	11400	80	2280	9120	38.0
P85	EO ₂₆ PO ₃₉ EO ₂₆	4600	50	2300	2300	29.0
P105	EO ₃₇ PO ₅₆ EO ₃₇	6500	50	3250	3250	21.5

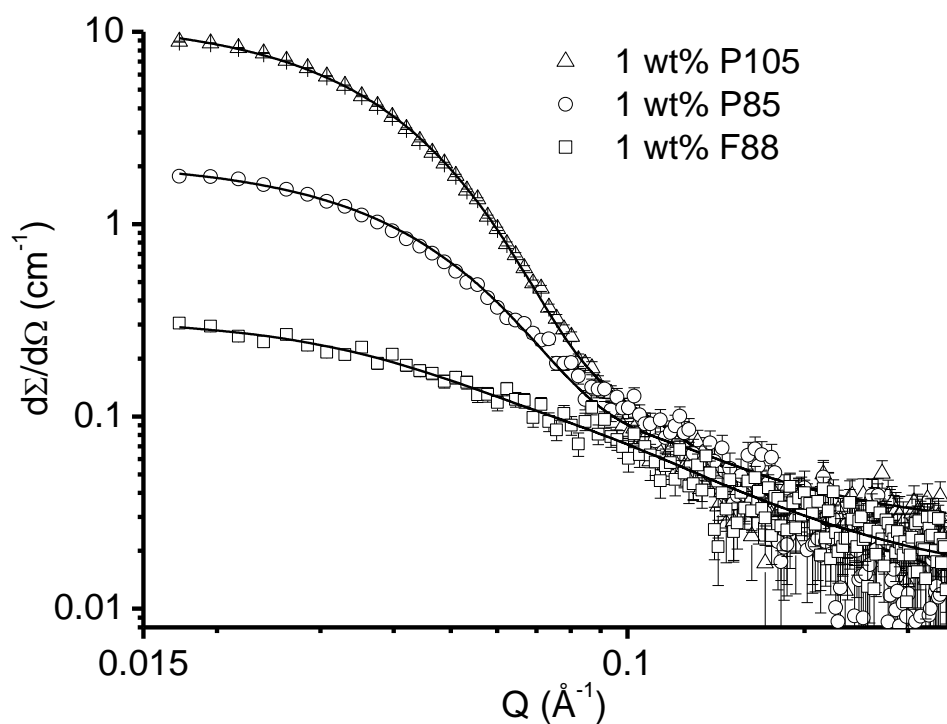


Figure 5.1. SANS data of pure 1 wt% block copolymer solutions. The solid lines are the theoretical fits to the experimental data.

Table 5.2. Fitted structural parameters of self-assembled micellar structures of block copolymers.

Block Copolymer System	Micellar Fraction (%)	Radius of Gyration of Unimers R_{gu} (nm)	Micellar Parameters		Aggregation Number N
			Core Radius R_c (nm)	Radius of Gyration of PEO Chain R_{gc} (nm)	
1 wt% F88	0	3.5	—		1
1 wt% P85	15	2.4	3.6	1.2	52
1 wt% P105	26	2.8	4.0	1.4	59

SANS studies have been performed on block copolymers to study the self-assembly of block copolymers. **Figure 5.1** shows the SANS data of pure 1 wt% block copolymer solutions in D₂O at room temperature (30 °C). The Q -dependence of the scattering is observed to be quite different for three block copolymers indicating differences in their propensity to self-assemble. Block copolymer are known to self-assemble above their CMT to form micelles consisting of core of PPO block surrounded by hydrated PEO shell. At CMT, both unimers and micelles coexist and the population of unimers converting into micelles increases with temperature. The low scattering from highly hydrophilic block copolymer F88 (measurement temperature is below the CMT) is because of this system consists of only unimers. In the case of P85 and P105, the build-up of scattering in the low- Q region, suggests the formation of micelles. As the volume of the scattering object increases on the formation of micelles, therefore scattering intensity increases. **Table 5.2** gives the structural details of block copolymer micelles as obtained from SANS analysis. It is found that F88 consists of only unimers. On the other hand, both unimers and micelles coexist in case of P85 and P105. These two block copolymers (P85 and P105) have the same percentage of hydrophilicity but P105 has the higher molecular weight and this gives rise to

higher fraction of micellization in this system. These block copolymers also form the micelles with different sizes and aggregation numbers.

Table 5.3. Hydrodynamic size of self-assembly of block copolymers as obtained by DLS.

Block Copolymer System	Hydrodynamic Radius (nm)
1 wt% F88	4.4
1 wt% P85	7.5
1 wt% P105	9.0

The above SANS results of self-assembly of block copolymers have been further confirmed by DLS data of the intensity autocorrelation function [$g^I(\tau)$] from the 1 wt% block copolymer samples. The functionality of the autocorrelation function depends on the diffusion coefficient of the particles and the data obtained suggest that three block copolymers show different autocorrelation functions indicating different structures in these systems. The calculated hydrodynamic sizes are given in **Table 5.3**. The effective size corresponding to micellar fraction and size is found to be largest for P105 than F88 and P85 similar to as observed by SANS. In all, both the SANS and DLS results suggest that P105 has higher tendency to self-assemble as compared to F88 and P85.

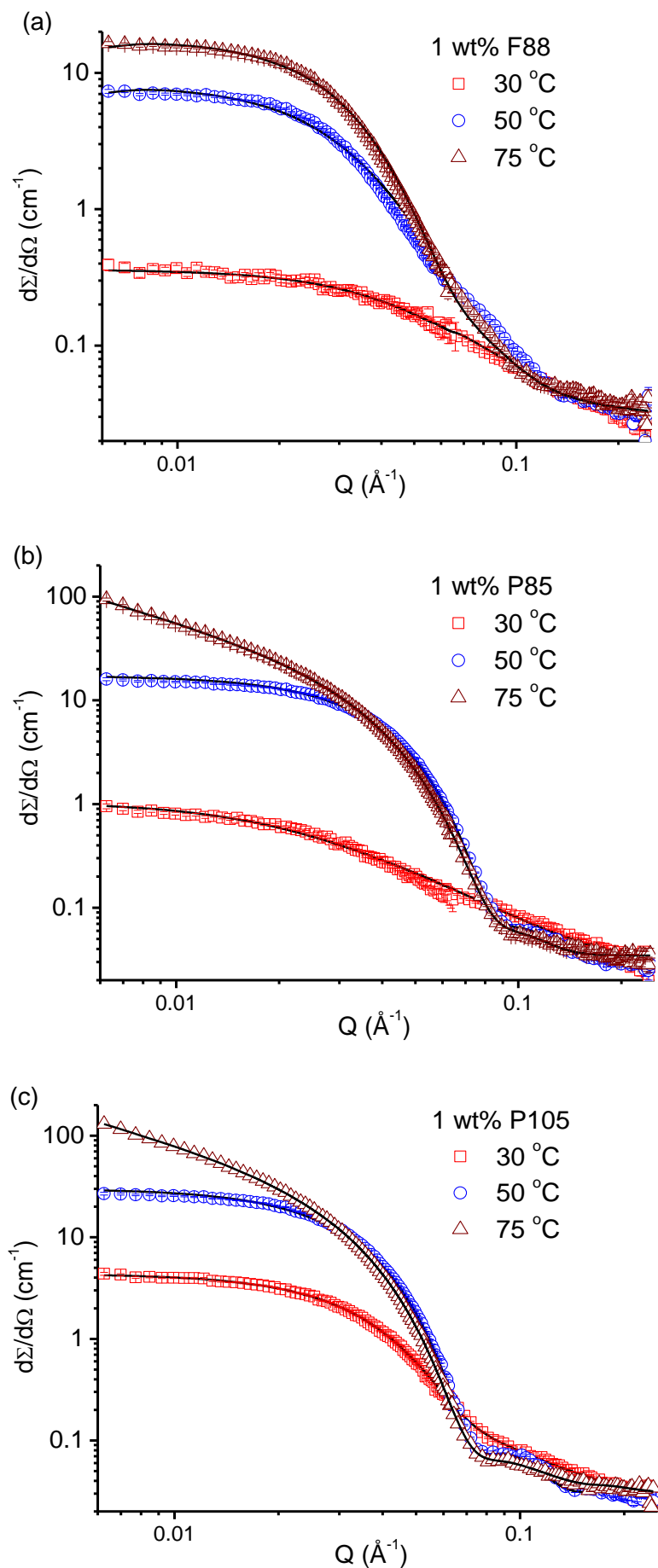


Figure 5.2. SANS data of 1 wt% block copolymer systems with varying temperature for (a) F88, (b) P85 and (c) P105. The solid curves are theoretical fits to the experimental data.

Table 5.4. Fitted structural parameters of self-assembled micellar structures of block copolymers F88, P85 and P105 with varying temperature. The dimension of spherical micelles is represented by radius (R), ellipsoidal micelles by semi-major axis (a) and semi-minor axis ($b = c$), and rod-like micelles by radius (R) and length (L). The fitted values of radii of gyration of unimers for F88, P85 and P105 are 3.5, 2.4 and 2.8 nm, respectively.

Block Copolymer System	Temperature (°C)	Micellar Fraction (%)	Micellar Parameters		
			Shape of the Micelle	Dimensions	R_g of PEO Chain (nm)
1 wt% F88	30	0	F88 exists as unimer ($R_g = 3.50$ nm)		
	50	100	Spherical	$R = 3.12$ nm	2.5
	75	100	Spherical	$R = 3.59$ nm	2.5
1 wt% P85	30	15	Spherical	$R = 3.60$ nm	1.2
	50	100	Ellipsoidal	$b = c = 4.27$ nm $a = 6.36$ nm	1.2
	75	100	Rod-like	$R = 4.30$ nm $L \gg R$	1.2
1 wt% P105	30	26	Spherical	$R = 4.35$ nm	1.4
	50	100	Ellipsoidal	$b = c = 4.85$ nm $a = 8.06$ nm	1.4
	75	100	Rod-like	$R = 5.10$ nm $L \gg R$	1.4

Figure 5.2 shows the SANS data from aqueous solution of 1 wt% block copolymers (F88, P85 and P105) at varying temperature. SANS data of all the three block copolymers

show strong build-up of scattering intensity in the low- Q region with increase in the temperature. This is an indication of enhanced micellization with the increase in the temperature for all the block copolymers. Unlike F88, it is observed for P85 and P105 that the scattering at higher temperature (75 °C) show a linear Q -dependence on log-log scale in low- Q region, suggesting temperature-induced sphere-to-rod-like transition for P85 and P105 micelles. This is expected as a result of dehydration of PEO shell. On the other hand, highly hydrophilic F88 block copolymers form spherical micelles even up to at higher temperature. The fitted micellar parameters in these systems are given in **Table 5.4**.

Table 5.4 shows that micelles coexist with unimers at lower temperature (30 °C). The micelles fraction depends on the hydrophilicity and increases in the order F88 < P85 < P105 as the hydrophilicity of the block copolymer decreases. As the temperature increases, more and more unimers convert to micelles. It is found that there are only micelles at 50 °C for all the block copolymers. The shape of the micelles remains same (spherical) for F88 whereas P85 and P105 micelles become ellipsoidal. As the temperature is increased to 75 °C, both P85 and P105 transform to rod-like micelles. It may be mentioned that since no lower cut-off in the SANS data for rod-like micelles are seen, the micelles are fitted having length greater than that can be measured from the accessible range ($> 2\pi/Q_{min} \sim 100$ nm) of the present data.

The role of self-assembly of block copolymer has been used to correlate with the synthesis of gold nanoparticles. The self-assembly is tuned as discussed above by varying chemical structure of block copolymer and temperature.

5.3.2. Gold Nanoparticle Synthesis with Different Block Copolymers

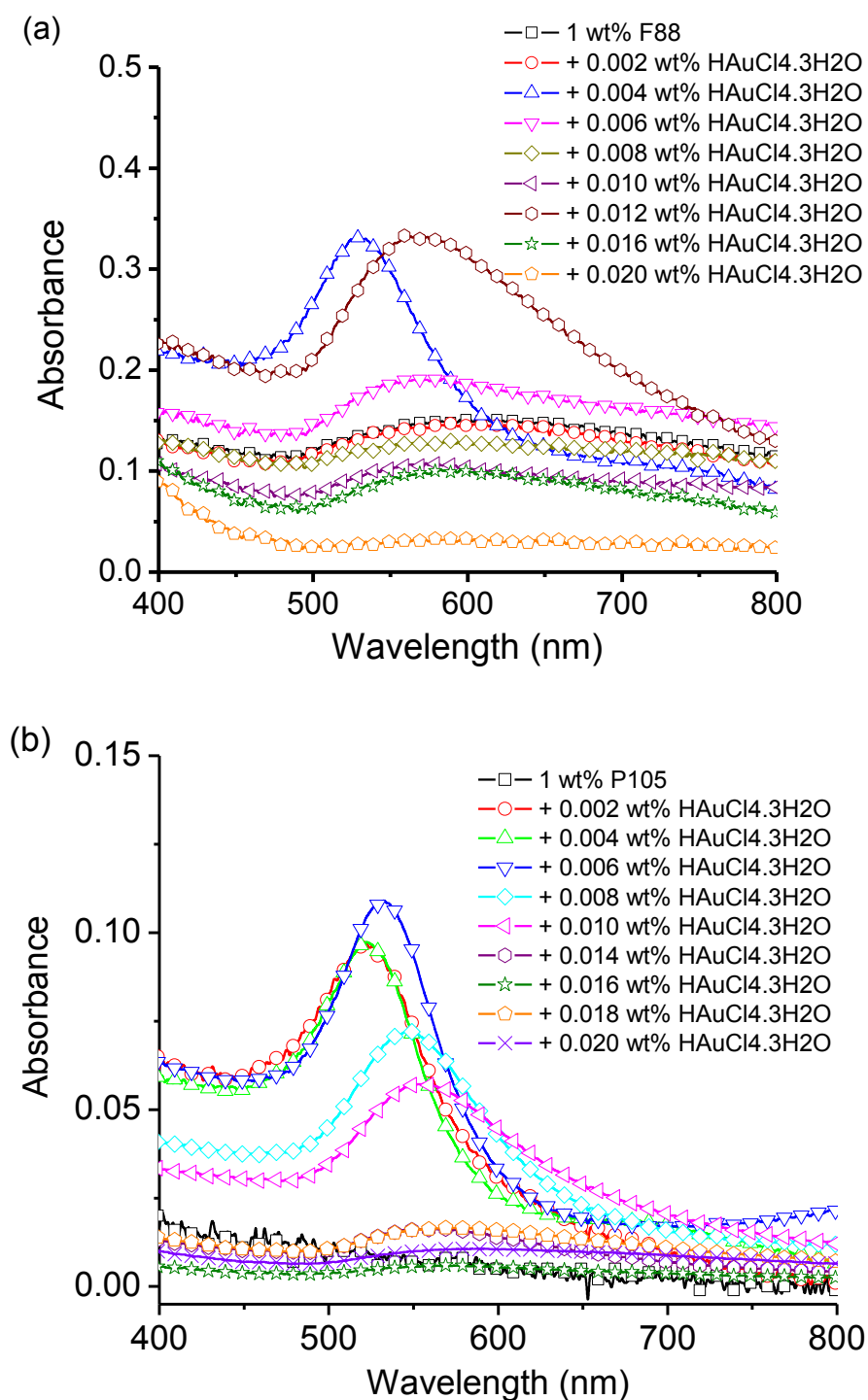


Figure 5.3. The gold salt concentration normalized SPR peaks of (a) 1 wt% F88 and (b) 1 wt% P105 with varying HAuCl₄·3H₂O concentration.

The synthesis of gold nanoparticles similar to that for P85 (see Chapter 4) has also been carried out with block copolymers F88 and P105. These block copolymers vary in their

overall molecular weight and their propensity to self-assemble. The synthesis of gold nanoparticles for F88 and P105 is carried out and compared to that for P85 at a fixed block copolymer concentration (1 wt%) and varying the gold salt concentration. **Figure 5.3** shows UV-visible absorption spectra for 1 wt% F88 and 1 wt% P105 as a function of varying concentration of gold salt. Similar to P85, all the spectra show a SPR peak confirming the formation of gold nanoparticles in all these systems irrespective of the different block copolymers used. The maximum absorbance at SPR (proportional to yield of gold nanoparticles) for 1 wt% F88 and 1 wt% P105 have been found to be for 0.004 wt% and 0.006 wt% $\text{HAuCl}_4 \cdot 3\text{H}_2\text{O}$, respectively. This trend is also consistent with the earlier data that the normalized SPR peak with respect to salt concentration shows a strong decrease in yield beyond a certain gold salt concentration. These concentrations seem to depend on the molecular weight of the block copolymer that decides the number of molecules available for reduction of the gold ions. The alcohol (hydroxyl) functionality at the two ends of a PEO-PPO-PEO block copolymer molecule is known to act as reductant for the metal ions [147,148]. Therefore the higher reduction is expected for the block copolymer with lower molecular weight. The molecular weight of P85 is the lowest and hence amongst all block copolymers for a given concentration (1 wt%) provides more number of block copolymer molecules which can reduce more number of gold ions. **Figure 5.4** shows the comparison of SPR peaks of the block copolymers used. The yield follows the trend in the order P105 > P85 > F88. It does not have the same trend to that of the gold salt concentration (P85 > P105 > F88) corresponding to the maximum yield of the block copolymer. The yield of gold nanoparticles follows the trend in the order P105 > P85 > F88 as governed by the order of self-assembly of the block copolymer in aqueous solution. On the other hand, the amount gold salt concentration for the maximum yield depends on the molecular weight and

thus follows the order P85 > P105 > F88 decreasing with the increase in molecular weight of block copolymer (Table 5.1).

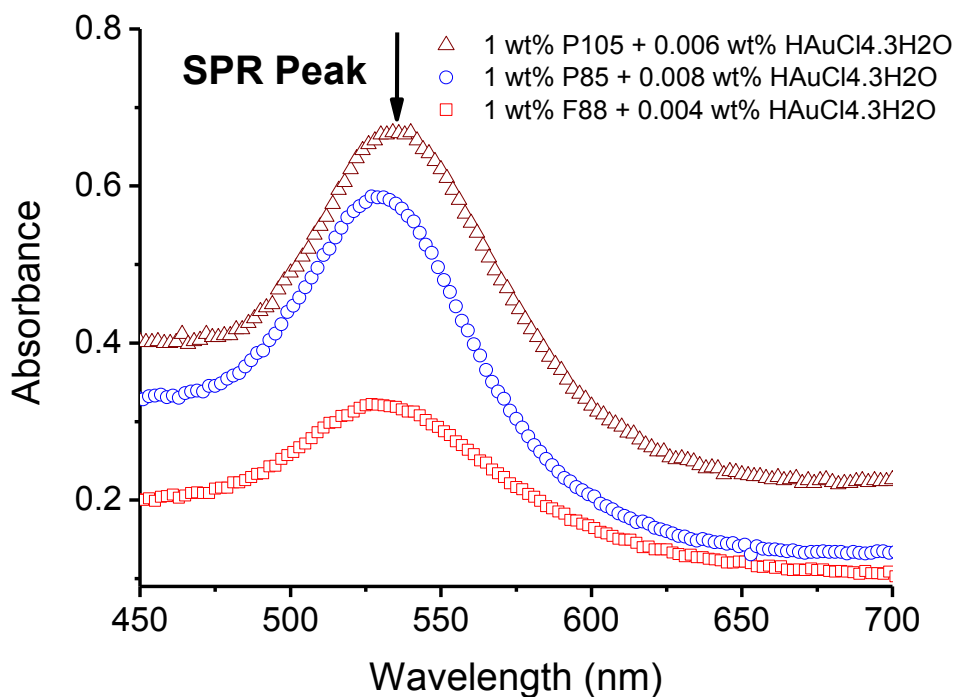


Figure 5.4. Comparison of SPR peaks for 1 wt% block copolymers (F88, P85 and P105) with gold salt concentration corresponding to their maximum yields.

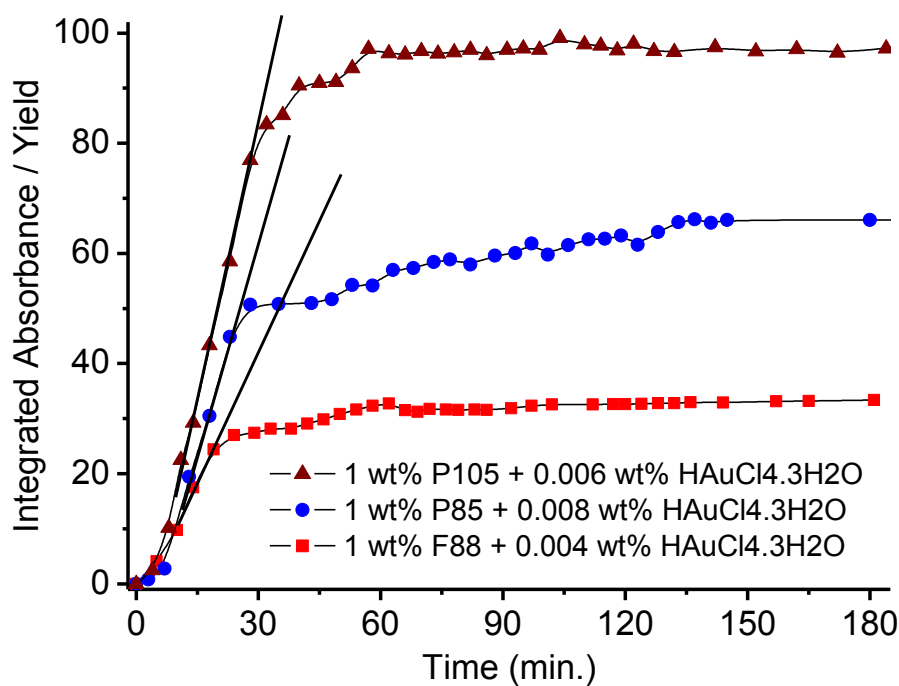


Figure 5.5. Time-dependent variation of yield of gold nanoparticles for 1 wt% block copolymers (F88, P85 and P105) at their corresponding gold salt concentrations of maximum yields.

The rate of formation and stability of gold nanoparticles for different block copolymers have also been examined. **Figure 5.5** shows the time dependence of yield for 1 wt% block copolymers at gold salt concentrations corresponding to their maximum yields. The formation rate is observed to be faster for the system having higher yield, as slope of the formation region is higher for P105 > P85 > F88. This higher tendency of P105 in self-assembling leads to the highest yield as well as faster formation rate of gold nanoparticles amongst three block copolymers used. However, the yield saturation is obtained at almost similar time (~ 1 hr) for all the block copolymers with high stability for a longer period of time. The self-assembly is utilized to control the nucleation and growth and hence the synthesis of nanoparticles.

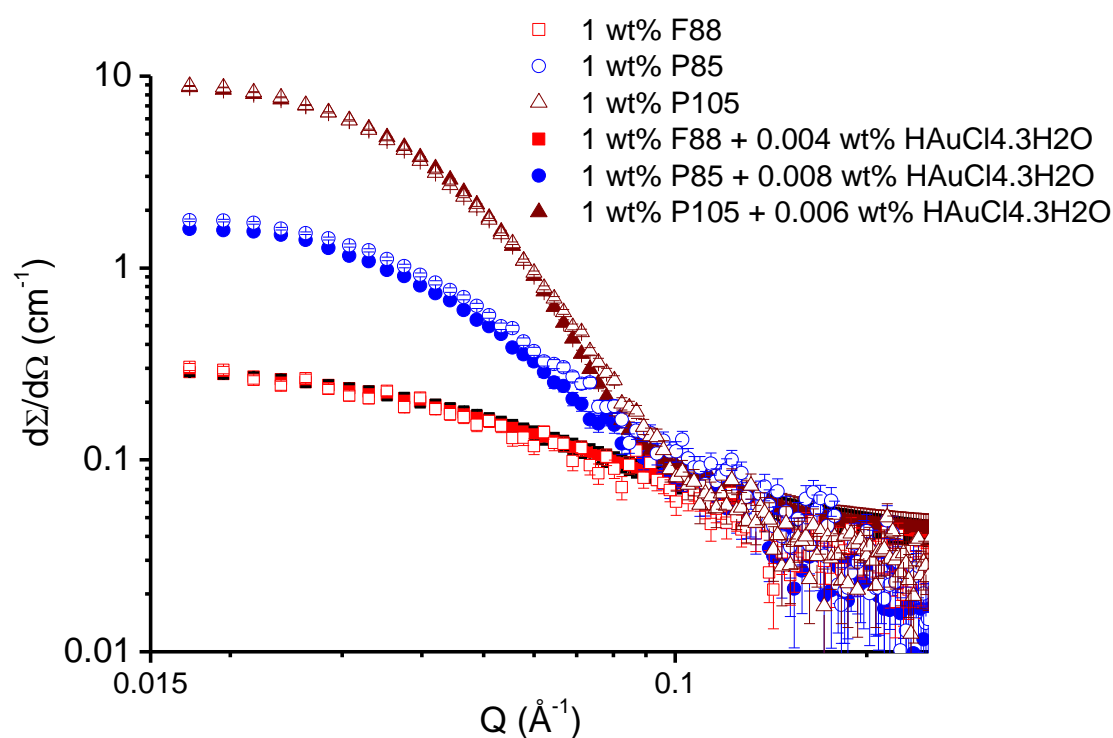


Figure 5.6. SANS data of 1 wt% block copolymer solutions without and with the gold salt corresponding to their maximum yields.

The comparison of SANS data without and with the addition of gold salt corresponding to maximum yields is given in **Figure 5.6**. There are no significant changes observed with gold nanoparticles. Block copolymers in salt solutions can either participate in

the formation of gold nanoparticles or form their own micelles. In the case of nanoparticles, they get coated on the particles, and will have a very different scattering pattern than that of the micelles. Therefore, the scattering from block copolymer coated gold nanoparticles is expected to be significantly different than from the micelles. The fact that the scattering curves do not change in presence of gold nanoparticles, suggests the formation of a very small fraction of gold nanoparticles in these systems. This behaviour can be understood on the basis if most of the block copolymers form their own micelles and the fraction associated with the gold nanoparticles is small as the gold nanoparticle concentration is much smaller than the block copolymer concentration.

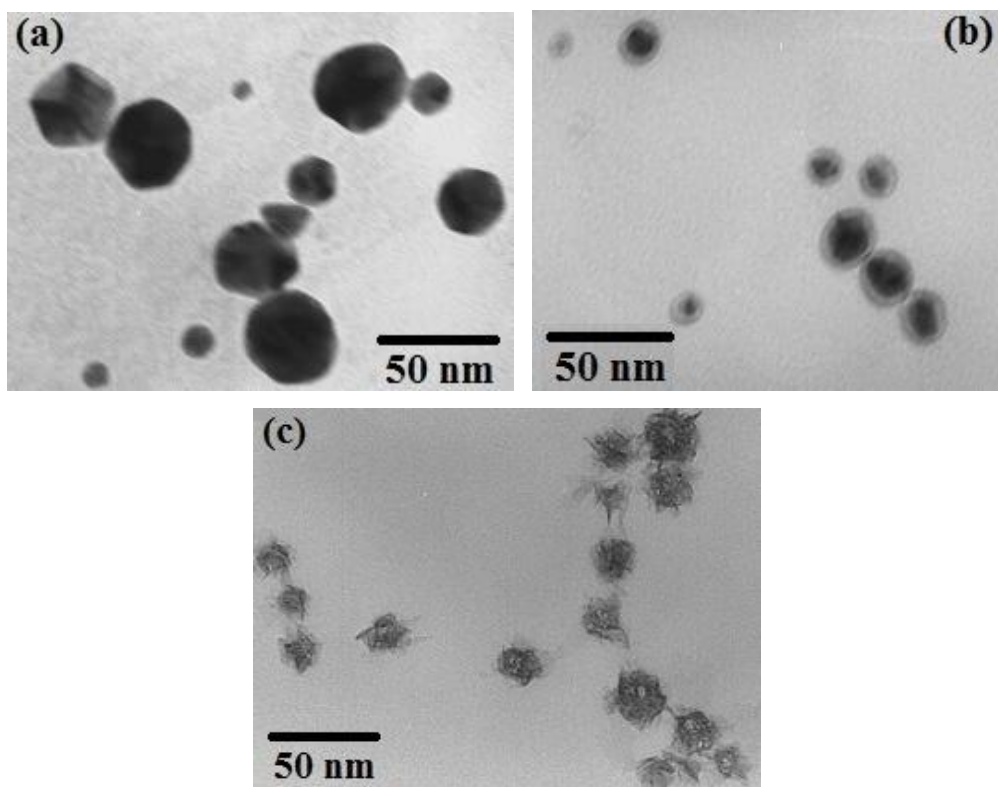


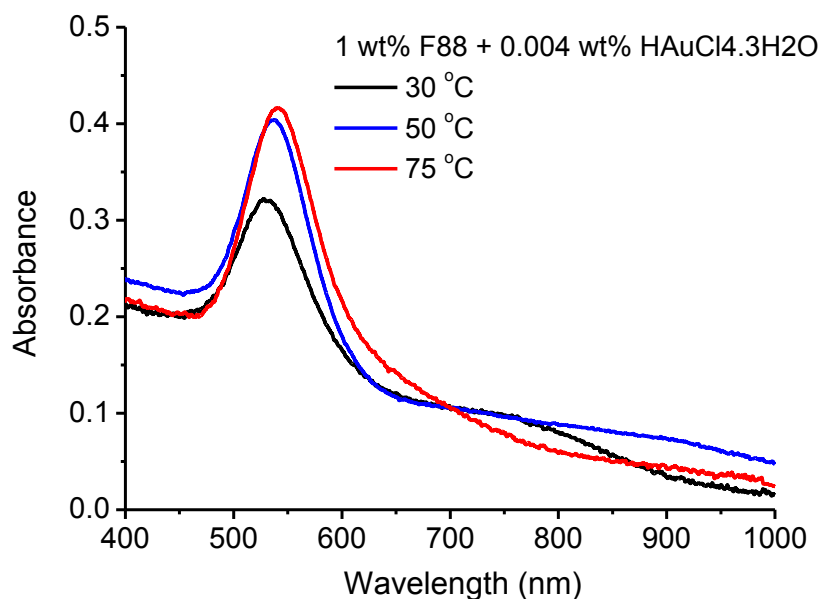
Figure 5.7. TEM images of gold nanoparticles synthesized using 1 wt% block copolymers (a) P105, (b) P85 and (c) F88 with gold salt in samples corresponding to their maximum yields.

We have observed that the yield (Figure 5.4) and formation rate (Figure 5.5) of synthesis of gold nanoparticles depend on the propensity of the self-assembly of block copolymers. Further, TEM has been used to find the structure of gold nanoparticles in these

systems. **Figure 5.7** shows transmission electron micrographs of gold nanoparticles for the block copolymers corresponding to the samples of their maximum yields. It is observed that the size of the nanoparticles depends on the block copolymer. The block copolymer F88 mostly consists of block copolymer cross-linked small gold nanoparticles while the size of the nanoparticles for P85 is ~ 15 nm. The P105 block copolymer having highest tendency of self-assembly forms the nanoparticles with largest sizes (~ 30 nm). These studies thus show that the self-assembly of block copolymers controls the yield and formation rate as well as the structure of the gold nanoparticles.

5.3.3. Temperature-Induced Synthesis

Micelle formation, in aqueous solutions of amphiphilic block copolymers, is critically dependent upon temperature [96,98,146]. This is a result of the successive dehydration of PO and EO chains upon the increase in temperature. At low temperatures, both types of blocks within block copolymer molecules are hydrated and therefore they are soluble in water. When the temperature increases, the PO block dehydrates and becomes insoluble, resulting in the formation of micelles. The temperature at which micelles are formed is referred to as the CMT and for most of the block copolymers it has value in the range of 25 to 40 °C.



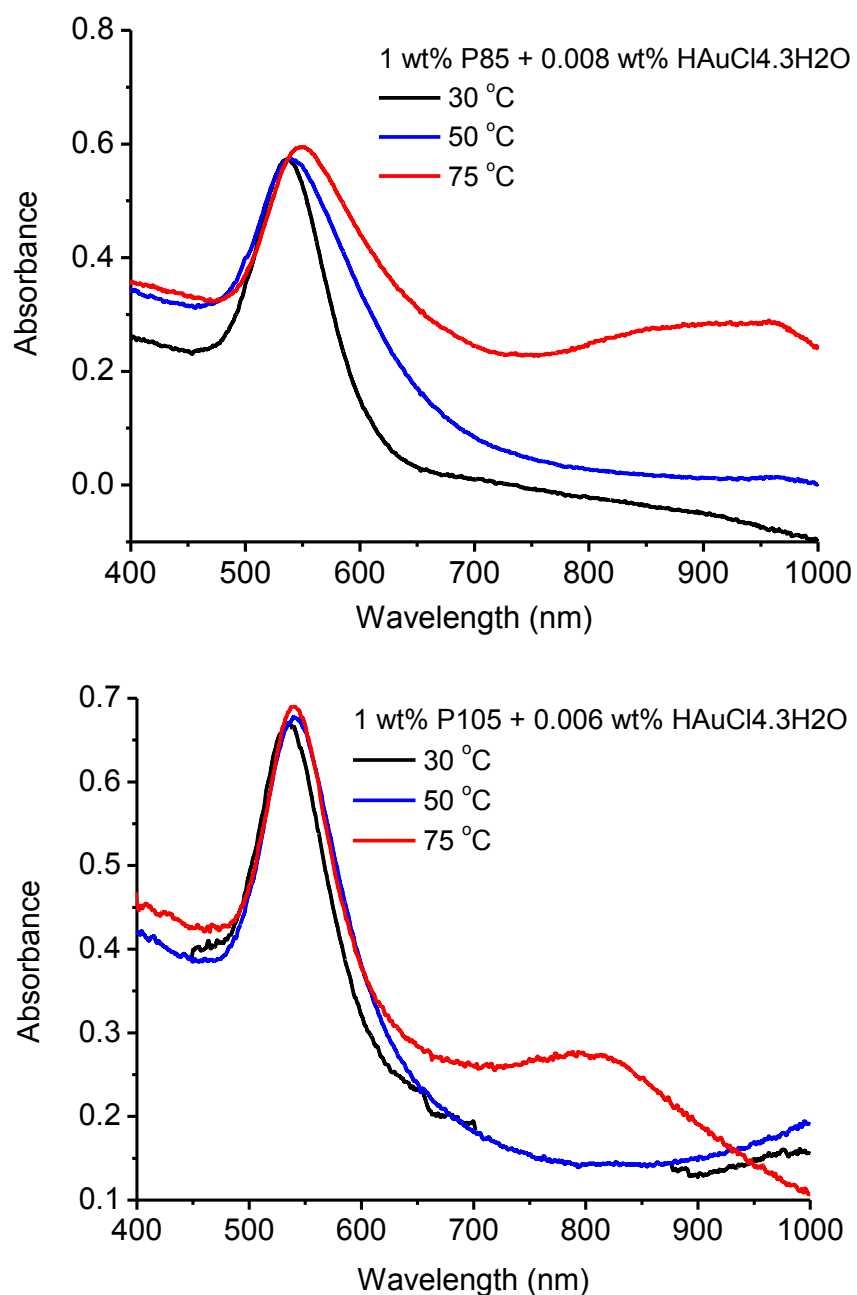


Figure 5.8. UV-visible absorption spectra of 1 wt% block copolymers with $\text{HAuCl}_4 \cdot 3\text{H}_2\text{O}$ corresponding to their maximum yields with varying temperature.

UV-visible absorption spectra of 1 wt% block copolymers at gold salt concentrations corresponding to their maximum yields with varying temperature are shown in **Figure 5.8**. All the three systems show SPR peaks whose position, height and width depend on the block copolymer and temperature used. The peak height (maximum absorbance, Abs_{max}), peak position (λ_{max}) and peak width ($FWHM$) of the SPR peak in absorption spectra in these

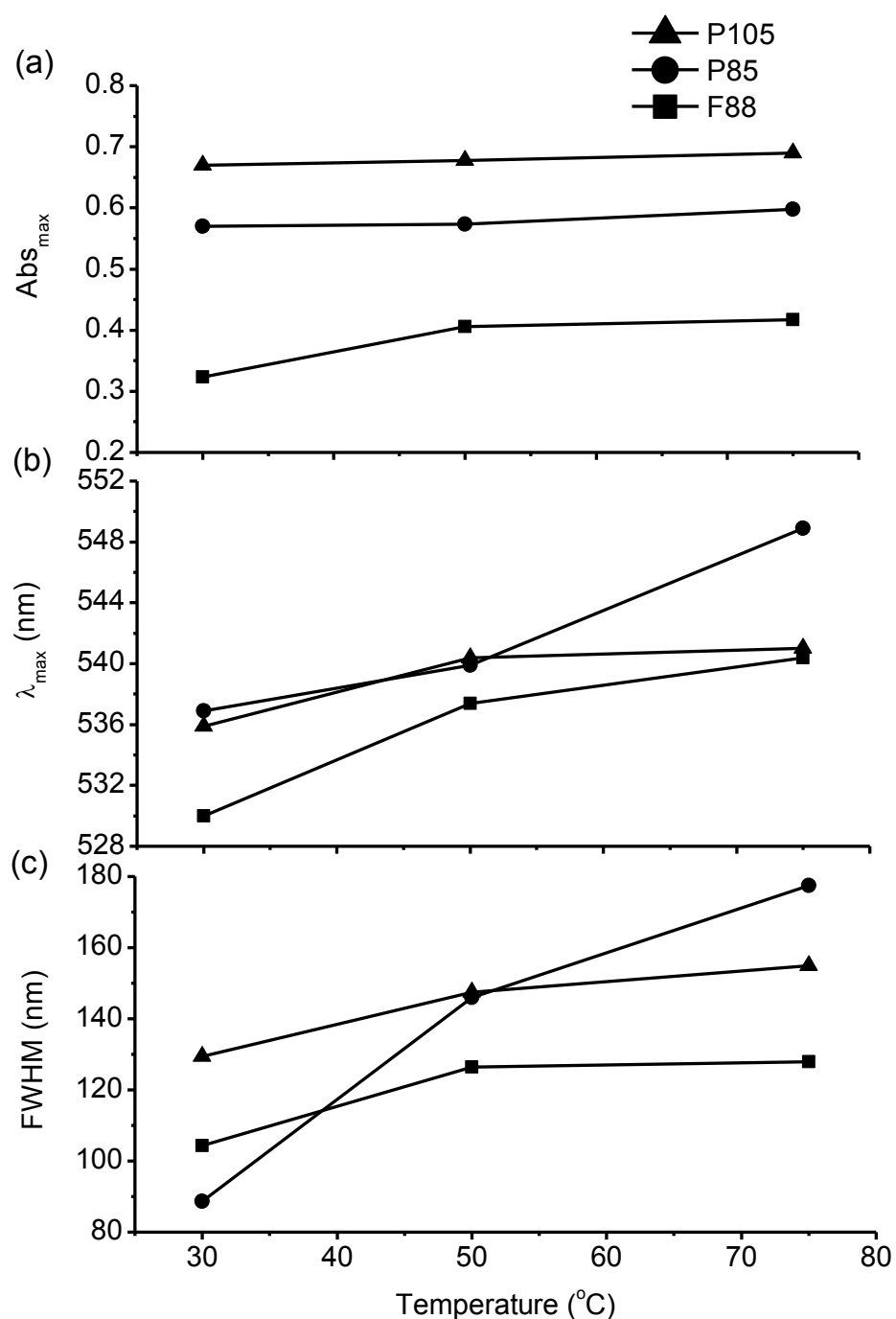


Figure 5.9. (a) Absorbance (Abs_{max}), (b) maximum wavelength (λ_{max}) and (c) full width at half-maximum ($FWHM$) of SPR peak of gold nanoparticles containing 1 wt% block copolymers as a function of temperature.

systems are plotted in **Figure 5.9** In the case of F88 block copolymer there is change in the SPR peak height and position, which suggests to the increase in the yield and size of the nanoparticles, respectively with increase in the temperature. These results can be explained

based on the enhanced micellization of F88 with increasing temperature that leads to higher yield and larger sizes of the nanoparticles. Unlike F88, P85 and P105 mostly show SPR peaks shift and broaden with increasing temperature. Also there is build-up of absorption spectra at higher wavelengths for higher temperature. The broadening of SPR is because of increase in the size of the nanoparticles. Though there is build-up at higher wavelengths but not as expected for nanorods if one expects them to be formed from the rod-like micelles at those temperatures [206]. It is possible that along with mostly spherical particles there exists a small fraction of nanorods or different asymmetric particles for the build-up of the absorption spectra at higher wavelengths.

The effect of temperature on the gold nanoparticle synthesis has been further investigated by SANS [205]. **Figure 5.10** shows SANS data of gold nanoparticles from 1 wt% P85 with 0.2 wt% $\text{HAuCl}_4 \cdot 3\text{H}_2\text{O}$ and in presence of Na_3Ct . It may be mentioned that SANS requires sufficiently high concentration of gold nanoparticles to able to get enough scattering from the sample. The high-yield of gold nanoparticles with block copolymers can be obtained with the help of additional reductant such as Na_3Ct , the details of which are discussed in the next chapter. The SANS data in Figure 5.10 are also taken for the solvent (85% H_2O in H_2O and D_2O mixture) where the block copolymers are contrast-matched. All the data show similar features irrespective of the temperature at which nanoparticles have been synthesized. The data are fitted with the polydispersed spherical nanoparticles. The fitted size parameters are given in **Table 5.5**. It is seen that the size of the nanoparticles and polydispersity increases with the increase in the temperature. Thus SANS clearly show while P85 forms rod-like micelles at higher temperatures but nanoparticles synthesized at that temperature are spherical similar to that formed at low temperatures.

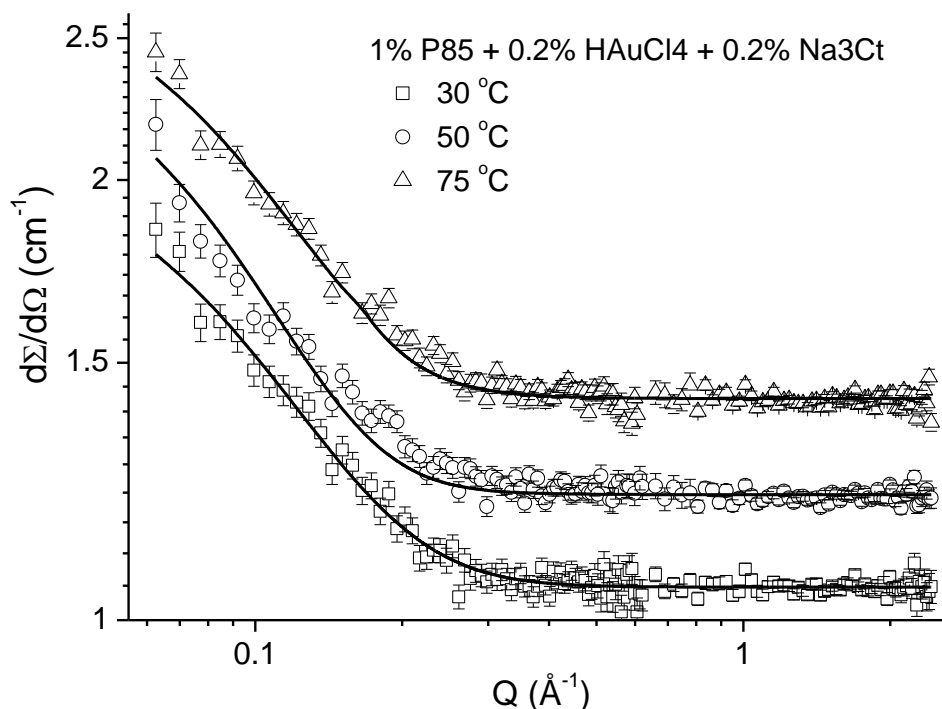


Figure 5.10. SANS data of 1 wt% P85 with 0.2 wt% $\text{HAuCl}_4 \cdot 3\text{H}_2\text{O}$ in presence of 0.2 wt% Na_3Ct at different temperatures. The solid curves are theoretical fits to the experimental data. The data of 50 and 75 °C are shifted vertically for clarity.

Table 5.5. Fitted structural parameters of gold nanoparticles as obtained by SANS in 1 wt% P85 with 0.2 wt% $\text{HAuCl}_4 \cdot 3\text{H}_2\text{O}$ in presence of 0.2 wt% Na_3Ct at different temperatures.

Temperature (°C)	Mean size (nm)	Polydispersity σ
30	10.1	0.41
50	11.6	0.36
75	12.7	0.32

The direct visualization of the structures of synthesized gold nanoparticles has also been carried out by TEM. **Figure 5.11** shows TEM images of gold nanoparticles at different temperatures from the nanoparticle system used in SANS studies in Figure 5.10. It is observed that irrespective of the temperature of synthesis nanoparticles formed are mostly spherical. The average size of the nanoparticle is of the order similar to that found by SANS.

We have also observed that a small fraction of non-spherical nanoparticles are also formed at higher temperature, which could be the reason for the build-up of SPR at higher wavelengths as observed in Figure 5.8. The fact that the presence of rod-like micelles does not lead the formation of rod-like nanoparticles, suggests interplay of different driving forces for block copolymer to self-assemble to micelles and synthesizing nanoparticles.

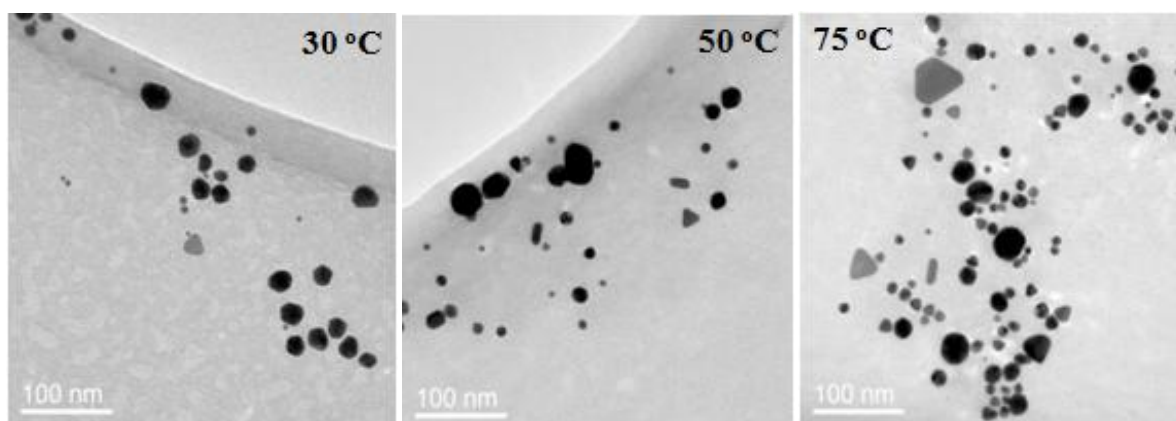


Figure 5.11. TEM images of gold nanoparticles in 1 wt% P85 with 0.2 wt% $\text{HAuCl}_4 \cdot 3\text{H}_2\text{O}$ in presence of 0.2 wt% Na_3Ct) at different temperatures.

5.4. Conclusions

The role of self-assembly of block copolymers to the gold nanoparticle synthesis has been studied. The self-assembly is tuned by varying the chemical structure of the block copolymer and solution temperature. The self-assembly has been studied for three different block copolymers F88, P85 and P105, which not only have varying molecular weight but also differ in hydrophobicity to hydrophilicity ratio. The propensity of these block copolymers to self-assemble to micelles has been found in the order $\text{P105} > \text{P85} > \text{F88}$. The self-assembly is enhanced with decreasing hydrophilicity ($\text{P85} > \text{F88}$) and increasing molecular weight for the block copolymers with similar percentage of hydrophilicity ($\text{P105} > \text{P85}$). The micelles remain spherical even up to very high temperature for highly hydrophilic block copolymer (F88) whereas sphere-to-rod transition of micelles has been observed for the block copolymers with low hydrophilicity (P85 and P105) as the temperature is increased. The

synthesis has been carried out using these three block copolymers at different temperatures. It has been found that the yield of gold nanoparticles increases in the order $F88 < P85 < P105$. As a fact that P105 has higher tendency to self-assemble, it results in higher yield as compared to F88 and P85. The formation rate is also found faster for the system having higher yield. Block copolymer P105, having the highest tendency of self-assembly, forms the nanoparticles with largest sizes whereas the size of the nanoparticles decreases for F88 and P85. It is also found that F88 unlike P85 and P105 mostly consists of block copolymer cross-linked small gold nanoparticles. Temperature dependent synthesis show that irrespective of shape of block copolymer micelles the synthesis carried out at different temperature gives rise to the formation of spherical nanoparticles in all the cases. This is believed to be because of the differences in the driving force of block copolymer to self-assemble to micelles and in synthesizing nanoparticles. However, it has been found that increasing temperature increases the reaction kinetics drastically, resulting in much faster synthesis of nanoparticles.

Chapter 6

High-Yield Synthesis of Gold Nanoparticles

6.1. Introduction

The various routes for synthesizing gold nanoparticles deal with controlling size and shape of the nanoparticles, reducing the number of synthesis steps and nanoparticle formation time, high yield and stability of nanoparticles. To obtain high nanoparticle yield is one of the challenging aspects in all the synthesis methods. The yield of nanoparticles can be tuned by varying ingredients used in the synthesis and solution conditions (concentration, temperature, pH, ionic strength etc.) as well as by control over shape and size of nanoparticles [96,98,146]. In the case of chemical reduction methods, the optimization of yield depend on capability of gold salt to be reduced followed by their nucleation and growth, control over shape and size of the nanoparticles and the way they are stabilized. Most of these methods of gold nanoparticle synthesis usually have a quite low yield of nanoparticles. The low yield is believed to be due to the limitation in reduction, control over size of the nanoparticles or by their stability.

The block copolymer-mediated synthesis of gold nanoparticles also gives a low yield of nanoparticles. It has been found in earlier chapter (Chapter 4) that the yield simply does not increase with the increase in gold salt concentration. At a given block copolymer concentration the yield only increase up to a gold salt concentration and above which the yield decreases. The maximum yield depends on the molar ratio of block copolymer to gold salt and is limited by the reduction capability of block copolymer. The yield increases with block copolymer concentration and this behaviour is linear only in the low concentration

regions of the block copolymer. At higher block copolymer concentrations the yield starts deviating from the linearity because of the formation of larger aggregates undergoing phase separation. It is therefore of interest to overcome these limitations by some means to achieve high yield of nanoparticles.

This chapter discusses the development of two methods of high-yield synthesis of gold nanoparticles, where the yield can be enhanced by manyfold [207-212]. The first method based on step-addition, the gold salt is added in small steps to maintain the continuous formation of nanoparticles [207]. This method works because: (i) gold salt is added in small steps maintaining required minimum ratio of block copolymer-to-gold salt (r_{min}) for all the gold salt to form nanoparticles and (ii) most of the block copolymer become available for next step. This method can be repeated as many as times to get high yield. The limitation of this method arises from the long time of synthesis which is sum of times of completion of each individual step. In another synthesis method (additional reductant method) the presence of an additional reductant is utilized to enhance the reduction and hence yield [209]. The trisodium citrate is a well known reducing agent for this purpose and is used along with block copolymer. This method provides faster synthesis of high yield gold nanoparticles. The dependence of high yield gold nanoparticle on various synthesis parameters have been characterized using UV-visible spectroscopy, TEM, SANS, SAXS and DLS [213-215].

6.2. Experimental Procedure

6.2.1. Materials

Pluronic P85 (EO₂₆PO₃₉EO₂₆, M.W. = 4600) was obtained from BASF Corp., New Jersey. The gold salt of hydrogen tetrachloroaurate(III) hydrate (HAuCl₄.3H₂O) and additional reductant trisodium citrate dihydrate (Na₃C₆H₅O₇.2H₂O) were used in the synthesis as

purchased from Alfa Aesar. D₂O (99.9 atom %D) was purchased from Sigma. All the solutions were prepared in millipore H₂O except in the case of neutron scattering experiments for which H₂O or D₂O is used as solvent depending on the requirement of contrast condition. All the products were used as received.

6.2.2. Synthesis of Gold Nanoparticles

The gold nanoparticles for obtaining high-yield in step-addition method were synthesized from 1 wt% P85 block copolymer solution in presence of 0.02 wt% (0.508 mM) of H₂AuCl₄·3H₂O added in steps of 0.004 wt% (5 times) in aqueous solution. This synthesis is compared when the gold salt (0.02 wt%) is added directly. In the case of additional reductant method, the amount of additional reductant (Na₃Ct) is optimized by keeping the gold salt concentration fixed and varying the Na₃Ct concentration. The gold nanoparticles have been synthesized using 1 wt% P85 up to gold salt concentration of 1 wt%. All the solutions were kept at room temperature without any disturbances for about 3 hrs for the completion of the reaction. The transparent solution becomes purple on the formation of nanoparticles.

6.2.3. Characterization of Gold Nanoparticles

The formation of gold nanoparticles is confirmed using UV-visible spectroscopy [19]. The measurements were carried out using 6505 Jenway UV-visible spectrophotometer. The data were collected in spectrum mode with a wavelength interval 1 nm from the samples held in quartz cuvettes of path length 10 mm.

SANS has been used to examine the structures of block copolymers and gold nanoparticles in the synthesis. The block copolymer structures were studied by preparing samples in D₂O where the block copolymer has a strong contrast. On the other hand, the scattering from gold nanoparticles was measured by contrast matching block copolymer in a mixed solvent of H₂O and D₂O (15% D₂O). The measurements were performed on the SANS

instrument at SANS-I facility, Swiss Spallation Neutron Source SINQ, Paul Scherrer Institut, Switzerland [189]. The wavelength of neutron beam used was 6 Å. The experiments were performed at sample-to-detector distances of 2 and 8 m to cover a Q -range of 0.007 to 0.32 Å⁻¹. The sample solutions were kept in a 2 mm thick quartz cell with Teflon stoppers. The scattered neutrons were detected using two-dimensional 96 × 96 cm² detector.

DLS experiment has been performed to complement the SANS results for high-yield nanoparticle systems [63]. Measurements were carried out using Autosizer 4800 (Malvern Instruments, UK) equipped with 7132 digital correlator and coherent (Innova 70C) Ar-ion laser source operated at wavelength 514.5 nm with a maximum output power of 2 W.

SAXS and TEM measurements have also been carried out to see the structure of gold nanoparticles [169,176]. SAXS experiments were performed using a Bruker Nanostar instrument equipped with a rotating anode generator (18 kW) operated at a voltage of 45kV and current of 100 mA. The X-rays are collimated through a 3 pin-hole system and data is acquired using a 2-D gas filled detector over a Q -range of 0.01 to 0.2 Å⁻¹. Samples were sealed in quartz capillaries having a diameter of 2 mm. Data were corrected for background scattering and circularly averaged using the software provided with the instrument. TEM was carried out in a JEOL 2000 FX transmission electron microscope. All TEM microphotographs were taken at acceleration voltage 160 kV, recorded on a photographic film.

6.3. Results and Discussion

The following two methods of high-yield synthesis of gold nanoparticle have been developed and their results are discussed.

- (i) Step-addition Method [207]
- (ii) Additional Reductant Method [209].

6.3.1. Step-Addition Method

We have observed that the maximum yield of gold nanoparticles for a fixed concentration of block copolymer occurs at a particular gold salt concentration, e.g. 0.008 wt% $\text{HAuCl}_4 \cdot 3\text{H}_2\text{O}$ for 1 wt% P85 (see Section 4.3.1 in Chapter 4). This concentration corresponds to the block copolymer-to-gold salt molar ratio of 11 and is related to the minimum number of block copolymer molecules (n) required for the reduction of a gold ion to take place. At lower salt concentrations when the molar ratio of block copolymer to salt ions (r) is much larger than $n = 11$, the yield increases with salt concentrations up to 0.008 wt%. Beyond this concentration the ratio r decreases and thus the probability of the reduction reaction in the sample to take place decreases. The distribution of a large number of ions and block copolymers makes it possible that a significant fraction of ions can still find n number of block copolymers and become reduced even though the average ratio r is less than n . Based on this explanation the yield is expected to be suppressed with increase in salt concentration, as has been experimentally observed. UV-visible spectroscopy suggests the increase in the size of the nanoparticles with the increase in the salt concentration beyond 0.008 wt% could be understood in terms of nanoparticle aggregation occurring due to insufficient stabilization by the block copolymers on the surface of the nanoparticles as the block copolymer to gold ion ratio decreases with the increase in the gold salt concentration. As a result we have observed that nanoparticles in these systems phase separate after some time (~ 1 day). At higher salt concentrations (> 0.02 wt%) the ratio r is too low to provide any significant probability within the system of being able to reduce the gold ions. Hence, UV-visible spectra only show the strong peak of unreduced gold ions and no SPR peak of gold nanoparticles is seen. We have seen that yield of gold nanoparticles that can be enhanced by increasing the concentration of gold salt and block copolymer or both are limited. This arises as a result of

limited reduction at lower block copolymer concentrations and existence of larger aggregates at higher block copolymer concentrations.

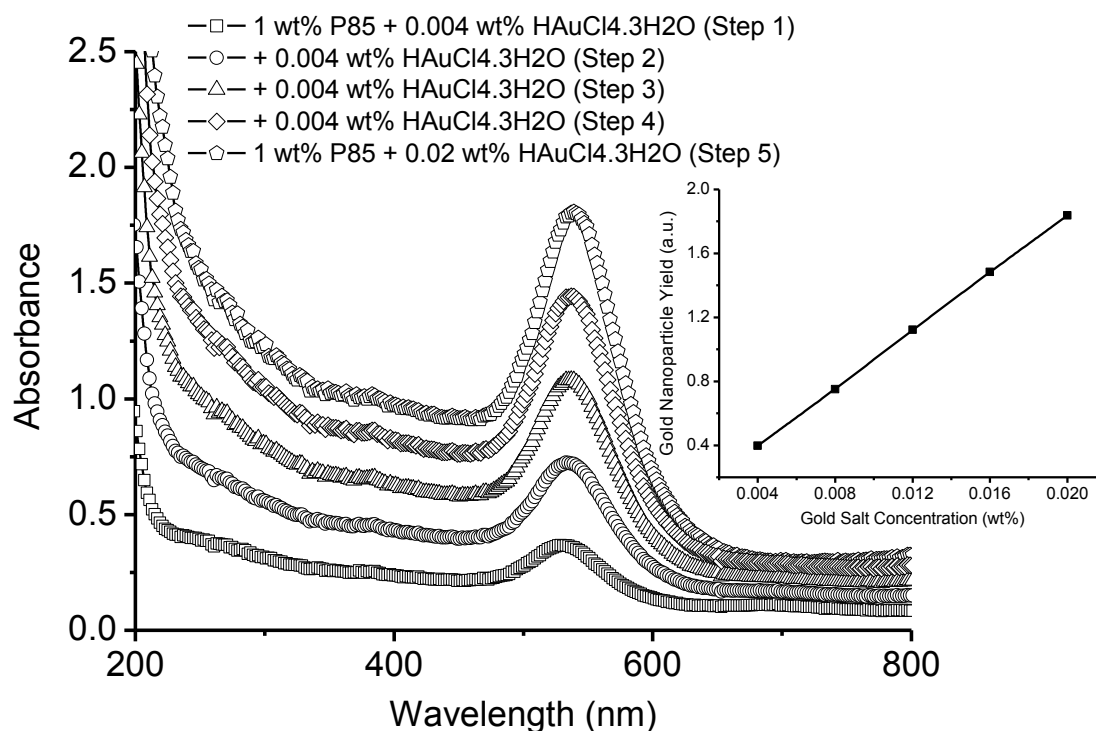


Figure 6.1. UV-Visible spectra of 1 wt% P85 with varying HAuCl₄·3H₂O concentration. The gold salt concentration is added in step of 0.004 wt%. Inset shows the yield-dependence on gold salt concentration.

The low yield of synthesized gold nanoparticles is limited due to the large value of n required for the reduction reaction of gold ions to occur. The fact that most of the block copolymers ($\sim 99\%$) remain free to form their own micelles can be used for synthesis of nanoparticles if the salt concentration is added in small steps (< 0.008 wt%) to maintain the ratio r greater than n . We have used this step-addition method to show the enhancement in the yield of the gold nanoparticles [207]. The step-addition method was used on 1 wt% P85 with addition steps of 0.004 wt%. The time between two steps (t_s) is decided by the time-dependent UV-visible spectroscopy. The time dependence of spectra was recorded from the freshly prepared sample by mixing the two components and from these data, integrated absorbance of SPR (proportional to the concentration of the nanoparticles) was plotted as a

function of time. The value of t_s (~ 3 hrs) corresponds to when at which the absorbance curve shows saturation. **Figure 6.1** shows the UV-visible spectroscopy of 1 wt% P85 with 0.004 wt% salt and after the gold salt added in next 4 steps of 0.004 wt% up to resultant salt concentration of 0.02 wt%. There is an increase in absorbance as the gold nanoparticles concentration increases with increasing salt by step addition. A linear gain in the nanoparticle yield is observed in step-addition method as expected if all the gold concentration is utilized in the formation of nanoparticles (**inset of Figure 6.1**).

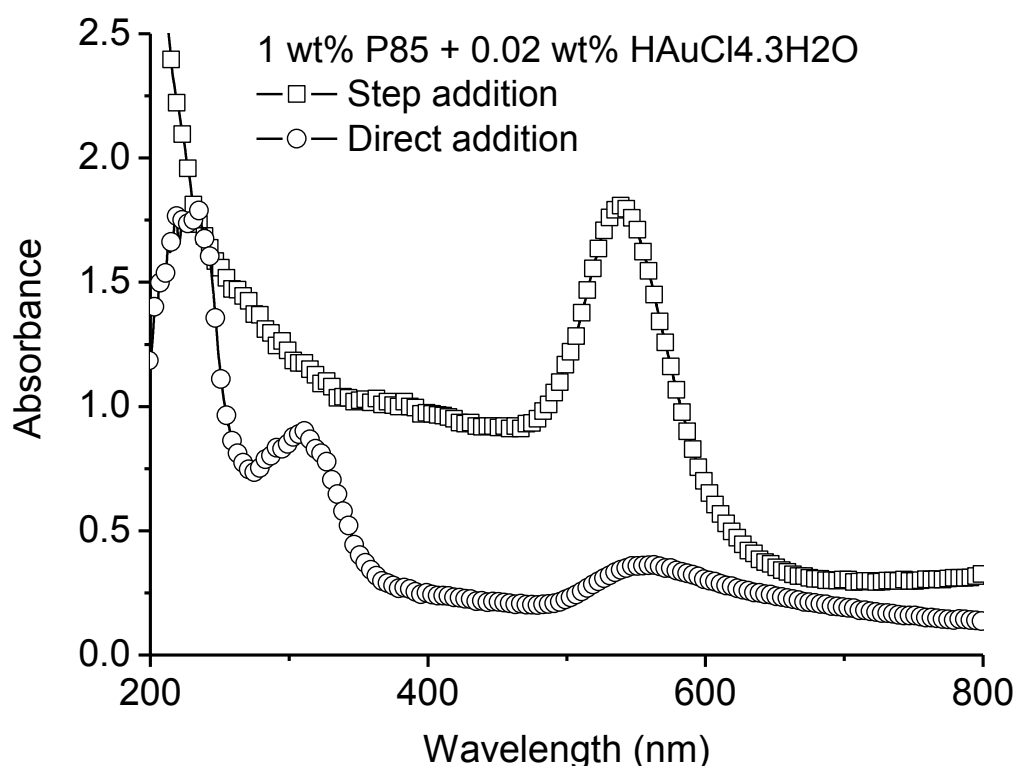


Figure 6.2. UV-Visible spectra of 1 wt% P85 with 0.02 wt% $\text{HAuCl}_4 \cdot 3\text{H}_2\text{O}$ compared with and without step-addition.

Figure 6.2 shows comparison of the data if the salt concentration of 0.02 wt% (5×0.004 wt%) is added directly instead of steps, which suggests a very low yield of gold nanoparticles. Thus step-addition method can be used to greatly enhance the yield of gold nanoparticles using block copolymers if the step addition concentration is sufficiently small in each step to maintain the reduction of gold ions. However, the application of this method is

limited by the longer synthesis time which increases as the number of steps increased to increase the yield. In the second method, we have made use of additional reductant by which the nanoparticle yield can be improved by manyfold in normal time.

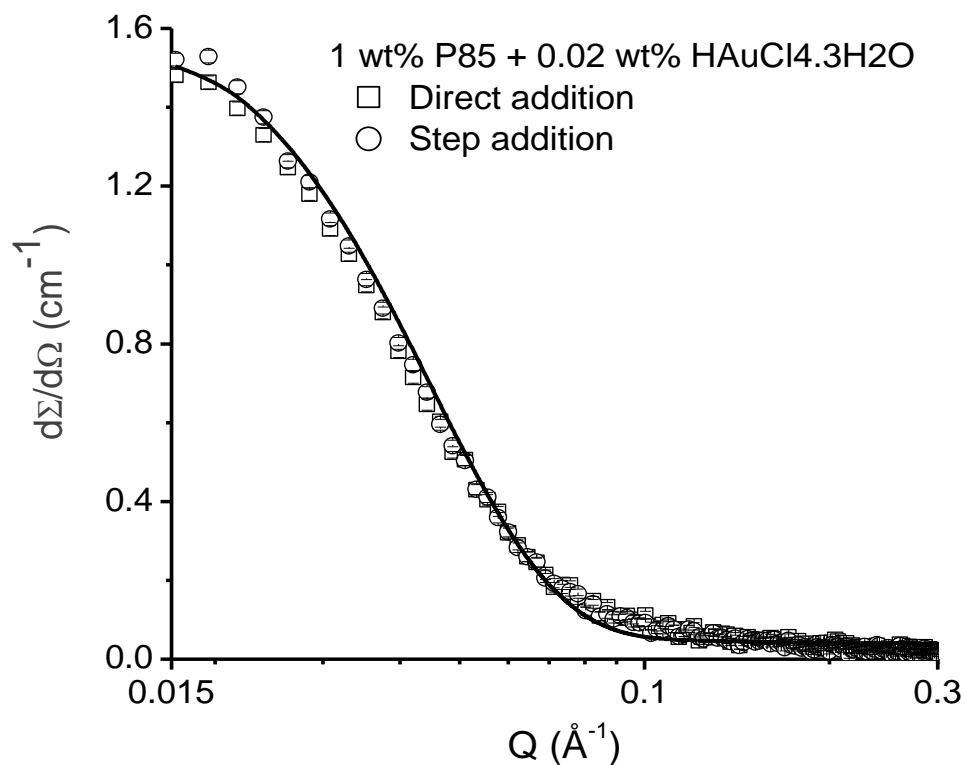


Figure 6.3. SANS data of 1 wt% P85 with 0.02 wt% HAuCl₄.3H₂O as obtained without and with step-addition.

Figure 6.3 shows the SANS data of 1 wt% P85 with 0.02 wt% HAuCl₄.3H₂O added directly and in step of 0.004 wt%. Although the yield of these two systems is very different SANS data are more or less found similar. This suggests that the scattering is negligible for gold nanoparticles and it is dominated by the presence of block copolymers in the system. It is therefore difficult to get any structural information of gold nanoparticles from these data. However, contrast variation SANS experiments can be carried out to separate the scattering contribution of gold nanoparticles from that of the block copolymers.

6.3.2. Additional Reductant Method

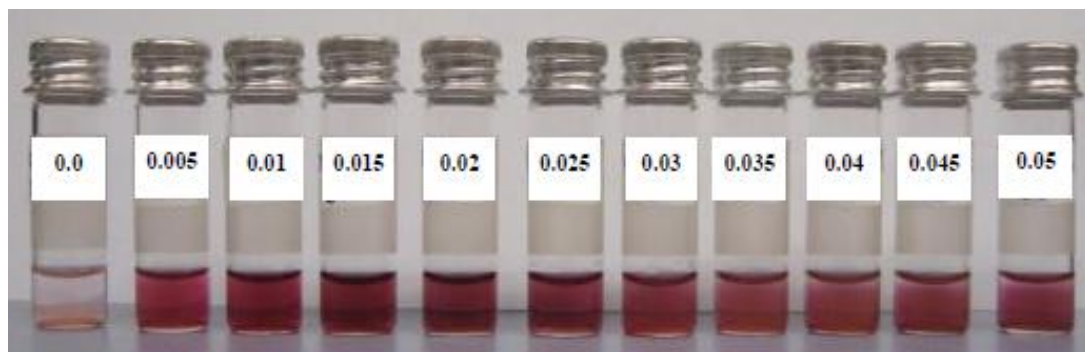


Figure 6.4. Photograph of gold nanoparticles in aqueous solutions of 1 wt% P85 + 0.02 wt% $\text{HAuCl}_4 \cdot 3\text{H}_2\text{O}$ with varying trisodium citrate (Na_3Ct) concentration. The labels show the concentration of Na_3Ct in wt%.

This method makes use of additional reductant to improve the reduction otherwise weak in the block copolymer-mediated synthesis of gold nanoparticles. Trisodium citrate (Na_3Ct), one of the most widely used reducing agents, is used for additional reduction [208]. The optimization of Na_3Ct for the synthesis is carried out by measuring the yield by varying its concentration for fixed block copolymer and gold salt concentrations. **Figure 6.4** shows the photograph of the yield improvement of the gold nanoparticles in 1 wt% P85 with 0.02 wt% $\text{HAuCl}_4 \cdot 3\text{H}_2\text{O}$ by varying the Na_3Ct concentration. It is seen that the nanoparticle yield increases with the increase in Na_3Ct concentration and has maximum around 0.02 wt%.

Figure 6.5 shows the variation of SPR peak absorbance of the gold nanoparticles in 1 wt% P85 with 0.01 wt% $\text{HAuCl}_4 \cdot 3\text{H}_2\text{O}$ with varying Na_3Ct concentration. It may be mentioned that a dilute gold nanoparticle system (1 wt% P85 with 0.01 wt% $\text{HAuCl}_4 \cdot 3\text{H}_2\text{O}$) had been chosen in Figure 6.5 as the UV-visible spectroscopy in these systems can be directly measured. However, one can also take the higher $\text{HAuCl}_4 \cdot 3\text{H}_2\text{O}$ concentrations but will require the dilution to avoid the saturation in the measurement of absorbance during UV-visible spectroscopy. These results give that the yield is maximum approximately for 1:1 wt ratio of Na_3Ct -to-gold salt concentration which is also consistent with the similar molecular

weights of $\text{HAuCl}_4 \cdot 3\text{H}_2\text{O}$ and Na_3Ct and typically 1:1 involvement of these two components in the reduction.

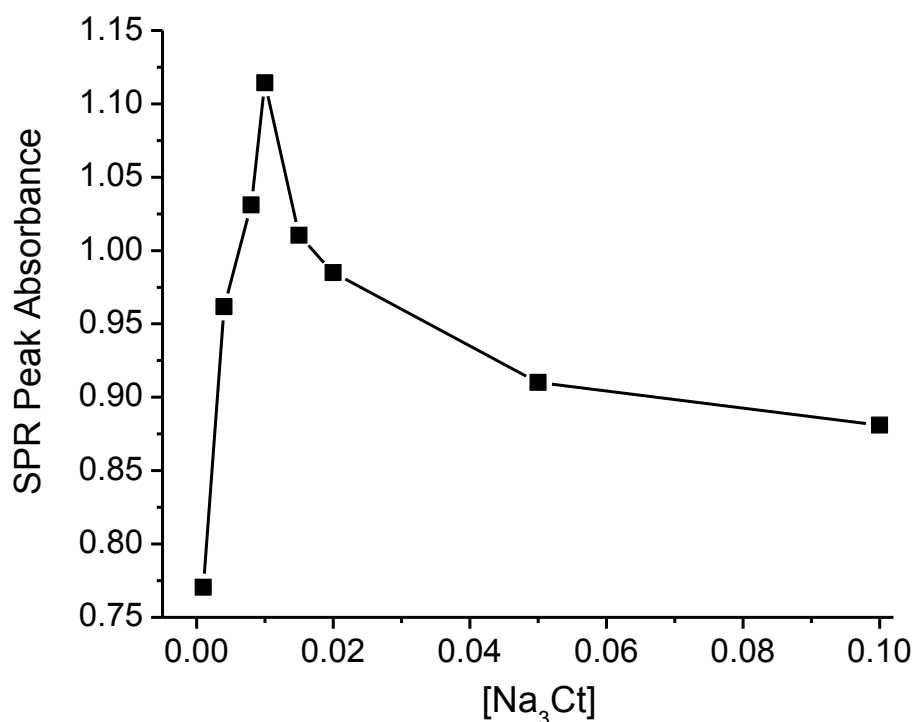


Figure 6.5. The variation of SPR peak absorbance in UV-visible absorption spectra of the gold nanoparticles for 1 wt% P85 with 0.01 wt% $\text{HAuCl}_4 \cdot 3\text{H}_2\text{O}$ and varying Na_3Ct concentration.

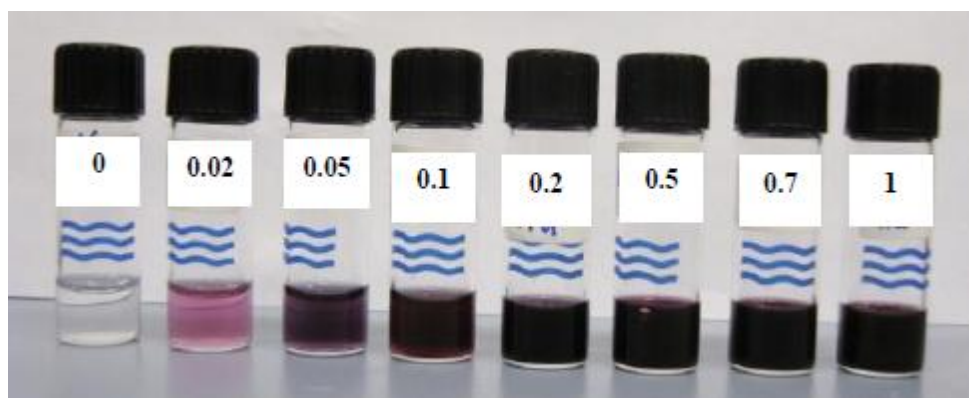


Figure 6.6. Photograph of gold nanoparticles in aqueous solutions of 1 wt% P85 with varying ($\text{HAuCl}_4 \cdot 3\text{H}_2\text{O} + \text{Na}_3\text{Ct}$) concentration. The labels show the concentration in wt%.

Using the additional reductant method, we have synthesized nanoparticles up to gold salt concentration of 1 wt% in presence of Na_3Ct (used 1:1 wt% ratio with gold salt) and the

yield is now found to be increasing with the gold salt concentration. **Figure 6.6** shows the photograph of gold nanoparticles prepared from aqueous solutions of 1 wt% P85 with varying $\text{HAuCl}_4 \cdot 3\text{H}_2\text{O}$ and Na_3Ct concentration. The synthesis of nanoparticles has been examined up to 1 wt% of gold salt concentration. The formation of gold nanoparticles is confirmed by measuring the SPR peak in the UV-visible spectroscopy data as shown in **Figure 6.7**. To avoid the saturation effect in absorption at high nanoparticle concentrations, these data were measured on the samples diluted to 0.005 wt%, and those shown in the Figure 6.7 are the measured data multiplied by the dilution factor.

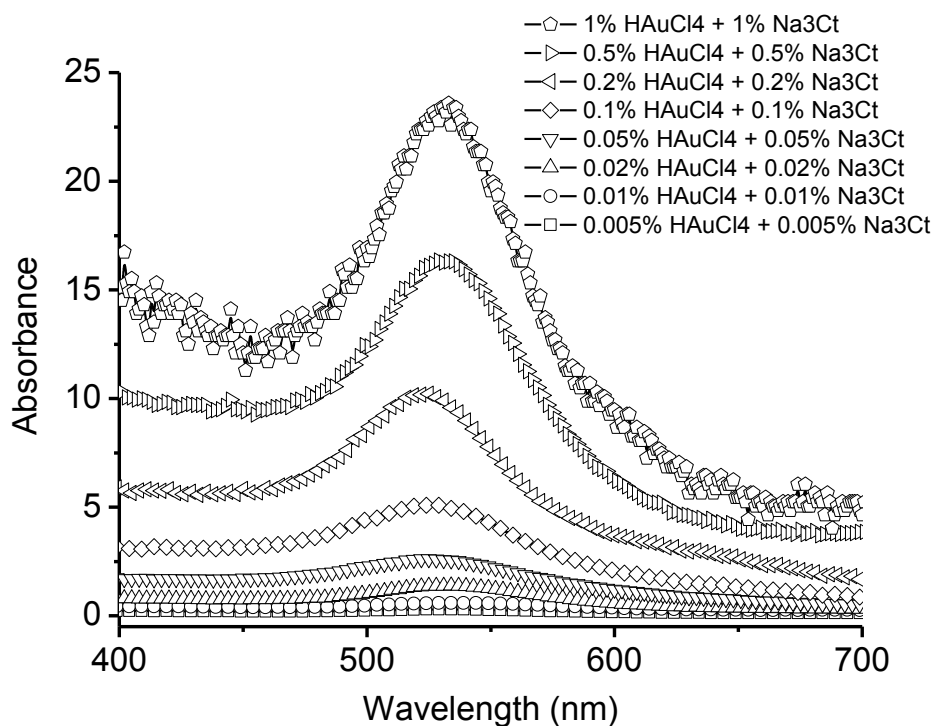


Figure 6.7. UV-visible absorption spectra of 1 wt% P85 with varying ($\text{HAuCl}_4 \cdot 3\text{H}_2\text{O}$ + Na_3Ct) concentration.

The calculated nanoparticle concentration from these samples as a function of gold salt concentration and the comparison of nanoparticle concentration in presence of Na_3Ct without the block copolymer are shown in **Figure 6.8**. The nanoparticle yield (proportional to the integrated absorbance) of the synthesis has been calculated from the area under the SPR peak covering wavelength range 450 to 700 nm. It is clear that the addition of Na_3Ct has

improved the reduction and subsequently the concentration of the gold nanoparticles, which only works in presence of block copolymer. The nanoparticle concentration is now shown to increase with gold salt concentration in presence of additional reductant.

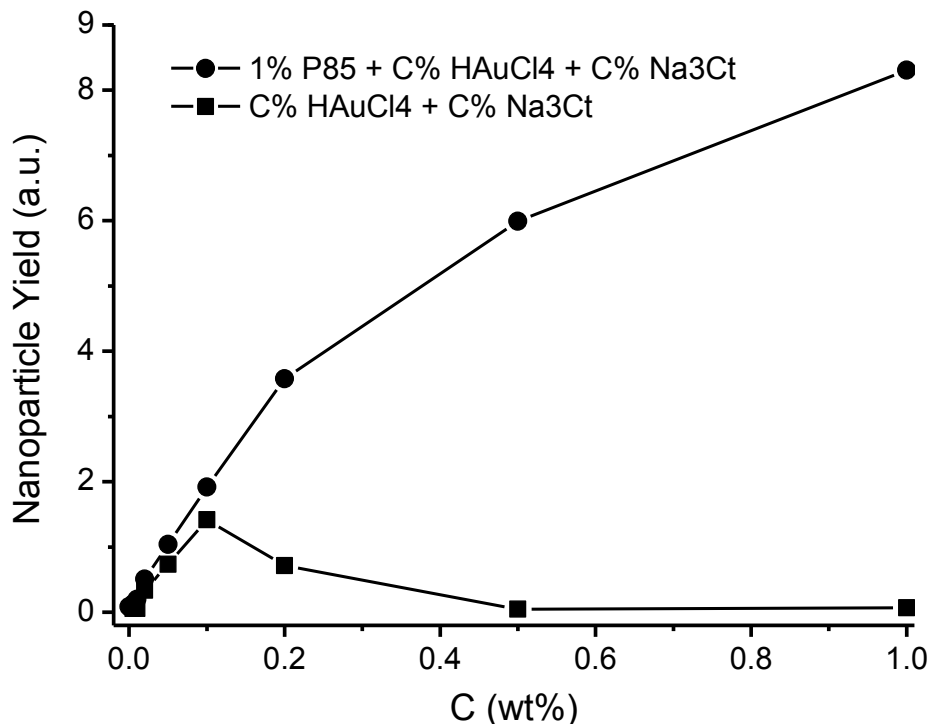


Figure 6.8. The calculated yield of gold nanoparticles in 1 wt% P85 with varying (HAuCl₄.3H₂O + Na₃Ct) concentration. The comparison of nanoparticle concentration without the use of block copolymer is also shown.

The high-yield nanoparticles have been characterized using SANS and SAXS. Unlike the case of neutrons where the scattering from hydrogenous system is high, X-rays are useful probe for such systems. The differences in scattering for neutrons and X-rays arise due to the fact that while neutrons are scattered by the nucleus of an atom, X-rays are scattered by the electron clouds around the nucleus. **Table 6.1** gives the calculated scattering length densities of different components of the block copolymer-mediated gold nanoparticle system for X-rays compared with neutrons. It is clear from the variation in scattering length density for neutrons that there exists a strong contrast for the block copolymers with respect to that from the gold nanoparticles in D₂O whereas this contrast is reversed when the solvent is H₂O. On

the other hand for X-rays, there is strong contrast for gold nanoparticles irrespective of the solvent.

Table 6.1. The neutrons and X-rays scattering length densities (ρ) of different components in block copolymer-mediated gold nanoparticle system.

Component	Scattering Length Density ρ ($\times 10^{10} \text{ cm}^{-2}$)	
	Neutron	X-ray
Au	4.66	131.36
P85	0.47	9.72
H ₂ O	-0.56	9.43
D ₂ O	6.40	9.43

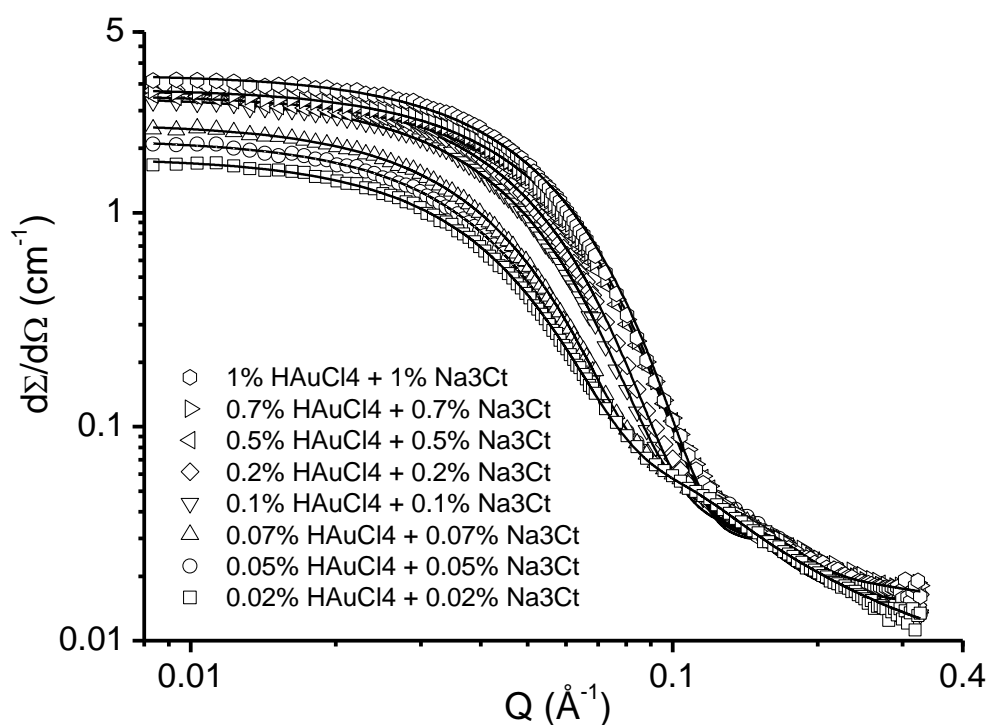


Figure 6.9. SANS data of 1 wt% P85 with varying (HAuCl₄.3H₂O + Na₃Ct) concentration in D₂O at 30 °C.

Table 6.2. Fitted micellar structure of 1 wt% P85 with varying gold salt and Na₃Ct concentration obtained from SANS data at 30 °C.

Block Copolymer System	Micellar Fraction (%)	Radius of Gyration of Unimers R_{gu} (nm)	Micellar Parameters		
			Core Radius R_c (nm)	Radius of Gyration of PEO Chain R_{gc} (nm)	Aggregation Number N
1% P85	11.3	2.3	3.84	1.2	63
1% P85 + 0.02% HAuCl ₄ .3H ₂ O + 0.02% Na ₃ Ct	19.1	2.3	3.88	1.2	65
1% P85 + 0.05% HAuCl ₄ .3H ₂ O + 0.05% Na ₃ Ct	29.4	2.3	3.93	1.2	68
1% P85 + 0.1% HAuCl ₄ .3H ₂ O + 0.1% Na ₃ Ct	34.6	2.3	3.97	1.2	70
1% P85 + 0.2% HAuCl ₄ .3H ₂ O + 0.2% Na ₃ Ct	37.6	2.3	3.97	1.2	70
1% P85 + 0.5% HAuCl ₄ .3H ₂ O + 0.5% Na ₃ Ct	39.3	2.3	3.97	1.2	70
1% P85 + 0.7% HAuCl ₄ .3H ₂ O + 0.7% Na ₃ Ct	40.6	2.3	4.01	1.2	72
1% P85 + 1% HAuCl ₄ .3H ₂ O + 1% Na ₃ Ct	41.3	2.3	4.00	1.2	71

Figure 6.9 shows the SANS data of 1 wt% P85 with varying HAuCl₄.3H₂O and Na₃Ct concentration in D₂O at 30 °C. There is also no scattering seen in particular in the low- Q region from the adsorbed block copolymers on the nanoparticles. The scattering at room

temperature does not show significant variation in their profile with respect to that of pure block copolymer solution suggests that most of the block copolymers remain free as micelles in gold nanoparticles solution. We have fitted these free block copolymers coexisting as micelles and unimers. The scattering from block copolymer micelles is calculated using core-shell particles with different scattering length densities for the core and shell. The structure of these micelles is described by a model consisting of non-interacting Gaussian PEO chains attached to the surface of the PPO core. The scattering from individual block copolymer unimer is calculated by the Gaussian chain conformation. The fitted parameters are given in **Table 6.2**. The fraction of block copolymer that forms micelles increases as a result of enhanced micellization (salting out effect) with the increase in the gold salt concentration. The micellar size is found to be almost similar having core radius of 4.0 nm surrounded by a PEO chain of radius of gyration of 1.2 nm and aggregation number around 70. The radius of gyration of unimer is found to be 2.3 nm. The schematic of gold nanoparticle is shown in **Figure 6.10**.

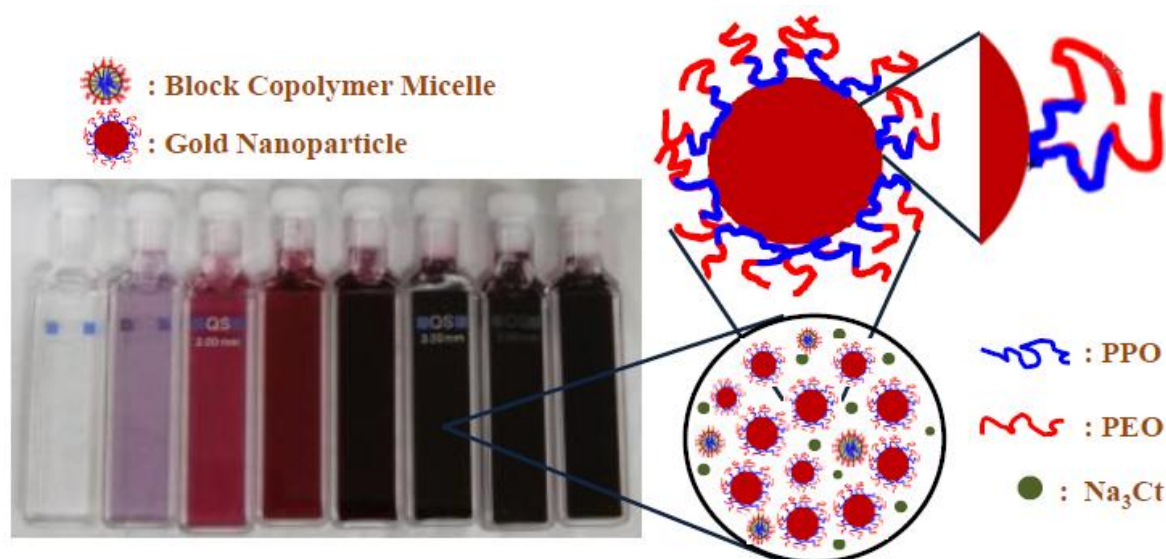


Figure 6.10. Schematic of structure of block copolymer-stabilized gold nanoparticles. The samples in cells show that the concentration of gold nanoparticles in presence of additional reductant can be enhanced.

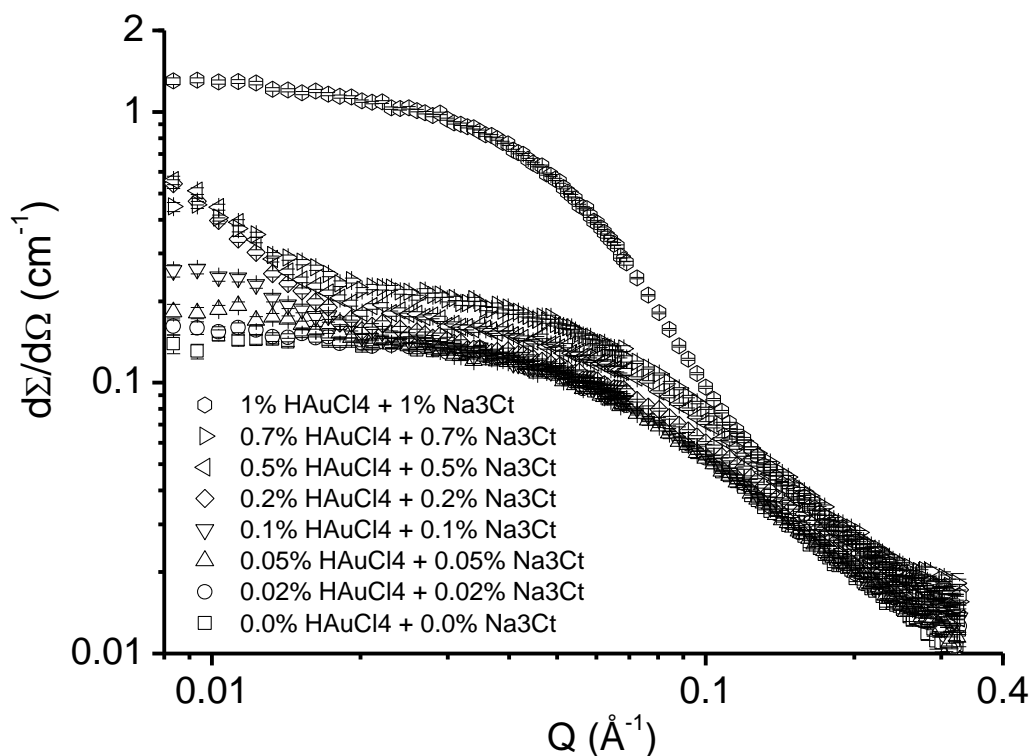


Figure 6.11. SANS data of 1 wt% P85 with varying ($\text{HAuCl}_4 \cdot 3\text{H}_2\text{O} + \text{Na}_3\text{Ct}$) concentration in D_2O at 15°C .

From the above SANS data (Figure 6.9), it is difficult to separate the relatively weak scattering from gold nanoparticles. Therefore, the SANS data have also been measured at low temperature (15°C) to avoid the strong scattering from block copolymer micelles as in **Figure 6.11**. At low temperature, block copolymers remain as unimers and therefore they give rise to much smaller scattering as compared to micelles at room temperature. A distinct scattering build-up in the low- Q region is seen because of the scattering from gold nanoparticles. This build-up is visible for gold salt concentration beyond 0.1 wt%. The overall increase in the scattering intensity at 1 wt% is again because of salt-induced micellization of block copolymers. The scattering in Figure 6.11 has contributions from gold nanoparticles coated with block copolymer as well as from block copolymers as unimers and their micelles if any. These data show that the scattering is mostly dominated by the individual block copolymers and the fact that it is difficult to fit the data of that adsorbed block copolymer on gold nanoparticle with core-shell structure.

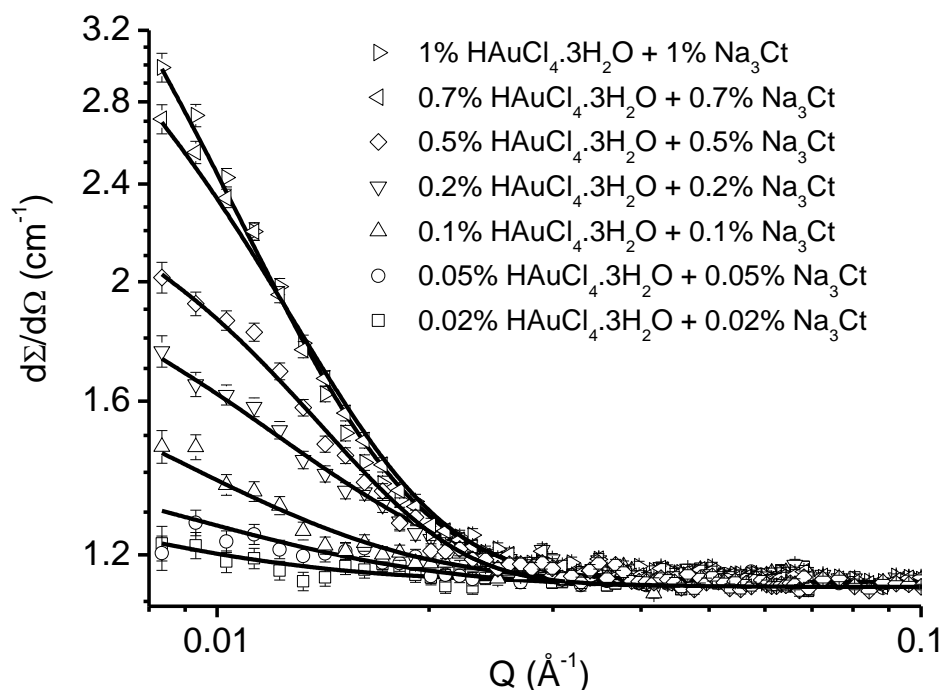


Figure 6.12. SANS data of 1 wt% P85 with varying ($\text{HAuCl}_4 \cdot 3\text{H}_2\text{O} + \text{Na}_3\text{Ct}$) concentration at 15 °C. The block copolymers are contrast-matched to the solvent (15% D_2O). The solid curves are theoretical fits to the experimental data.

To simplify the analysis, SANS data have also been taken for block copolymers contrast-matched to the solvent (85% H_2O in H_2O and D_2O mixture) as in **Figure 6.12**. In this case, no scattering from block copolymers is seen and whatever is measured is the scattering from gold nanoparticles. The scattering increases as the number density of the gold nanoparticles increases with increasing gold salt concentration. The gold nanoparticles are fitted with polydispersed spherical particles. Although we do not directly measure the adsorbed block copolymers on the nanoparticle surface but their stability particularly observed at higher temperature do suggest that the hydrophobic PPO should be covering the surface of the gold nanoparticles surrounded by the solvated PEO. Na_3Ct remain uniformly dissolved in the solution as it is highly soluble in aqueous solution (Solubility in water ~ 42.5 gm/100 ml at 25 °C). The particle size is found to increase with decrease in polydispersity

with increasing gold salt concentration. The calculated size distributions of the nanoparticles with increasing concentration for some of the systems are shown in **Figure 6.13**.

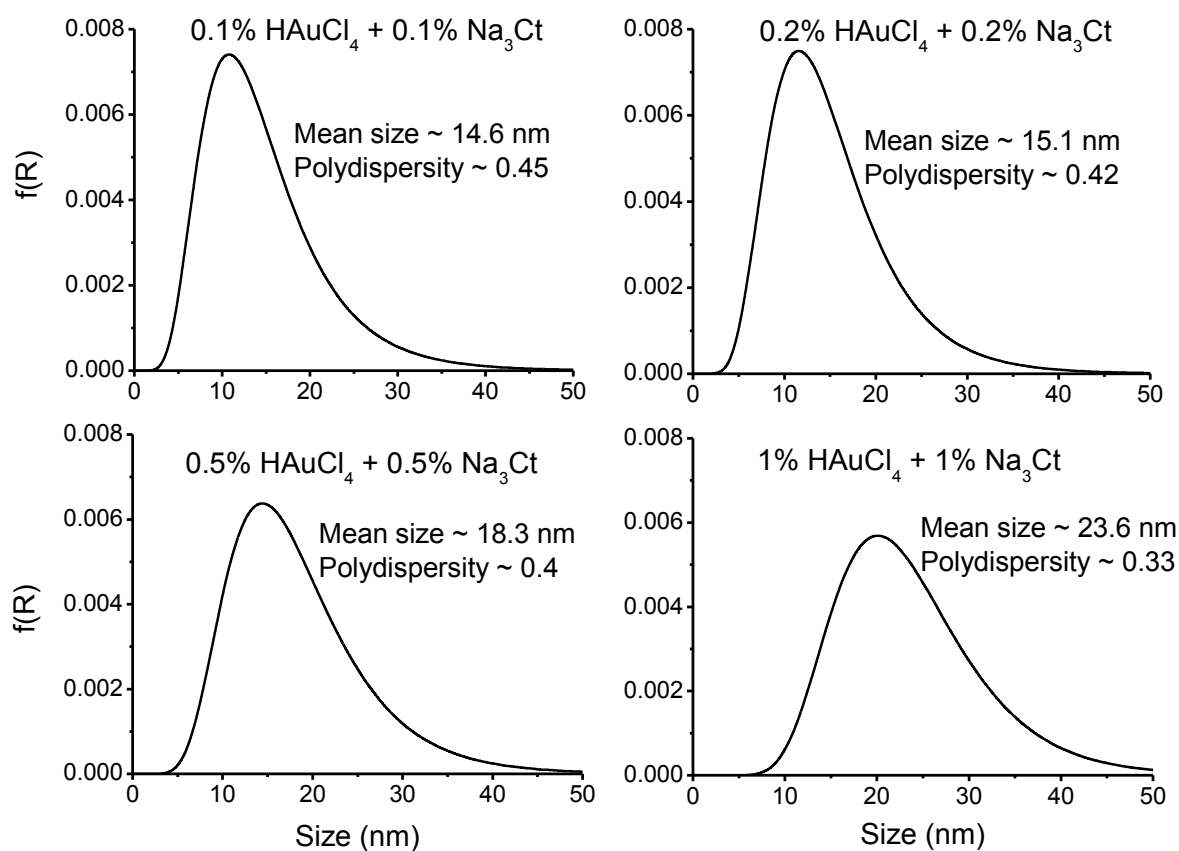


Figure 6.13. The calculated size distributions of gold nanoparticles in 1wt% P85 at varying gold nanoparticle concentration.

SAXS data of nanoparticles with different gold salt concentrations are shown in **Figure 6.14**. Since scattering length is proportional to the atomic number in the case of X-rays, there is very low contrast for hydrogenous systems such as block copolymer whereas higher Z elements such as gold show a strong contrast (Table 6.1). Therefore, SAXS data are mostly from the gold nanoparticles (scattering from block copolymers is negligible). The mean size of the nanoparticles increases and polydispersity decreases with the increase in gold salt concentration as shown in **Table 6.3** and are found to be consistent with that obtained from SANS. The resultant size and size distribution of gold nanoparticles is decided

by their formation mechanism. The high concentration of gold salt in presence of Na_3Ct favours the mechanism which results in high yield and increase in the size of the particle.

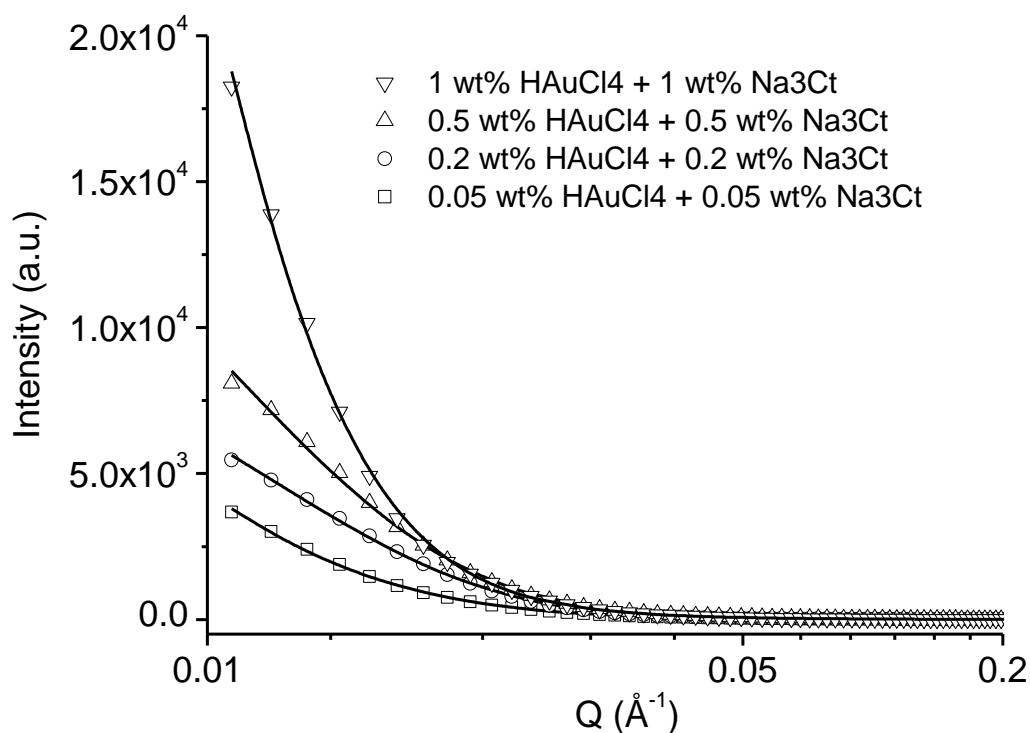


Figure 6.14. SAXS data of 1 wt% P85 with varying ($\text{HAuCl}_4 \cdot 3\text{H}_2\text{O} + \text{Na}_3\text{Ct}$) concentration. The solid curves are theoretical fits to the experimental data.

Table 6.3. Size parameters of gold nanoparticles as obtained by SAXS in 1 wt% P85 with varying ($\text{HAuCl}_4 \cdot 3\text{H}_2\text{O} + \text{Na}_3\text{Ct}$) concentration.

Gold Nanoparticle System	Mean Size (nm)	Polydispersity σ
1% P85 + 0.05% $\text{HAuCl}_4 \cdot 3\text{H}_2\text{O}$ + 0.05% Na_3Ct	12.5	0.52
1% P85 + 0.2% $\text{HAuCl}_4 \cdot 3\text{H}_2\text{O}$ + 0.2% Na_3Ct	14.2	0.47
1% P85 + 0.5% $\text{HAuCl}_4 \cdot 3\text{H}_2\text{O}$ + 0.5% Na_3Ct	18.2	0.41
1% P85 + 1% $\text{HAuCl}_4 \cdot 3\text{H}_2\text{O}$ + 1% Na_3Ct	22.6	0.35

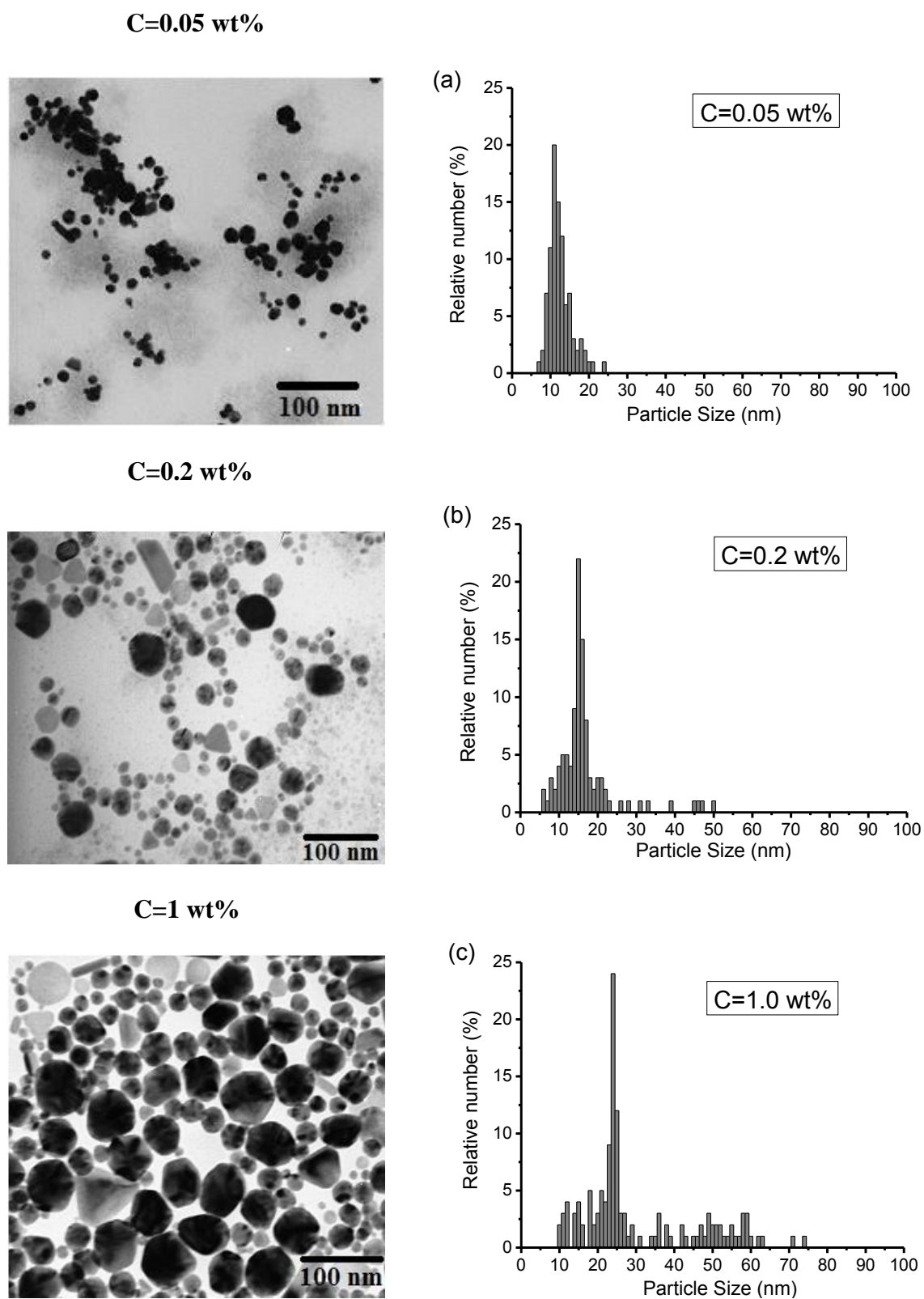


Figure 6.15. TEM micrographs and the calculated size distribution histograms of gold nanoparticles in 1 wt% P85 with varying (H₂AuCl₄·3H₂O + Na₃Ct) concentration.

TEM has been used for the direct visualization of the gold nanoparticles. **Figure 6.15** shows the TEM micrographs of the gold nanoparticles of different salt concentrations. Although there are different shapes of the particles observed, however, most of them are spherical. The gold nanoparticles formed are polydispersed and the mean size increases with the gold salt concentration. The calculated size distributions as obtained from number of TEM micrographs for each gold concentration are also shown in Figure 6.15. These results are found to be similar to that of SANS and SAXS. The fact that there is poor electron contrast for block copolymers, and they are not seen in the micrographs either as micelles or layer on the gold nanoparticles.

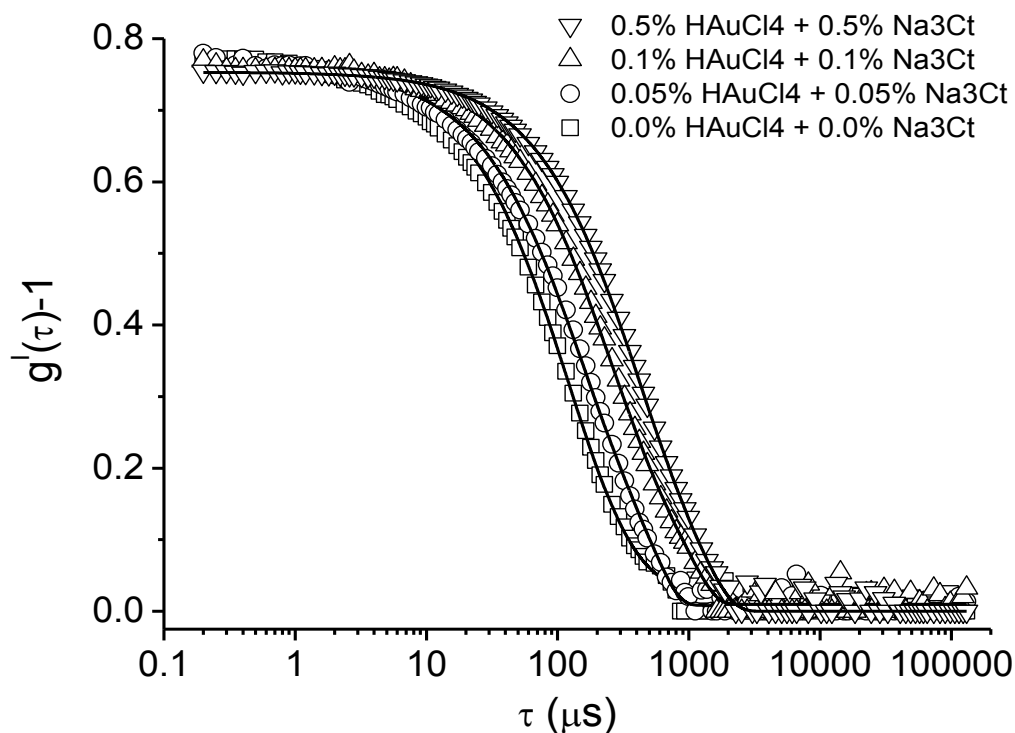


Figure 6.16. DLS data of 1 wt% P85 with varying ($\text{HAuCl}_4 \cdot 3\text{H}_2\text{O} + \text{Na}_3\text{Ct}$) concentration. The solid curves are the theoretical fits to the experimental data.

Table 6.4. Fitted parameters for the system of block copolymer P85 with varying gold salt and Na_3Ct concentration obtained from DLS data at 30 °C. The diffusion coefficient of micelles ($32.4 \times 10^{-6} \text{ cm}^2/\text{sec}$) is kept constant that obtained for the pure block copolymer solution.

Gold Nanoparticle System	Diffusion Coefficient $D \times 10^{-6} \text{ (cm}^2\text{/sec)}$	Hydrodynamic Size (nm)
1% P85 + 0.05% H _{Au} Cl ₄ .3H ₂ O + 0.05% Na ₃ Ct	18.3	30.4
1% P85 + 0.1% H _{Au} Cl ₄ .3H ₂ O + 0.1% Na ₃ Ct	16.1	34.6
1% P85 + 0.5% H _{Au} Cl ₄ .3H ₂ O + 0.5% Na ₃ Ct	14.6	38.2

DLS has also been used to confirm the coexistence of gold nanoparticles and micelles during the synthesis. The measured intensity autocorrelation functions of gold nanoparticles at different salt concentrations are shown in **Figure 6.16**. It shows that the autocorrelation function broadens with the increase in the gold salt concentration with respect to that from pure block copolymer solution. It has been already found using SANS studies that structure of block copolymer micelle does not change significantly during the synthesis of gold nanoparticles and these changes in the autocorrelation function are believed to be because of the presence of gold nanoparticles. The DLS data have been fitted with two exponentials using the equation of intensity autocorrelation function $g^I(\tau) = 1 + \exp(-2\Gamma\tau)$ where one exponential corresponds to that from pure block copolymer micelles has been kept fixed and second for gold nanoparticles varies with gold salt concentration. The fitted parameters for the system of block copolymer P85 with varying gold salt and Na₃Ct concentration obtained from DLS data are shown in **Table 6.4**. The sizes measured by DLS are comparatively larger than those measured directly. This arises as DLS measures overall size consisting gold nanoparticles covered by block copolymer coating and hydration attached it.

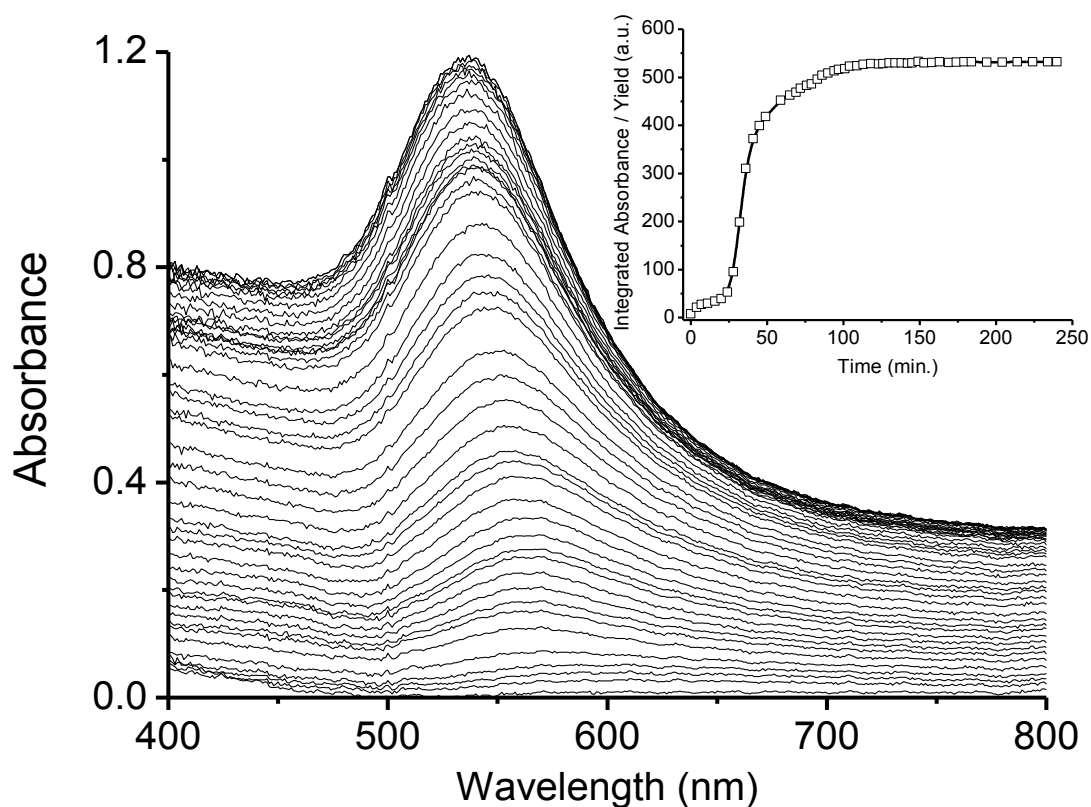


Figure 6.17. Time-dependent UV-visible absorption spectra of 1 wt% P85 with 0.05 wt% $\text{HAuCl}_4 \cdot 3\text{H}_2\text{O}$ + 0.05 wt% Na_3Ct . The different data sets from bottom to top correspond to increase in absorbance with time. Inset gives the variation of the integrated absorbance of SPR peak as a function of time.

Figure 6.17 shows the temporal evolution of UV-visible spectra recorded during the synthesis of gold nanoparticles for 1 wt% P85 with 0.05 wt% $\text{HAuCl}_4 \cdot 3\text{H}_2\text{O}$ and 0.05 wt% Na_3Ct over a wide period of time. The spectra were measured with an interval of 5 minutes up to about 3 hours. The formation of nanoparticles is observed through the building of SPR peak. The peak intensity increases as more and more nanoparticles are synthesized with time and saturates in about an hour. Thus present method provides a quite fast synthesis of gold nanoparticles. The variation of the integrated absorbance (proportional to the nanoparticle concentration) of SPR peak as a function of time is shown in the **inset of Figure 6.17**.

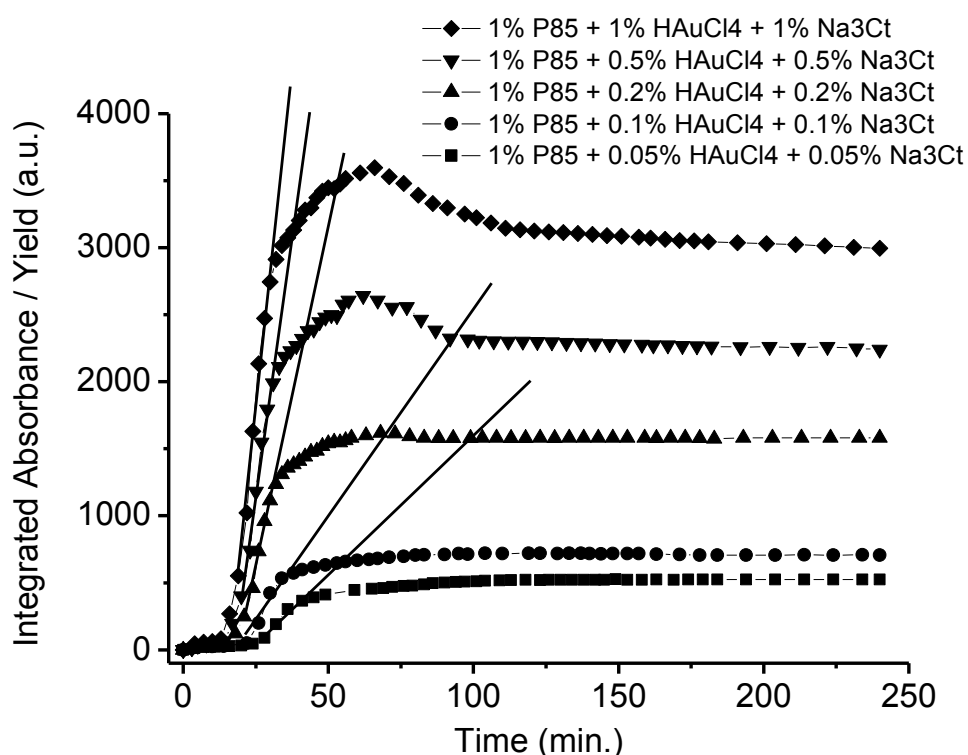


Figure 6.18. The time-dependent variation of the integrated absorbance (400–800 nm) of SPR peak in 1wt% P85 at different nanoparticle concentrations.

Further the time-dependent synthesis is compared for three different gold concentrations (0.05, 0.2 and 1 wt%) in **Figure 6.18**. All these curves can be divided in three distinct regions of synthesis process as (i) formation region, (ii) saturation region and (iii) stability region. The formation region is the initial period where the yield of nanoparticles increases with time. It is observed that higher value of salt concentration results in a faster formation rate. The saturation region follows the formation region after achieving the maximum nanoparticle concentration and is obtained when most of the gold ions undergoing nucleation have been utilized in the formation of nanoparticles. The stability region relates to the stability of gold nanoparticles over time. There is substantial decrease in the stability at higher salt concentrations and this could be because of the increase in the ionic strength of the solution due to large amount of citrate and/or larger size of the nanoparticles formed with increase in the salt concentration.

6.4. Conclusions

The development of two methods of high-yield synthesis of gold nanoparticles, where the yield can be enhanced by manyfold, has been addressed. In the first method based on step addition, the gold salt is added in small steps to maintain the continuous formation of nanoparticles by maintaining the minimum ratio of block copolymer-to-gold salt (r_{min}) for the reduction to take place. The step size is decided by the gold salt concentration little less than that of the r_{min} . The time between two steps is decided by the time required to complete the synthesis in each step. In this method thus the yield can be increased by number of steps used. However, the application of this method is limited by the longer synthesis time which increases as the number of steps increased to increase the yield.

In the second method (additional reductant method), the presence of additional reductant (e.g. trisodium citrate) is utilized to enhance the reduction and hence yield. The nanoparticle yield has been found to increase drastically with gold salt concentration in presence of additional reductant and has been synthesized up to two order higher gold salt concentrations than earlier works. This method can be viewed as the additive effect of the enhanced reduction by trisodium citrate with control and stabilization by the block copolymers. The size of the nanoparticles also increases with the nanoparticle concentration. The time-dependent decrease in the concentration of nanoparticles observed at higher gold salt concentrations is related to the increased surface coating of gold nanoparticles.

Chapter 7

Interaction of Gold Nanoparticle with Proteins

7.1. Introduction

The interfacing of nanoparticle with biomolecules such as protein is useful for applications ranging from nano-biotechnology (molecular diagnostics and biosensors) to medicine (therapeutic and drug delivery) to nano-electronics [1,19]. For example, the recognition properties of proteins are used in sensing and assembly of nanoparticles in to controlled structures. A better understanding of the biological effects requires knowledge of the binding properties of proteins that associate with the nanoparticle. The affinity of protein towards nanoparticles is modulated by surface properties of nanoparticles through its chemical composition, shape and size of the nanoparticles, surface functionalization, charge density etc. The conjugation of proteins with nanoparticles not only introduces biocompatible functionalities into these systems but also leads to the stabilization of the complex. The different interactions involved in nanoparticle-protein conjugate systems are van der Waals forces, electrostatic forces, hydrogen bonding etc. depending on the constituents participating in the system. The interplay of these interactions decides the formation of nanoparticle-protein conjugate structures [216-219].

There are many ways for the formation of nanoparticle-protein conjugates [216-219]. The four main approaches have been utilized so far are: (i) electrostatic adsorption, (ii) conjugation to the ligand on the nanoparticle surface, (ii) conjugation to a small cofactor molecule that the protein can recognize and bind and (iv) direct conjugation to the

nanoparticle surface. The adsorption of various proteins on gold nanoparticles has been examined under different conditions by varying protein concentration, solution temperature, pH, ionic strength etc. It has been found that the amount of protein, the composition of the protein layer, the conformational changes or rearrangement of the proteins on the particle surface vary depending on the conditions used. The nanoparticle size also strongly influences the amount of adsorbed protein and their conformational modifications. Recently, the concept of protein corona, a dynamic layer of proteins that covers the surface of nanoparticles when they come into contact with biological fluids, has been introduced. The composition of this layer depends on the affinity of the different proteins for a given nanoparticle surface. A number of techniques have been used to determine the protein-nanoparticle interactions and resultant conjugate structures [216-219].

In this chapter, we have examined the interaction of our synthesized gold nanoparticles with proteins. For this purpose, we have first optimized the synthesis to minimize any direct interaction of proteins with the block copolymer, where a stable high yield synthesis with additional reductant can be achieved for very low block copolymer concentration [220]. The interaction of these gold nanoparticles is investigated with two model proteins [lysozyme and bovine serum albumin (BSA)] at physiological conditions [221]. Lysozyme is relatively a small protein with a molecular weight of 14.4 kDa containing 129 amino acids and 4 disulfide bridges. It has an isoelectric point at pH 11. BSA has a molecular weight of 66.4 kDa and consists of 583 amino acids in a single polypeptide chain. This protein contains 17 disulfide bridges and its isoelectric point is at pH 4.7. The interaction of gold nanoparticle with proteins has been studied by UV-visible spectroscopy, zeta potential and SANS.

7.2. Experimental Procedure

7.2.1. Materials

Pluronic block copolymer P85 was obtained from BASF Corp., Mount Olive, New Jersey. The gold salt of hydrogen tetrachloroaurate(III) hydrate ($\text{HAuCl}_4 \cdot 3\text{H}_2\text{O}$), additional reductant trisodium citrate dihydrate ($\text{Na}_3\text{C}_6\text{H}_5\text{O}_7 \cdot 2\text{H}_2\text{O}$) and lysozyme and bovine serum albumin (BSA) were purchased from Sigma-Aldrich, Alfa Aesar and SAF, respectively. The nanoparticles were synthesized in H_2O (Millipore) or D_2O (99.9 atom %D) as per the requirement of measuring techniques.

7.2.2. Synthesis of Gold Nanoparticles and their Interaction with Proteins

The synthesis involves the reduction of the gold salt in the presence of block copolymer in aqueous solution. Synthesis of high-yield gold nanoparticles (up to 0.2 wt% gold salt) was carried out by the addition of optimized trisodium citrate (Na_3Ct). The minimization of the use of block copolymer on high-yield synthesis was studied by systematically decreasing the block copolymer concentration by several orders of magnitude (i.e. 0.001 from 1 wt%). All the syntheses were carried out by mixing the concentrated stock solutions of the components in the sequence of block copolymer followed by Na_3Ct and gold salt, respectively at room temperature without any disturbances. The interaction of these gold nanoparticles was examined with varying concentration 1 to 5 wt% of proteins (lysozyme and BSA) at pH 7 and room temperature (30 °C).

7.2.3. Characterization of Gold Nanoparticles and Nanoparticle-Protein Conjugates

The formation of gold nanoparticles and their interaction with proteins are confirmed using UV-visible spectroscopy [19]. UV-visible measurements were carried out using 6505 Jenway

UV-visible spectrophotometer. The instrument was operated in spectrum mode with a wavelength interval 1 nm and sample holder was quartz cell of path length 1 cm.

SANS has been used to examine the structures of gold nanoparticle-protein conjugates upon their interaction. SANS measurements were carried out at SANS-I facility, Swiss Spallation Neutron Source SINQ, Paul Scherrer Institut, Switzerland [189]. The wavelength of neutron beam used was 6 Å. The experiments were performed at sample-to-detector distances of 2 and 6 m to cover a Q -range of 0.007 to 0.32 Å⁻¹. The sample solutions were kept in 2 mm thick quartz cells with Teflon stoppers. The scattered neutrons were detected using two-dimensional 96 × 96 cm² detector.

TEM measurements have been carried out to see the structure of gold nanoparticles during optimization of block copolymer concentration [169]. TEM has been carried out in a JEOL JEM-2100 high resolution transmission electron microscope. All HRTEM microphotographs were taken at acceleration voltage 160 kV.

Zeta potentials of gold nanoparticles and their conjugates with proteins have been determined for examining their stability. Zeta potentials have been measured with a Nanosizer Z (Malvern Instruments, Malvern, UK) by phase analysis light scattering. The light source was He-Ne laser (633 nm) operating at 4 mW. The zeta potential (ζ) values are calculated from the electrophoretic mobility data using Smoluchowski approximation [222]. The experiment was carried out using a quartz cuvette (universal 'dip' cell) with 10 mm light pathway.

7.3. Results and Discussion

To examine the interaction of protein on gold nanoparticles requires the optimization of high yield synthesis of nanoparticles with minimum use of block copolymers [220,221]. The interaction of protein with nanoparticles has been studied by UV-visible spectroscopy and

zeta potential. Further, the resultant structures of nanoparticle-protein complexes are characterized by SANS.

7.3.1. Optimization of Synthesis

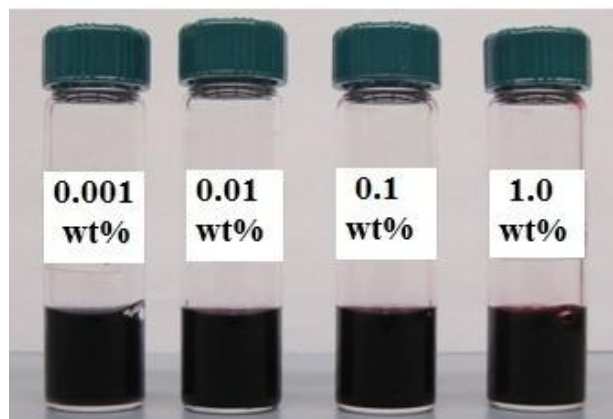


Figure 7.1. Photograph of stable gold nanoparticles at different P85 concentration for 0.2 wt% gold salt and in presence of 0.2 wt% Na₃Ct.

In the absence of additional reductant, the concentration of block copolymer is important to decide the yield. For example, the observance of maximum yield was changed from 0.008 to 0.016 wt% gold salt when the block copolymer concentration increased from 1 to 2 wt%. The concentration effect at such values is known to be mostly controlling the reduction and hence higher concentration of block copolymer is required to achieve higher yield. In the case of additional reductant method for higher yield, it becomes important to know the dependence on block copolymer concentration when the reduction can be controlled by the additional reductant. **Figure 7.1** shows the photograph of the gold nanoparticles synthesized with varying P85 concentration (0.001 to 1 wt%) for 0.2 wt% gold salt with Na₃Ct. All the samples were found to be similar and equally stable. The similar SPR peak observed in UV-visible absorption spectra of the corresponding samples in **Figure 7.2** clearly shows that these systems have the same yield and gold nanoparticle structures irrespective of the different block copolymer concentrations. On the other hand, the gold nanoparticle synthesis is almost fully diminished in the absence of block copolymer, suggesting that the presence of some

small amount of block copolymer must be required to enhance the synthesis. In this synthesis, the role of P85 where Na_3Ct dominates the reduction is mostly in enhancing nucleation and growth of the gold nanoparticles. The block copolymers are expected to exist on the surface of the nanoparticles providing them stability.

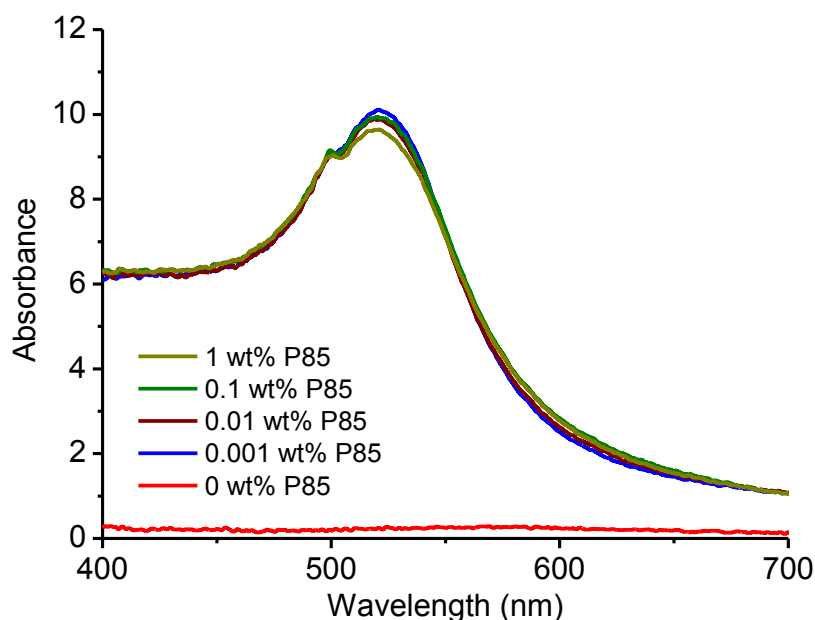


Figure 7.2. SPR peak in UV-visible absorption spectra of varying P85 concentration for 0.2 wt% $\text{HAuCl}_4 \cdot 3\text{H}_2\text{O}$ with 0.2 wt% Na_3Ct .

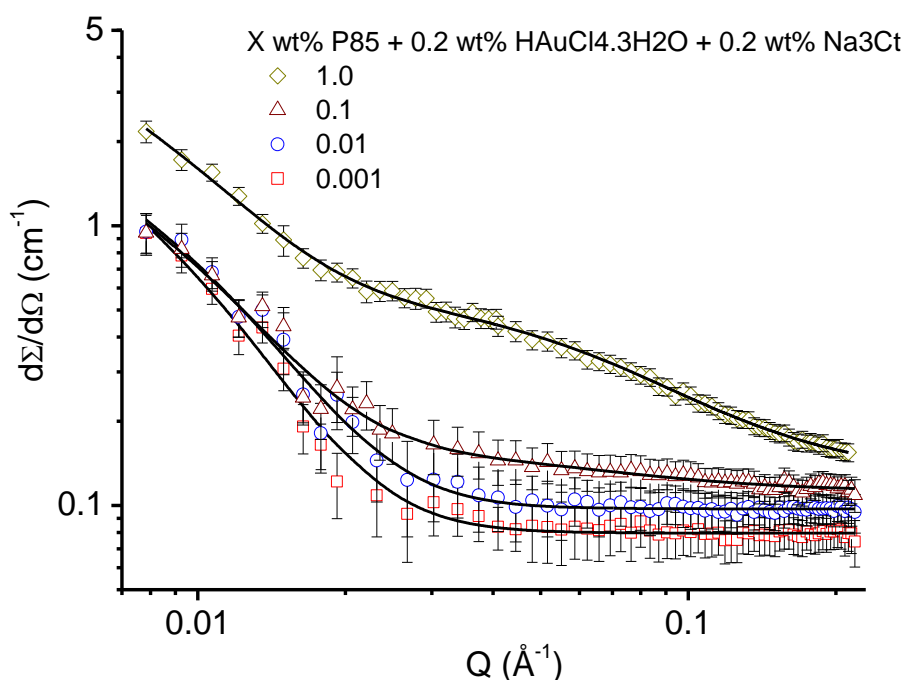


Figure 7.3. SANS data of varying P85 concentration for 0.2 wt% $\text{HAuCl}_4 \cdot 3\text{H}_2\text{O}$ with 0.2 wt% Na_3Ct in D_2O at 15 °C. The solid curves are the theoretical fits to the experimental data.

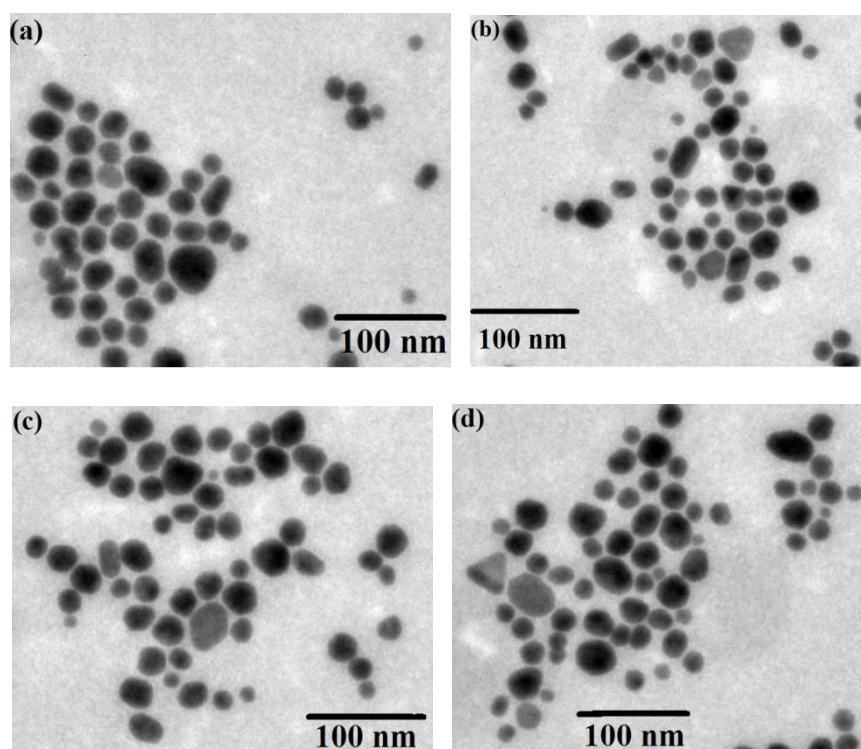


Figure 7.4. TEM micrographs of gold nanoparticles for 0.2 wt% $\text{HAuCl}_4 \cdot 3\text{H}_2\text{O}$ with 0.2 wt% Na_3Ct as prepared with varying P85 concentration (a) 0.001, (b) 0.01, (c) 0.1 and (d) 1 wt%.

The structure of nanoparticles has been characterized using SANS and TEM. **Figure 7.3** shows the SANS data of gold nanoparticles synthesized from 0.2 wt% $\text{HAuCl}_4 \cdot 3\text{H}_2\text{O}$ with 0.2 wt% Na_3Ct for the varying concentration of block copolymer (0.001 to 1 wt%) at 15 °C. The measurements were carried out at a low temperature (15 °C), much less than the critical micelle temperature (CMT of 1 wt% P85 is about 29 °C) of the block copolymer P85, to avoid the scattering from the block copolymer micelles [198]. At temperature below CMT, block copolymers remain dissolved as unimers and their lower effective volume compared to when they form micelles gives rise to low scattering. All the data in Figure 7.3 have been found to have two contributions, from gold nanoparticle dominating in the lower- Q region and from block copolymer unimers at higher- Q values. The block copolymer contribution behaves as expected, to decrease with the decrease in its concentration. The data have been fitted considering gold nanoparticles as polydispersed spheres whereas the individual block copolymer by Gaussian chain. The value of radius of gyration of block copolymer is found to

be 2.3 nm and matches with that reported in literature [209,213]. The particle structure is found identical irrespective of the block copolymer concentration, having sizes about 20 ± 2 nm with a polydispersity of 0.4. Similar results of gold nanoparticles are also obtained by TEM as shown in **Figure 7.4**. The block copolymers are not seen in the TEM micrographs because of their poor electron contrast compared to that for the gold nanoparticles.

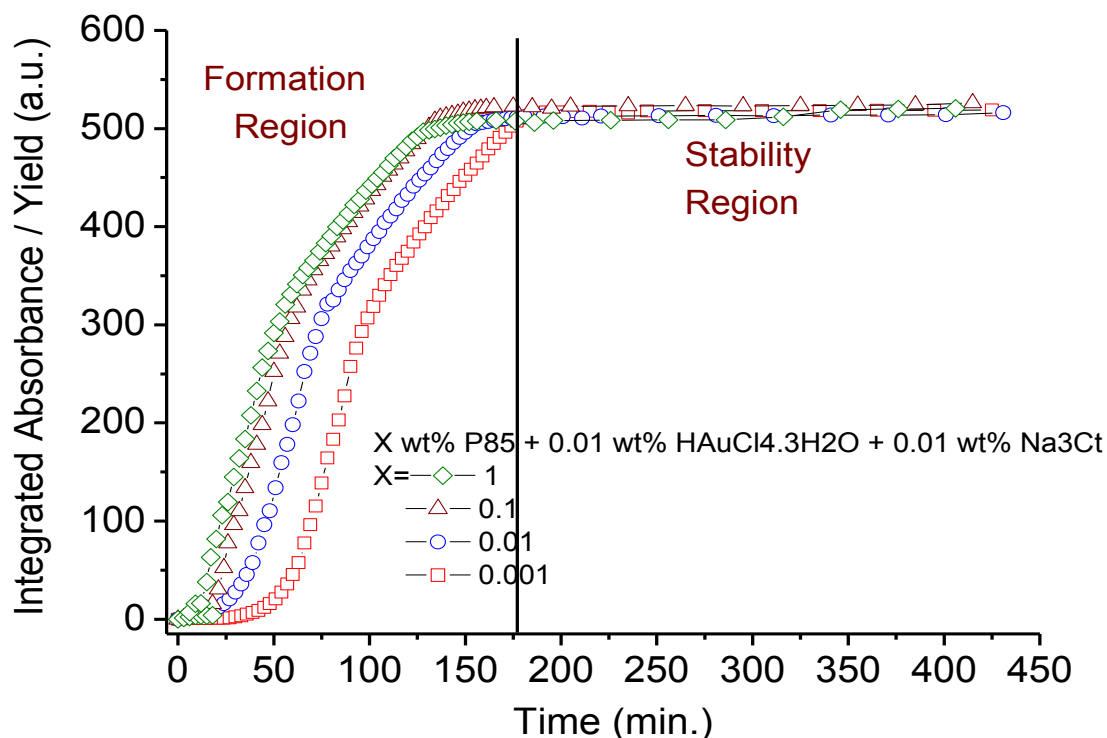


Figure 7.5. Integrated absorbance of SPR peaks as a function of time for varying P85 concentration with 0.01 wt% $\text{HAuCl}_4 \cdot 3\text{H}_2\text{O}$ and 0.01 wt% Na_3Ct .

Figure 7.5 shows the variation of the integrated absorbance of SPR peak for different concentrations (0.001 to 1 wt%) of block copolymer while keeping the concentration of other components same. These curves can be divided in two distinct regions as (i) formation region and (ii) saturation region. The formation region is the initial period ($\sim 2\text{--}3$ hrs) where the yield of nanoparticles increases with time. The faster formation rate is found with higher value of block copolymer concentration. The saturation region is obtained when most of the gold ions undergoing nucleation have been utilized in the nanoparticle formation. It is

interesting to note that stability and yield of nanoparticle remain same irrespective of the large decrease in block copolymer concentration.

7.3.2. Gold Nanoparticle Interaction with Lysozyme and BSA Proteins

Based on the optimization of different components, stable and high-yield gold nanoparticles have been synthesized even at very low block copolymer concentration [220]. This requires additional reductant (Na_3Ct) used in the amount approximately equal to that of gold salt to enhance the reduction of gold ions. The nucleation and growth of reduced gold ions to nanoparticles is improved in the presence of block copolymer. The additional reductant is also believed to help in stabilizing the gold nanoparticles to reduce the requirement of high block copolymer concentration. Therefore, an additional reductant block copolymer-mediated synthesis provides an ideal method for synthesizing stable and high-yield gold nanoparticles. This kind of systems can be directly used for the applications such as drug delivery where the interaction of drug with the nanoparticles is prominent. The present synthesis with low block copolymer concentration helps to minimize any direct interaction of drug with the block copolymer. The interaction of high-yield gold nanoparticles with two model proteins [lysozyme and bovine serum albumin (BSA)] has been studied [221].

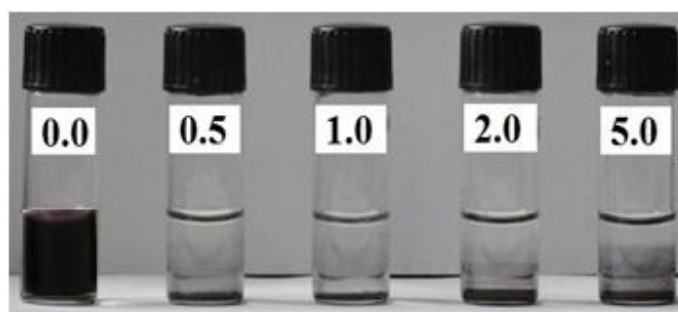


Figure 7.6. Photograph of solutions of lysozyme protein with gold nanoparticles. The gold nanoparticles are prepared from 0.01 wt% P85 for 0.2 wt% $\text{HAuCl}_4 \cdot 3\text{H}_2\text{O}$ with 0.2 wt% Na_3Ct whereas lysozyme concentration is varied. The labels show the lysozyme concentrations in wt%.

The interaction of gold nanoparticles with lysozyme and BSA proteins has been found to be very different. It is observed that gold nanoparticle-lysozyme complex phase separate immediately when the two components are mixed. **Figure 7.6** shows the systems of gold nanoparticles (prepared from 0.01 wt% P85 for 0.2 wt% $\text{HAuCl}_4 \cdot 3\text{H}_2\text{O}$ with 0.2 wt% Na_3Ct) with lysozyme for the concentrations 1 to 5 wt%. On the other hand, gold nanoparticle-BSA complex form a stable systems over the wide range of BSA concentration. **Figure 7.7** shows the stable systems of gold nanoparticles with BSA for the concentrations 1 to 5 wt%. These results can be explained on the basis of that citrate ions are adsorbed on the gold nanoparticles make their surface negative, as a result their complex with positively charged lysozyme phase separates whereas it remains stable with similarly charged BSA (pH 7). In the case of oppositely charged nanoparticle and protein (lysozyme) the charge neutralization in the conjugate leads to the aggregation in the system. However, the site-specific adsorption of similarly charged protein (BSA) increases the overall charge in the conjugate and hence enhancing their stability. The interaction of gold nanoparticles with BSA has been examined using UV-visible spectroscopy and zeta potential.

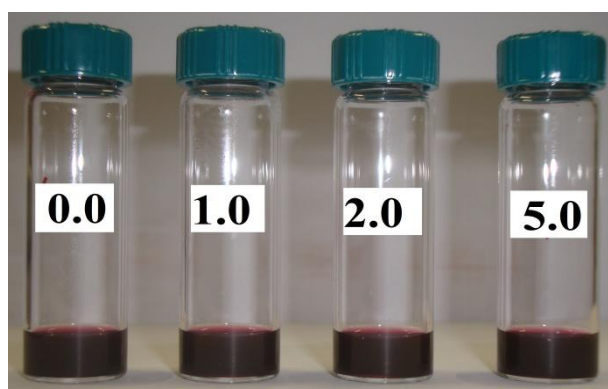


Figure 7.7. Photograph of solutions of BSA protein with gold nanoparticles. The gold nanoparticles are prepared from 0.01 wt% P85 for 0.2 wt% $\text{HAuCl}_4 \cdot 3\text{H}_2\text{O}$ with 0.2 wt% Na_3Ct whereas BSA concentration is varied. The labels show the BSA concentrations in wt%.

The zeta potential measurement of gold nanoparticles in presence of varying BSA protein concentration is shown in **Figure 7.8**. For charge stabilized particles, the zeta potential is a measure of the particle stability. Typically, nanoparticles with zeta potentials greater than 25 mV or less than -25 mV have sufficient electrostatic repulsion to remain stable in solution. Gold nanoparticles prepared in aqueous solutions have a zeta potential of -39 mV and therefore are highly stable. On the other hand, it has been observed that if the gold nanoparticles prepared in aqueous solution are diluted by the buffer solution of pH 7, the gold nanoparticles become unstable. In the buffer solution the residue citrate ions continue to react with the protons in solution to form citrics, leaving gold to tend to aggregate [223]. The increase in zeta potential i.e. stability of the gold nanoparticles in the presence of BSA support to the conjugation of protein with nanoparticles.

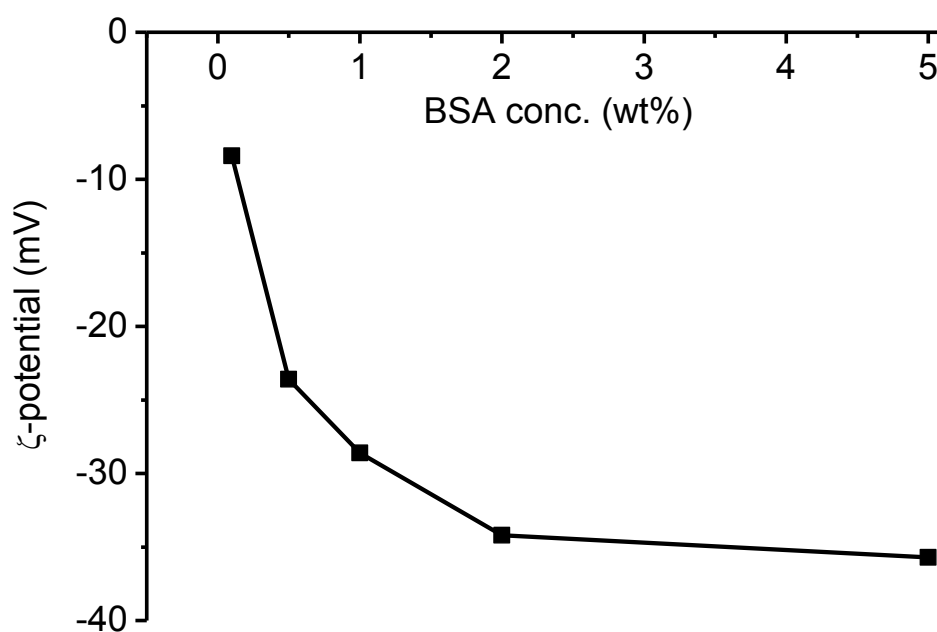


Figure 7.8. Zeta potential of gold nanoparticle-protein conjugates with varying BSA concentration.

Figure 7.9 shows the SPR peak in UV-visible spectra of gold nanoparticles without and with BSA. A strong SPR of the gold nanoparticles is observed whereas the presence of BSA shows a red shift in the SPR peak from 532 to 536 nm. The resonance wavelength and

bandwidth of gold nanoparticles depend on the particle size and shape, the refractive index of the surrounding medium, and the temperature. This shift is attributed to the changes in the dielectric nature surrounding the nanoparticles without and with protein conjugation [168,223].

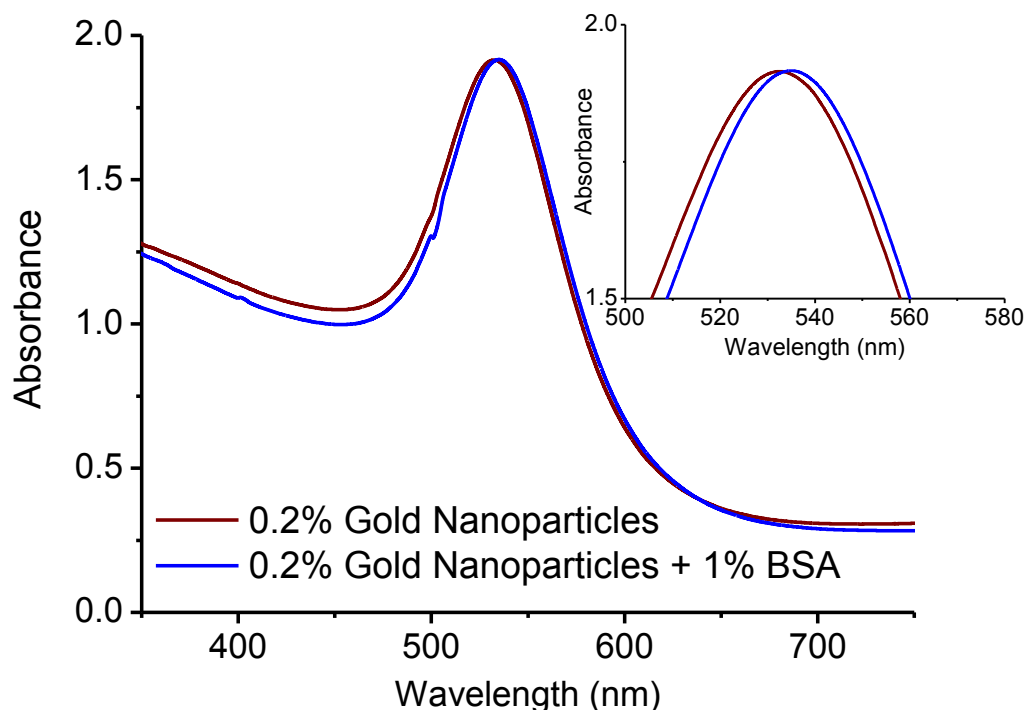


Figure 7.9. UV-Visible spectra of gold nanoparticles without and with BSA.

7.3.3. Structure of Gold Nanoparticle-Protein Conjugates

SANS data from gold nanoparticles using 0.01 wt% P85 + 0.2 wt% $\text{HAuCl}_4 \cdot 3\text{H}_2\text{O}$ + 0.2 wt% Na_3Ct system, 1 wt% BSA protein and their nanoparticle-protein conjugates all prepared in D_2O are shown in **Figure 7.10**. These systems individually (gold nanoparticles, BSA and gold nanoparticle-BSA conjugate) show very different SANS data. It is also seen that SANS data of addition of contributions from gold nanoparticles and BSA is significantly different than that of the measured data of nanoparticle-protein conjugates. The build up of scattering intensity in the low- Q region for the nanoparticle-protein conjugate confirms the interaction

of two components in the system. The changes in the scattering data are expected arising due to the formation of core-shell structure of adsorbed proteins on gold nanoparticle [180,181].

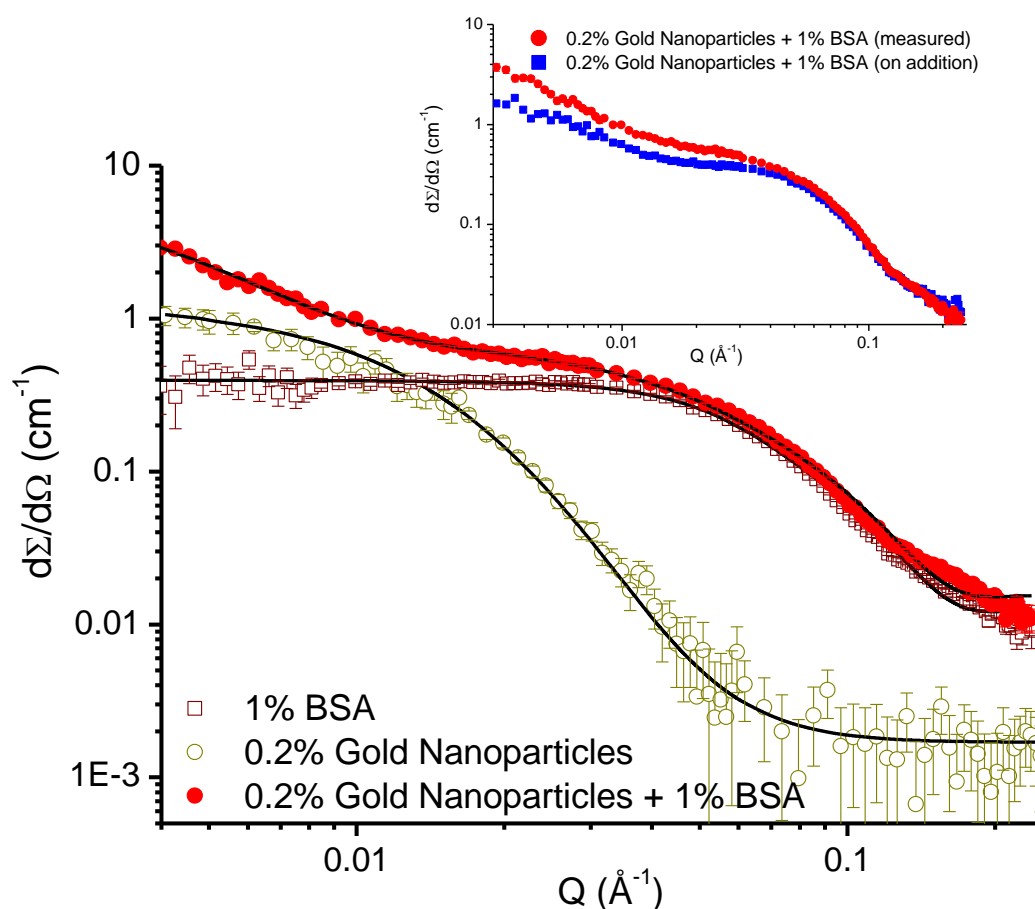


Figure 7.10. SANS data of gold nanoparticles, BSA and their conjugates. The gold nanoparticles in these studies are prepared using 0.01 wt% P85 + 0.2 wt% $\text{HAuCl}_4 \cdot 3\text{H}_2\text{O}$ + 0.2 wt% Na_3Ct system. The pH for BSA is kept at 7.

The SANS data of gold nanoparticles are fitted using polydispersed spheres. BSA protein macromolecules are fitted with the prolate ellipsoidal shape as is known in the literature. The adsorption of protein on the gold nanoparticles is fitted using the spherical core-shell structure consisting of adsorbed protein forming a shell around the gold nanoparticle. The fitted values of mean size and polydispersity of gold nanoparticles are 20.2 nm and 0.4, respectively. The dimensions of BSA proteins semi-major axis (a) and semi-minor axis ($b = c$) are found to be 7.0 and 2.2 nm, respectively. In the case of nanoparticle-protein conjugate system, proteins are adsorbed over a thickness (4.5 nm) which is about that

of the value of minor axis of the protein, suggesting adsorption of protein through the contact of major axis at the nanoparticle surface. The number of protein molecules adsorbed per nanoparticle in nanoparticle-protein complex is calculated to be 28. This number has been derived from the scattering measured on absolute scale as sum of the scattering from nanoparticle-BSA conjugates (core-shell structure) and remaining non-adsorbed BSA in the complex. It is also found that fraction of protein attached to nanoparticles is quite low about 0.05 wt%.

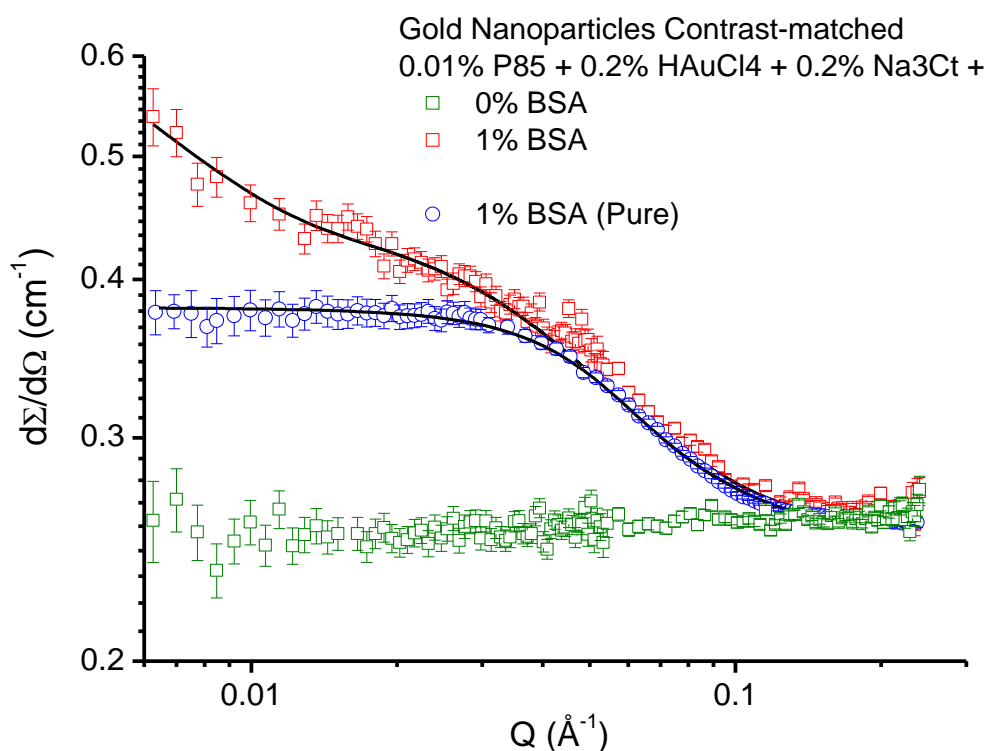


Figure 7.11. SANS data of gold nanoparticles, BSA and their conjugates in the gold nanoparticle contrast-matched solvent. The gold nanoparticles in these studies are prepared using 0.01 wt% P85 + 0.2 wt% HAuCl₄.3H₂O + 0.2 wt% Na₃Ct system. The pH for BSA is kept at 7.

We have further carried out contrast variation SANS studies to confirm the protein adsorption on the nanoparticle. The gold nanoparticles are contrast matched with the mixed solvent of H₂O and D₂O having 25% of H₂O. In this case only the scattering from protein is observed. SANS data from gold, nanoparticle, BSA protein and their conjugate under gold

nanoparticle-contrast matched condition are shown in **Figure 7.11**. The SANS data of gold nanoparticles show a flat pattern corresponding to incoherent background for the solvent. There is significant difference observed between the data of nanoparticle-protein conjugate and protein particularly in the low- Q region. This suggests that some of the protein is part of the large structure (i.e. adsorbed shell around the nanoparticle) in the case of nanoparticle-protein system. The data fitting is found to be consistent with that in Figure 7.10. The thickness of adsorbed protein shell is obtained about 4.5 nm. The calculated number of adsorbed protein macromolecules per nanoparticle is 28 with about only 0.05 wt% protein adsorbed on the nanoparticles.

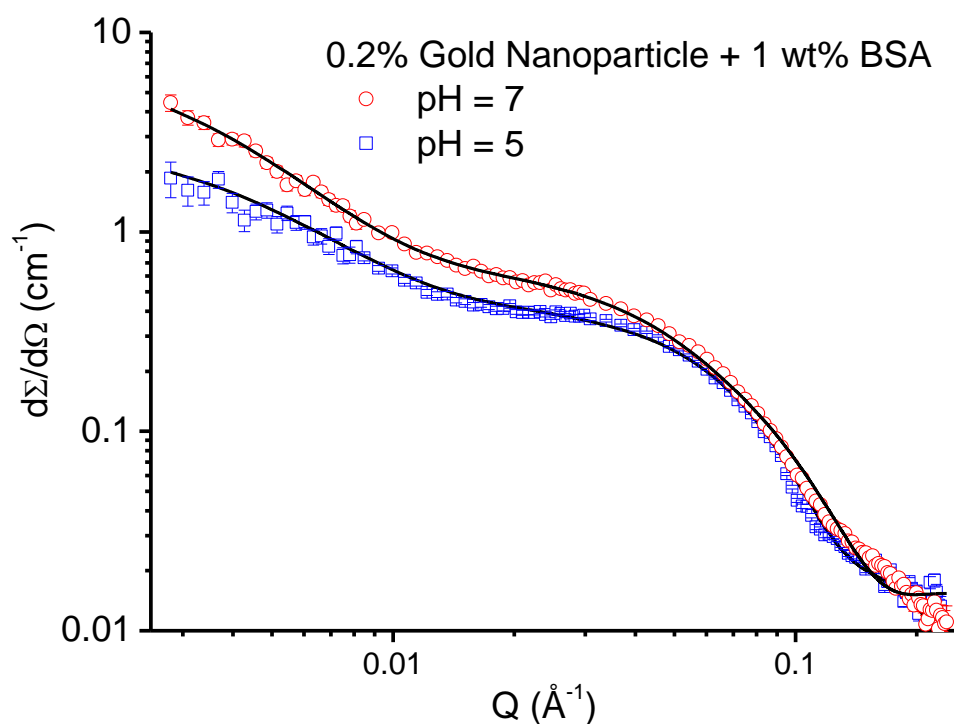


Figure 7.12. SANS data of BSA-gold nanoparticle conjugates of gold nanoparticles (0.01 wt% P85 + 0.2 wt% $\text{HAuCl}_4 \cdot 3\text{H}_2\text{O}$ + 0.2 wt% Na_3Ct) with 1 wt% BSA for two different pH values.

The mechanism of adsorption of similarly charged BSA on nanoparticles is based on the charge specificity of protein molecules. As a result, even though the net charge of the BSA protein molecule is negative it has positively charged surface patches which get

attached to the negatively charged nanoparticle surface. At pH = 7 the BSA has net negative charge whereas the gold nanoparticles also carry negative charge because of the presence of some of the citrate ions at nanoparticle surface. **Figure 7.12** shows the effect of varying pH on the interaction of protein with nanoparticle. It is seen that when the pH is decreased to 5 near to the isoelectric point (4.9), the data of the nanoparticle-protein conjugate are significantly different from that at pH = 7. The scattering in the low- Q region is decreased for pH = 5 as compared to pH = 7. This indicates to the suppression of adsorbed protein for pH = 5 where the protein macromolecules are neutral. In fact, the data of individual components of nanoparticle and protein add to that the scattering of the nanoparticle-protein conjugate system. Most of the nanoparticles and protein macromolecules dispersed without any interaction at pH = 5.

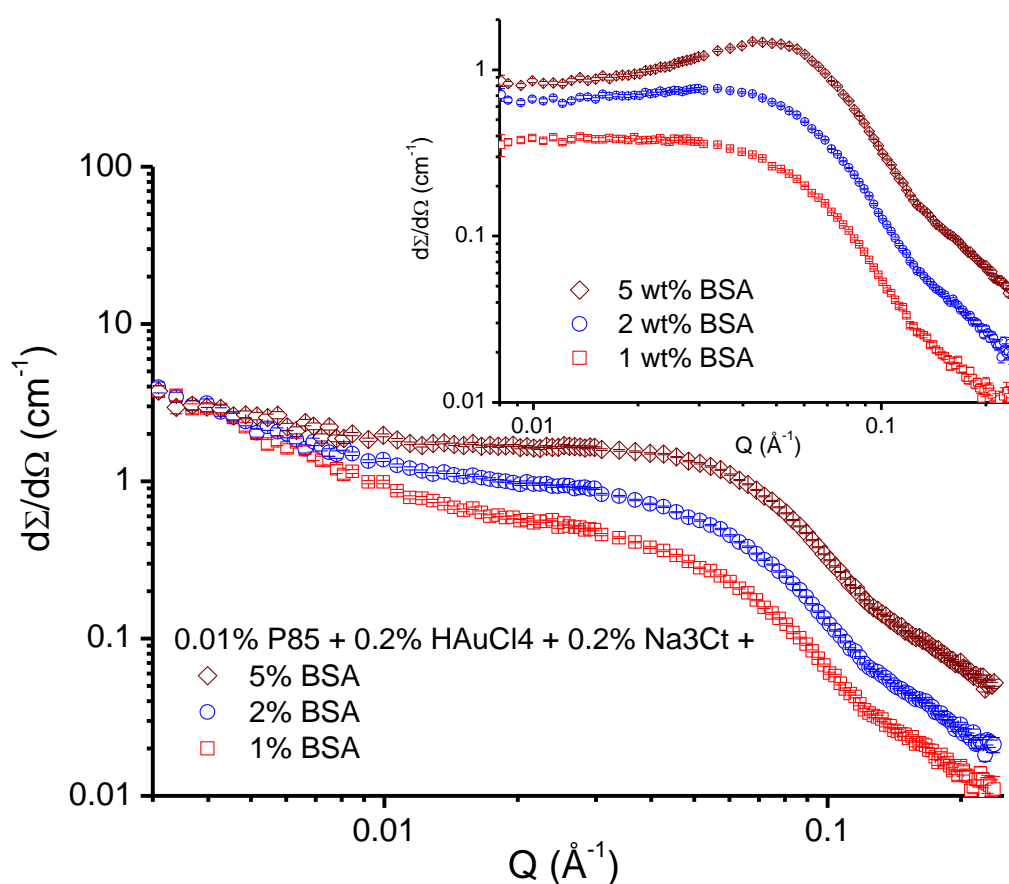


Figure 7.13. SANS data of gold nanoparticles (0.01 wt% P85 + 0.2 wt% HAuCl₄.3H₂O + 0.2 wt% Na₃Ct) with varying concentration of BSA. Inset shows the SANS data of corresponding pure BSA system. The pH in all the samples was 7.

Figure 7.13 shows SANS data of gold nanoparticles (0.01 wt% P85 + 0.2 wt% $\text{HAuCl}_4 \cdot 3\text{H}_2\text{O}$ + 0.2 wt% Na_3Ct) with varying concentration of BSA protein. All these nanoparticle-protein conjugate systems are found to be stable. SANS data of the conjugates show the almost similar scattering patterns in the low- Q region and difference are observed at the larger Q values. The SANS data from corresponding pure protein solutions are given in the inset of Figure 7.13. The data at higher protein concentrations show correlation peak of structure factor an indication of interacting protein in the solution. The data of nanoparticle-protein conjugate suggest that the adsorbed protein on the nanoparticles surface does not vary much with the increase in the protein concentration. The build-up of scattering in the higher Q region with increase in protein concentration is as a result of increase in the free protein (not adsorbed on the nanoparticle) concentration.

7.4. Conclusions

The optimization of high yield synthesis of gold nanoparticle for probing their interaction with proteins has been examined. The stable and high-yield gold nanoparticles have been synthesized at very low block copolymer concentration (decrease of 3 orders) to minimize any direct interaction of proteins with the block copolymer. The faster formation rate of gold nanoparticles is found with higher value of block copolymer concentration in these systems. The stability and yield of nanoparticle remain same irrespective of the large decrease in block copolymer concentration. The nanoparticle structure is also found identical irrespective of block copolymer concentration. The interaction of these gold nanoparticles with two model proteins [lysozyme and bovine serum albumin (BSA)] has been examined. It has been found that gold nanoparticles form stable solutions over a wide concentration range of BSA whereas phase separate even with small amount of lysozyme protein at physiological conditions. These results can be explained on the basis of that citrate ions are adsorbed on the gold nanoparticles make it negative, as a result their complex with positively charged lysozyme phase separates whereas it remains stable with similarly charged BSA. The

complexes of gold nanoparticles with BSA have been studied using UV-visible spectroscopy, zeta potential and SANS. The red shift in the SPR peak and the build-up of scattering intensity in the low- Q region of SANS data confirms the adsorption of protein on nanoparticles. The increase in zeta potential of the gold nanoparticles in the presence of BSA also support to the conjugation of protein with nanoparticles. The adsorption of protein on the gold nanoparticles has been modeled in SANS by a core-shell structure consisting of adsorbed protein forming a shell around the gold nanoparticle.

Chapter 8

Summary

The gold nanoparticle synthesis using PEO-PPO-PEO block copolymers has been recently developed, which is single-step and fast as well as environmentally benign and economical [94-98]. The present thesis has looked into the understanding of tuning of different components and role of solution conditions for improvement of this block copolymer-mediated synthesis of gold nanoparticles [191-196]. A multi-technique approach combining UV-visible spectroscopy, TEM, DLS, SAXS and SANS techniques has been used for the characterization of gold nanoparticles for obtaining complementary information for detailed studies of these systems [213-215]. The role of chemical structure of block copolymer, solution conditions such as concentration and temperature, and additional reductant on the synthesis has been established [192,202-205]. This thesis has led to the stable high yield synthesis of gold nanoparticles, where the yield can be enhanced by manyfold [206-208]. Also the nanoparticle synthesis has been optimized for applications such as their interaction with proteins [220,221].

This thesis consists of eight chapters including this chapter on summary of thesis. The general background of gold nanoparticles covering synthesis, their characterization and various applications are discussed in Chapter 1. Chapter 2 provides introduction to block copolymers and its application in the synthesis of gold nanoparticles as used in the present thesis. A multi-technique approach combining different useful techniques has been applied for the characterization of gold nanoparticles, which are described in Chapter 3. The results of the studies on different aspects of block copolymer-mediated synthesis of gold nanoparticles are discussed in Chapters 4 to 7.

Chapter 1 introduces different methods to synthesize gold nanoparticles, their characterization and various applications [1,19]. All the different methods of synthesis of gold nanoparticles can be broadly classified in two categories as top-down and bottom-up methods. These two types of synthesis methods have been elaborated with their pros and cons. In particular the advantages of chemical reduction method, which is one of the mostly commonly used bottom-up methods and also used in the present thesis, have been discussed. The variety of techniques comprising spectroscopic techniques (Absorption and transmission spectroscopy, photoluminescence, infrared spectroscopy, Raman spectroscopy, electron spectroscopy, ionic spectrometry), microscopic techniques (Scanning electron microscopy, transmission electron microscopy, scanning probe microscopy, scanning tunneling microscopy, atomic force microscopy) and scattering techniques (X-ray diffraction, small angle X-ray scattering) used for the characterization of nanoparticles have been described. Gold nanoparticles are extensively used in the various fields and their application in particular in the field of biology, nanoelectronics and catalysis has been discussed.

In Chapter 2, the background of block copolymer-mediated synthesis of gold nanoparticles has been presented [111,113]. PEO-PPO-PEO triblock copolymers are well-known amphiphilic molecules with hydrophilic PEO block and hydrophobic PPO block within the same molecule. The block copolymer structure and classification have been discussed in detail. The significance of self-assembly of amphiphilic block copolymers and their applications have also been emphasized. The block copolymers have been found to produce metal nanoparticles due to their ability to reduce metal ions. On mixing the aqueous solution of metal (e.g. gold) salt and block copolymers, these polymeric nanostructured matrixes engulf the ionic metal precursors, which after subsequent reduction form nanoparticles. The synthesis mechanism and the role of block copolymer in tuning the synthesis have been discussed.

A combination of spectroscopy, microscopy and scattering techniques has been used in this thesis for the characterization of gold nanoparticles [2]. The details of these techniques and the kind of information that can be obtained from them are discussed in Chapter 3. UV-visible spectroscopy measures the absorbance or transmittance of the sample solution to characterize nanoparticles through the characteristic SPR peak. The high contrast of gold nanoparticles for electrons enables TEM to determine directly the shape and size of gold nanoparticles. The different scattering techniques (DLS, SAXS and SANS) probe systems under native conditions and over large sample volumes. In DLS, the measurement of intensity fluctuations enables the determination of diffusion coefficients associated with different structures in the system. X-rays are scattered by the electron density fluctuation, which is proportional to the atomic number, and thus SAXS provides the size distribution of the nanoparticles (low Z components are not seen). However, the possibility to vary contrast in SANS allows it to study role of different components (e.g. gold nanoparticle and block copolymer) in the synthesis. The complementary results as obtained from these techniques have been used for the detailed studies of block copolymer-mediated synthesis of gold nanoparticles (chapters 4 – 7) [213-215].

The main results of this thesis are:

One of the limitations of block copolymer-mediated synthesis has been its quite low yield. The optimization of synthesis of gold nanoparticles for its dependence on block copolymer and gold salt concentration to improve the yield has been studied in Chapter 4 [191-196]. It is observed that the yield of gold nanoparticles simply does not increase with the increase in block copolymer or gold salt concentration. The yield of gold nanoparticles at a given block copolymer concentration shows the maximum at a gold salt concentration, below and above which the yield decreases. This suggests that there is a minimum molar ratio of block copolymer-to-gold salt required for block copolymer to reduce the gold ions and

hence synthesis. At higher gold salt concentrations, the decrease in their molar ratio suppresses the reduction and hence the decrease in the resultant yield. The overall yield increases with the increase in block copolymer concentration but is not found to be proportional to the gold salt concentration and decreases from linearity at higher block copolymer concentrations. SANS and DLS studies show that these systems are mostly dominated by the presence of large number of free block copolymers as unimers and/or micelles not associated with gold nanoparticles. The size distribution of gold nanoparticles has been determined by TEM and the average size in these systems is found to be in the range 10-30 nm. The stability of gold nanoparticles has been examined by time-dependent UV-visible spectroscopy measurements. All these data show three distinct regions as (i) Formation region, (ii) Saturation region and (iii) Stability region. In the formation region, the yield of nanoparticles increases linearly with time. Higher the values of block copolymer concentration and gold salt concentration, higher will be its tendency to nucleate and grow the nanoparticles. The saturation region is obtained when most of gold ions have been utilized in the formation of nanoparticles. The substantial decrease in the stability for higher block copolymer concentration arises because of large size of the nanoparticles formed in these systems.

Chapter 5 presents results on correlation of self-assembly of block copolymers to the gold nanoparticle synthesis [202-205]. The synthesis has been carried out using three different block copolymers P85, F88 and P105, which vary in molecular weight as well as differ in their hydrophobicity-to-hydrophilicity ratio. The yield of gold nanoparticles for these block copolymers has been found increasing as $F88 < P85 < P105$ in the order governed by their increasing tendency of self-assembly. The formation rate is also found faster for the system having higher yield. P105 block copolymer forms the nanoparticles with the largest sizes whereas the size of the nanoparticles decreases for P85 and F88. Block copolymer

self-assembly for P85 and P105 leads to a sphere-to-rod micellar shape transition at higher temperatures and its effect on the gold nanoparticle synthesis has been examined. It is found that irrespective of the shape of block copolymer micelles the synthesis carried out at different temperature gives rise to the spherical nanoparticles in all the cases. However, increasing temperature increases the reaction kinetics drastically, resulting in much faster synthesis of nanoparticles.

We have developed two methods of high-yield synthesis of gold nanoparticles, where the yield can be enhanced by manifold, and are discussed in Chapter 6 [207-209]. In the first method based on step addition, the gold salt is added in small steps for the continuous formation of nanoparticles. This method works as the minimum ratio of block copolymer-to-gold salt can be maintained by the choice of the step size and the resultant yield by the number of steps. The time between two steps is decided by the time required to complete the synthesis in each step. The application of this method is limited by the longer synthesis time which increases as the number of steps increased to increase the yield. In the second method (additional reductant method), the presence of additional reductant (e.g. trisodium citrate) is utilized to enhance the reduction and hence yield. The nanoparticle yield has been found to increase drastically with gold salt concentration in presence of additional reductant and has been synthesized up to two order higher gold salt concentrations than earlier works. This method can be viewed as the additive effect of the enhanced reduction by trisodium citrate with control and stabilization by the block copolymers.

Chapter 7 discusses the optimization of high-yield synthesis of gold nanoparticle for probing their interaction with proteins [220,221]. The stable and high-yield gold nanoparticles using additional reductant method have been synthesized at very low block copolymer concentration to minimize any direct interaction of proteins with the block copolymer. The stability, yield and structure of nanoparticle have been found same

irrespective of the large decrease in block copolymer concentration. The interaction of these gold nanoparticles with two model proteins (lysozyme and BSA) has been examined. It has been found that gold nanoparticles form stable solutions over a wide concentration range of BSA whereas phase separate even with small amount of lysozyme protein at physiological conditions. The stable complexes of gold nanoparticles with BSA protein have been characterized by UV-visible spectroscopy, zeta potential and SANS. The red shift in the SPR peak confirms the adsorption of protein on nanoparticles. The increase in zeta potential of the gold nanoparticles in the presence of BSA also support to the conjugation of protein with nanoparticles. The adsorption of protein on the gold nanoparticles has been modeled in SANS by a core-shell structure consisting of adsorbed proteins forming a shell around the gold nanoparticle.

To summarize, this thesis has provided an extensive study of block copolymer-mediated synthesis of gold nanoparticles as characterized by a combination of techniques. The synthesis has advantages that it is fast, easy to tune and environmentally benign. The role of various components (gold salt, block copolymer and additional reductant) and solution conditions (concentration and temperature) on the optimization of synthesis parameters such as formation rate, yield, stability, structure of gold nanoparticles has been established. Two novel methods (step-addition method and additional reductant method) to achieve stable high yield of gold nanoparticles have been developed. The interaction of these gold nanoparticles with two model proteins (lysozyme and BSA) has been studied. The future interests in this work may involve the utilization of these gold nanoparticles for applications such as in drug delivery [70-73] and bio-sensing [78-81]. In these applications, there is a lot of current interest to develop an understanding of biological effects of nanoparticles and how these effects are mediated by biomolecules that are adsorbed on the nanoparticles under different biological circumstances.

References

1. G. Cao and Y. Wang, *Nanostructures and Nanomaterials: Synthesis, Properties and Applications*; World Scientific: Singapore (2011).
2. D.L. Feldhim and C.A. Foss, Jr., *Metal Nanoparticles: Synthesis, Characterization, and Applications*; Marcel Dekker Inc: New York (2002).
3. A.P. Alivisatos, *Science* **271**, 933 (1996).
4. U. Kreibig and M. Vollmer, *Optical Properties of Metal Clusters*, Vol. 25; Springer: Berlin (1995).
5. A.K. Gupta and M. Gupta, *Biomaterials* **26**, 3995 (2005).
6. M.-C. Daniel and D. Astruc, *Chem. Rev.* **104**, 293 (2004).
7. D.A. Giljohann, D.S. Seferos, W.L. Daniel, M.D. Massich, P.C. Patel and C.A. Mirkin, *Angew. Chem. Int. Ed.* **49**, 3280 (2010).
8. M. Homberger and U. Simon, *Phil. Trans. R. Soc. A* **368**, 1405 (2010).
9. R.A. Sperling, P.R. Gil, F. Zhang, M. Zanella and W.J. Parak, *Chem. Soc. Rev.* **37**, 1896 (2008).
10. M. Faraday, *Philos. Trans. R. Soc. London* **147**, 145 (1857).
11. E.A. Hauser, *Aurum Potabile. J. Chem. Educ.* 456 (1952).
12. G. Savage, *Glass and Glassware*; Octopus Book: London (1975).
13. T. Pradeep, *Nano: The Essentials*; Tata McGraw-Hill: New Delhi (2007).
14. P. Mulvaney, *MRS Bull.* **26**, 1009 (2001).
15. R.P. Feynman, *Eng. Sci.* **23**, 22 (1960).
16. R.P. Feynman, *J. MEMS* **1**, 60 (1992).
17. J.C. Love, L.A. Estroff, J.K. Kriebel, R.G. Nuzzo and G.M. Whitesides, *Chem. Rev.* **105**, 1103 (2005).
18. K. Mougín, E. Gnecco, A. Rao, M.T. Cuberes, S. Jayaraman, E.W. McFarland, H. Haidara and E. Meyer, *Langmuir* **24**, 1577 (2008).
19. P.E. Chow, Ed. *Gold Nanoparticles: Properties, Characterization and Fabrication*; Nova Science Publishers Inc.: New York (2010).
20. S. Eustis and M.A. El-Sayed, *Chem. Soc. Rev.* **35**, 209 (2006).
21. L.M. Liz-Marzán, *Langmuir* **22**, 32 (2006).
22. S.K. Ghosh and T. Pal, *Chem. Rev.* **107**, 4797 (2007).
23. C.A. Mirkin, R.L. Letsinger, R.C. Mucic and J.J. Storhoff, *Nature* **382**, 607 (1996).

24. R. Elghanian, J.J. Storhoff, R.C. Mucic, R.L. Letsinger, C.A. Mirkin, *Science* **277**, 1078 (1997).
25. R. Rigler and H. Vogel, Eds. *Single Molecules and Nanotechnology*; Springer: Berlin (2008).
26. D. Vanmaekelbergh, *Nat. Nanotech.* **4**, 475 (2009).
27. V.H. Grassian, *J. Phys. Chem. C* **112**, 18303 (2008).
28. A. Verma and F. Stellacci, *Small* **6**, 12 (2010).
29. M-A. Neouze and U. Schubert, *Chemical Monthly* **139**, 183 (2008).
30. R.G. Ispasoiu, L. Balogh, O.P. Varnavski, D.A. Tomalia and T. Goodson, III, *J. Am. Chem. Soc.* **122**, 11005 (2000).
31. J. Turkevich, P.C. Stevenson and J. Hillier, *Discuss. Faraday Soc.* **11**, 55 (1951).
32. G. Frens, *Nature (London), Phys. Sci.* **241**, 20 (1973).
33. M.A. Hayat, *Colloidal Gold, Principles, Methods and Applications*; Academic Press: New York (1989).
34. G. Schmid, Ed. *Clusters and Colloids*; VCH: Weinheim (1994).
35. J. Zhou, J. Ralston, R. Sedev and D.A. Beattie, *J. Colloid Interface Sci.* **331**, 251 (2009).
36. K.J. Klabunde and R.M. Richards, *Nanoscale materials in chemistry*; John Wiley & Sons: New Jersey (2009).
37. P. Ghosh, G. Han, M. De, C.K. Kim and V.M. Rotello, *Adv. Drug Del.* **60**, 1307 (2008).
38. G. Schmid, *Chem. Rev.* **92**, 1709 (1992).
39. M. Brust, M. Walker, D. Bethell, D. J. Schiffrin and R. Whyman, *J. Chem. Soc., Chem. Commun.* 801 (1994).
40. A.C. Templeton, W.P. Wuelfing and R.W. Murray, *Acc. Chem. Res.* **33**, 27 (2000).
41. K.C. Grabar, R.G. Freeman, M.B. Hommer and M.J. Natan, *Anal. Chem.* **67**, 735 (1995).
42. Y. Leng, *Materials Characterization: Introduction to Microscopic and Spectroscopic Methods*; John Wiley & Sons: Singapore (2008).
43. V. Amendola and M. Meneghetti. *J. Phys. Chem. C* **113**, 4277 (2009).
44. W. Haiss, N.T.K. Thanh, J. Aveyard and D.G. Fernig, *Anal. Chem.* **79**, 4215 (2007).
45. V.A. Sinani, P. Podsiadlo, J. Lee, N.A. Kotov and K. Kempa, *Int. J. Nanotech.* **4**, 239 (2007).
46. C.D. Geddes, A. Parfenov, I. Gryczynski and J.R. Lakowicz, *Chem. Phys. Lett.* **380**, 269 (2003).
47. T.J. Norman Jr., C.D. Grant, D. Magana and J.Z. Zhang, *J. Phys. Chem. B* **106**, 7005 (2002).

48. F. Boccuzzi, A. Chiorino and M. Manzoli, *Surf. Sci.* **454-456**, 942 (2000).
49. S. Nie and S.R. Emory, *Science* **275**, 1102 (1997).
50. Z. Zhu, T. Zhu and Z. Liu, *Nanotechnology* **15**, 357 (2004).
51. X.-M. Qian and S.M. Nie, *Chem. Soc. Rev.* **37**, 912 (2008).
52. E. Buhr, N. Senftleben, T. Klein, D. Bergmann, D. Gnieser, C.G. Frase and H. Bosse, *Meas. Sci. Technol.* **20**, 084025 (2009).
53. S.P. Hau-Riege, *High-Intensity X-rays - Interaction with Matter: Processes in Plasmas, Clusters, Molecules, and Solids*; Wiley-VCH 2011.
54. A.I. Kirkland and J.L. Hutchison, Ed. *Nanocharacterisation*; RSC Publishing: Cambridge (2007).
55. P.M. Vilarinho, Y. Rosenwaks and A.I. Kingon, *Scanning Probe Microscopy: Characterization, Nanofabrication and Device Application of Functional Materials*. Nato Science Series II; Springer Netherlands: Dordrecht (2005).
56. B. Chu and T. Liu, *J. Nanopart. Res.* **2**, 29 (2000).
57. B.D. Cullity, *Elements of X-ray diffraction*; Addison-Wesley Publishing Company: Massachusetts (1956).
58. B.D. Cullity and S.R. Stock, *Elements of X-Ray Diffraction*; Prentice-Hall Inc.: (2001).
59. P. Scherrer, *Göttinger Nachrichten Gesell.* **2**, 98 (1918).
60. R. Borsali and R. Pecora, *Soft Matter Characterization*; Springer: New York (2008).
61. A. Einstein, *Ann. d. Phys.* **17**, 549 (1905).
62. A. Einstein, *Investigations on The Theory of The Brownian Movement*; Dover Publications, Inc.: Mineola, New York (1956).
63. W. Schärtl, *Light Scattering from Polymer Solutions and Nanoparticle Dispersions*; Springer: Mainz (2007).
64. H. Brumberger, *Modern Aspects of Small-Angle Scattering*; Springer: (2010).
65. S.W. Lovesey, *Theory of neutron scattering from condensed matter*; Oxford University Press: New York (2003).
66. A. Guinier, G. Fournet, K.L. Yudowitch and C.B. Walker, *Small-angle scattering of X-rays*; Wiley: (1995).
67. A. Csáki, R. Möller and W. Fritzsche, *Expert Review of Molecular Diagnostics* **2**, 187 (2002).
68. R.H. Menk, E. Schültke, C. Hall, F. Arfelli, A. Astolfo, L. Rigon, A. Round, K. Ataelmannan, S.R. MacDonald and B.H.J. Juurlink, *Nanomedicine: Nanotechnology, Biology and Medicine* **7**, 647 (2011).

69. J.F. Hainfeld, D.N. Slatkin, T.M. Focella and H.M. Smilowitz, *British Journal of Radiology* **79**, 248 (2006).
70. S.D. Brown, P. Nativo, J.-A. Smith, D. Stirling, P.R. Edwards, B. Venugopal, D.J. Flint, J.A. Plumb, D. Graham and N.J. Wheate, *J. Am. Chem. Soc.* **132**, 4678 (2010).
71. G. Han, P. Ghosh and V.M. Rotello, *Nanomedicine* **2**, 113 (2007).
72. P.K. Jain, I.H. El-Sayed and M.A. El-Sayed, *Nano Today* **2**, 18 (2007).
73. G. Han, C.-C. You, B.-j. Kim, R.S. Turingan, N.S. Forbes, C.T. Martin and V.M. Rotello, *Angew. Chem., Int. Ed.* **45**, 3165 (2006).
74. P.M. Bendix, S.N.S. Reihani and L.B. Oddershede, *ACS Nano* **4**, 2256 (2010).
75. D. Pissuwan, S.M. Valenzuela and M.B. Cortie, *Trends Biotechnol.* **24**, 62 (2006).
76. L.C. Kennedy, L.R. Bickford, N.A. Lewinski, A.J. Coughlin, Y. Hu, E.S. Day, J.L. West and R.A. Drezek, *Small* **7**, 169 (2011).
77. M.R. Choi, K.J. Stanton-Maxey, J.K. Stanley, C.S. Levin, R. Bardhan, D. Akin, S. Badve, J. Sturgis, J.P. Robinson, R. Bashir, N.J. Halas and S.E. Clare, *Nano Lett.* **7**, 3759 (2007).
78. J. Zhang, S. Song, L. Wang, D. Pan and C. Fan, *Nature Protocols* **2**, 2888 (2007).
79. T.A. Klar, *Nanophotonics with Surface Plasmons*. Eds. V. Shalaev and S. Kawata; Elsevier: The Netherlands (2007) pp. 219-270.
80. C.A. Mirkin, R.L. Letsinger, R.C. Mucic and J.J. Storhoff, *Nature* **382**, 607 (1996).
81. R. Elghanian, J.J. Storhoff, R.C. Mucic, R.L. Letsinger and C.A. Mirkin, *Science* **277**, 1078 (1997).
82. H. Grabert, *Z. Phys. B* **85**, 319 (1991).
83. G. Schmid and U. Simon, *Chem. Commun.* **6**, 697 (2005).
84. G. Schmid, *Chem. Soc. Rev.* **37**, 1909 (2008).
85. U. Simon, G. Schön and G. Schmid, *Angew. Chem. Int. Ed.* **32**, 250 (1993).
86. E. Koplín and U. Simon, *Application of metal nanoclusters in nanoelectronics*. In *Metal nanoparticles in catalysis and materials science: the issue of size control*. Eds B. Corain, G. Schmid and H. Toshima; Elsevier: Weinheim (2007) pp. 107-128.
87. D. Astruc, Ed. *Nanoparticles and Catalysis*; Wiley-VCH Verlag: Weinheim (2008).
88. R.M.T. Sanchez, A. Ueda, K. Tanaka and M. Haruta, *J. Catal.* **168**, 125 (1997).
89. A.S.K. Hashmi and G.J. Hutchings, *Angew. Chem., Int. Ed.* **45**, 7896 (2006).
90. D.T. Thompson, *Nanotoday* **2**, 40 (2007).
91. M.B. Cortie and E. van der Lingen, *Materials Forum* **26**, 1 (2002).
92. M.K. Corbierre and R.B. Lennox, *Chem. Mater.* **17**, 5691 (2005).

93. J. Polte, T.T. Ahner, F. Delissen, S. Sokolov, F. Emmerling, A.F. Thunemann and R. Kraehnert, *J. Am. Chem. Soc.* **132**, 1296 (2010).
94. P. Alexandridis, *Chem. Eng. Technol.* **34**, 15 (2011).
95. T. Sakai and P. Alexandridis, *Langmuir* **20**, 8426 (2004).
96. T. Sakai and P. Alexandridis, *Nanotechnology* **16**, S344 (2005).
97. T. Sakai and P. Alexandridis, *J. Phys. Chem. B* **109**, 7766 (2005).
98. T. Sakai and P. Alexandridis, *Langmuir* **21**, 8019 (2005).
99. W.M. Tolles, *MRS Bull.* **25**, 36 (2000).
100. M. Boncheva and G.M. Whitesides, *MRS Bull.* **30**, 736 (2005).
101. M. Lazzari, C. Rodriguez-Abreu, J. Rivas and M.A. Lopez-Quintela, *J. Nanosci. Nanotechnol.* **6**, 892 (2006).
102. C.T. Seto and G.M. Whitesides, *J. Am. Chem. Soc.* **112**, 6409 (1990).
103. J.S. Manka and D.S. Lawrence, *J. Am. Chem. Soc.* **112**, 2440 (1990).
104. U. Koert, M.M. Harding and J.-M. Lehn, *Nature (London)* **346**, 339 (1990).
105. I.W. Hamley, *Introduction to Soft Matter*; Wiley: Chichester (2000).
106. L. Leibler, *Macromolecules* **13**, 1602 (1980).
107. F.S. Bates, *Science* **251**, 898 (1991).
108. G.H. Fredrickson and F.S. Bates, *Annu. Rev. Mater. Sci.* **26**, 501 (1996).
109. H.-A. Klok, S. Lecommandoux, *Adv. Mater.* **13**, 1217 (2001).
110. Z. Zhong, H. Lee, S. Shen and A. Gedanken, *Soft Matter* **5**, 2558 (2009).
111. P. Alexandridis and B. Lindman, *Amphiphilic Block Copolymers: Self-Assembly and Applications*; Elsevier: Amsterdam (2000).
112. V.K. Aswal and J. Kohlbrecher, *Chem. Phys. Lett.* **425**, 118 (2006).
113. I.W. Hamley, *Block Copolymers in Solution: Fundamentals and Applications*; Wiley: New York (2005).
114. T. Smart, H. Lomas, M. Massignani, M.V. Flores-Merino, L.R. Perez and G. Battaglia, *Nanotoday* **13**, 38 (2008).
115. A.H.E. Müller and O. Borisov, *Self Organized Nanostructures of Amphiphilic Block Copolymers II (Advances in Polymer Science)*; Springer: (2011).
116. V.M. Nace, Nace Nace and V.Ed. Nace, *Nonionic Surfactants: Polyoxyalkylene Block Copolymer*; CRC Press: (1996).
117. J. Rodriguez-Hernandez, F. Checot, Y. Gnanou and S. Lecommandoux, *Progress in Polymer Science* **30**, 691 (2005).
118. I.R. Schmolka, *J. Am. Oil Chem. Soc.* **54**, 110 (1977).

119. N.S. Cameron, M.K. Corbierre and A. Eisenberg, *Can. J. Chem.* **77**, 1311 (1999).
120. J.F. Ding, G.J. Liu, M.L. Yang, *Polymer* **38**, 5497 (1997).
121. S. Foerster, Amphiphilic block copolymers for templating applications. *Topics in Current Chemistry*, 226 (Colloid Chemistry I); 1 (2003).
122. S. Forster and T. Plantenberg, *Angewandte Chemie, International Edition* **41**, 688 (2002).
123. Z. Tuzar, P. Štěpánek, Č. Koňák and P. Kratochvíl, *J. Colloid Interface Sci.* **105**, 372 (1985).
124. K. Mortensen, *J. Phys.: Condens. Matter* **8**, A103 (1996).
125. M.W. Urban, Ed. *Handbook of Stimuli-Responsive Materials*; Wiley-VCH: (2011).
126. D. Han, X. Tong and Y. Zhao, *Langmuir* **28**, 2327 (2012).
127. C. He, C. Zhao, X. Chen, Z. Guo, X. Zhuang and X. Jing, *Macromolecular Rapid Communications* **29**, 490 (2008).
128. T.J. Martin, K. Prochazka, P. Munk and S.E. Webber, *Macromolecules* **29**, 6071 (1996).
129. M.W. Edens and R.H. Whitmarsh, *Applications of Block Copolymer Surfactants. In Developments in Block Copolymer Science and Technology*. I.W. Hamley, Ed.; John Wiley & Sons: Chichester (2004).
130. H. Endo, J. Allgaier, G. Gompper, B. Jakobs, M. Monkenbusch, D. Richter, T. Sottmann, and R. Strey, *Phys. Rev. Lett.* **85**, 102 (2000).
131. G. Gaucher, M.-H. Dufresne, V.P. Sant, N. Kang, D. Maysinger and J.-C. Leroux, *Journal of Controlled Release* **109**, 169 (2005).
132. B. Jeong, Y.H. Bae, D.S. Lee and S.W. Kim, *Nature* **388**, 860 (1997).
133. I.W. Hamley, *Nanotechnology* **14**, R39 (2003).
134. D. Zhao, J. Feng, Q. Huo, N. Melosh, G.H. Fredrickson, B.F. Chmelka and G.D. Stucky, *Science* **279**, 548 (1998).
135. K. Yu, A.J. Hurd, A. Eisenberg and C.J. Blinker, *Langmuir* **17**, 7961 (2001).
136. K. Yu, B. Smarsly and C.J. Brinker, *Adv. Functional Mater.* **13**, 47 (2003).
137. S. Bhaviripudi, A. Reina, Jifa Qi, J. Kong and A.M. Belcher, *Nanotechnology* **17**, 5080 (2006).
138. R.E. Cohen, *Curr. Opin. Sol. Stat. Mater. Sci.* **4**, 587 (1999).
139. L. Wang and Y. Yamauchi, *J. Am. Chem. Soc.* **131**, 9152 (2009).
140. P.K. Jain, I.H. El-Sayed and M.A. El-Sayed, *Nanotoday* **2**, 18 (2007).
141. J. Shan and H. Tenhu, *Chem. Commun.* 2007, 4580.

142. S.K. Bajpai, Y.M. Mohan, M. Bajpai, R. Tankhiwale and V. Thomas, *J. Nanosci. Nanotechnol.* **7**, 2994 (2007).
143. S. Goy-Lopez, E. Castro, P. Taboada and V. Mosquera, *Langmuir* **24**, 13186 (2008).
144. T.K. Sau and C.J. Murphy, *J. Am. Chem. Soc.* **126**, 8648 (2004).
145. P. Alexandridis and M. Tsianou, *Eur. Polym. J.* **47**, 569 (2011).
146. P. Khullar, A. Mahal, V. Singh, T.S. Banipal, G. Kaur and M.S. Bakshi, *Langmuir* **26**, 11363 (2010).
147. M.P. Pileni, *Metal Particles Made in Various Colloidal Self-Assemblies: Syntheses and Properties*. In *Fine Particles: Synthesis, Characterization, and Mechanisms of Growth*; T. Sugimoto, Ed.; Marcel Dekker: New York (2000).
148. P. Barnickel and A. Wokaun, *Mol. Phys.* **69**, 1 (1990).
149. L. Wang, X. Chen, J. Zhan, Z. Sui, J. Zhao and Z. Sun, *Chem. Lett.* 2004, **33**, 720.
150. L.M. Liz-Marzan and I. Lado-Tourino, *Langmuir* **12**, 3585 (1996).
151. H. Beyer and W. Walter, In *Lehrbuch der Organischen Chemie*; Hirzel (1981).
152. K.-J. Liu, *Macromolecules* **1**, 308 (1968).
153. B.J. Elliott, A.B. Scranton, J.H. Cameron and C.N. Bowman, *Chem. Mater.* **12**, 633 (2000).
154. A. Warshawsky, R. Kalir, A. Deshe, H. Berkovitz and A. Patchornik, *J. Am. Chem. Soc.* **101**, 4249 (1979).
155. S. Yanagida, K. Takahashi and M. Okahara, *Bull. Chem. Soc. Jpn.* **50**, 1386 (1977).
156. Y. Sakai, K. Ono, T. Hidaka, M. Takagi and R.W. Cattrall, *Bull. Chem. Soc. Jpn.* **73**, 1165 (2000).
157. L. Longenberger and G. Mills, *J. Phys. Chem.* **99**, 475 (1995).
158. G. Cao, *Nanostructures and Nanomaterials: Synthesis, Properties, and Applications*; Imperial College Press: London (2004).
159. D.L. Feldhim and C.A. Foss, Jr., *Metal Nanoparticles: Synthesis, Characterization, and Applications*; Marcel Dekker Inc: New York (2002).
160. Y. Leng, *Materials Characterization: Introduction to Microscopic and Spectroscopic Methods*; John Wiley & Sons: Singapore (2008).
161. V. Amendola and M. Meneghetti. *J. Phys. Chem. C* **113**, 4277 (2009).
162. W. Haiss, N.T.K. Thanh, J. Aveyard and D.G. Fernig, *Anal. Chem.* **79**, 4215 (2007).
163. U. Kreibig and M. Vollmer, *Optical Properties of Metal Clusters*; Springer-Verlag: New York (1995).
164. K.L. Kelly, E. Coronado, L.L. Zhao and G.C. Schatz, *J. Phys. Chem. B* **107**, 668 (2003).

165. J.H. Lambert, *Photometria sive de mensura et gradibus luminis, colorum et umbrae* [Photometry, or, On the measure and gradations of light, colors, and shade] (Augsburg ("Augusta Vindelicorum"), Germany: Eberhardt Klett (1760) p. 391.
166. Beer, Bestimmung der Absorption des rothen Lichts in farbigen Flüssigkeiten (Determination of the absorption of red light in colored liquids), *Annalen der Physik und Chemie* 86, 78 (1852).
167. C.J. Murphy, *Anal. Chem.* **74**, 520A (2002).
168. S. Kumar, J. Aaron and K. Sokolov, *Nature Protocols* **3**, 314 (2008).
169. D.B. Williams and C.B. Carter, *Transmission Electron Microscopy: A Textbook for Materials Science*; Springer: (2009).
170. N.P. Young, M.A. van Huis, H.W. Zandbergen, H. Xu and A.I. Kirkland, *Ultramicroscopy* **110**, 506 (2010).
171. W. Brown, *Light Scattering: Principles and Development*; Oxford University Press: New York (1996).
172. R. Pecora, *Dynamic Light Scattering*; New York: Plenum (1985).
173. P. Lindner and Th. Zemb, *Neutrons, X-rays and Light Scattering Methods Applied to Soft Condensed Matter*; North Holland: North Holland Delta Series (2002).
174. B.J. Berne and R. Pecora, *Dynamic Light Scattering With Applications to Chemistry, Biology, and Physics*; John Wiley and Sons: (2000).
175. H. Jans, X. Liu, L. Austin, G. Maes and Q. Huo, *Anal. Chem.* **81**, 9425 (2009).
176. A. Guinier and G. Fournet, *Small-Angle Scattering of X-Rays*, John Wiley & Sons: New York (1955).
177. O. Glatter and O. Kratky, *Small-Angle X-Ray Scattering*, Academic Press: New York (1982).
178. S.H. Chen and T.L. Lin, In *Methods of Experimental Physics*, D.L. Price and K. Skold, Eds.; Academic Press: New York (1987).
179. L.A. Feigin and D.I. Svergun, *Structure Analysis by Small-Angle Neutron X-ray and Neutron Scattering*; Plenum Press: New York (1987).
180. J.S. Pedersen, *Adv. Colloid Interface Sci.* **70**, 171 (1997).
181. J.S. Pedersen, *J. Appl. Crystallogr.* **33**, 637 (2000).
182. J.K. Percus and G. Yevik, *J. Phys. Rev.* **110**, 1 (1958).
183. R.V. Sharma and K.C. Sharma, *Physica A* **89**, 213 (1977).
184. P.A. Egelstaff, *An Introduction to Liquid State Physics*; Academic Press: London (1967).

185. L. Reatto and M. Tau, *Chem. Phys. Lett.* **292**, 108 (1984).
186. M. Ballauff, *Advanced Engineering Materials* **13**, 793 (2011).
187. A.E. Whitten and J. Trehwella, *Micro and Nano Technologies in Bioanalysis Methods in Molecular Biology* **544**, 307 (2009).
188. V.K. Aswal and P.S. Goyal, *Curr. Sci. India* **79**, 947 (2000).
189. J. Kohlbrecher and W. Wagner, *J. Appl. Cryst.* **33**, 804 (2000).
190. J.P. Rao and K.E. Geckeler, *Progress in Polymer Science* **36**, 887 (2011).
191. D. Ray and V.K. Aswal, *AIP Conf. Proc.* **1202**, 219 (2009).
192. D. Ray, V.K. Aswal and D. Srivastava, *J. Nanosci. Nanotechnol.* **10**, 6356 (2010).
193. D. Ray, V.K. Aswal and D. Srivastava, *Int. J. Nanosci.* **10**, 1035 (2011).
194. D. Ray, V.K. Aswal and J. Kohlbrecher, *AIP Conf. Proc.* (2012), in press.
195. D. Ray and V.K. Aswal, 20th Annual General Meeting of Materials Research Society of India, Saha Institute of Nuclear Physics, Kolkata, India (2009).
196. D. Ray and V.K. Aswal, *Proceedings of DAE Solid State Physics Symposium* **54**, 303 (2009).
197. K. Mortensen, *Polym. Adv. Technol.* **12**, 2 (2001).
198. P. Alexandridis, J.F. Holzwarthf and T.A. Hatton, *Macromolecules* **27**, 2414 (1994).
199. P. Alexandridis and T.A. Hatton, *Colloids and Surfaces A: Physicochemical and Engineering Aspects* **96**, 1 (1995).
200. B. Clover and B. Hammouda, *Langmuir* **26**, 6625 (2010).
201. G. Riess, *Prog. Polym. Sci.* **28**, 1107 (2003).
202. D. Ray, V.K. Aswal and D. Srivastava, *J. Nanosci. Nanotechnol.* **11**, 1905 (2011).
203. L. Jyoti, D. Ray and V.K. Aswal, *Proceedings of DAE Solid State Physics Symposium* **54**, 285 (2009).
204. L. Jyoti, D. Ray and V.K. Aswal, *Conference on Neutron Scattering and Mesoscopic Systems, International Centre/Goa University, Goa, India* (2009).
205. D. Ray and V.K. Aswal, 1st Asia-Oceania Conference on Neutron Scattering, held at Tsukuba, Japan (2011).
206. C.J. Murphy, L.B. Thompson, A.M. Alkilany, P.N. Sisco, S.P. Boulos, S.T. Sivapalan, J.A. Yang, D.J. Chernak and J. Huang, *J. Phys. Chem. Lett.* **1**, 2867 (2010).
207. D. Ray and V.K. Aswal, *J. Macromol. Sci. Part B: Phys.* **49**, 810 (2010).
208. D. Ray, V.K. Aswal and J. Kohlbrecher, *AIP Conf. Proc.* **1313**, 192 (2010).
209. D. Ray, V.K. Aswal and J. Kohlbrecher, *Langmuir* **27**, 4048 (2011).

210. D. Ray and V.K. Aswal, Conference on Neutron Scattering and Mesoscopic Systems, International Centre/Goa University, Goa, India (2009).
211. D. Ray, V.K. Aswal and D. Srivastava, SERC School-cum-Conference on Rheology of Complex Fluids, IIT Madras, Chennai, India (2010).
212. D. Ray, V.K. Aswal and D. Srivastava, International Conference on Advances in Electron Microscopy and Related Techniques, held at BARC, Mumbai, India (2010).
213. D. Ray and V.K. Aswal, *Nanosci. Nanotechnol. Lett.* **3**, 603 (2011).
214. D. Ray and V.K. Aswal, *AIP Conf. Proc.* **1349**, 405 (2011).
215. D. Ray and V.K. Aswal, 3rd International Symposium on Materials Chemistry, held at BARC, Mumbai, India (2010).
216. S.H. Brewer, W.R. Glomm, M.C. Johnson, M.K. Knag and S. Franzen, *Langmuir* **21**, 9303 (2005).
217. P. Roach, D. Farrar and C.C. Perry, *J. Am. Chem. Soc.* **128**, 3939 (2006).
218. M.-E. Aubin-Tam and K. Hamad-Schifferli, *Biomed. Mater.* **3**, 034001 (2008).
219. I. Lynch, T. Cedervall, M. Lundqvist, C. Cabaleiro-Lago, S. Linse and K.A. Dawson, *Advances in Colloid and Interface Science* **134-135**, 167 (2007).
220. D. Ray and V.K. Aswal, *J. Nanopart. Res.* **14**, 778 (2012).
221. D. Ray and V.K. Aswal, International Conference on Nanoscience and Nanotechnology, held at Hyderabad, India (2012).
222. M. von Smoluchowski, "Zur kinetischen Theorie der Brownschen Molekularbewegung und der Suspensionen" (in German). *Annalen der Physik* **326**, 756 (1906).
223. T.H.L. Nghiem, T.H. La, X.H. Vu, V.H. Chu, T.H. Nguyen, Q.H. Le, E. Fort, Q.H. Do and H.N. Tran, *Adv. Nat. Sci.: Nanosci. Nanotechnol.* **1**, 025009 (2010).

List of Publications

In Refereed Journals

1. *Step-addition method for enhancing the yield of gold nanoparticles in block copolymer solution*

D. Ray and V.K. Aswal

J. Macromol. Sci. Part B: Phys. **49**, 810-820 (2010).

2. *Concentration Effect on Tuning of Block Copolymer-mediated Synthesis of Gold Nanoparticles*

D. Ray, V.K. Aswal and D. Srivastava

J. Nanosci. Nanotechnol. **10**, 6356-6362 (2010).

3. *Correlating Self-Assembly of Block Copolymers for their Application in Synthesis of Gold Nanoparticles*

D. Ray, V.K. Aswal and D. Srivastava

J. Nanosci. Nanotechnol. **11**, 1905-1913 (2011).

4. *Synthesis and Characterization of High Concentration Block Copolymer-mediated Gold Nanoparticles*

D. Ray, V.K. Aswal and J. Kohlbrecher

Langmuir **27**, 4048-4056 (2011).

5. *Tuning of block copolymer-mediated synthesis of gold nanoparticles*

D. Ray, V.K. Aswal and D. Srivastava

Int. J. Nanosci. **10**, 1035-1038 (2011).

6. *Multi-technique Approach for the Study of Block Copolymer-mediated Gold Nanoparticles*

D. Ray and V.K. Aswal

Nanosci. Nanotechnol. Lett. **3**, 603-611 (2011).

7. *Optimization of Components in High-yield Synthesis of Block copolymer-mediated Gold Nanoparticles*

D. Ray and V.K. Aswal

J. Nanopart. Res. **14**, 778 (2012).

8. *Probing Protein Adsorption on Gold Nanoparticles*

D. Ray and V.K. Aswal

(Under preparation).

9. *SANS Studies of Temperature-dependent Block Copolymer-mediated Synthesis of Gold Nanoparticles*

D. Ray, V.K. Aswal and J. Kohlbrecher

(Under preparation).

In Conferences and Symposia:

1. *SANS studies insight into improving of yield of block copolymer-stabilized gold nanoparticles*

D. Ray and V.K. Aswal

AIP Conf. Proc. 1202, 219-224 (2009).

2. *Room Temperature, High-yield Synthesis of Block Copolymer-mediated Gold Nanoparticles*

D. Ray, V.K. Aswal and J. Kohlbrecher

AIP Conf. Proc. 1313, 192-194 (2010).

3. *Block copolymer-mediated gold nanoparticles: Small-angle scattering studies*

D. Ray and V.K. Aswal

Acta Cryst. A67, C401 (2011).

4. *Combined Small-angle Neutron and X-ray Scattering Studies of Block Copolymer-mediated Gold Nanoparticles*

D. Ray and V.K. Aswal

AIP Conf. Proc. 1349, 405-406 (2011).

5. *Block Copolymer-dependence on High-Yield Synthesis of Gold Nanoparticles*

D. Ray, V.K. Aswal and J. Kohlbrecher

AIP Conf. Proc. (in press).

6. *Synthesis and characterization of block copolymer stabilized gold nanoparticles in aqueous solution at room temperature*

D. Ray and V.K. Aswal

20th Annual General Meeting of Materials Research Society of India, Saha Institute of Nuclear Physics, Kolkata, India (2009).

7. *SANS study reveals for enhancing the yield of Gold Nanoparticles in Block Copolymer Solution*

D. Ray and V.K. Aswal

Conference on Neutron Scattering and Mesoscopic Systems, International Centre/Goa University, Goa, India (2009).

8. *SANS Study for Correlating Self-Assembly of Block Copolymers for their Application in Synthesis of Gold Nanoparticles*

L. Jyoti, **D. Ray** and V.K. Aswal

Conference on Neutron Scattering and Mesoscopic Systems, International Centre/Goa University, Goa, India (2009).

9. *Concentration Dependence Tuning of Block Copolymer-mediated Synthesis of Gold Nanoparticles*

D. Ray and V.K. Aswal

Proceedings of DAE Solid State Physics Symposium 54, 303 (2009).

10. *Effect of Variation of Chemical Structure of Block Copolymer on the Synthesis of Gold Nanoparticles*

L. Jyoti, **D. Ray** and V.K. Aswal

Proceedings of DAE Solid State Physics Symposium 54, 285 (2009).

11. *Synthesis and Characterization of Block Copolymer-mediated Gold Nanoparticles*

D. Ray, V.K. Aswal and D. Srivastava

SERC School-cum-Conference on Rheology of Complex Fluids, IIT Madras, Chennai, India (2010).

12. *Synthesis and Characterization of Block Copolymer-mediated Gold Nanoparticles*

D. Ray, V.K. Aswal and D. Srivastava

International Conference on Advances in Electron Microscopy and Related Techniques, held at BARC, Mumbai, India (2010).

13. *Synthesis and Characterization of High-Yield Gold Nanoparticles*

D. Ray and V.K. Aswal

Mumbai-Pune Soft Matter Meeting, held at IIT Bombay, Mumbai, India (2010).

14. *Multi-technique Approach for the Characterization of Block Copolymer-mediated Gold Nanoparticles*

D. Ray and V.K. Aswal

3rd International Symposium on Materials Chemistry, held at BARC, Mumbai, India (2010).

15. *Multi-technique Approach for the Study of Block Copolymer-mediated Gold Nanoparticles*

D. Ray, V.K. Aswal, J. Kohlbrecher, E. Venugopal, G. Kumaraswamy and D. Srivastava

Mumbai-Pune Soft Matter Meeting, held at TIFR, Mumbai, India (2011).

16. *High Yield Synthesis of Gold Nanoparticles for their Interaction with Proteins*

D. Ray, S. Kumar and V.K. Aswal

Mumbai-Pune Soft Matter Meeting, held at NCL, Pune, India (2011).

17. *Stimuli-responsive tuning of Block Copolymer-mediated Gold Nanoparticles as characterized by SANS*

D. Ray and V.K. Aswal

1st Asia-Oceania Conference on Neutron Scattering, held at Tsukuba, Japan (2011).

18. *Probing Protein Adsorption on Gold Nanoparticles*

D. Ray and V.K. Aswal

International Conference on Nanoscience and Nanotechnology, held at Hyderabad, India (2012).